

**Rotating Machine Fault Diagnostics Using Vibration and
Acoustic Emission Sensors**

BY

RUOYU LI

B.S., Automatic Control, Guilin Institute of Electronic Technology, 2002
M.S., Control Theory & Control Engineering, Guilin Institute of Electronic Technology, 2005

THESIS

Submitted as partial fulfillment of the requirements
for the degree Doctor of Philosophy in Industrial Engineering and Operations Research
in the Graduate College of the
University of Illinois at Chicago, 2012

Chicago, Illinois

Defense Committee:

David He, Chair and Advisor
Houshang Darabi
Sabri Cetinkunt
Thomas Royston
Eric Bechhoefer, NRG Systems Inc.

*Dedicated to my parents, Bihua Li and Guifang Chen,
and my grandparents, Shilun Li and Shufang Jiang.*

ACKNOWLEDGEMENTS

During my Ph.D. study at University of Illinois at Chicago, I have fortunately received scientific, technical, moral, and/or financial support from my advisor, colleagues, friends and family.

First of all, I would like to thank my academic advisor Dr. David He for his encouragement, supervision and support throughout my doctoral study. I appreciate all of his contributions of time, ideas, and funding to make my Ph.D. research productive and exciting. I would not have completed this dissertation without the guidance and support of Dr. He.

I express my sincere gratitude to Dr. Eric Bechhoefer from NRG System Inc. for his helpful comments, encouragement, and support during my research. I also would like to acknowledge my defense committee members Dr. Thomas Royston, Dr. Houshang Darabi, and Dr. Sabri Cetinkunt for their time and valuable suggestions necessary to complete this dissertation.

I would also like to thank Junda Zhu for helping me with the drawing of the 3D gear models.

Finally, and most importantly, I would thank my parents, Bihua Li and Guifang Chen and my grandparents, Shilun Li and Shufang Jiang for all their love, encouragement, and support. Without you, none of this would have been possible.

SUMMARY

Rotating machines are widely used in various industrial applications. Implementation of condition based maintenance for rotating machines is becoming necessary in order to prevent failure, increase availability, and decrease maintenance cost. Rotating machine fault detection and diagnostics is a critical component of condition based maintenance. In order for condition based maintenance to work for rotating machines, especially for new designs and materials, effective and advanced rotational machine fault detection and diagnostic methods and tools need to be developed. In developing rotating machine fault detection and diagnostics algorithms, one critical issue is signal processing based fault feature extraction or quantification. Currently, vibration signal based techniques are the most widely used techniques in rotating machinery fault detection and diagnosis. However, the current vibration signal processing methods for rotating machine fault detection and diagnostics have their own limitations. In practice, the faulty vibration signals are often buried into the vibration signals generated by the healthy components and mechanical background noises. Investigating and developing new advanced signal processing methods based vibration signal fault feature extraction methods and fault detection methods and tools is necessary. To do so, two advanced signal processing methods, empirical mode decomposition and interference cancellation algorithm has been investigated and developed in this dissertation.

Recently, acoustic emission signal based methods are attracting researchers' interests because acoustic emission signals have some advantages over the vibration signals.

SUMMARY (continued)

Unlike vibration signals, advanced signal processing techniques for extracting fault features from acoustic emission signals have not been well developed for rotating machine fault detection and diagnostics. Development of acoustic emission signal quantification methods and diagnostic methods and tools are in a great need. In this dissertation, acoustic emission signal quantification methodologies using Laplace wavelet and empirical mode decomposition have been developed.

Plastic bearings are widely used in medical applications, food processing industries, semi-conductor industries, and aircraft components. Unlike their steel counterparts, effective fault diagnosis methods for plastic bearings have not been developed. In reviewing steel bearing fault diagnostic approaches reported in the literature, a common practice of using vibration fault features to diagnose all bearing faults in one step has been observed. The vibration fault features are not equally sensitive to all bearing faults. Moreover, the fault impulses generated by the plastic bearings are more random and weaker than those of the steel bearings. Therefore, developing effective bearing fault diagnostic method using different fault features at different steps becomes more attractive. In this dissertation, a two-step data mining based approach for plastic bearing fault diagnostics using vibration based condition indicators (CIs) have been developed.

To validate the effectiveness of the developed diagnostic methods and tools, seeded fault test data are needed. To obtain seeded fault test data, a split-torque type gearbox test rig has been designed and developed. The seeded fault experiments have been designed and

SUMMERY (continued)

conducted on both the split-torque gearbox test rig and the bearing run-to-failure test rig. The developed fault detection and diagnostic methods and tools have been validated using the seeded fault test data collected.

Specifically, the contributions of the dissertation are summarized as follows:

- (1) An empirical mode decomposition based vibration feature and condition indicator extraction methodology for rotating machinery fault detection and diagnosis has been developed.
- (2) A two-step vibration signal based bearing fault diagnostics methodology for plastic bearings has been developed.
- (3) A vibration signal based gear fault detection system based on interference cancellation has been developed.
- (4) A Laplace wavelet based acoustic emission signal quantification methodology for rotating machinery fault detection and diagnostics has been developed.
- (5) An empirical mode decomposition based acoustic emission quantification methodology has been developed.
- (6) A notional split-torque gearbox test rig has been designed and developed.
- (7) Experiments have been designed and implemented on the custom designed notional split-torque gearbox test rig and bearing run-to-failure test rig. Both vibration and acoustic emission signals have been collected during the experiments. The effectiveness of the developed methodologies has been validated by the bearing and gear seeded fault test data.

TABLE OF CONTENTS

<u>CHAPTER</u>	<u>PAGE</u>
1 INTRODUCTION	1
1.1 Research Motivation	1
1.2 Goal and Objectives	4
1.3 Contributions of the Dissertation	4
1.4 The Outline	7
2 LITERATURE REVIEW	9
2.1 Rotating Machine Fault Detection and Diagnostics	9
2.2 Rotating Machinery Fault Detection and Diagnostic Techniques	10
3 DESIGN AND DEVELOPMENT OF NOTIONAL SPLIT TORQUE GEARBOX TEST RIG.....	15
3.1 Notional STG Type Gearbox	17
3.2 Sensors and Data Acquisition Systems	22
3.3 Drive and Loading Systems	29
4 VIBRATION SIGNAL BASED ROTATING MACHINERY FAULT DETECTION AND DIAGNOSIS	31
4.1 Introduction.....	31
4.2 Theoretical Basis.....	36
4.2.1 Hilbert-Huang Transform	36
4.2.2 Statistical Threshold for Machine Fault Detection	51
4.2.3 Adaptive Narrowband Interference Cancellation	52

TABLE OF CONTENTS

<u>CHAPTER</u>	<u>PAGE</u>
4.2.4 Threshold Based De-noising.....	57
4.2.5 The K-Nearest Neighbor (KNN) Based Fault Classifier [134]	59
4.3 Experimental Setup and Data Acquisition.....	61
4.3.1 Gear Test Experimental Setup and Data Acquisition	61
4.3.2 Bearing Test Experimental Setup and Data Acquisition	64
4.4 EMD Based Vibration Feature Extraction and CI Development.....	73
4.4.1 Case Study I: Split Torque Gear Fault Diagnostics	75
4.4.2 Case Study II: Full Ceramic Bearing Fault Diagnostics.....	82
4.5 A Two-Step Vibration Signal Based Plastic Bearing Fault Diagnostics	92
4.5.1 Frequency Features of Plastic Bearings.....	94
4.5.2 Case Study: Plastic Bearing Fault Diagnostics.....	101
4.6 Interference Cancellation Based Gear Fault Detection.....	117
5 AE BASED ROTATING MACHINERY FAULT DETECTION AND	
DIAGNOSIS	127
5.1 Introduction.....	127
5.2 Theoretical Basis.....	132
5.2.1 Laplace Wavelet.....	132
5.3 Experiment Setup and Data Acquisition.....	137
5.3.1 Pencil Break Test for Sampling Rate Selection	137
5.3.2 Gear Seeded Fault Test	140

TABLE OF CONTENTS (continued)

<u>CHAPTER</u>	<u>PAGE</u>
5.3.3 Full Ceramic Bearing Fault Test.....	143
5.4 Traditional AE Feature Based Gear Fault Detection	144
5.5 Laplace Wavelet Based AE Signal Quantification Methodology.....	152
5.5.1 Case Study: STG Gear Test Rig Experiment.....	162
5.6 EMD Based AE Quantification Methodology	172
5.6.1 The EMD Based AE Feature Quantification	174
5.6.2 The Statistical Analysis Based Fault Detection	176
5.6.3 Gear Seeded Fault Case Study Results	177
6 CONCLUSIONS.....	191
CITED LITERATURE	193
VITA	212

LIST OF TABLES

<u>TABLE</u>	<u>PAGE</u>
I. Major Parameters of the gears	20
II. Parameters of the 603C01 accelerometer	25
III. Parameters of the WD type acoustic emission sensor.....	27
IV. Materials comparison among plastic bearings, steel bearings and ceramic bearings	67
V. Parameters of the 6025 2RS bearing.....	71
VI. The classification confusion matrix using the two dimensional CIs of the STG gearbox	80
VII. The KNN fault diagnosis results using the two dimensional CIs of the STG gearbox	81
VIII. The classification confusion matrix using the two dimensional CIs	90
IX. The KNN fault diagnosis results using the two dimensional CIs	91
X. Fundamental frequency rate.....	96
XI. The classification results of the KNN algorithm using frequency domain CIs	108
XII. The classification results of the KNN algorithm using time domain CIs at the second step of the two-step approach.....	114
XIII. The Two-Step classification results	115
XIV. The one step classification results using only time domain CIs	116
XV. The one step classification results using combination of frequency domain and time domain CIs	117
XVI. The RMS and SNR of the AE bursts under different sampling rates	140
XVII. The confusion matrix for fault detection using AE signals.....	149
XVIII. The confusion matrix for fault detection using vibration	151
XIX. The AE features of the gearbox with 0% damage level.....	162
XX. The feature of the gearbox with 20% damage	163
XXI. The features of the gearbox with 50% damage.....	164

LIST OF TABLES (continued)

<u>TABLE</u>		<u>PAGE</u>
XXII.	The features of the gearbox with 100% damage.....	165
XXIII.	The AE features of both healthy gearbox and damaged gearbox	182
XXIV.	The energy ratio means and the standard deviations of the first four IMF components of both healthy gearbox and damaged gearbox	187
XXV.	Comparison of % compressed fault features that are greater than the fault detection threshold	189

LIST OF FIGURES

<u>FIGURE</u>	<u>PAGE</u>
1. The notional STG type gearbox	17
2. Schematic drawing of the notional STG type gearbox	19
3. Schematic of the experimental setup	22
4. The model 603c01 accelerometer	25
5. The WD type acoustic emission sensor	27
6. The locations of the sensors	29
7. The simulated Gaussian noise signal	41
8. The Fourier spectrum of the simulated Gaussian noise signal	41
9. The Fourier spectrum of the IMF components of the simulated signal	43
10. The gear test rig	44
11. The simplified structure of the gearbox	45
12. The damaged gear with tooth loss	46
13. The sample vibration signal of the healthy gearbox	47
14. The sample vibration signal of the damaged gearbox with tooth loss	47
15. The first eight IMF components of the damaged gearbox	48
16. The first eight IMF components of the healthy gearbox	49
17. The Hilbert spectrum of the healthy gearbox	50
18. The Hilbert spectrum of the damaged gearbox with tooth loss	50
19. The process of the adaptive narrowband interference cancellation	55
20. The general steps of the fast wavelet decomposition	58
21. The healthy driving gear on the output side	62
22. The damaged gear with 50% tooth loss	63
23. The gear with a tooth root crack	64
24. The bearing test rig	65
25. The four types of full ceramic bearing seeded faults	69
26. The four types of plastic bearing seeded faults	70
27. The drawing of the 6025 2RS bearing	71

LIST OF FIGURES (continued)

<u>FIGURE</u>	<u>PAGE</u>
28. The locations of the AE sensors.....	72
29. The process of the EMD based vibration feature extraction.....	73
30. Sample vibration signal of healthy gearbox and its first three IMF components	76
31. Sample vibration signal of damaged gearbox with 50% tooth loss and its first three IMF components	77
32. Sample vibration signal of damaged gearbox with 50% root crack and its first three IMF components	78
33. The feature vectors of healthy gearbox, damaged gearbox with 50% tooth loss, and damaged gearbox with 50% root crack.....	79
34. Sample vibration signal of the healthy bearing and its first three IMF components.....	83
35. Sample vibration signal of the bearing with outer race fault and its first three IMF components	84
36. Sample vibration signal of the bearing with inner race fault and its first three IMF components	85
37. Sample vibration signal of the bearing with ball fault and its first three IMF components	86
38. Sample vibration signal of the bearing with cage fault and its first three IMF components	87
39. The distance value of the full ceramic bearing with different states	88
40. The entropy value of the full ceramic bearing with different states	89
41. Process of the two-step fault diagnosis approach for plastic bearing	93
42. The simulated impulse signal with fixed time intervals and its frequency spectrum	99
43. The simulated impulse signal with random time intervals and its frequency spectrum	100

LIST OF FIGURES (continued)

<u>FIGURE</u>	<u>PAGE</u>
44. The sample vibration signal of the healthy plastic bearing.....	101
45. The sample vibration signal of the plastic bearing with outer race fault	102
46. The sample vibration signal of the plastic bearing with inner fault.....	102
47. The sample vibration signal of the plastic bearing with ball fault.....	103
48. The sample vibration signals of the plastic bearing with cage fault	103
49. The frequency domain features of the healthy and the bearing with different types of fault with 10 Hz input speed	104
50. The frequency domain features of the healthy and the bearing with different types of fault with 20 Hz input speed	105
51. The frequency domain features of the healthy and the bearing with different types of fault with 40 Hz input speed	106
52. The frequency domain features of the healthy and the bearing with different types of fault with 60 Hz input speed	107
53. The time domain feature vectors of the plastic bearing running under 10 Hz input frequency	109
54. The time domain feature vectors of the plastic bearing running under 20 Hz input frequency	110
55. The time domain feature vectors of the plastic bearing running under 40 Hz input frequency	111
56. The time domain feature vectors of the plastic bearing running under 60 Hz input frequency	112
57. The process of the interference cancellation based gear fault detection methodology.....	118
58. The simulated signal	119
59. The processed result with the cancellation of the periodic signal	120
60. The processed result with the cancellation of both the periodic signal and the background noise	120

LIST OF FIGURES (continued)

<u>FIGURE</u>	<u>PAGE</u>
61. The sample vibration signal of the damaged gearbox	121
62. The frequency spectrum of the sample vibration signal of the damaged gearbox	122
63. The processed results of the gearbox running under 36 Hz using the interference cancellation algorithm	123
64. The Fourier spectrum of the processed signal	124
65. Sample vibration signal collected under input rotational frequency of 24 Hz	125
66. The processed results of the gearbox running under 24 Hz using the interference cancellation algorithm	125
67. Laplace wavelet	134
68. The simulated results	136
69. The pencil lead break test and its Fourier spectrum	139
70. The damaged gear with 20% tooth loss	141
71. The damaged gear with 50% tooth loss	142
72. The damaged gear with 100% tooth loss	142
73. The location of the AE sensors	144
74. The process for fault diagnostics on STG	145
75. The sample acoustic emission signals of the healthy gearbox	147
76. The sample acoustic emission signals of the damaged gearbox	148
77. The vibration signal of the healthy gearbox	150
78. The vibration signal of the damaged gearbox	150
79. The process of Laplace wavelet based AE signal quantification methodology	153
80. A sample AE burst generated by the damaged gearbox	156
81. The correlation coefficient between the AE burst and the Laplace wavelet	157

LIST OF FIGURES (continued)

<u>FIGURE</u>	<u>PAGE</u>
82. The flowchart of finding window length	159
83. The simulated results	160
84. The real AE waveform generated by the damaged gearbox and its correlation coefficients	161
85. The features extracted from the raw AE bursts of the gearbox with 0% loadings	166
86. The features extracted from the processed AE signals of the gearbox with 0% loadings	167
87. The features extracted from the raw AE signals of the gearbox with 50% loadings	168
88. The features extracted from the processed AE signals of the gearbox with 50% loadings	169
89. The features extracted from the raw AE signals of the gearbox with 100% loadings	170
90. The features extracted from the processed AE signals of the gearbox with 100% loadings	171
91. The framework of the EMD based AE quantification methodology for rotating machine fault detection methodology	173
92. The first four IMF components of the healthy gearbox under 0% loading condition	178
93. The first four IMF components of the damaged gearbox under 0% loading condition	179
94. The de-noised signal of the healthy gearbox by using Hilbert-Huang transform under 0% loading condition	180
95. The de-noised signal of the damaged gearbox by using Hilbert-Huang transform under 0% loading condition	181
96. The compressed AE features for healthy and damaged gearbox under	

LIST OF FIGURES (continued)

<u>FIGURE</u>	<u>PAGE</u>
0% loading condition.....	184
97. The compressed AE features for healthy and damaged gearbox under 50% loading condition	184
98. The compressed AE features for healthy and damaged gearbox under 100% loading condition.....	185
99. The compressed AE features calculated by using the energy ratio of the IMF components for healthy and damaged gearbox under 0% loading condition.....	189
100. The compressed AE features calculated by using the energy ratio of the IMF components for healthy and damaged gearbox under 50% loading condition.....	190
101. The compressed AE features calculated by using the energy ratio of the IMF components for healthy and damaged gearbox under 100% loading condition.....	190

LIST OF ABBREVIATIONS

AE	Acoustic emission
AR	Auto-regressive
CBM	Condition based maintenance
CI	Condition indicator
CWT	Continuous wavelet transform
EMD	Empirical mode decomposition
FFT	Fast Fourier Transform
HHT	Hilbert-Huang transform
IMF	Intrinsic mode function
KNN	K-nearest neighbor
NDT	Non-destructive testing
QMF	Quadrature mirror filters
RMS	Root mean square
SNR	Signal to noise ratio
STFT	Short-time Fourier transform
STG	Split torque gearbox
SVM	Support vector machine
TSA	Time synchronous average
WVD	Wigner-Ville distribution

1 INTRODUCTION

1.1 **Research Motivation**

Condition based maintenance (CBM) is a maintenance strategy, which guides the maintenance actions based on the measured current and predicted future machine states. The implementation of CBM could prevent machine failure, increase reliability of the whole system, and decrease maintenance cost. Thus CBM is becoming widely utilized in many real industrial applications such as helicopter transmission system, wind turbine systems, and etc. In general, the implementation of CMB could be divided into three main steps [1]:

- (1) Relevant signals are measured by the corresponding sensors such as accelerometers, hall sensors, torque sensors, and so on.
- (2) Collected signals are pre-processed by using signal processing methods and different condition indicators (CIs) are extracted to present the states of the monitored rotating components such as gears, bearings, shaft, and so on. And then fault detection, diagnostics and prognostics algorithms will be applied to analyze the CIs.
- (3) Decide the maintenance policies based on the diagnostic results.

To design an efficient CBM strategy, effective rotational machine fault detection and diagnostic methods and tools need to be developed. Especially, when new designs, new materials, and new sensor technologies are used, the effectiveness of the current fault

detection and diagnostic algorithms needs to be improved and advanced fault detection and diagnostic methodologies need to be developed.

In developing rotating machine fault detection and diagnostics methods and tools, one critical issue is the development of effective signal processing based fault feature extraction or quantification. In general, the major techniques used in rotating machinery fault detection and diagnostics include: vibration signal based methods, temperature analysis, current signature analysis, oil debris analysis, and acoustic emission signal based techniques. Among these techniques, vibration signal based techniques are the most widely used techniques in rotating machine fault detection and diagnosis. However, the current vibration signal processing methods for rotating machine fault detection and diagnostics have their own limitations. In practice, the faulty vibration signals are often buried into the vibration signals generated by the healthy components and mechanical background noises. Investigating and developing new and advanced signal processing methods based vibration signal fault feature extraction methods and fault diagnostic methods and tools are necessary.

Recently, acoustic emission (AE) sensors are introduced to rotating machine fault detection and diagnostics. As reported in [2], in comparison with vibration signals, acoustic emission signals have the following advantages: (1) insensitive to structural resonance and unaffected by typical mechanical background noises, (2) more sensitive to activities of faults, (3) provide good trending parameters, (4) localization of measurements to the machine being monitored, i.e., AE signals are sensitive to the

location of the faults. Currently, most commonly used AE signal quantification methods are the statistical methods used in the non-destructive testing (NDT) and the AE based fault features are root mean square (rms), peak value, rise time, rise time slope, and duration. Few advanced signal processing methods have been investigated and developed for AE signal quantification and diagnostics. Thus developing acoustic emission signal quantification methods and diagnostic algorithms are in a great need.

Plastic bearings are widely used in medical applications, food processing industries, semi-conductor industries, and aircraft components[3-5]. In comparison with traditional steel bearings, plastic bearings have following advantages: (1) corrosion resistance; (2) light weight; (3) non-metallic and non-magnetic; (4) lubrication free; (5) consistent coefficient of friction. Unlike their steel counterparts, effective fault diagnosis methods for plastic bearings have not been developed. In reviewing steel bearing fault diagnostic approaches reported in the literature, a common practice of using vibration fault features to diagnose all bearing faults in one step has been observed. The vibration fault features are not equally sensitive to all bearing faults. Moreover, in comparison with steel bearings, plastic bearings are more loosely assembled and easier to be deformed. These inherent properties of plastic bearings add more degrees of randomness into the behavior of the fault impulses and weaken the fault impulse signals than those of the steel bearing. Therefore, developing effective bearing fault diagnostic method using different fault features at different steps becomes attractive.

1.2 **Goal and Objectives**

The goal of this dissertation is to develop effective rotating machine fault diagnostic methods and tools using vibration and acoustic emission sensors and validate the methods and tools using seeded fault test data collected from both vibration and acoustic emission sensors. In particular, the following objectives have been achieved:

- (1) Development of vibration signal based fault feature extraction methods and tools utilizing advanced signal processing methods.
- (2) Development of acoustic emission signal quantification methods using advanced signal processing methods.
- (3) Development of data mining based rotating machine fault diagnostics using both vibration and acoustic emission signals.
- (4) Design and development of split torque gearbox test rig and real seeded fault experiments for validating the developed methodologies.
- (5) Validation of the developed fault detection and diagnostic methods and tools using seeded fault test data.

1.3 **Contributions of the Dissertation**

The contributions of this research are summarized as follows:

- (1) An empirical mode decomposition (EMD) based vibration feature and CI extraction methodology for rotating machinery fault detection and diagnosis has been developed. The methodology utilizes the EMD technique to

decompose the vibration signals into intrinsic mode function (IMF) components. And then a two-dimensional fault features are extracted based on the decomposed vibration signals. Two case studies, gear fault diagnosis on the developed STG type gearbox and full ceramic bearing fault diagnosis on a bearing run-to-failure test rig are used in this dissertation to demonstrate the effectiveness of the developed methodology.

- (2) A two-step vibration signal based bearing fault diagnostics algorithm has been developed. This approach is developed by integrating the statistical method, pattern recognition, and signal processing techniques. The two-step approach utilizes envelope analysis and empirical mode decomposition to pre-process vibration signals and extract frequency domain and time domain fault features as condition indicators for plastic bearing fault diagnosis. In the first step, the frequency domain condition indicators are used by a statistical classification model to identify bearing outer race faults. In particular, new bearing fault CIs extracted using EMD method are developed for classification of bearing non-outer race faults at the second step. Seeded fault tests on plastic bearing outer race, inner race, balls, and cage are conducted on a bearing diagnostic test rig and vibration signals are collected. The effectiveness of the two-step approach is validated using real plastic bearing seeded fault testing data.
- (3) A vibration signal based gear fault detection system based on interference cancellation has been developed. The narrowband interference cancellation is used to remove the narrowband interference signals, which are the periodic components of the vibration signals. And then a threshold based de-noising

technique is applied to remove the wideband interference signals, which are the random background noise. The simulated signal and the real seeded gear fault on the developed STG type gearbox are used to demonstrate the developed methods under a dynamic operation conditions. Both the simulation results and the experimental results have shown the effectiveness of the proposed methodology.

- (4) A Laplace wavelet based AE signal quantification methodology for rotating machinery fault detection and diagnostics has been developed. The effectiveness of the extracted AE features for gear fault detection has been validated by using gear seeded fault signals with three damage mode of the designed STG gearbox. The correlation between the AE based fault features and the gear damage levels has been also investigated. In total, four gear damage levels are investigated: 0% tooth loss (healthy gear), 20% tooth loss, 50% and 100% tooth loss. The energy ratio value of the Laplace wavelet processed signal shows a consistent correlation between the AE feature values and damage levels under different loading conditions.
- (5) An EMD based AE quantification methodology and a data mining based bearing fault diagnostic tool have been developed. The methodology incorporates a threshold based de-noising technique into EMD to increase the signal-to-noise ratio. Multiple features are extracted from the de-noised signals and then fused into a single compressed AE feature. The compressed AE features are then used for fault detection based on a statistical method. The statistical method does not require AE data for damaged state. A threshold for

separating the damaged states and the healthy states is determined by using only the compressed AE feature of the healthy states. A gear fault detection case study has been conducted on a notional split-torque gearbox and real gear fault AE data have been collected to demonstrate the effectiveness of the methodology. The case study results have shown that the developed method is effective in extracting the AE based fault features for gear fault detection.

- (6) A split-torque gearbox test rig has been designed and developed.
- (7) Experiments have been designed and conducted on the custom designed notional split-torque gearbox test rig and bearing run-to-failure test rig.

1.4 **The Outline**

The reminder of the dissertation is outlined next.

Chapter 2 provides the literature review on rotating machinery fault detection and diagnosis. The techniques used in rotating machinery fault detection and diagnostics and the general information on gear failure modes and bearing failure modes are also provided in this chapter.

Chapter 3 gives the detailed description of the developed notional split torque gearbox test rig. The test rig contains three main parts: notional STG type gear transmission system, sensors and data acquisition systems, and motor drive and loading systems. The

development and the implementation of different components of the STG test rig are presented.

Chapter 4 first presents literature review on the vibration based techniques on rotating machinery fault detection and diagnostics. The theoretical basis used in this chapter is provided. And then the developed vibration based methodologies and the real seeded fault test are explained.

In Chapter 5, theoretical basis used in developing AE signal based fault detection and diagnostics is provided. It is then followed by a comprehensive review on the AE signal based methodology on rotating machinery fault detection, and diagnostics. The developed AE based methodologies and the real seeded fault tests are explained in this chapter.

Chapter 6 concludes the dissertation and gives the future research.

2 LITERATURE REVIEW

2.1 Rotating Machine Fault Detection and Diagnostics

Fault detection detects the status of the machine, while diagnosis identifies what types of fault and which components of the machine being monitored have the fault. In general, there are two popular types of techniques for machinery fault detection and diagnostics.

One rotating machine diagnostic technique is physical model based method. These techniques establish mathematical model of the machine to be monitored and then by monitoring the change of the model parameters or the residual signal between the model and the collected signal the machine fault can be classified. Successful physical model based rotating machine fault detection and diagnostics applications have been reported in [6-15]. As stated in [1], model-based approaches can be more effective and accurate than other model-free approaches if a precise model can be established. However, in real applications, to establish a precise model for the monitored rotating machine is computational expensive. Moreover, for complex systems it is infeasible to obtain an accurate model. Therefore, the performances of the model-based techniques are degraded in many real applications. Another drawback of the model-based techniques is that different models are needed to be established for different applications. Thus it is hard to apply the model-based techniques to different industrial applications.

Another rotating machine diagnostic is data mining or data driven based method. Data mining based methods use signal processing methods to extract the fault features from the collected sensor data. And then by analyzing the signature of the fault features, machine faults are detected and diagnosed. Data mining based methodologies are widely applied in machinery fault detection and diagnosis. Data mining based methods discover rotating machine faults from the historic data and does not necessarily need to understand the physics of the monitored applications. Thus the complexity of designing the diagnostic methodology is greatly reduced, especially for the new and complex systems. Data mining based methods can be easily applied to brand new and complex systems and adapted to applications with different system parameters. Successful data mining based machinery fault detection and diagnostics applications have been reported by [16-29]. Unlike the model-based methods, data mining based methods do not necessarily need to understand the physical model of the monitored applications. Thus the complexity of design the methodology is greatly reduced, especially for the complex systems. Data mining based approaches are more easily applied in complex systems and adapt to applications with different system parameters.

2.2 Rotating Machinery Fault Detection and Diagnostic Techniques

Currently, five types of sensor technique are widely used in rotating machinery fault detection and diagnostics. They are temperature analysis, lubrication based analysis, motor current signature analysis, vibration signal based analysis, and AE signal based analysis.

Temperature based analysis is a simple fault detection technique and provides limited information about the monitored machinery. When the transmission system works under abnormal situation, the temperature will increase dramatically. By monitoring the sharp increasing temperature, the faulty states of the rotating machinery can be determined. However, by using only the temperature monitoring technique it cannot provide information in rotating machinery fault diagnostics. Therefore, usually temperature analysis is used along only for rotating machinery fault detection.

Lubricant based analysis method analyzes the physical wear particles or chemical contaminants by using sensors such as, chip detectors, spectrographic equipments, and so on. Lubricant based analysis is applied to both the gear and bearing fault detection, diagnostics, and prognostics both online monitoring and off-line monitoring[30]. By measuring the size and the shape of the debris, the oil debris based technique can not only the fault detection, but also the fault types and the wear levels[31]. Successful applications of lubricant analysis based techniques on rotating machine fault detection and diagnostics are reported in [32-34] . According to a research reported by [35], oil debris monitoring techniques usually provide more reliable detection on the early pitting failure detection than the vibration signal based techniques. However, one of the disadvantages of the oil debris monitoring is that data collected from the oil debris sensors do not contain the rotating information. So it is impossible to use the lubricant analysis based techniques to locate the fault in a complex mechanical system.

Motor current signature analysis is widely applied for detecting and diagnosing both electrical machine electrical faults, such as broken rotor bars, airgap eccentricities and so on, and mechanical faults, such as misalignment, bearing faults and so on. The effectiveness of current signature analysis based methods for motor electrical faults has been investigated in [36-40]. Also, successful applications on mechanical fault diagnosis in the electric machines using current signals have been reported in [41-49]. More recent comprehensive investigation paper on the diagnostic techniques including motor current analysis were given by [50, 51]. Mechanical faults could be identified by the current analysis techniques as the defects could cause torque change. The torque change could affect the motor current. Thus the fault signature could be reflected by the current signature. One advantage in using current signature analysis for rotating machine fault detection and diagnostics is that it does not need additional sensors comparing with the other four techniques. However, one difficulty in using current signature analysis for mechanical fault diagnosis is the sensitivity of the current signals collected from the motor. When the mechanical components are not on the motor, the torque change caused by the mechanical defects may have little impact on motor current, especially, if a flexible coupling is used to connect the motor drive and the mechanical transmission system.

Vibration signal based techniques are the most widely applied to rotating machinery fault detection and diagnostics. When there is fault developing inside rotational machinery, the signature of the collected vibration signal is changing [52]. According to [52], vibration signals contain almost all the mechanical signature information. By properly

selecting signal processing methods to process the vibration signal and designing pattern classification methodology and predicting algorithms, the fault in the rotating machinery can be detected, diagnosed and predicted. Comprehensive reviews on vibration based techniques for rotating machine fault detection and diagnostics can be found in [53, 54]. A more detailed literature review of vibration signal based techniques can be found in Section 4.1 of Chapter 4.

Recently, AE signal based techniques have gained some popularity in machine fault diagnosis and prognosis. According to [55], AE is defined as the range of phenomena that results in generation of structure-borne and fluid-borne (liquid, gas) propagating waves due to the rapid release of energy from localized sources within and /or on the surface of a material. By properly selecting signal processing methods to process the AE signal and designing pattern classification methodology and predicting algorithms, the fault in the rotating machinery can be detected and diagnosed. The application of AE technique can be found in many successful applications, such as, engine fault detection [56], monitoring the precession manufacturing [57], and wear monitoring and control [58]. Recently AE signal is beginning to attract the researchers' attention on the machine healthy monitoring [59-65]. Typical sources of AE waveforms generated in the rotational machinery include [60, 66]: (1) Plastic deformation, (2) Micro-fracture, (3) Wear, (4) Bubble, (5) Friction, and (6) Impacts. In comparison with vibration signal, acoustic emission signal has the advantages as listed below[2]:

- (1) Insensitive to structural resonances and unaffected by typical mechanical background noise,

- (2) More sensitive to activity from faults,
- (3) Provides good trending parameters,
- (4) Localization of measurements to the machine being monitored.

These advantages make the acoustic emission based fault diagnostics technique potentially more competitive than the vibration based fault diagnostics technique for the rotating machine fault detection and diagnostics. A more detailed literature review of vibration signal based techniques can be found in Section 5.1 of Chapter 5.

3 DESIGN AND DEVELOPMENT OF NOTIONAL SPLIT TORQUE GEARBOX TEST RIG

According to [67], the most common gear transmission system in a helicopter is an epicyclical gear transmission system, or planetary gear transmission system, which features an output shaft driven by several planets. For example, UH-60A Black Hawk helicopter uses this type of gear transmission system. In a planetary gear transmission system, a central sun gear is surrounded by two or more rotating planets in the planetary gear system. The torque is transmitted from the central sun gear through the planets gears to the planet carrier and from the planet carrier to the main rotor shaft.

The requirement of a high energy density transmissions (lower weight) in helicopters has lead to the development of the split torque gearbox (STG) to replace the traditionally planetary gearbox by the drive drain designer [68]. In a split torque gear train design, multiple pinions connected by a parallel shaft arrangement mesh simultaneously with the central gear transmit the torque. In comparison with traditionally planetary gearbox, STG potentially offers the following benefits [68]: (1) High ratio of speed reduction at final stage, (2) Reduced number of speed reduction stages, (3) Lower energy losses, (4) Increased reliability of the separate drive paths, (5) Fewer gears and bearings, (6) Lower noise.

Due to the advantages on the STG type gear transmission over the traditional planetary gear transmission system the helicopter OEMs will develop their new products using the STG type gear transmission system. For example, the Comanche helicopter was

designed with a STG, and the new Sikorsky CH-53K will incorporate the STG design to transmit over 18,000 hps to the rotor blades. It is likely that STG will be incorporated into more designs in the future [69].

According to [70], because of the limited experience in building helicopter with STG, there is no condition based monitoring data on this type of gear box. In order to investigate the current gear fault detection, diagnostic algorithms and develop new gear fault detection methodology, a notional STG type gearbox test rig was designed and developed. The main purpose of developing the notional split torque gearbox was to simulate the simultaneously meshing behavior of the split torque gear transmission train. The whole system is shown in Figure 1. As shown in the following Figure, the test rig contains three main parts: notional STG type gear transmission system, sensors and data acquisition systems, and drive and loading systems.

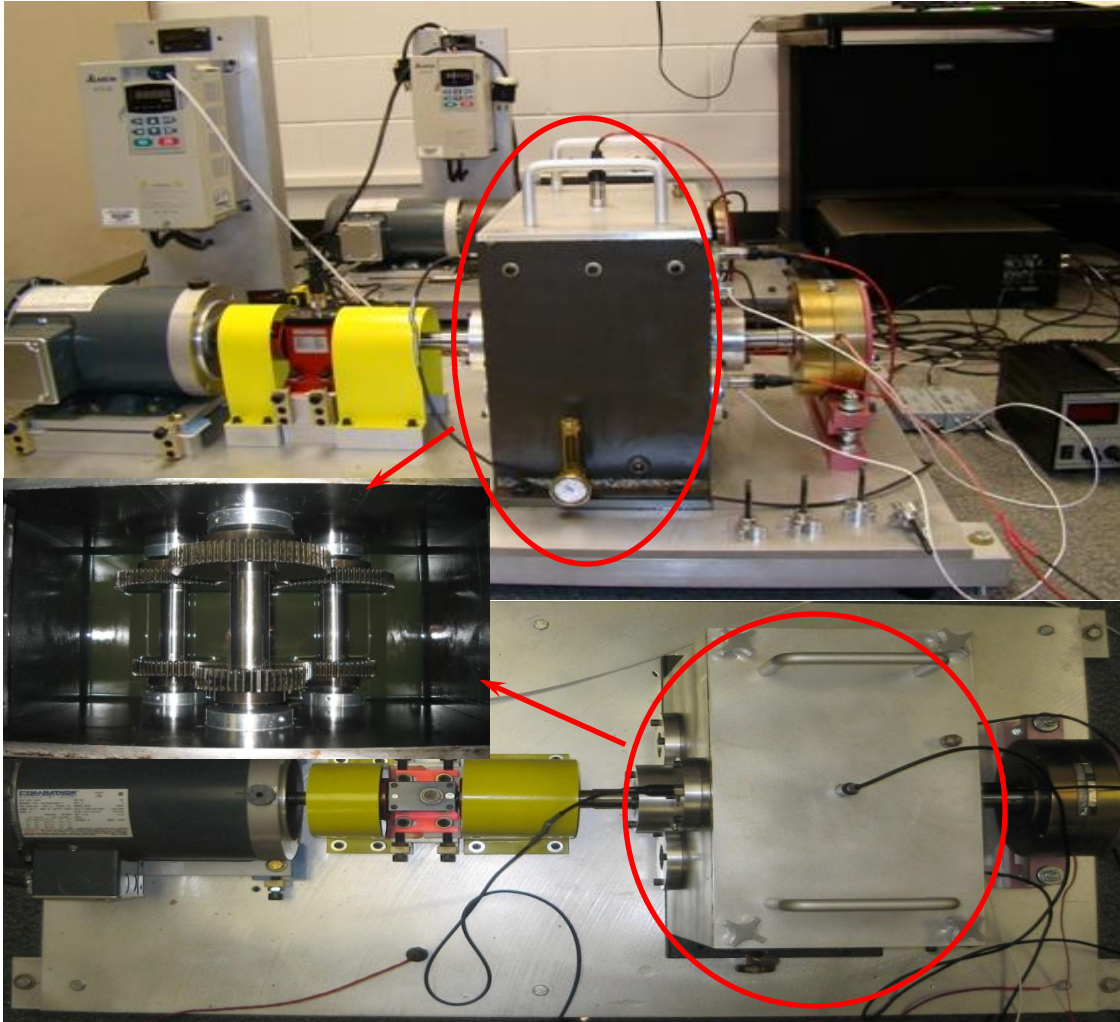


Figure 1. The notional STG type gearbox

3.1 Notional STG Type Gearbox

According to [71], in a STG type gear transmission train, there are several pairs of gears meshing simultaneously with the output shaft driving gear. Generally speaking, there are

several gear types. They are spur gear, internal ring gear, helical gear, double helical gear, face gear, worm gear, hypoid gear, straight bevel gear, spiral bevel gear, and screw gear. Since the primary design considerations in this paper were to simulate the simultaneously gear meshing behavior in a helicopter STG type gear transmission system, three gear types, spur gear, helical gear, and double helical gear, could be used in the notional STG type gearbox design. To design and development of the notional STG type gearbox, two main factors were considered. The one is the manufacturability and the other is how easy the gear system is assembled. The first factor determines the costs of the whole system while the second factor affects the difficulty and feasibility of the experimental design under academic laboratory conditions. Among the three gear types, spur gear is the simplest gear to design and manufacture and the easiest to assemble over the other two gear types. In this research, spur gears were chosen and for both the input side and output side of the gearbox, parallel shaft layout is used. The materials used to produce the spur gears are the common Carbon steel. The schematic drawing of the notional STG type gearbox is shown in Figure 2.

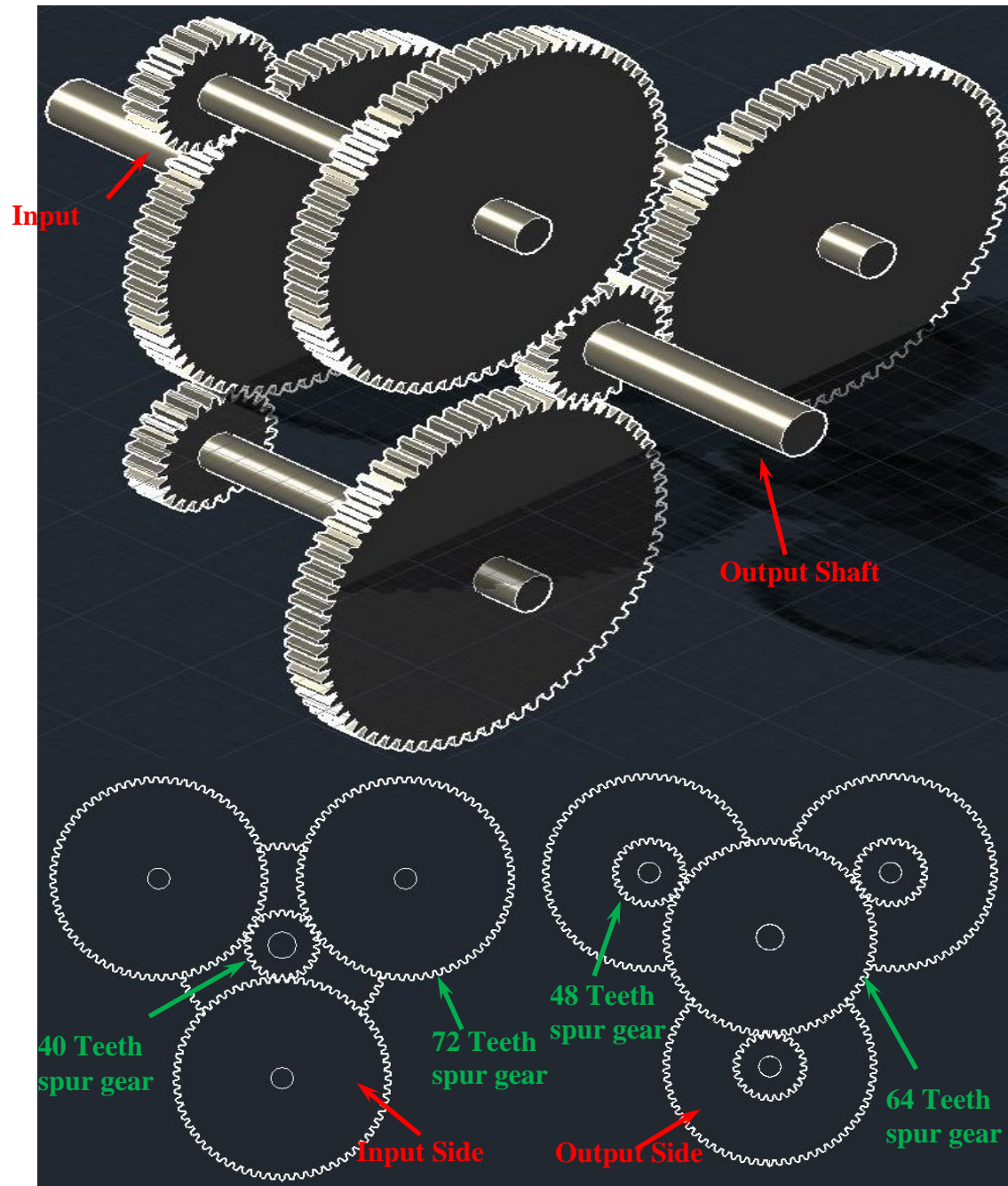


Figure 2. Schematic drawing of the notional STG type gearbox

On the input side, the input driving gear is a 40 teeth spur gear which drives three input driving gear that are 72 teeth spur gears. On the output side, three output driving gears are 48 teeth spur gears which drive a 64 teeth spur gear. Major gear parameters are listed in Table I.

Table I. Major Parameters of the gears

Parameters \ Gear	40 Tooth	72 Tooth	48 Tooth	64 Tooth
Diametric Pitch (dp)	16.000	16.000	16.000	16.000
Pressure Angle (degree)	20.000	20.000	20.000	20.000
Pitch Diameter (inch)	2.500	4.500	3.000	4.00
Face Width (inch)	0.75	0.75	0.75	0.75
Circular Thickness (inch)	0.098	0.098	0.098	0.098
Circular Pitch (inch)	0.1963	0.1963	0.1963	0.1963
Addendum (inch)	0.0625	0.0625	0.0625	0.0625
Dedendum (inch)	0.0781	0.0781	0.0781	0.0781

The contact ratio of the gear pairs is also an important parameter. It is defined as the average number of teeth in contact during the period in which a tooth comes and goes out

of contact with the mating gear. The contact ratio of the spur gear pairs can be calculated by using the following equation,

$$ContactRatio = \frac{\sqrt{(r_{a1}^2 - r_{b1}^2)} + \sqrt{(r_{a2}^2 - r_{b2}^2)} - C \sin \varphi}{P_c \cos \varphi} \quad (1)$$

where, φ is the pressure angle, r_{a1}, r_{a2} are the addendum radius of gear 1 and gear 2, respectively, which equal to the pitch radius plus addendum, r_{b1}, r_{b2} are the circle radius of gear 1 and gear 2, respectively, which equal to the pitch radius multiples $\cos \varphi$, C is the center distance and P_c is the circular pitch.

For the 40-72 teeth pair, $r_{a1} = \frac{2.5}{2} + 0.0625 = 1.3125$ inches, $r_{a2} = \frac{4.5}{2} + 0.0625 = 2.3125$ inches, $r_{b1} = \frac{2.5}{2} \cos 20^\circ = 1.1746$ inches, $r_{b2} = \frac{4.5}{2} \cos 20^\circ = 2.1143$ inches, $C = 3.543$ inches, $P_c = 0.1963$ inches. The contact ratio is 1.68.

For the 48-64 teeth pair, $r_{a1} = \frac{3}{2} + 0.0625 = 1.5625$ inches, $r_{a2} = \frac{4}{2} + 0.0625 = 2.0625$ inches, $r_{b1} = \frac{3}{2} \cos 20^\circ = 1.4095$ inches, $r_{b2} = \frac{4}{2} \cos 20^\circ = 1.8794$ inches, $C = 3.625$ inches, $P_c = 0.1963$ inches. The contact ratio is 1.54.

The velocity ratio is calculated by using the following equation,

$$VelocityRatio = \frac{\omega_1}{\omega_2} = \frac{N_2}{N_1} \quad (2)$$

where, ω_1 is the rotational speed of gear 1 and ω_2 is the rotational speed of gear 2. N_1 is the number of the tooth of gear 1 and N_2 is the number of the tooth of gear 2. For the 40-

72 teeth pair, the velocity ratio is 1.800. For the 48-64 teeth pair, the velocity ratio is 1.333. The velocity ratio from the input driving gear to the output driven gear is 2.4. That means, if the input speed is set to be 60 Hz then the output speed of the gearbox is 25 Hz.

3.2 Sensors and Data Acquisition Systems

The schematic of the data acquisition system is shown in Figure 3.

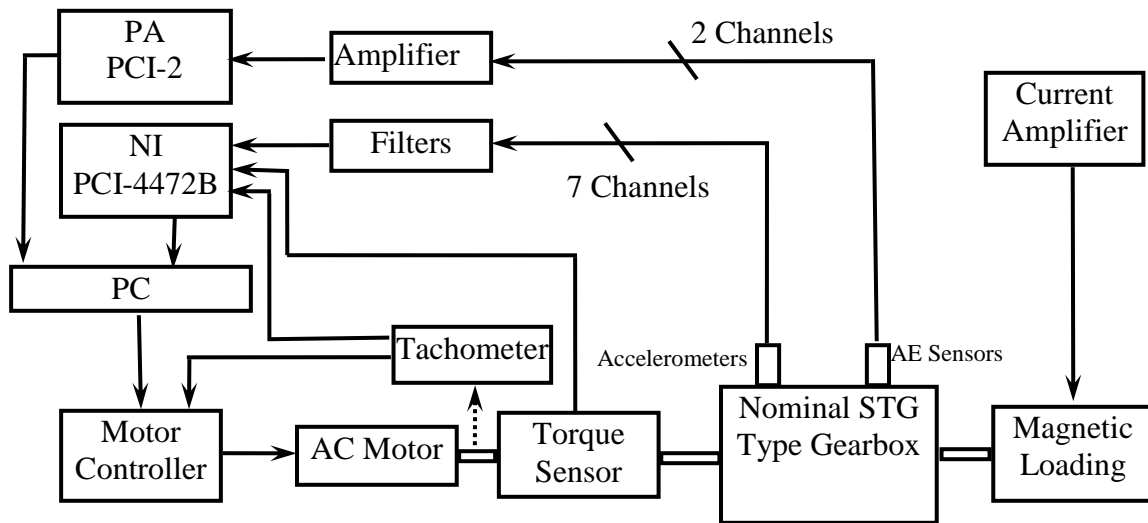


Figure 3. Schematic of the experimental setup

For gear fault detection and diagnostics, high precision speed information is not necessarily needed. Commonly once per revolution signal is enough. To simplify the whole system design, a photo tachometer, which generates 1 pulse per revolution of the shaft, rather than high resolution encoder, which generates N pulses per revolution of the shaft, was installed to measure the rotational speed of the motor.

For vibration signal collection, basically there are three types of transducer could be used. They are proximity probes, velocity transducers, and accelerometers. Proximity probes measure the relative displacement between the shaft and casing. Velocity transducers output a signal, which is proportional to absolute velocity. Accelerometers produce a signal, which is proportional to absolute acceleration. According to [72], the proximity probe has the following problems:

- (1) It is sometimes impossible to fit this type of probe if the machine has not been prepared for it during the initial design.
- (2) Probe bracket resonances can be a problem with high speed machines and should be avoided if meaningful results are to be obtained
- (3) The target surface, if a rotor journal, should not have an eccentricity or surface roughness greater than 6 μm pp.
- (4) In addition to mechanical run-out, it is possible that the shaft exhibits magnetic run-out effects. This is not normally a problem, but where it is, the effect is best removed by de-gaussing the rotor.
- (5) The sensitivity is dependent on the material of the target surface and each application requires a separate calibration.

- (6) A regulated power supply should be available to feed the electronics, otherwise the sensitivity will not be constant, i.e. a simple battery supply will not be adequate.
- (7) Care should be taken to ensure that the probe will operate over its linear range.

The velocity sensors usually have very low noise levels and often utilized for machine balancing. Their frequency range is usually limited to 10 to 1000Hz. The accelerometers are small and easy to be installed and most importantly they have the highest dynamic range. Based on the consideration above, accelerometer was chosen to measure the vibration in the gearbox test rig. The 603C01 wide range accelerometer produced by PCB Piezotronics Inc. is used. A picture of the sensor is shown in Figure 4. The major parameters of this type of sensor are listed in Table II. More detail information on this type of sensor can be found in [73].

Table II. Parameters of the 603C01 accelerometer

Parameters	Value
Sensitivity ($\pm 10\%$)	10.2 mV/(m/s ²)
Measurement Range	± 490 m/s ²
Resonant Frequency	25 kHz
Broadband Resolution (1 to 10,000 Hz)	3,434 μ m/s ²
Non-Linearity	$\pm 1\%$
Overload Limit (Shock)	49,050 m/s ²
Settling Time (within 1% of bias)	≤ 2.0 s

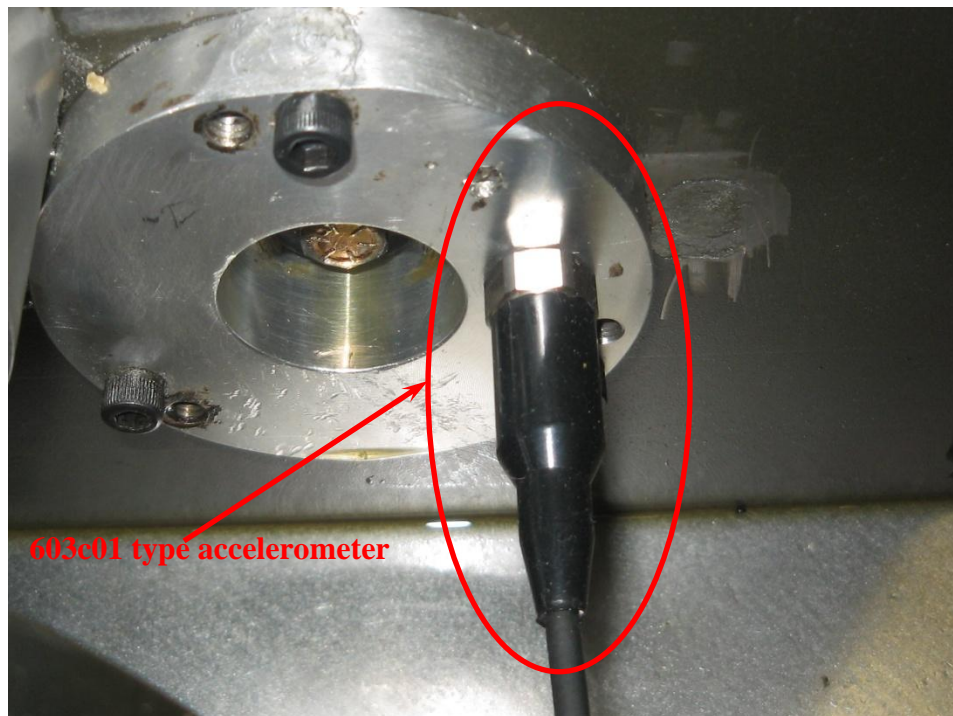


Figure 4. The model 603c01 accelerometer

The frequency range for the 603C01 accelerometer is 0.5 Hz to 10 kHz, which is wide enough to cover the resonance frequency of the mechanical system. Usually, the resonance frequency for the mechanical system is below 3 kHz. According to the user manual of the model 603C01 user manual, there are six ways of mounting the sensors [73]. They are stud mounting, adhesive mounting, mounting pad, flat magnetic mounting, dual rail magnetic mounting and hand-held probe. The effects on high frequency range of different mounting configurations are listed in [73]. Among these mounting methods, the stud mount configuration has the highest frequency response range which is up to nearly 10 kHz. Based on this consideration, we choose the stud mounting method. In the experimental setup, totally seven accelerometers, placed on different locations on the surface of the framework of the gearbox were used to collect the vibration signal of the designed notional STG type gearbox.

For AE signals, a WD type AE sensor produced by Physical Acoustics Co. was used. A picture of the sensor is shown in Figure 5. The major parameters of this type of sensor are listed in Table III. More detail information can be found in [74]. The operation frequency range for this type of sensor is 100 kHz to 900 kHz. It covers the AE source frequency range.

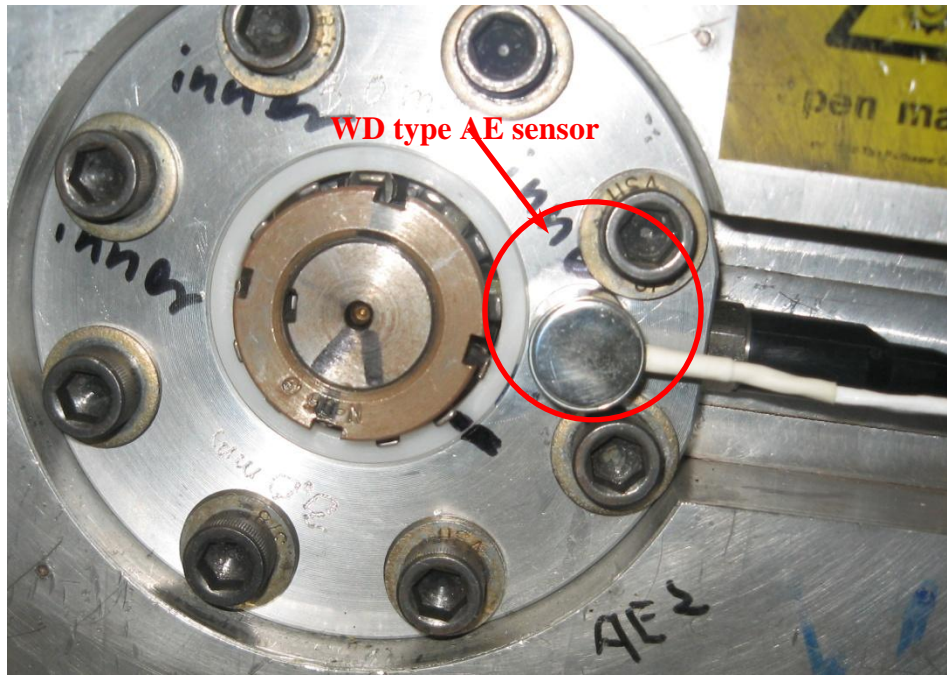


Figure 5. The WD type acoustic emission sensor

Table III. Parameters of the WD type acoustic emission sensor

Parameters	Value
Peak Sensitivity (Ref $v/(m/s)$)	96 dB
Operating Frequency Range	100-900 kHz
Shock Limit	500 g
Temperature Range	-35 to 75 °C

For the designed notional STG type gearbox test rig, there are seven channels accelerometers, one channel tachometer, and two AE sensors were used. To select a suitable data acquisition card, the highest sampling frequency of the card is the most important thing to be considered. Based on Shannon theory, the sampling frequency should be at least twice of the bandwidth of the signal. The highest frequency of the tachometer is 60 Hz while that of the accelerometers and the AE sensors is 10 kHz and 900 kHz, respectively. For collecting accelerometer and tachometer signals, the data acquisition card PCI-4472B produced by National Instrument Co. is used. PCI-4472B is an eight channel dynamic signal acquisition card with 24-bit resolution, ± 10 v input range and the maximum sampling frequency is 102.4 kHz, which is ten times of the highest response frequency of 10 kHz of the accelerometer. For the AE sensors, the data acquisition card PCI-2 produced by Physical Acoustics Co. is selected. The PCI-2 is a two channel data acquisition card with 18-bit resolution and the maximum sampling frequency is 40 MHz, which is forty times of the highest response frequency of the AE sensors. Totally seven accelerometers and two AE sensors are mounted on the frame of the gearbox. The locations of the sensors are shown in Figure 6.

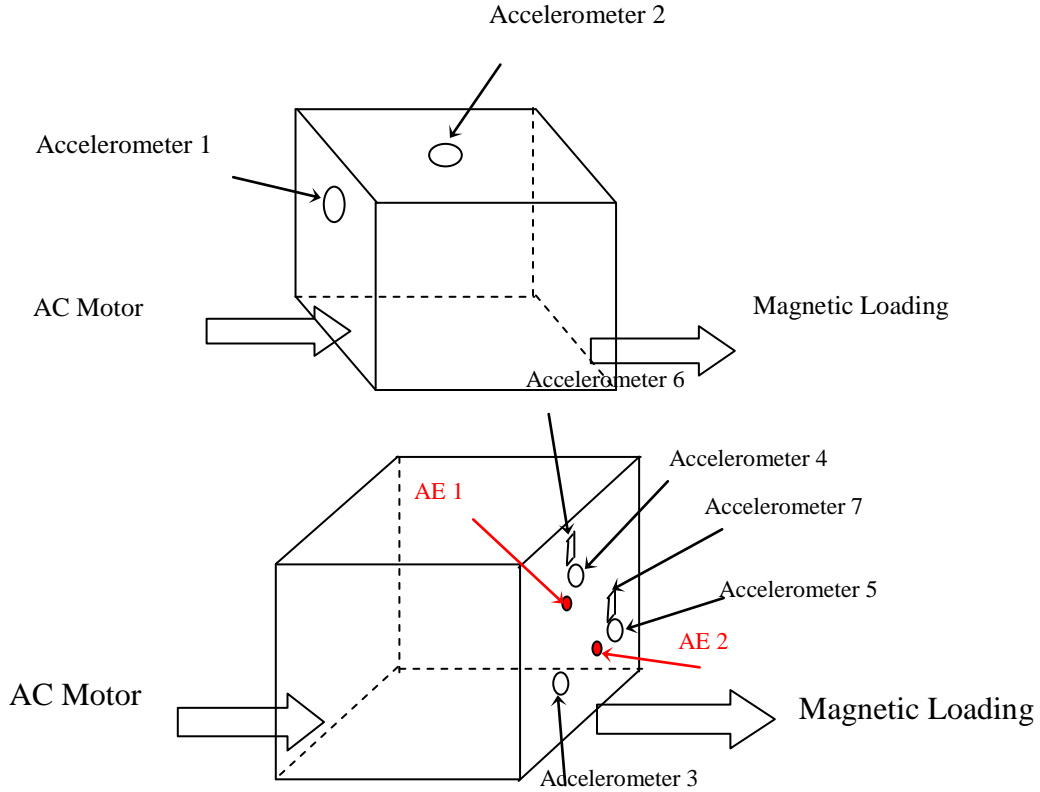


Figure 6. The locations of the sensors

3.3 Drive and Loading Systems

Basically speaking, there are two types of motor, DC motor and AC motor. Compared with DC motor, AC motors are more cost effective and mechanically robust. Since the major purpose in this test rig design is for gear transmission system fault detection, diagnostics and the operation under high precision speed is not the major concern. A 3 HP three phase induction AC motor with a maximum speed of 3600 rpm is used to drive the notional gearbox and VFD S1 type converter produced by Delta Cop. is used to drive

the motor. To accommodate for shaft misalignment and reduce the vibration transmission, a disc type coupling is utilized to transmit the torque from the motor to the driving shaft. A magnetic loading system is controlled by a power supply and the load can be adjusted by changing the output current of the amplifier.

4 VIBRATION SIGNAL BASED ROTATING MACHINERY FAULT DETECTION AND DIAGNOSIS

4.1 Introduction

For rotating machinery fault detection and diagnostic, vibration signal based techniques are the most widely applied technique comparing to the other sensor signal based techniques, such as oil debris, temperature, motor current and acoustic emission and so on. Generally speaking, rotating machine faults such as gear faults, bearing faults and so on, can be classified as distributed faults, such as wear, and localized faults, such as root crack, chipping, and tooth loss and so on. The distributed faults increase the transmission errors, while the localized faults not only affect the transmission accuracy but also cause catastrophic failure of the transmission system. In this dissertation, the research was conducted on only the rotating machinery localized faults. Throughout the dissertation, the gear faults and bearing faults refer to gear localized faults and bearing localized faults.

In general, there are three categories of vibration signal processing techniques for rotating machinery fault detection and diagnostics. They are frequency domain methods, time domain methods, and time-frequency methods. The early researches on vibration signal based gear fault detection and diagnostics were focused on frequency domain analysis. Spectral analysis was applied for rotational machinery fault detection and diagnostics. The development of the Fast Fourier Transform (FFT) algorithm [75] and the computational capability of the digital processor made the real-time spectral analyze possible. And thus the frequency domain methods were widely applied to the rotational

machinery fault detection and diagnostics. Successful applications could be found in [76, 77]. The spectral analysis assumes that the signal is stationary. However, in [78], the author presented that localized machine faults introduce non-stationary property into the vibration signal. For time domain methods, simple statistical parameters, such as root mean square value, peak value, kurtosis value of the measured time domain raw vibration signal could be easily utilized to capture the fault symptoms for rotational machinery fault detection. The calculation of these values is simple and direct. However, in real applications, the fault symptoms are buried into the background noises and the vibration signals generated by the other healthy components, such as the gearbox, shaft and bearings. Therefore techniques were developed to increase the fault symptom signal-to-noise ratio (SNR). One group of methods of increasing the fault SNR is to use time synchronous average (TSA) [79-81]. TSA increases the SNR by separating the vibration signal of the component being interested from other components and suppressing the background noise. TSA is a powerful tool in preprocessing the vibration signal and is the most popular technique in gear fault detection [80-86]. The drawbacks of the TSA include that it requires an additional synchronous signal, the tachometer signal and it usually needs several cycles of the vibration signals in order to achieve the required SNR. Thus a relatively long sampling period is needed. Another way to increase the signal-to-noise ratio is to use model based methods to remove the periodic signals or the background noise from the raw vibration signals. These methods include auto-regressive (AR) model based methods[87], adaptive noise cancellation [88], narrowband interference cancellation [70] *etc.* One shortcoming for these methods is that all these techniques need to determine the structure of the model. More recently, a new technique

called joint time-frequency analysis methods are developed for rotational machinery fault detection and diagnostics. The time-frequency analysis methods are found to be very useful in analyzing the vibration signal generated by the rotational machinery. The fundamental idea of joint time-frequency analysis techniques is to find a way to represent the energy density of a signal in time and frequency domain simultaneously. In rotating machinery diagnostics, simultaneous time and frequency information of a non-stationary signal can provide important diagnostic information on a monitored machine [89]. Most popular time-frequency analysis techniques applied to process the rotating machine vibration signals include: short-time Fourier transform (STFT) [90-92], Wigner-Ville distribution (WVD) [89, 93-96], continuous wavelet analysis (CWT) [27, 49, 97-103], and Hilbert-Huang transform (HHT) analysis [104-109]. By using STFT to analyze signal, the discrete signal is divided into several consecutive blocks in time. Each blocks of the signal is then analyzed by using FFT. Major advantage by using STFT is the ability of representing time-frequency content of signals free of cross terms and implementing easily [110]. However, by using STFT, it provides constant frequency resolution. The tradeoff between time and frequency resolution limits the effectiveness of the STFT. WVD combines FFT and auto-correlation calculation. By using WVD to analyze a signal, the time-frequency energy density is obtained by correlating the signal with a time and frequency translation of itself. Unlike STFT, it provides a high-resolution in both time and frequency domain. However, the energy distribution obtained by traditional WVD contains severe cross-terms between components in different time-frequency regions. This effect makes the energy distribution difficult to interpret and leads to further misinterpretation and confusion. To analyze vibration signal using CWT, the

signal analysis is performed by using a single function called mother wavelet. Through dilation and translation, the CWT can be applied to multi-scale analysis of a signal with non-stationary property. In contrast to STFT, CWT uses narrow time windows at high frequencies and wide window at low frequencies [111], therefore, CWT analysis can provide good frequency resolution and low time resolution for low-frequency components and low frequency resolution and good time resolution for high-frequency components. However, the CWT method has its own limitations. As pointed out in several papers [112, 113], when applying wavelet transform to analyze the signals, the basic wavelet function (mother wavelet) need to be determined first. That means, the type of the basic wavelet function affects the effectiveness of the wavelet methods greatly. Until now, there is no systemic way on choosing the mother wavelet in vibration signal analysis. According to [99, 114, 115], Morlet wavelet was used in vibration analyzing as it is simple and similar to the impulse vibration generated by the faulty components. In [103, 116], Gabor function was adopted as mother wavelet in vibration feature extraction, because it provides the smaller area of the time–frequency window than any other functions. In [117], Gaussian-envelope oscillating wavelet was utilized in gearbox fault detection. As suggested by the authors in [117], by changing the scaling factor in its corresponding wavelet family, the Gaussian-envelope oscillating function could become similar to all sizes of oscillating transients in a gear vibration signal. A recent developed method is called Hilbert-Huang Transform (HHT), first proposed by Huang [112]. By using HHT to analyze vibration signal, the empirical method decomposition (EMD) is applied to decompose the signal into intrinsic mode function (IMF) and then the Hilbert transform is applied to the IMF components to obtain the instantaneous amplitude and

frequency of the analyzed signal. HHT is an adaptive method. It has been proven to be effective in various applications, such as rotational machine fault detection and diagnosis[104, 118-121], structure health monitoring[122], bio-tech signals processing[123], audio signal processing [124], and so on.

In this chapter, the effectiveness of the HHT on gear fault detection is investigated. The vibration features extraction methodology based on EMD technique has been developed. The gear and full ceramic bearing seeded fault test data were used to demonstrate the effectiveness of the developed method. A two-step vibration signal based plastic bearing fault diagnostic methodology has been developed. Seeded plastic bearing fault tests were used to demonstrate the effectiveness of the developed method. An interference cancellation based methodology on gear fault detection has been developed. Vibration signals collected from a notional gearbox test rig were used to demonstrate the effectiveness of the developed methodology.

The remainder of the chapter is organized as follows. Section 4.2 provides the theoretical basis. Section 4.3 presents the experimental setup and data collection. The EMD based vibration signal fault feature extraction method is shown in Section 4.4. A two-step plastic bearing fault diagnostic methodology is described in Section 4.5. Section 4.6 presents interference cancellation based gear fault detection methodology.

4.2 **Theoretical Basis**

4.2.1 **Hilbert-Huang Transform**

HHT was developed by Huang [112]. Recently HHT has been applied to rotational machinery fault detection [104, 118]. HHT has been proven to be an effective method in analyzing the vibration signals for rotational machinery fault detection. When HHT is applied to analyze the signals, the signals are first decomposed into several IMF components by EMD and then Hilbert transform is applied to calculate the instant amplitudes and instant frequency of the IMFs to form the Hilbert spectrum.

The steps of obtaining Hilbert-Huang spectrum of the signal is described as following,

Step 1. Decompose the signal by using EMD technique to get the IMF components,

Step 2. Calculate the Hilbert transform of each IMF component to form analytical signal,

Step 3. Calculate instantaneous amplitude and frequency from the analytical signals,

Step 4. Form Hilbert spectrum with time and frequency information using time and instantaneous amplitude and frequency information.

4.2.1.1 Empirical Mode Decomposition

EMD was a main part of the HHT [112]. Define a collected signal by $Sig(t)$, the steps of the EMD procedure are provided as follows[112]:

- Step 1. Find the local maxima and local minima of the signals.
- Step 2. Construct the lower and upper envelopes of the signals by the cubic spline respectively based on the local maxima and local minima.
- Step 3. Calculate the mean values $m(t)$ by averaging the lower envelope and the upper envelope.
- Step 4. Subtract the mean values from the original signals to produce the IMF candidate component $h_1(t) = sig(t) - m(t)$. If it is the true intrinsic mode function, go to the next step. And the IMF component $C_i(t) = h_m(t)$ is saved. If it is not the intrinsic mode function, repeat Step 1 to Step 4. The stop condition for the iteration is given by Eq. (3):

$$\sum_{t=0}^T \frac{[h_{m-1}(t) - h_m(t)]^2}{h_{m-1}^2(t)} \leq SD \quad (3)$$

where $h_{m-1}(t)$ and $h_m(t)$ denote the IMF candidates of the $m-1$ and m iterations, respectively and usually SD is set between 0.2 and 0.3.

- Step 5. Calculate the residual component by subtracting IMF component obtained in Step 4 from the original signals $res_i(t) = sig(t) - C_i(t)$. This residual component is treated as new data and is subjected to the same processes described above to calculate the next IMF component.

Step 6. Repeat the Steps 1 to 5 until the final residual component becomes a monotonic function and no more IMF component can be extracted or the envelopes becomes smaller than a pre-determined value.

Through Steps 1 to 6, the original signals $Sig(t)$ can be decomposed into N empirical modes ($C_1 - C_N$).

According to Huang *et al.* [112], a function $f(t)$ is defined to be an IMF, if it satisfies two characteristic properties:

- (1) In the whole data set, the number of extrema and the number of zero crossings must either equal or differ at most by one;
- (2) At any point, the mean value of the envelope defined by the local maxima and the envelope defined by the local minima is zero.

4.2.1.2 Hilbert Spectrum

Assuming a signal, $sig(t)$ was decomposed by EMD into N IMF components, $[C_1(t), C_2(t), \dots, C_N(t)]$, then the Hilbert transform of one of the IMF components can be defined as,

$$H[C_i(t)] = \frac{1}{\pi} \int_{-\infty}^{+\infty} \frac{C_i(\tau)}{\tau - t} d\tau \quad (4)$$

where $C_i(t)$ is the i^{th} IMF components and i is the integer number between 1 and N .

The analytic signal $z_i(t)$ can be defined as,

$$z_i(t) = C_i(t) + jH[C_i(t)] = E_i(t)e^{j\phi_i(t)} \quad (5)$$

where $E_i(t) = |C_i(t) + jH[C_i(t)]| = \sqrt{C_i^2(t) + H^2[C_i(t)]}$ and $\phi_i(t) = \tan^{-1} \frac{H[C_i(t)]}{C_i(t)}$.

From the above definition, the ‘instantaneous frequency’ $\omega_i(t)$ could be calculated as the following equation,

$$\omega_i(t) = \frac{d}{dt} \phi_i(t) \quad (6)$$

According to Eq. (5), the original signal, $sig(t)$, could be expressed as the real part in the following equation:

$$sig(t) = real \left[\sum_{i=1}^N E_i(t) e^{j \int \omega_i(\tau) d\tau} \right] \quad (7)$$

where $real[\bullet]$ denotes the real part of the complex number.

As described in [112], the time-frequency domain Hilbert spectrum $H(\omega, t)$ could be obtained by the following equation:

$$H(\omega, t) = real \left[\sum_{i=1}^N C_i(t) e^{j \int \omega_i(\tau) d\tau} \right] \quad (8)$$

From equation (8), one can see that the Hilbert spectrum contains both time and frequency domain information.

The marginal spectrum $h(\omega)$ can then be defined as,

$$h(\omega) = \int_0^{T_0} H(\omega, t) dt \quad (9)$$

where T_0 is the total signal length.

The frequency domain energy $FE(t)$ is obtained by

$$FE(t) = \int_{\omega_1}^{\omega_2} H^2(\omega, t) d\omega \quad (10)$$

As shown in [125], the EMD acts essentially as a dyadic filter bank, which resembling those involved in wavelet decompositions. This property makes EMD capable of adaptively decompose the vibration signal or AE signals into sub-band signals with different frequency contents. Thus the information contains in the different frequency band could be analyzed. A simulation example is used here to demonstrate this property of the EMD technique. A Gaussian random noise signal was used here. The sampling frequency was set to be 102.4 kHz and totally 16384 points samples were used in the calculation. The simulated Gaussian random noise and its Fourier spectrum are shown in Figure 7 and Figure 8, respectively. From Figure 8, one can see that the spectrum is flat in the whole spectrum.

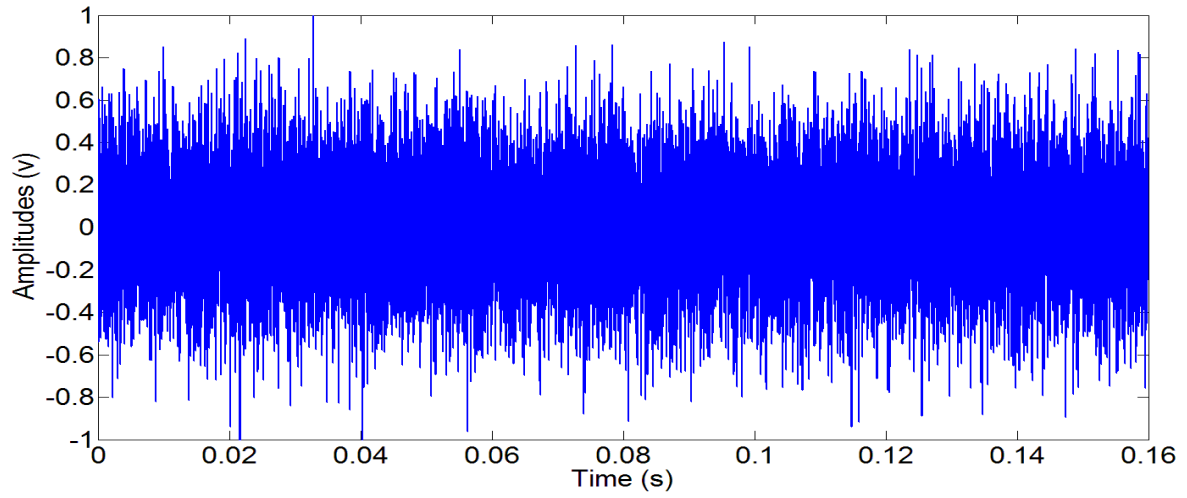


Figure 7. The simulated Gaussian noise signal

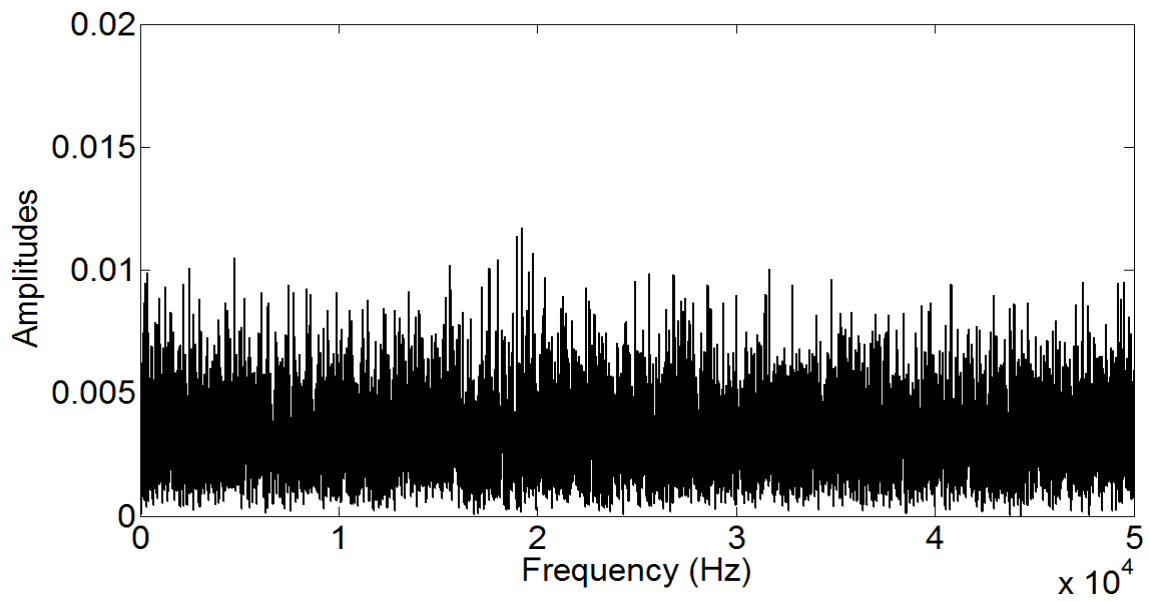


Figure 8. The Fourier spectrum of the simulated Gaussian noise signal

The signal shown in Figure 7 was decomposed by EMD to obtain the IMF components. To investigate the frequency contents of each IMF component, frequency spectrum of each IMF component was calculated and the frequency spectrums of the first 8 IMF components are shown in Figure 9.

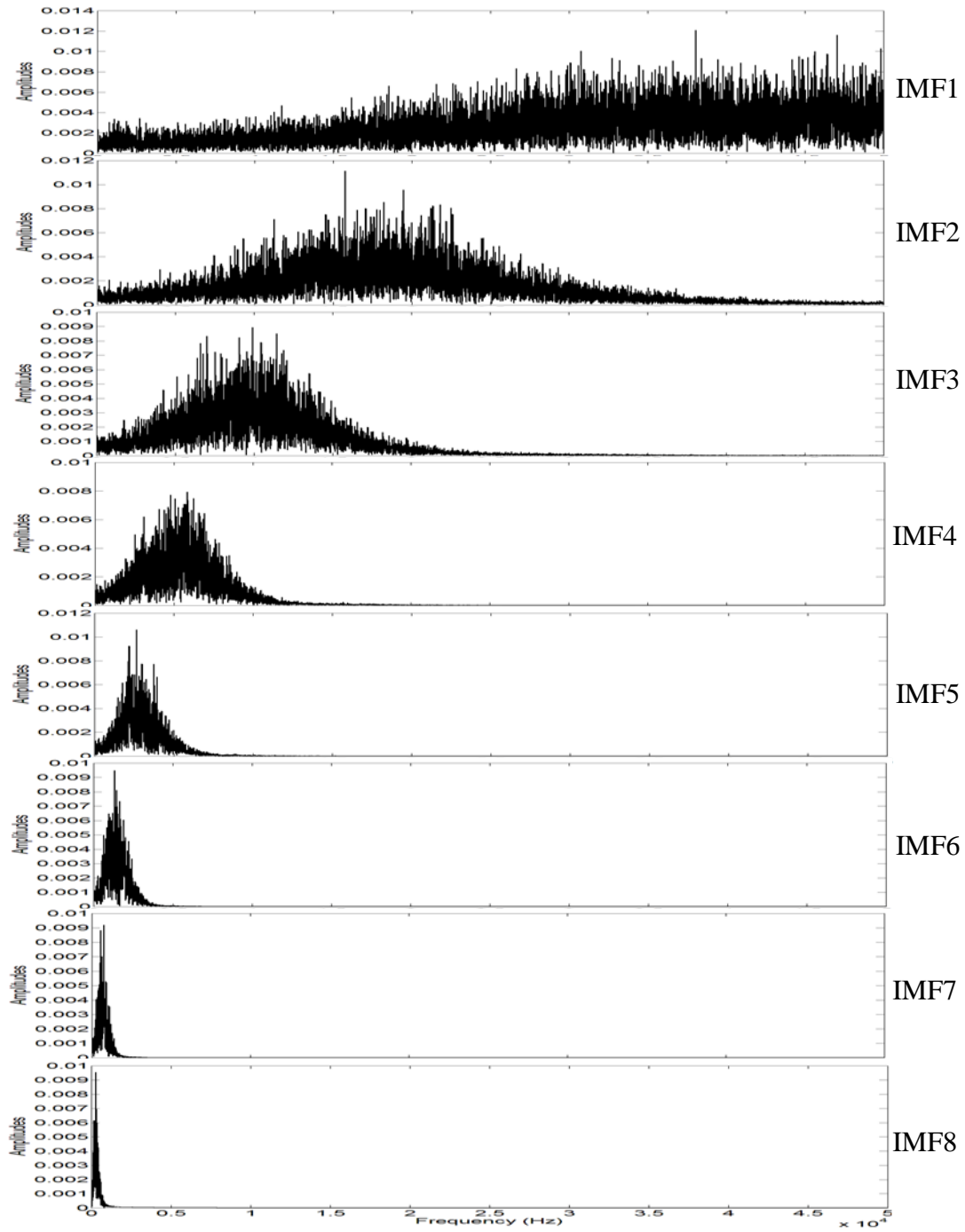


Figure 9. The Fourier spectrum of the IMF components of the simulated signal

A gear seeded fault study was conducted to demonstrate the effectiveness of HHT on rotational machinery fault detection. In this seeded fault study, an ordinary gearbox with 4 spur gears was used. The gear test rig is shown in Figure 10 and the simplified structure of the gearbox is shown in Figure 11.

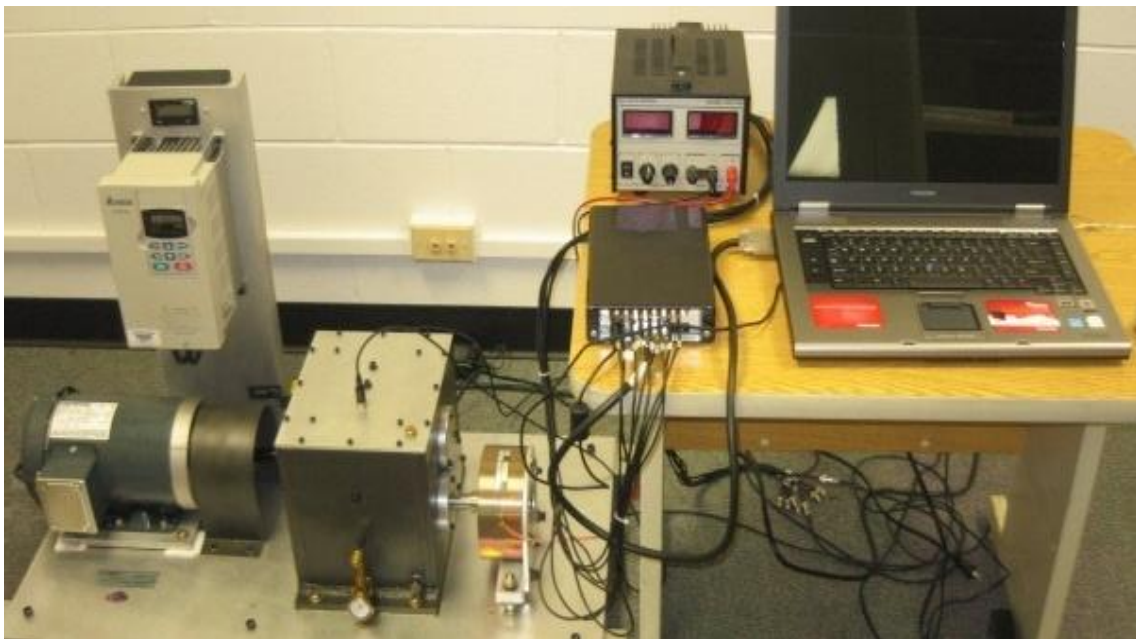


Figure 10. The gear test rig

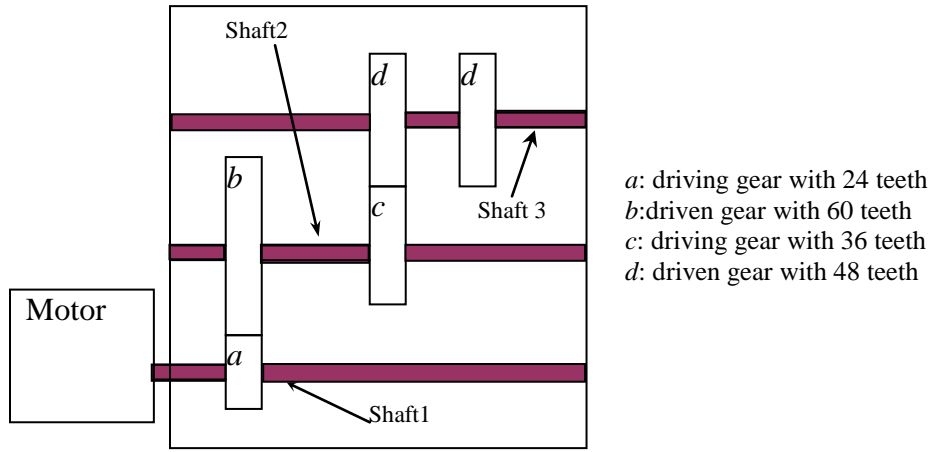


Figure 11. The simplified structure of the gearbox

During the experiment, the speed of the motor was set to 1000 rpm, which is approximate 16.67 Hz. At this speed the characteristic frequencies of the gearbox can be calculated based on the transmission path shown in Figure 11. Based on the structure of the gearbox, the rotating frequencies of shaft 1, shaft 2 and shaft 3 were 16.667 Hz, 6.667 Hz and 5 Hz respectively. The meshing frequency of gear pairs *a* to *b* was 400 Hz and that of gear pairs *c* to *d* was 240 Hz. The gear *a* was damaged with one of the tooth removed to simulate the tooth loss fault in the gearbox. The damaged gear is shown in Figure 12. Both the vibration data of the healthy gearbox and the damaged gearbox were collected using the two accelerometers. The sampling interval was 0.039 ms corresponding to the sampling frequency of 25.6 kHz. For each data set, 0.8 seconds long data was collected.

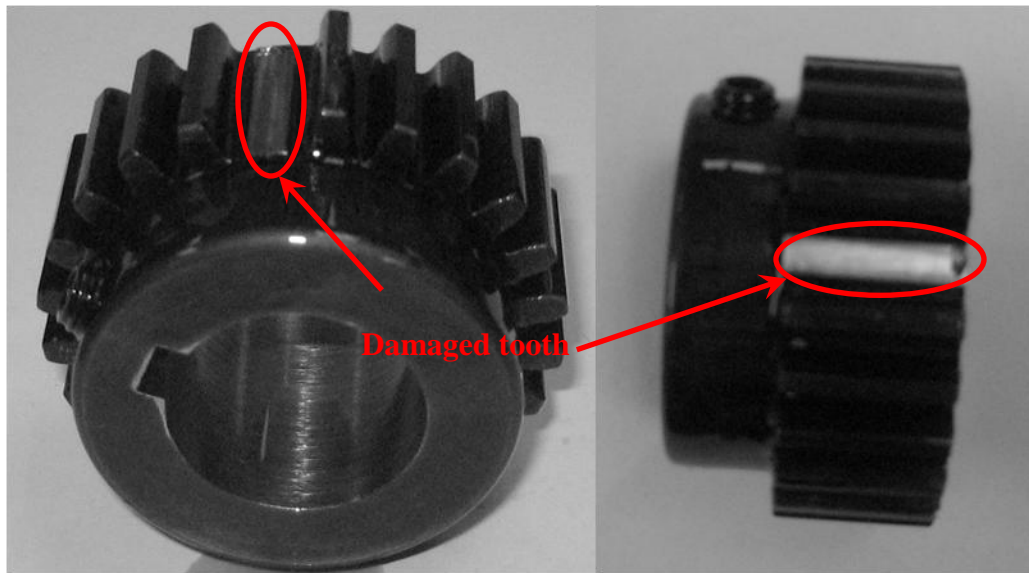


Figure 12. The damaged gear with tooth loss

Figure 13 and Figure 14 show the sample vibration signals from the healthy gearbox and damaged gearbox, respectively.

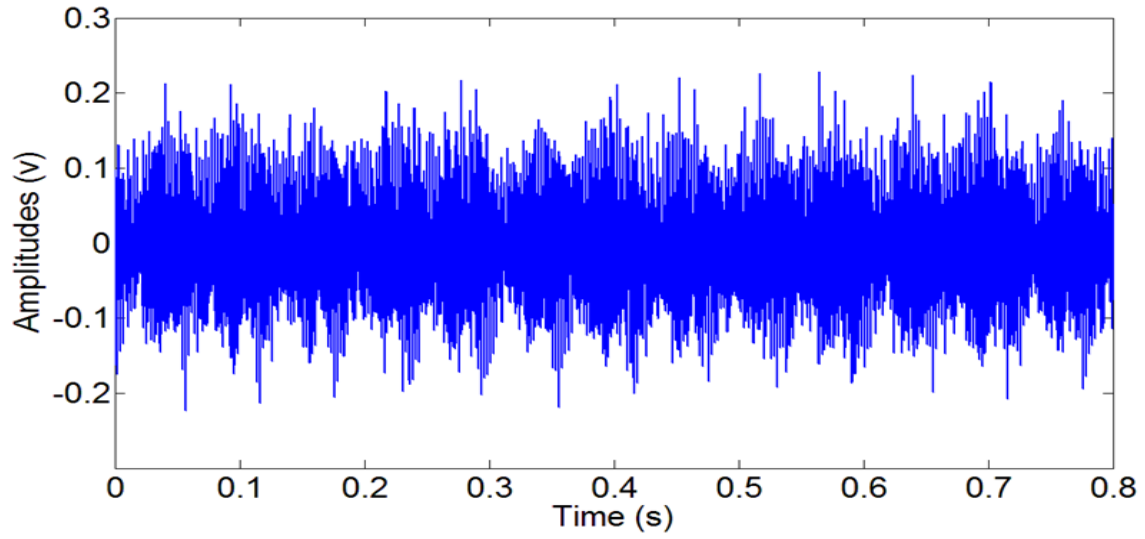


Figure 13. The sample vibration signal of the healthy gearbox

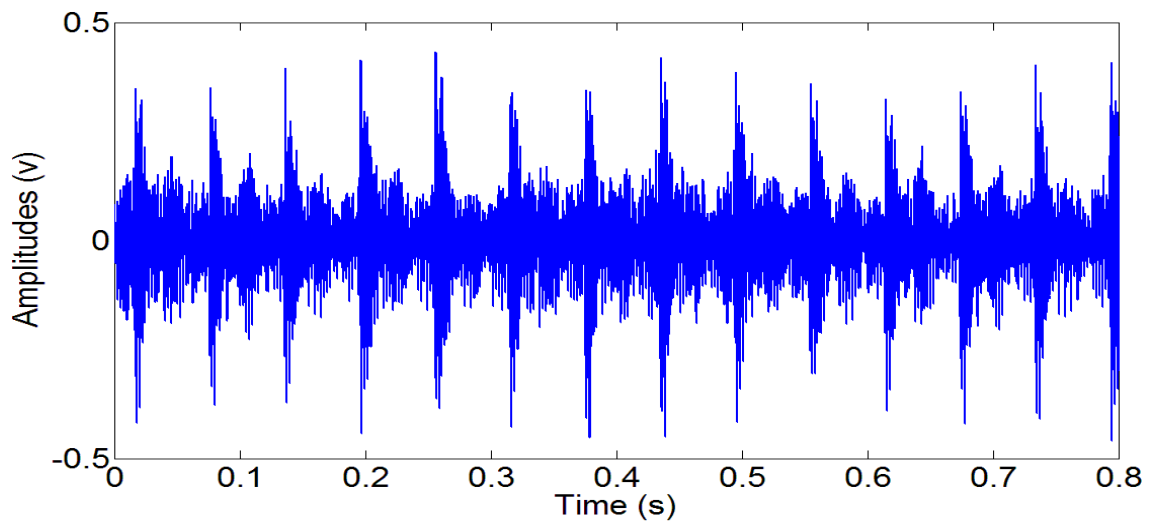


Figure 14. The sample vibration signal of the damaged gearbox with tooth loss

The EMD technique was used to decompose the vibration signals into thirteen IMF components. Only the first eight IMF components $C_1 - C_8$ were shown in Figure 15 and Figure 16 because the energy in the rest IMF components $C_8 - C_{13}$ was very low.

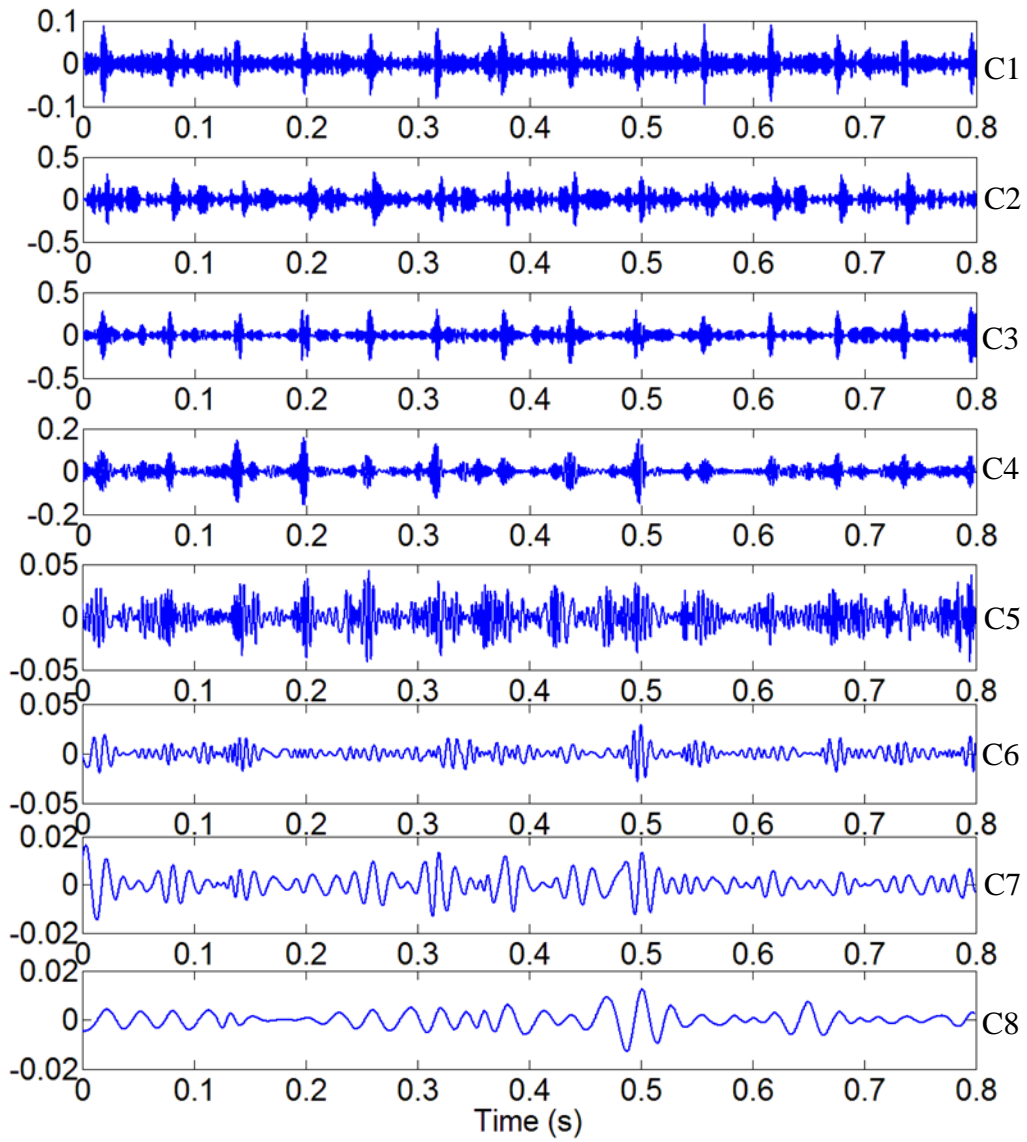


Figure 15. The first eight IMF components of the damaged gearbox

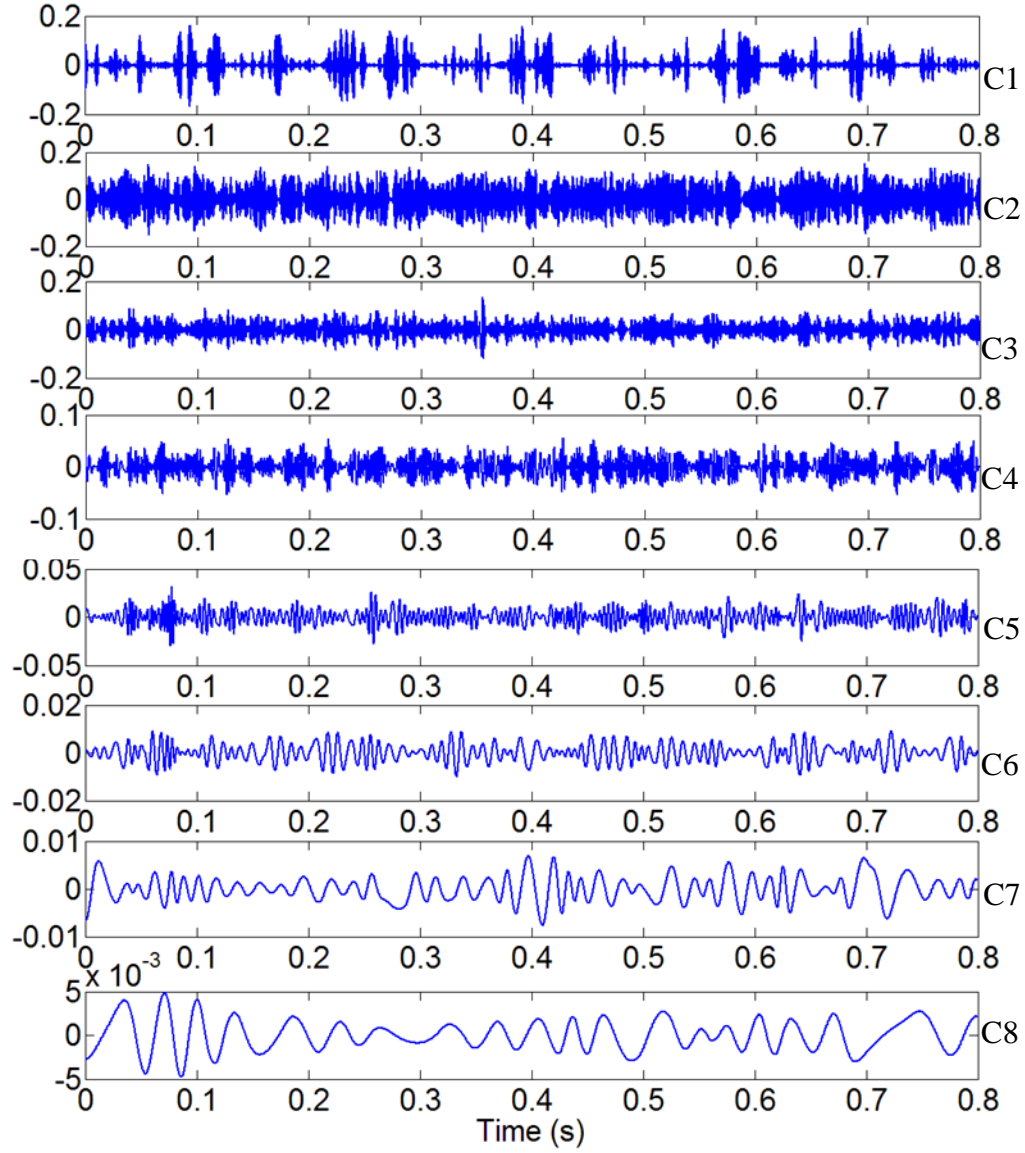


Figure 16. The first eight IMF components of the healthy gearbox

The Hilbert spectrum of the healthy gearbox and the damaged gearbox is shown in Figure 17 and Figure 18, respectively.

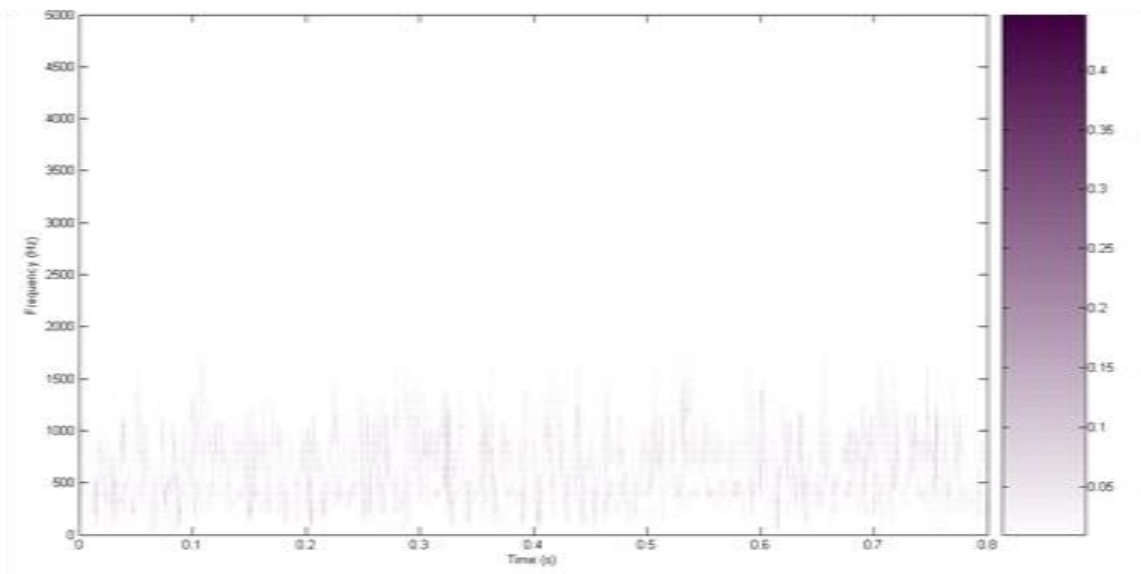


Figure 17. The Hilbert spectrum of the healthy gearbox

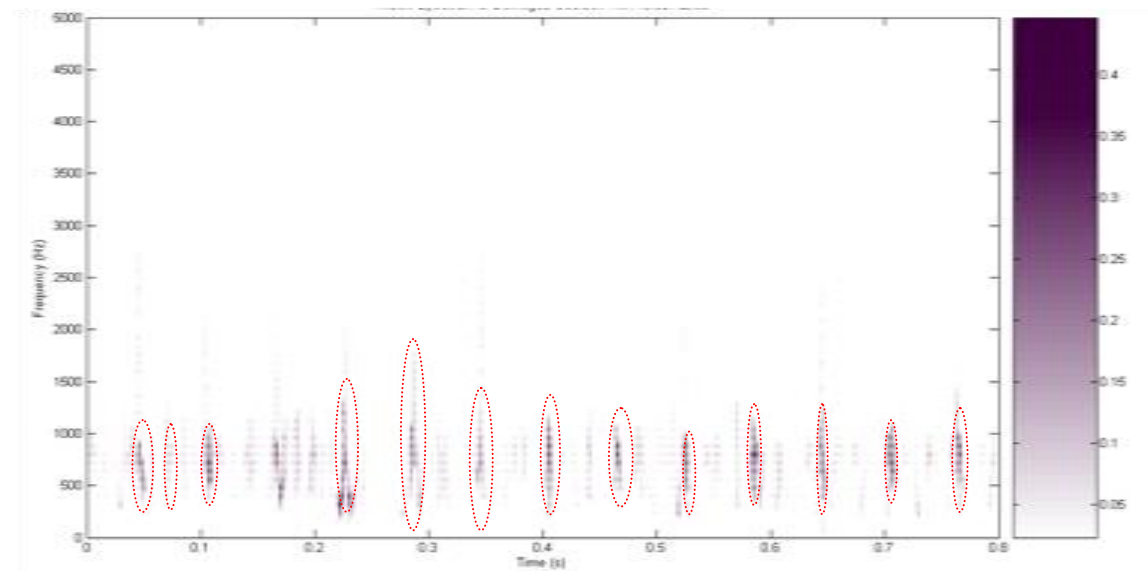


Figure 18. The Hilbert spectrum of the damaged gearbox with tooth loss

Comparing Figure 17 with Figure 18, one can see clearly that there were dark patches in Figure 18, which were circled by the red circles. And the time space between the neighboring black patches was approximately in 0.06 s which was corresponding to the shaft of frequency of 16.667 Hz with the damaged gear a . This clearly indicates that one of the teeth of the gear pairs connected to the shaft 1 had been damaged.

4.2.2 Statistical Threshold for Machine Fault Detection

In rotating machine fault detection and diagnostics, finding an effective way to obtain the threshold value, which provides boundary of different machine states, is very important. Since the vibration signal generated by the rotational machinery is with non-stationary property and the CIs extracted from the vibration signal will not be a static value for a specific machine state, combining statistical method in threshold calculation will help enhance the robust of the fault detection and decrease the false alarm rate. In the real industrial applications, the distribution of the CIs cannot guarantee to follow a specific distribution, such as normal distribution, exponential distribution and so on, the known distribution cannot be used to set the threshold value. Chebyshev's inequality can be used for any unknown distribution. Chebyshev's inequality specifies the upper bond of the probability that the CI of a healthy bearing is k standard deviations away from its mean value as:

$$\Pr(CF - \mu \geq k\sigma) \leq \frac{1}{k^2} \quad (11)$$

In Eq. (11), μ and σ^2 are mean and variance of the CI context of fault detection, the probability upper bond $1/k^2$ specified by Eq. (11) is actually the false alarm rate for a single CI. For a group of CI $1/k^2$ is the tolerance rate. This means that if the CIs are computed from a healthy state, then statistically there should be no more than $1/k^2\%$ of the CIs that are greater than $\mu + k\sigma$. Based on uncorrelated CIs, here one can set $\mu + k\sigma$ as the fault detection threshold. Therefore, if one wishes to detect the fault with a desired false alarm rate of $1/k^2$, one should conclude that the compressed features are from a damaged state when there are more than $1/k^2\%$ of compressed features that are greater than the fault detection threshold: $\mu + k\sigma$. Let $CF(i)$ be the i^{th} data point of the CI. Then, for any k , the fault detection threshold can be computed as:

$$\theta_{fault_detection} = \frac{1}{N} \sum_{i=1}^N CF(i) + k \sqrt{\frac{1}{N-1} \left[\sum_{i=1}^N \left(CF(i) - \frac{1}{N} \sum_{i=1}^N CF(i) \right)^2 \right]} \quad (12)$$

For example, if we set the desired false alarm rate as 0.05, then $1/k^2 = 0.05$. Then the fault detection threshold can be computed as:

$$\theta_{fault_detection} = \frac{1}{N} \sum_{i=1}^N CF(i) + 4.4721 \sqrt{\frac{1}{N-1} \left[\sum_{i=1}^N \left(CF(i) - \frac{1}{N} \sum_{i=1}^N CF(i) \right)^2 \right]} \quad (13)$$

4.2.3 Adaptive Narrowband Interference Cancellation

According to [126], the major vibration of a healthy geared transmission system contains periodic signals at the tooth-meshing rate caused by the deviations from the ideal tooth profile with amplitude modulation effects caused by the variations of the loadings and

frequency modulation effects caused by the fluctuations of the rotational speed or the tooth spacing errors. When there are gear localized fault, additive impulses generated by the meshing of the damaged teeth will be added to the gear vibration signals. This effect will add the sideband components around the related gear meshing frequencies and their harmonics [52]. Based on the results shown in [87, 126], for one healthy gear, the vibration signal can be described by using the following equation,

$$V_g(t) = \sum_{m=0}^M A_m [1 + a_m(t)] \cos[2\pi f_m t + \beta_m + \theta_m(t)] \quad (14)$$

where, $m(0,1,...,M)$ is the meshing harmonic number, A_m is the amplitude at the m^{th} harmonic frequency f_m , $a_m(t)$ is the amplitude modulation function, β_m is the initial phase, and $\theta_m(t)$ is the phase modulation function at the m^{th} harmonic. The harmonic frequency f_m can be expressed as the following equation,

$$f_m = m \times N \times f_s \quad (15)$$

where N is the tooth number and f_s is the shaft rotational frequency. The shaft is the one which is connected to the gear. The localized gear additive vibration can be expressed as the following equation,

$$V_d = d(t) \cos(2\pi f_r t + \beta_r) \quad (16)$$

where $d(t)$ is the envelope function of the resonant vibration, f_r is the resonance frequency and β_r is the initial phase. Combining Eq. (14) and Eq. (16), and considering the background noise, the vibration signal generated by gears with localized fault is expressed as the following equation,

$$V_{dg}(t) = \sum_{m=0}^M A_m [1 + a_m(t)] \cos[2\pi f_m t + \beta_m + \theta_m(t)] + d(t) \cos(2\pi f_r t + \beta_r) + d_{noise}(t) \quad (17)$$

where $d_{noise}(t)$ is the background noise. The Eq. (17) could be further simplified as the following equations [127],

$$z(n) = S_{impulse}(n) + S_{periodic}(n) + d_{noise}(n) \quad (18)$$

In Eq. (18), $z(n)$ is the whole vibration signal, $S_{impulse}(n)$ the impulse signal, $S_{periodic}(n)$ the periodic signal, and n the sampling point index.

From a signal processing point of view, as the impulse signal is generated by the meshing behavior of the damaged gear tooth, it should be separated from the periodic signal to increase the fault symptom SNR.

According to Eq.(18), the periodic signal $y(n)$ should be estimated and then removed from the whole vibration signal as described in the following equation:

$$e(n) = Z(n) - \hat{y}(n) = S_{impulse}(n) + y(n) + S_{noise}(n) - \hat{y}(n) \approx S_{impulse}(n) + S_{noise}(n) \quad (19)$$

In Eq. (19), $\hat{y}(n)$ is the estimated signal of $y(n)$.

The periodic signal $y(n)$ is a deterministic signal and it is uncorrelated to the random parts, the background noise and the impulse signal of the vibration signal. Since based on the system identification theory [128], the deterministic signal could be perfectly predicted by using the infinite past values, the delayed version of the original vibration signal is utilized as the input signal to the train the prediction model and the parameters of the prediction model are trained by the error signal. Successful application of

narrowband interference cancellation based gear fault detection has been reported in [70].

The process of the adaptive narrowband interference cancellation is shown in Figure 19.

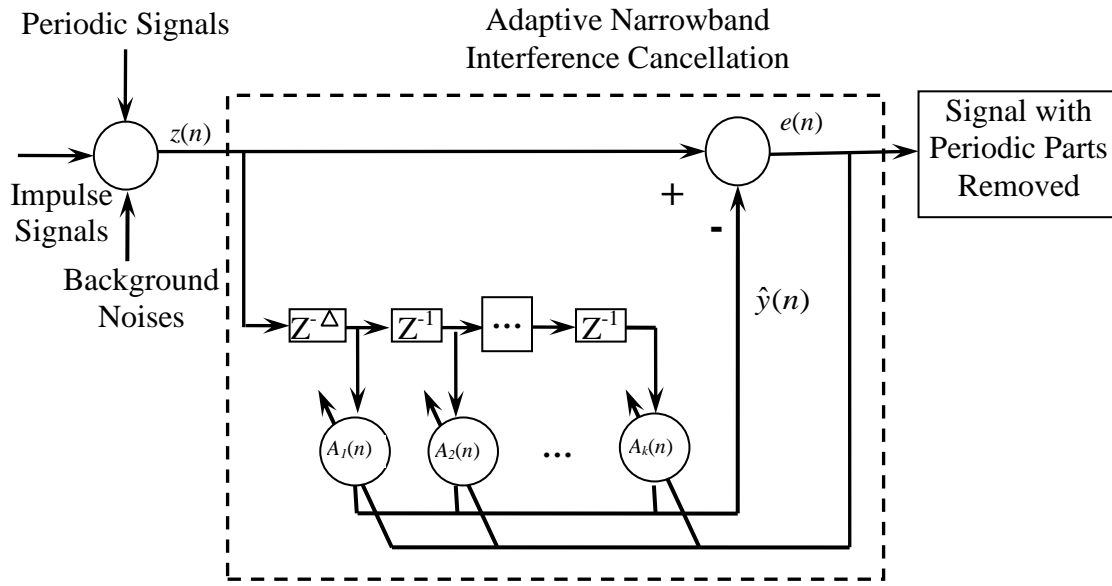


Figure 19. The process of the adaptive narrowband interference cancellation

The way for searching the optimal parameters of the prediction model is to minimize the mean squared error between the original signal and the predicted signal. Expressed in the discrete format, the error signal could be expressed in Eq. (19).

To adaptively adjust the coefficient of the prediction model, the least mean squared algorithm is applied to update the coefficients online. The update equations are shown in Eq. (20) and Eq. (21)[129, 130]:

$$\hat{y}(n) = \sum_{k=0}^{L-1} A_k(n) z(n-k-\Delta) \quad (20)$$

$$A_k(n+1) = A_k(n) + \mu e(n) z(n-k-\Delta) \quad (21)$$

where, $z(n)$ is the input vibration signal, $\hat{y}(n)$ is the estimated output signal, $e(n)$ is the error between $z(n)$ and $\hat{y}(n)$, $A_k(n)$ is the k^{th} parameters of the algorithm, Δ is the delay time, n is the sampling points and μ is the learning step size.

The adaptive algorithm is summarized in the following steps:

- Step 1. Obtain Δ delayed version of the signal $z(n-\Delta)$;
- Step 2. Calculate the estimated signal using Eq. (20);
- Step 3. Calculate the error $e(n)$ by Eq. (19);
- Step 4. Update the confidents A_k by using Eq.(21);
- Step 5. Go back to Step 1.

For demonstrating purpose, assume the coefficients of the prediction model of the $(n+1)^{th}$ step are updated by using Eq. (21) with the coefficients and the error signal of the n th step. The error signal of the n th step is computed by using Eq. (19) with the predicted signal calculated by using Eq. (20) and real signal of the n th step. Through the adaptive process, the system will capture the dynamics of the changing signals.

4.2.4 Threshold Based De-noising

The threshold-based de-noising method was firstly proposed by Donoho [131]. It is an effective method for removing the noise from the original signals. To apply threshold-based de-noising approach using wavelet analysis, first we need to calculate the wavelet coefficients of the signal and then a hard or soft threshold [131] is applied to wavelet coefficients and finally the de-noised signal is reconstructed.

Assume a signal $e(n)$ contains impulse signal $S_{impulse}(n)$ and background noises $d_{noise}(n)$. In vector format, we could represent e , $S_{impulse}(n)$, and $d_{noise}(n)$ as the following equations:

$$\begin{aligned} e &= [e(1), e(2), \dots, e(n), \dots, e(N)]^T, \\ S_{impulse} &= [S_{impulse}(1), S_{impulse}(2), \dots, S_{impulse}(n), \dots, S_{impulse}(N)]^T, \\ d_{noise} &= [d_{noise}(1), d_{noise}(2), \dots, d_{noise}(n), \dots, d_{noise}(N)]^T. \end{aligned} \quad (22)$$

In Eq. (22), N is the total number of the sample points. According to [132], a periodic discrete wavelet transform (DWT) is a linear orthonormal transform and therefore there exists a $N \times N$ orthonormal matrix \mathbf{W} . This matrix transforms the vector e into

$$w = \mathbf{W}e \quad (23)$$

And signal e could be reconstructed as following:

$$e = \mathbf{W}^T w = \mathbf{W}^T w_{d_{noise}} + \mathbf{W}^T w_{S_{impulse}} \quad (24)$$

In Eq. (24), $w_{d_{noise}}$ and $w_{S_{impulse}}$ are the wavelet coefficient vectors of the noise signal d_{noise} and the impulse signal $S_{impulse}$, respectively. The above transformation can be implemented by a pyramidal process [132]. In practical computation, Mallat [133] proposed a fast wavelet decomposition and reconstruction algorithm. In that algorithm, a pair of quadrature mirror filters (QMF) is used to obtain the approximation and the detail signals. At the level 1 decomposition, the signal e is decomposed into two sets of coefficients: the approximation coefficients vector A_1 and detail coefficients vector w_1 . This is called the level-1 decomposition. And then at the level-2 decomposition, the approximation coefficient vector A_1 is split into two sets of coefficients: the approximation coefficients A_2 and detail coefficients w_2 , and so on. The general steps of the decomposition at level j are shown in Figure 20.

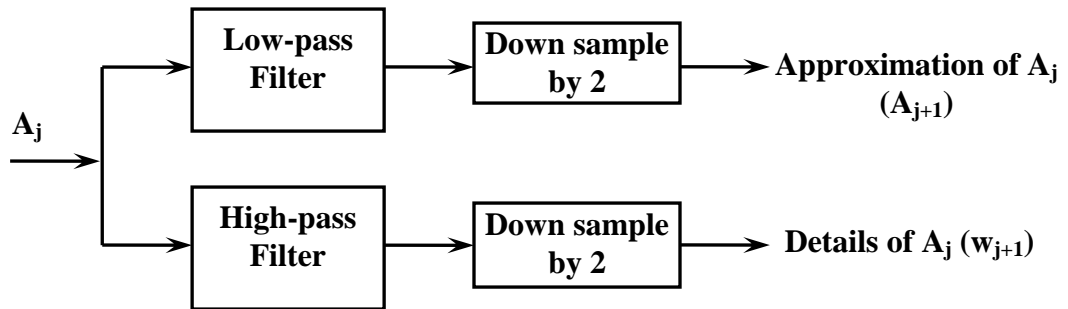


Figure 20. The general steps of the fast wavelet decomposition

In [131], two thresholding calculation methods, the soft-thresholding and hard-thresholding were proposed. The soft-thresholding can be expressed in the following formula[131]:

$$\mathbf{w}_{jde} = \begin{cases} \mathbf{w}_j - \theta, & \mathbf{w}_j > \theta \\ 0 & |\mathbf{w}_j| < \theta \\ \mathbf{w}_j + \theta, & \mathbf{w}_j < -\theta \end{cases} \quad (25)$$

The hard threshold can be expressed in the following formula[131]:

$$\mathbf{w}_{jde} = \begin{cases} \mathbf{w}_j, & |\mathbf{w}_j| > \theta \\ 0, & |\mathbf{w}_j| < \theta \end{cases} \quad (26)$$

where $\theta = \hat{\sigma}\sqrt{2\log N}$, $\hat{\sigma}$ is the estimation of the standard deviation of the signal, N the length of signal, \mathbf{W}_j is the wavelet coefficient of the j^{th} level decomposition and \mathbf{W}_{jde} is the thresholding modified coefficient of \mathbf{W}_j . In our research, the soft-threshold rule is employed because it has the advantages of obtaining near optimal minimax rate, smaller risk, and visual improvement and it modifies a signal without leaving discontinuous points[131].

4.2.5 The K-Nearest Neighbor (KNN) Based Fault Classifier [134]

KNN [135, 136] is a ‘lazy learning’ algorithm. KNN assumes all observations correspond to points in the p-dimensional space. The nearest neighbors of an observation are defined in terms of the standard Euclidean distance. An observation is classified by a

majority vote of its neighbors, with the observation being assigned the class most common amongst its K nearest neighbors. Suppose we have a database consisting of a total of n observations $(\mathbf{x}_i; y_i)$, for $i=1, 2, \dots, n$, where \mathbf{x}_i could be any point in a p -dimensional Euclidean space, \mathfrak{R}^p , denoted as $\mathbf{x}_i = \{x_{i1}, x_{i2}, \dots, x_{ip}\}$ and y_i is an outcome from m class $\omega = \{\omega_1, \omega_2, \dots, \omega_m\}$. The database is called the training set for the KNN algorithm. Given any two observations, \mathbf{x}_i and \mathbf{x}_j , let $s(\mathbf{x}_i, \mathbf{x}_j)$ be a measure of their similarity based on the p varieties, it can be derived as:

$$s(\mathbf{x}_i, \mathbf{x}_j) = \sqrt{\sum_{k=1}^p (x_{ik} - x_{jk})^2} \quad (27)$$

To classify the response for a new observation \mathbf{x}_u with the KNN algorithm, we first identify k observations in the training set that are most similar to \mathbf{x}_u . They form the set of k -nearest neighbors of \mathbf{x}_u , denoted by $N(\mathbf{x}_u, k)$. These similarities can be ordered. Denote the ordered similarities with $s_{(i)}$, i.e., $s_{(1)} \geq s_{(2)} \geq \dots \geq s_{(n)}$. In other words, if $s_j = s_{(k)}$, it means \mathbf{x}_j is the k th most similar observation in the training set to \mathbf{x}_u . The set of the k -nearest neighbors of \mathbf{x}_u , $N(\mathbf{x}_u, k)$, can then be defined as all observations whose similarities to \mathbf{x}_u are at least $s_{(k)}$, i.e., $N(\mathbf{x}_u, k) = \{\mathbf{x}_i : s_i \geq s_{(k)}\}$. The KNN algorithm then estimates the probability that $y_u = \omega_i$ by the average responses of these k -

nearest neighbors and classifies the response to be ω_i if the estimated probability exceeds a certain threshold c :

$$\hat{P} = \frac{\sum_{x_i \in N(\mathbf{x}_u, K)} y_i}{|N(\mathbf{x}_u, K)|} \quad (28)$$

where $|N(\mathbf{x}_u, k)|$ is the number of items contained in the set $N(\mathbf{x}_u, k)$. This is usually equal to k exactly, but may exceed k depending on how ties are treated. The response is then predicted to be ω_i if $\hat{P} \geq c$, where c is a pre-specified threshold parameter.

4.3 Experimental Setup and Data Acquisition

Vibration signals collected from both the designed notional STG gearbox test rig and a bearing test rig were used in this chapter.

4.3.1 Gear Test Experimental Setup and Data Acquisition

To simulate gear faults developed on the gear tooth, two types of seeded gear fault were created on the output side driving gear of the notional STG gearbox test rig. One was gear with tooth loss; the other was gear with root tooth crack. For the gear with tooth loss fault, 50% of one gear tooth on the output side driving gear was chipped. The healthy driving gear on the output side is shown in Figure 21.

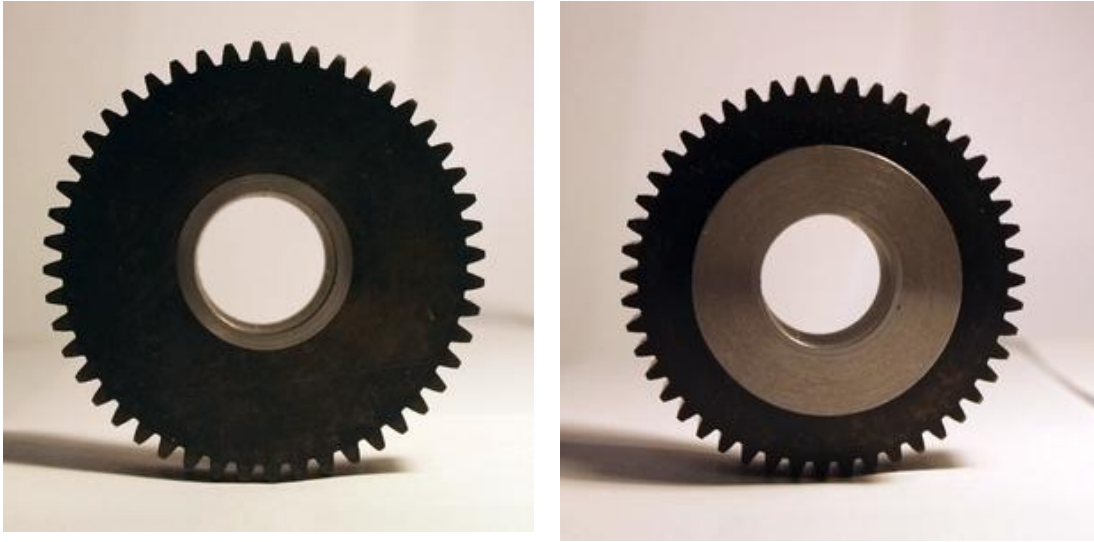


Figure 21. The healthy driving gear on the output side

The damaged gear with 50% tooth loss is shown in Figure 22.

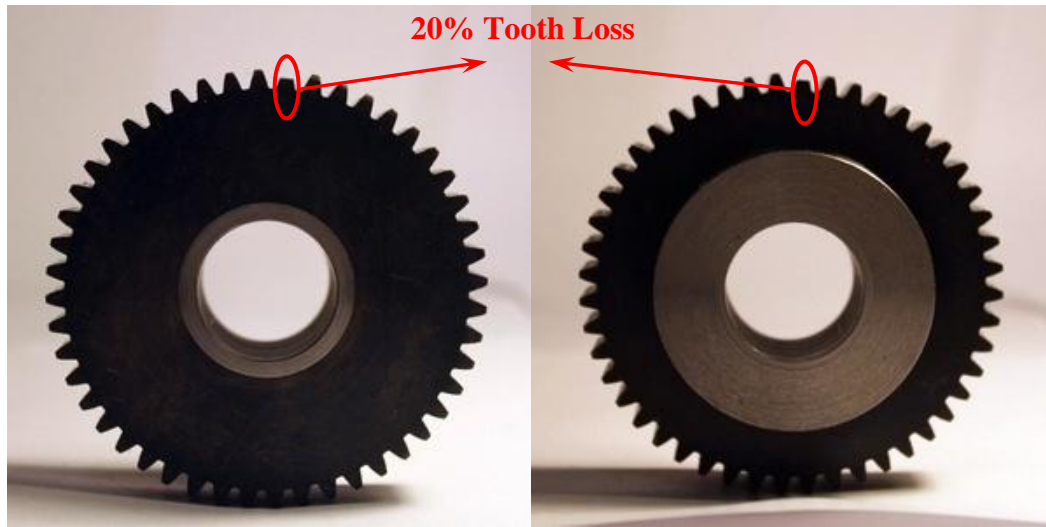


Figure 22. The damaged gear with 50% tooth loss

The damaged gear with 50% root tooth crack is shown in Figure 23. The gear was damaged by cutting the root of a gear tooth with a depth equal to half width of the gear tooth by EDM with a wire of 0.5 mm diameter to simulate the root crack damage in real applications.

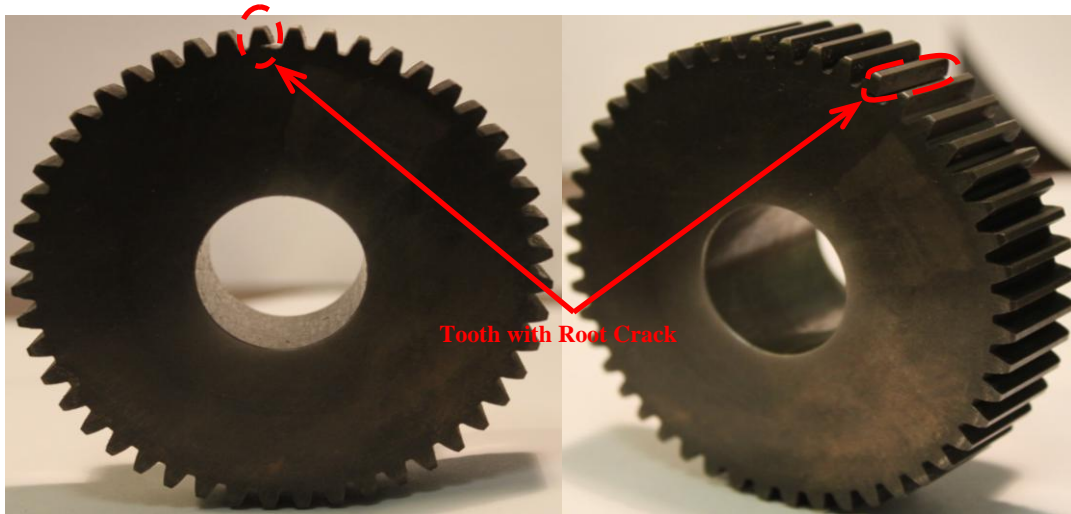


Figure 23. The gear with a tooth root crack

4.3.2 Bearing Test Experimental Setup and Data Acquisition

To simulate bearing faults, four types of seeded bearing faults were created on the rolling element bearing mounted inside the designed bearing house of the bearing test rig. The bearing test rig is shown in Figure 24. A 3-HP AC induction motor with a maximal rotational speed of 3600 rpm, was used to drive the test rig.

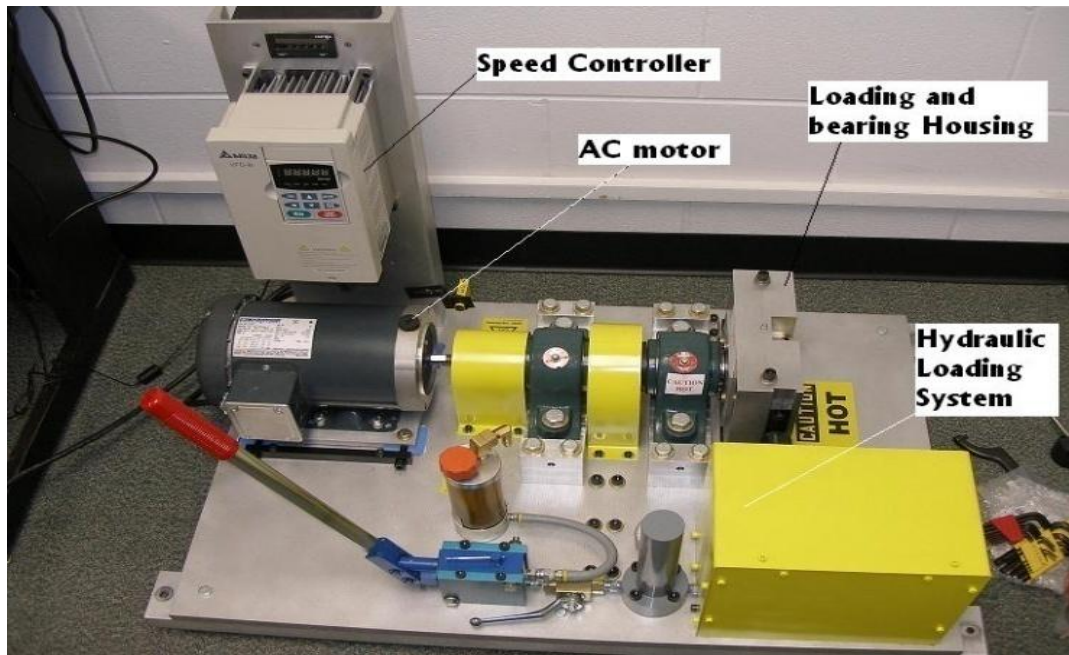


Figure 24. The bearing test rig

During the experiments, two types of bearing were used. The first is plastic bearing and the other is full ceramic bearing. Rolling element bearings are widely applied in rotational machinery in modern industries. Recently, full ceramic rolling element bearings have been replacing the conventional steel bearings in some applications in harsh environments [137] as they have higher resistance to both corrosion and rolling contact fatigue than the traditional steel bearings [138]. Additionally, they are thirty percent harder and forty percent lighter than the conventional steel bearings [139]. As the full-ceramic bearings are relatively new to the industrial applications, there is only limited research on the full-ceramic bearing fault detection and diagnostics. Plastic

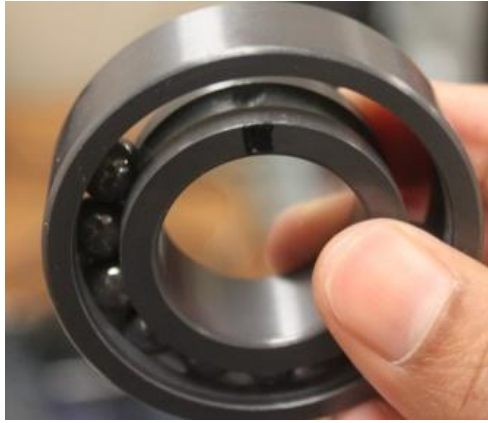
bearings are widely used in medical applications, food processing industries, semiconductor industries, aircraft components, and so on [3-5]. In comparison with traditional steel bearings, plastic bearings have following advantages: (1) corrosion resistance; (2) light weight; (3) non-metallic and non-magnetic; (4) lubrication free; (5) consistent coefficient of friction. Up to today, no research has been conducted on plastic bearing fault diagnosis. Unlike their steel counterparts, effective fault diagnosis methods for plastic bearing have not been developed. According to [140, 141], a more detail description of the plastic bearings and ceramic bearings are listed in Table IV.

Table IV. Materials comparison among plastic bearings, steel bearings and ceramic bearings

Item	Units	Polyphenylene Sulfide (Plastic)	M250 (Plastic)	Si3N4 (Ceramic)	Bearing Steel
Density	g/cm ³	1.35	1.14	3.23	7.85
Water Absorption	%	0.01	0.0014	0	0
Coefficient of Linear Thermal Expansion	10 ⁻⁶ /k	9.6	10	3.2	12.5
Modulus of Elasticity	GPa	3.45	0.8377	300	208
Hardness	MPa	95	47	1500	700
Flexural Strength	MPa	145	150	720	520
Compressive Strength	MPa	148	150	2300	/
Thermal Conductivity	W/m*k	0.288	0.24	25	40

To create the localized faults on a bearing, four different types of ceramic bearing and plastic bearing faults were generated: inner and outer race contact surface fault, rolling element fault, and cage fault (Figure 25 and Figure 26). The damages of the contact surface on the full ceramic bearing inner race, outer race and ball were generated by grinding the race surface using an electric drill with a diamond tip. The diameter of the damaged surface area was about one third of the ball diameter. The broken cage was created by cutting the Teflon retainer using a pair of sharp scissors. The damages of the

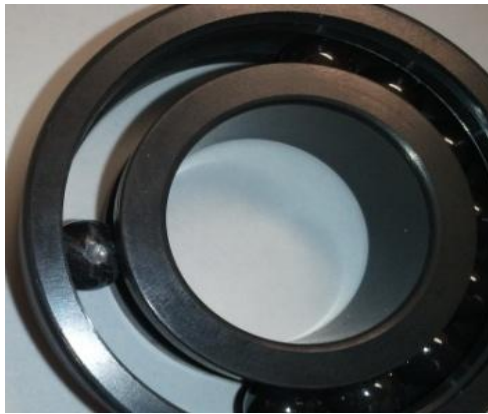
contact surface on the plastic bearing inner race and outer race were generated by scratching the race surface using an electric solder iron with a heated tip. The diameter of the damaged surface area was about one third of the ball diameter. The rolling element damage was created by scratching one of bearing balls with a grinding wheel. Roughly 40% of the ball volume was ground off. The broken cage was created by cutting the Teflon retainer using a pair of sharp scissors.



Inner race fault



Outer race fault



Ball fault



Cage fault

Figure 25. The four types of full ceramic bearing seeded faults



Figure 26. The four types of plastic bearing seeded faults

The 6205-2RS type bearing was used in the experiments. The races of the bearing are made of plastic materials. The bearing ball is made of glass. The seals of the bearing are made of Teflon. The drawing of this type of bearing is shown in Figure 27. The parameters of the bearing are listed in Table V.

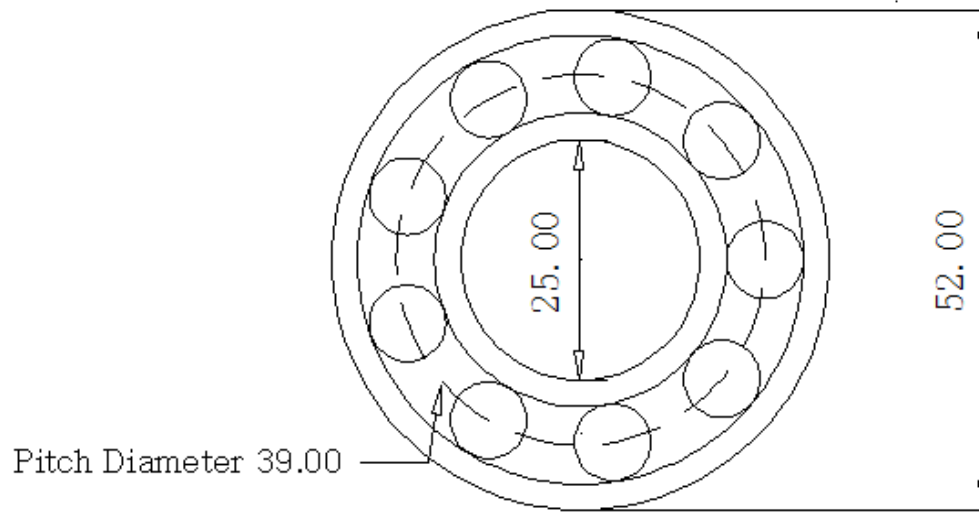


Figure 27. The drawing of the 6025 2RS bearing

Table V. Parameters of the 6025 2RS bearing

Parameters	Inside Diameter	Outside Diameter	Thickness
Size (mm)	25	52	15
Parameters	Ball Diameter	Pitch Diameter	Number of the balls
Size (mm)	8	39	9

For vibration data acquisition, two 603C01 wide range accelerometer and a data acquisition card NI PCI-4472B were used for collecting the vibration signal of both full

ceramic bearing and plastic bearing. The accelerometer was mounted on the surface of the bearing house. The locations of the vibration sensors are shown in Figure 28.

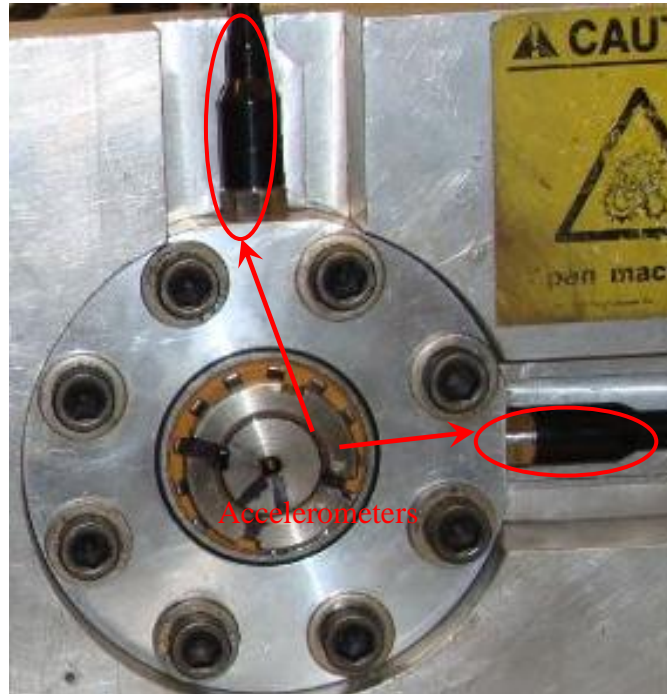


Figure 28. The locations of the AE sensors

During the testing, vibration signals were collected with a sampling rate of 102.4 kHz. The input rotating speed was set to be 10 Hz for full ceramic bearing and four different rotating speeds, 10 Hz, 20 Hz, 40 Hz, and 60 Hz were applied during the plastic bearing test.

4.4 EMD Based Vibration Feature Extraction and CI Development

The process of the EMD based vibration feature extraction method is shown in Figure 29.

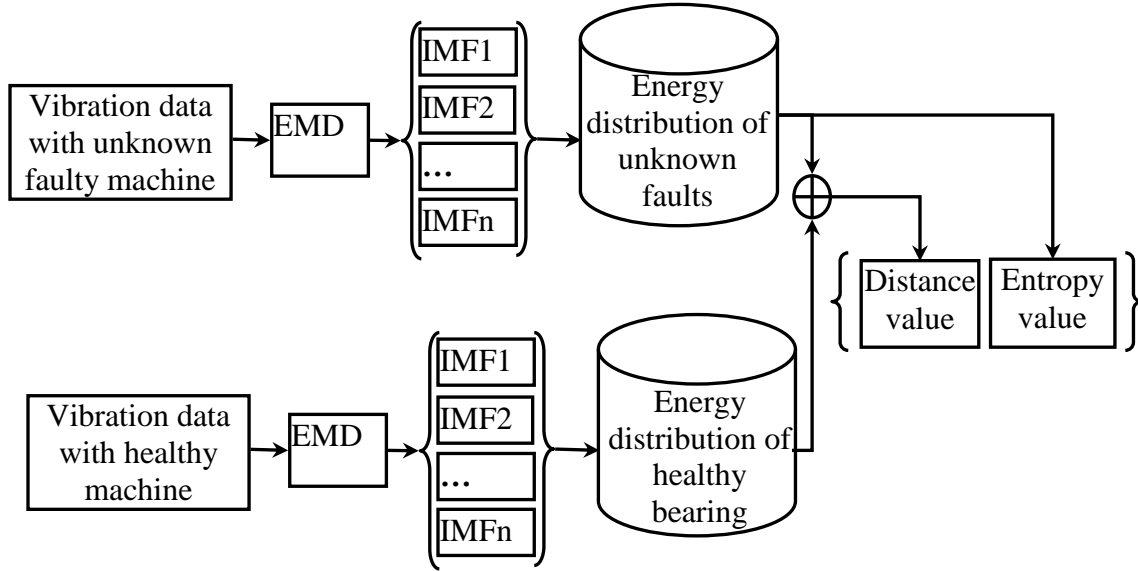


Figure 29. The process of the EMD based vibration feature extraction

As shown in Figure 29, the steps of the time domain feature extraction procedure are provided as follows:

Step 1. Given the N IMF components: $C_1, \dots, C_i, \dots, C_N$ obtained by the EMD, the energy and the energy ratio of the IMF components are calculated. They are expressed in Eq. (29) and (30), as shown below:

$$E_i = \sum_{n=1}^{N_i} C_i(n)^2 \quad (29)$$

$$P_{Ei} = \frac{E_i}{\sum_{i=1}^N E_i} \quad (30)$$

where, E_i is the energy of i^{th} IMF component, N_i is the number of the sampling points of one IMF component, P_{Ei} is the energy ratio of the i^{th} IMF components, N is the number of the IMF components.

Step 2. The energy ratio vector is formed:

$$\mathbf{P}_E = [P_{E_1}, P_{E_2}, \dots, P_{E_{N_1}}] \quad (31)$$

Step 3. The entropy of the energy vector is defined by the following equation:

$$E_{Entropy} = -\sum_{i=1}^N P_{E_i} \log P_{E_i} \quad (32)$$

The entropy value calculated in Eq. (32) is treated as rotating machinery fault feature.

Step 4. The Euclidean distance is defined by the following equation:

$$D = \sum_{i=1}^N |P_{Eunknown_i} - P_{Ehealth_i}| \quad (33)$$

In Eq. (33), $P_{Eunknown_i}$ is the energy ratio of the i^{th} IMF component of the rotating machine with unknown states $P_{Ehealth_i}$ is the energy ratio of the i^{th} IMF component of healthy bearing, and N is the total number of the IMF components. The distance value calculated in Eq. (33) is treated as bearing fault feature.

By using the steps shown above, a two-dimensional fault features are obtained. To demonstrate the effectiveness of the extracted fault features, the KNN classification algorithm was applied to the extracted feature. The two dimensional features with unknown states are used as the input to the trained KNN algorithm to obtain the fault classification results.

Two case studies, gear fault diagnosis and full ceramic bearing fault diagnosis, were used in this dissertation to demonstrate the effectiveness of the proposed methodology.

4.4.1 Case Study I: Split Torque Gear Fault Diagnostics

A total of twenty seven group of vibration signals were collected and sample vibration signals of the healthy gearbox, damaged gearbox with 50% tooth loss and damaged gearbox with 50% root crack are shown in Figures from Figure 30 to Figure 32.

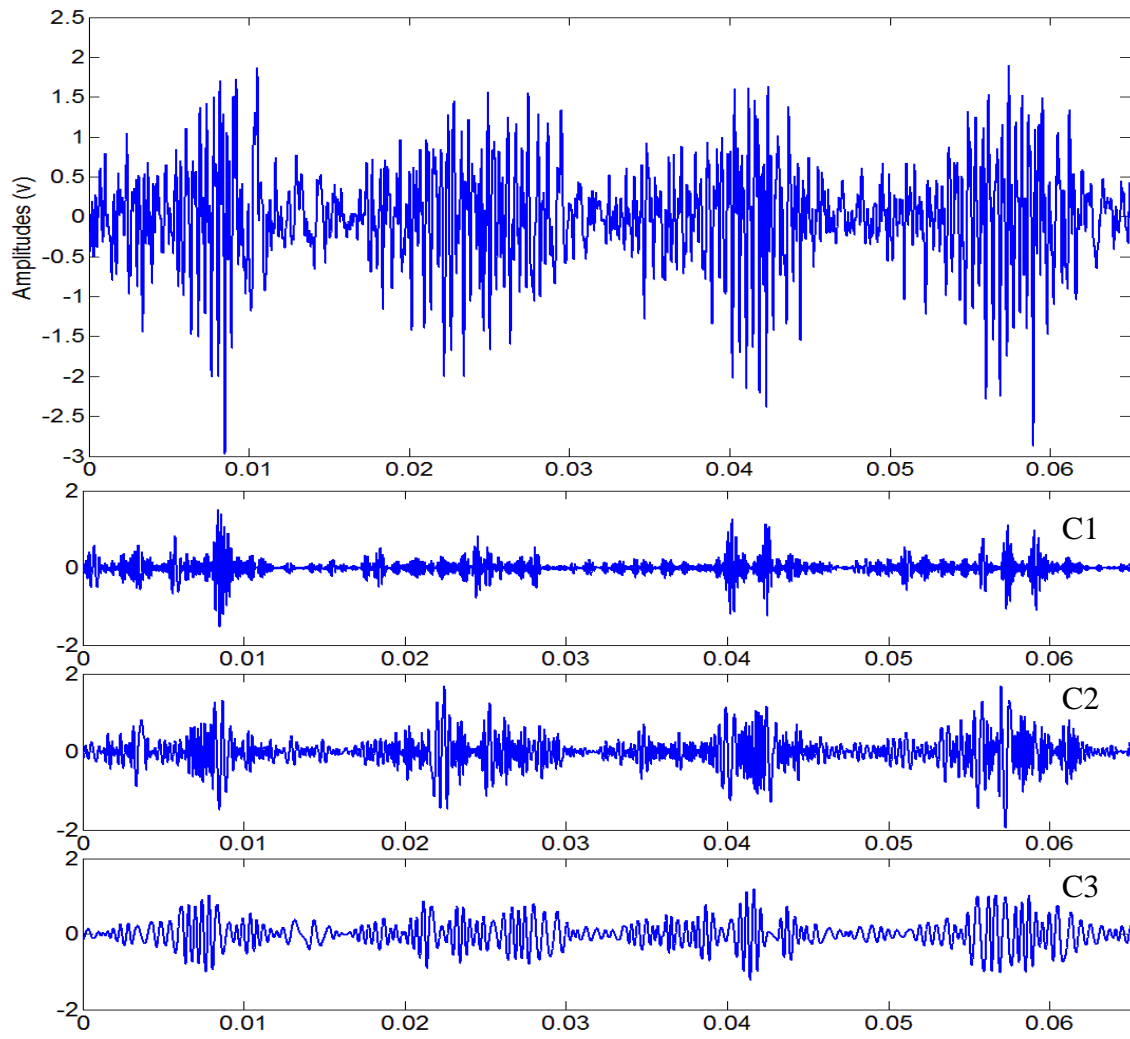


Figure 30. Sample vibration signal of healthy gearbox and its first three IMF components

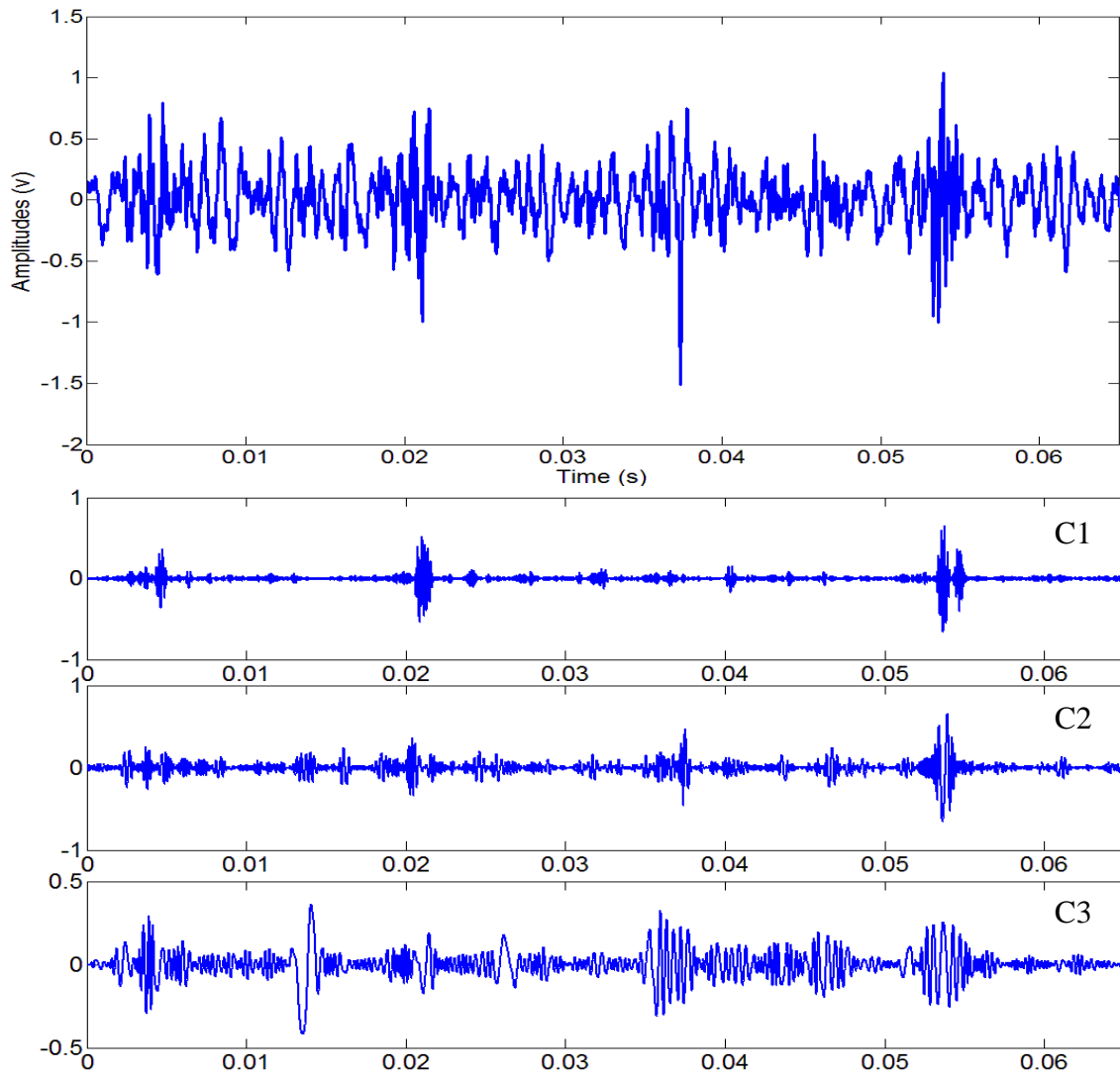


Figure 31. Sample vibration signal of damaged gearbox with 50% tooth loss and its first three IMF components

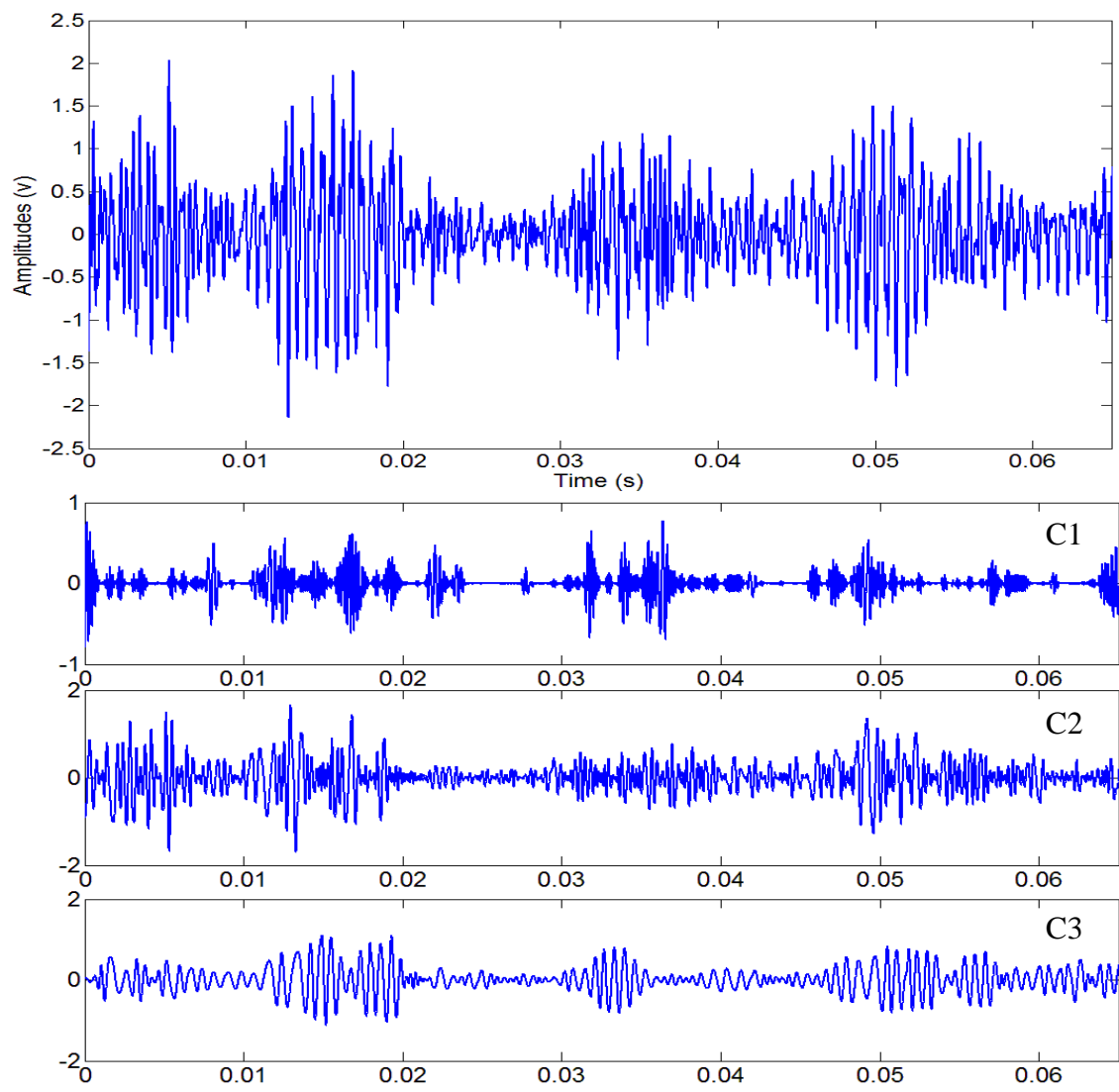


Figure 32. Sample vibration signal of damaged gearbox with 50% root crack and its first three IMF components

After the EMD technique was applied to the vibration signals, the entropy value and the distance value of the energy ratio were calculated as the fault features. The feature vectors are shown in Figure 33.

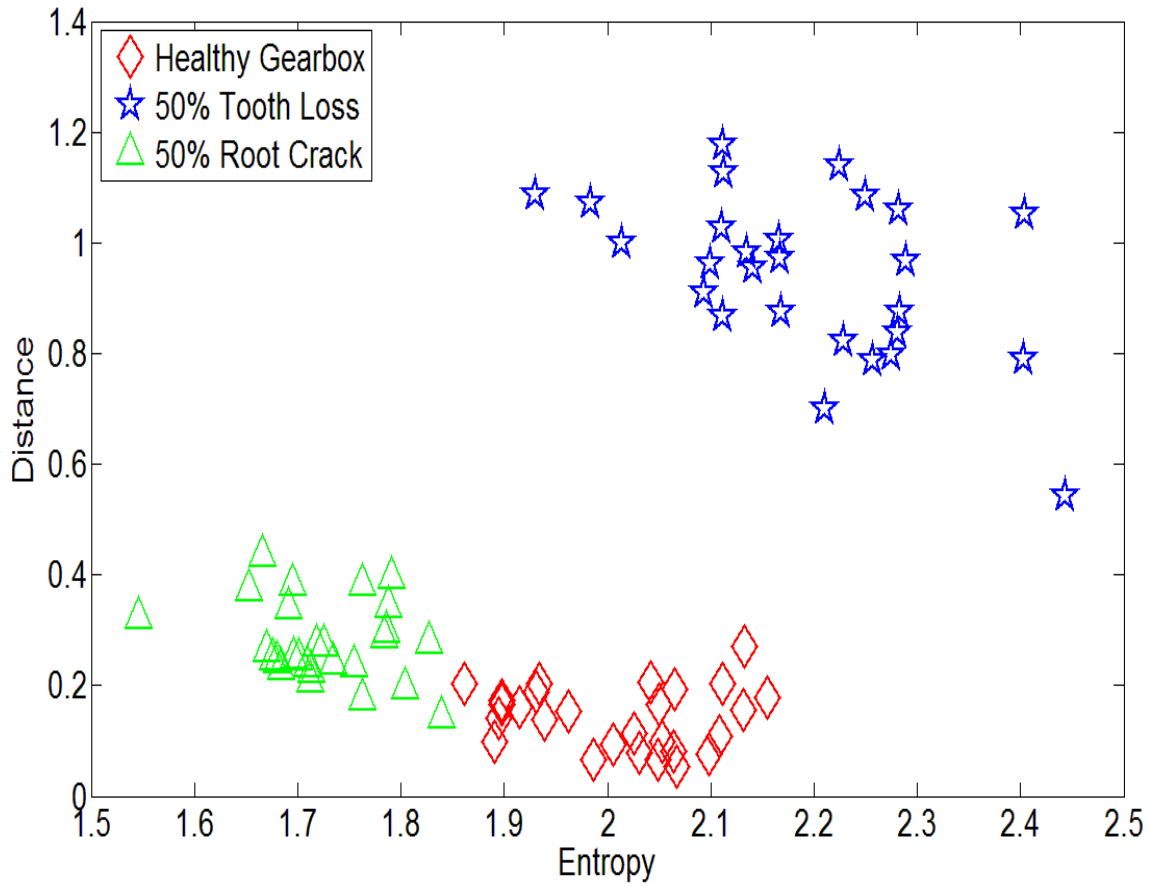


Figure 33. The feature vectors of healthy gearbox, damaged gearbox with 50% tooth loss, and damaged gearbox with 50% root crack

All the vibration CI data generated were split into two groups: 60% of the data were used for training purpose to build the fault classifier and 40% of the data were used for validation to test the performance of the fault classifier. The classification confusion matrix using KNN are provided in Table VI and the classification results are shown in Table VII. Note that in Table VI, the values of k are the best k values with the minimum % error determined by the KNN algorithm. The % error is defined as the percentage of data points of a fault type that were misclassified. On the contrary, the % accuracy is defined as the percentage of data points of a fault type that were correctly classified.

Table VI. The classification confusion matrix using the two dimensional CIs of the STG gearbox

CIs: <i>distance + entropy</i> ($k = 1$)			
	Predicted Class		
Actual Class	Healthy	50% Tooth loss	50% Root crack
Healthy	13	0	0
50% Tooth loss	0	8	0
50% Root crack	1	0	10

Table VII. The KNN fault diagnosis results using the two dimensional CIs of the STG gearbox

Class	Error (%)	Accuracy (%)
Healthy Gearbox	0.00	100.00
Damaged Gearbox with 50% Tooth Loss	0.00	100.00
Damaged Gearbox with 50% Root Crack	9.00	91.00
Total	3.13	96.87

From the results shown in Table VI and Table VII, one can see that high classification accuracy (96.87%) is achieved by using the two dimensional fault features. From the observations of the features shown in Figure 33, one can see that there are large overlapping area of distance value between the healthy gearbox and the damaged gearbox with 50% tooth loss. Also, there are large overlapping area of the entropy value between the healthy gearbox and the damaged gearbox with 50% root crack. That means by using only one dimensional fault feature, the classification error will be high.

4.4.2 Case Study II: Full Ceramic Bearing Fault Diagnostics

A total of fourteen groups of vibration signals were recorded with a length of 0.2 seconds for five full ceramic bearings: healthy bearing, bearing with inner race fault, bearing with outer race fault, bearing with ball fault, and bearing with cage fault were collected. Sample vibration signals of the five different fault types and their first three IMF components are shown in Figures from Figure 34 to Figure 38.

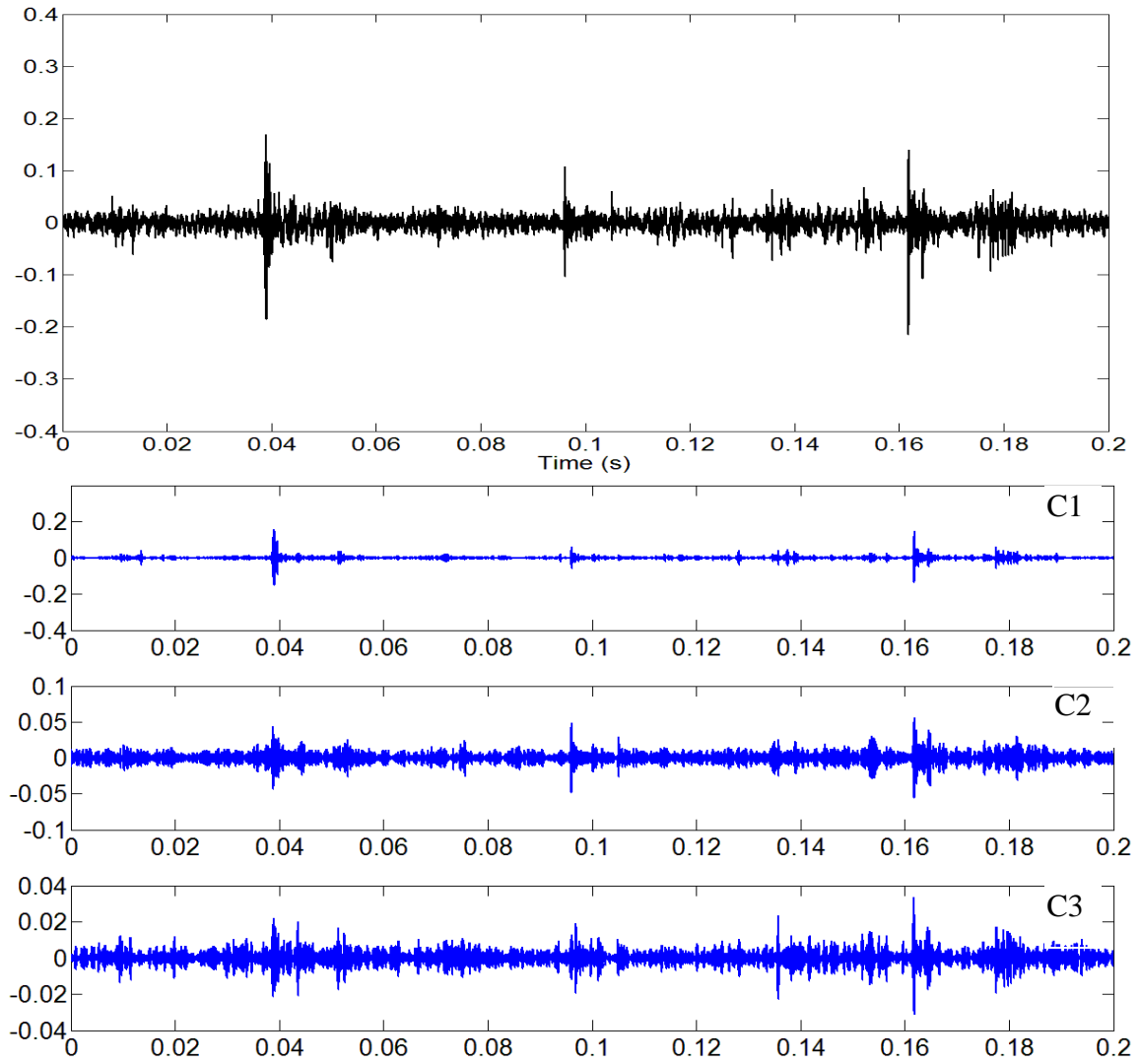


Figure 34. Sample vibration signal of the healthy bearing and its first three IMF components

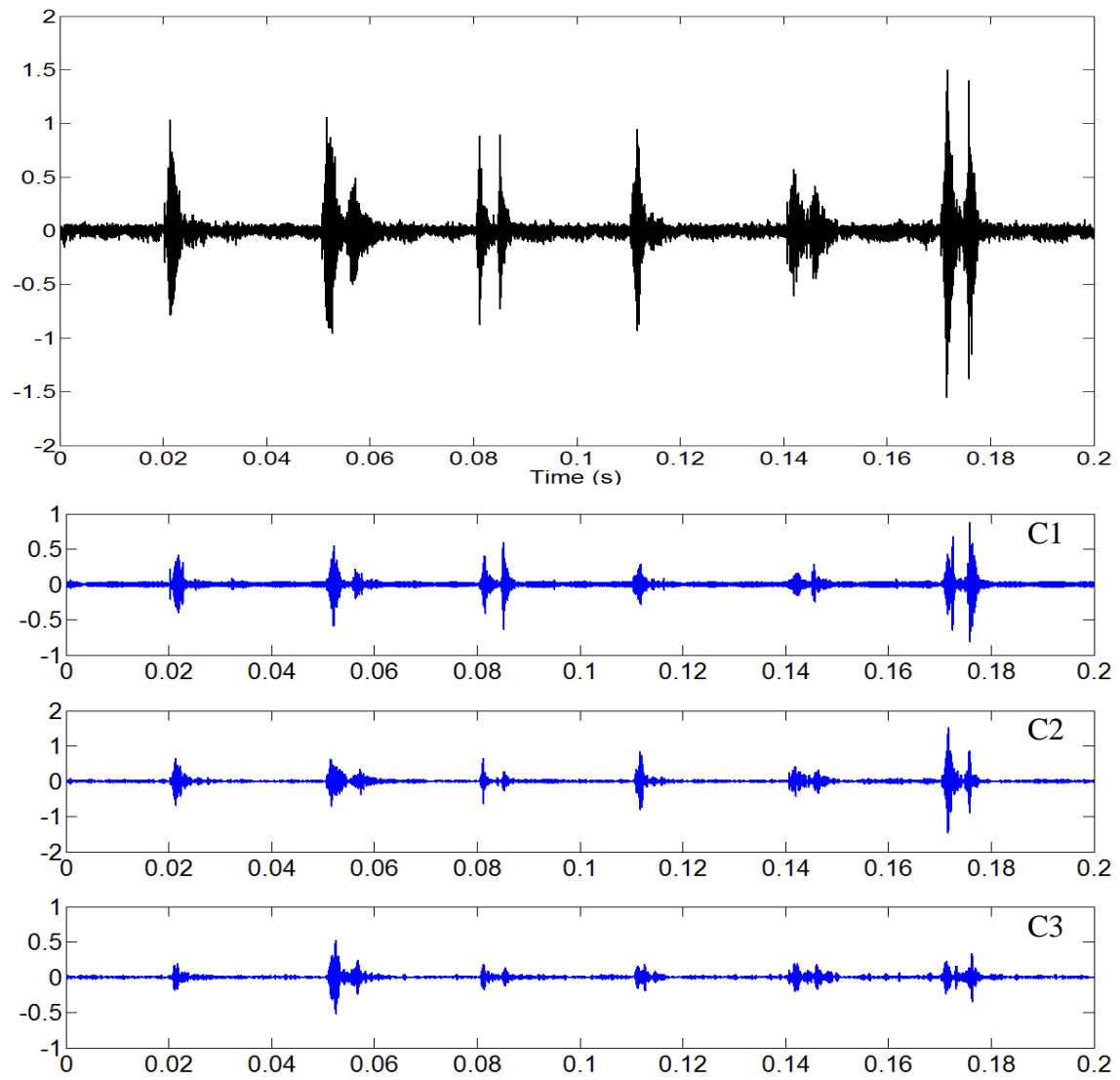


Figure 35. Sample vibration signal of the bearing with outer race fault and its first three IMF components

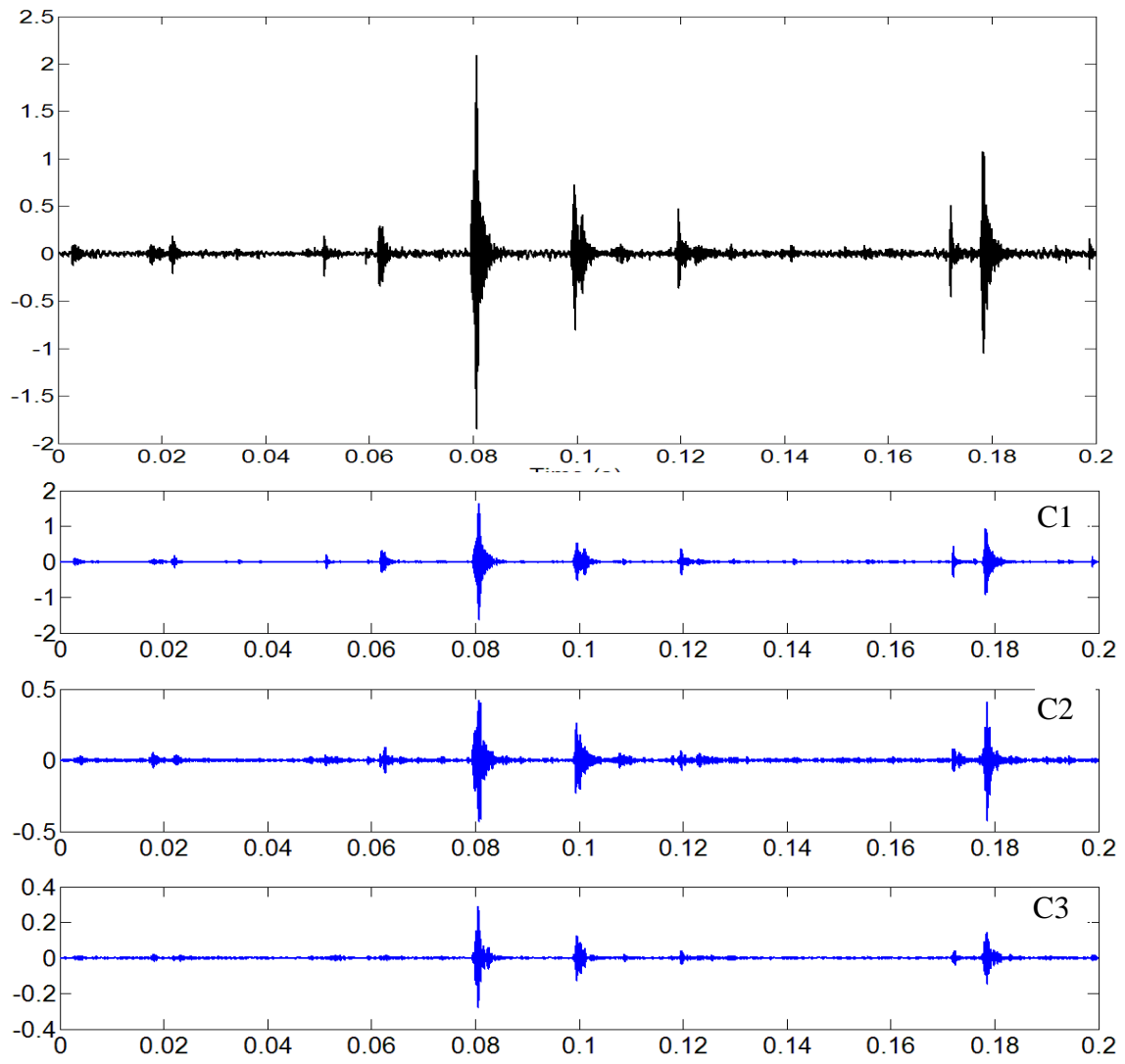


Figure 36. Sample vibration signal of the bearing with inner race fault and its first three IMF components

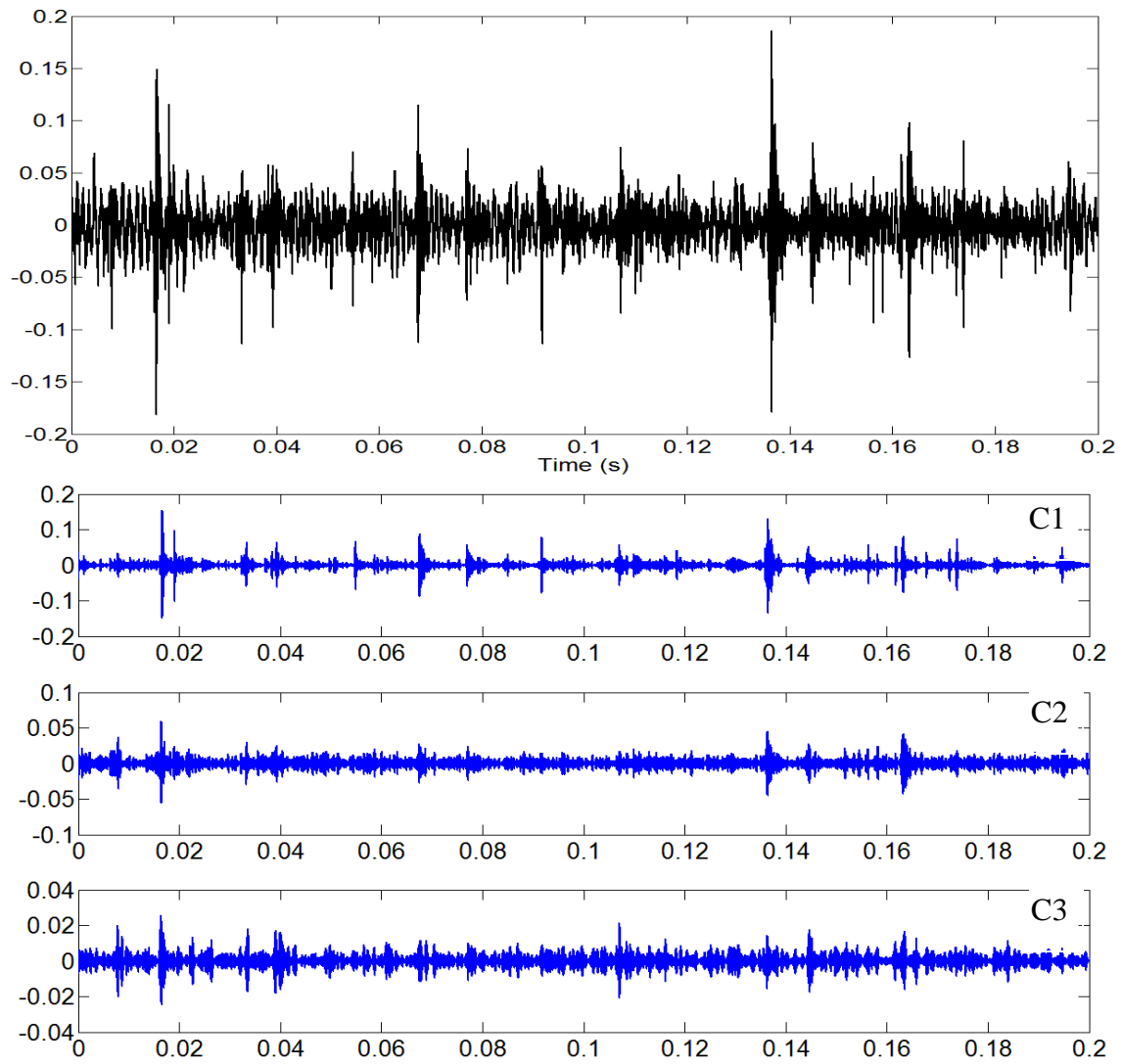


Figure 37. Sample vibration signal of the bearing with ball fault and its first three IMF components

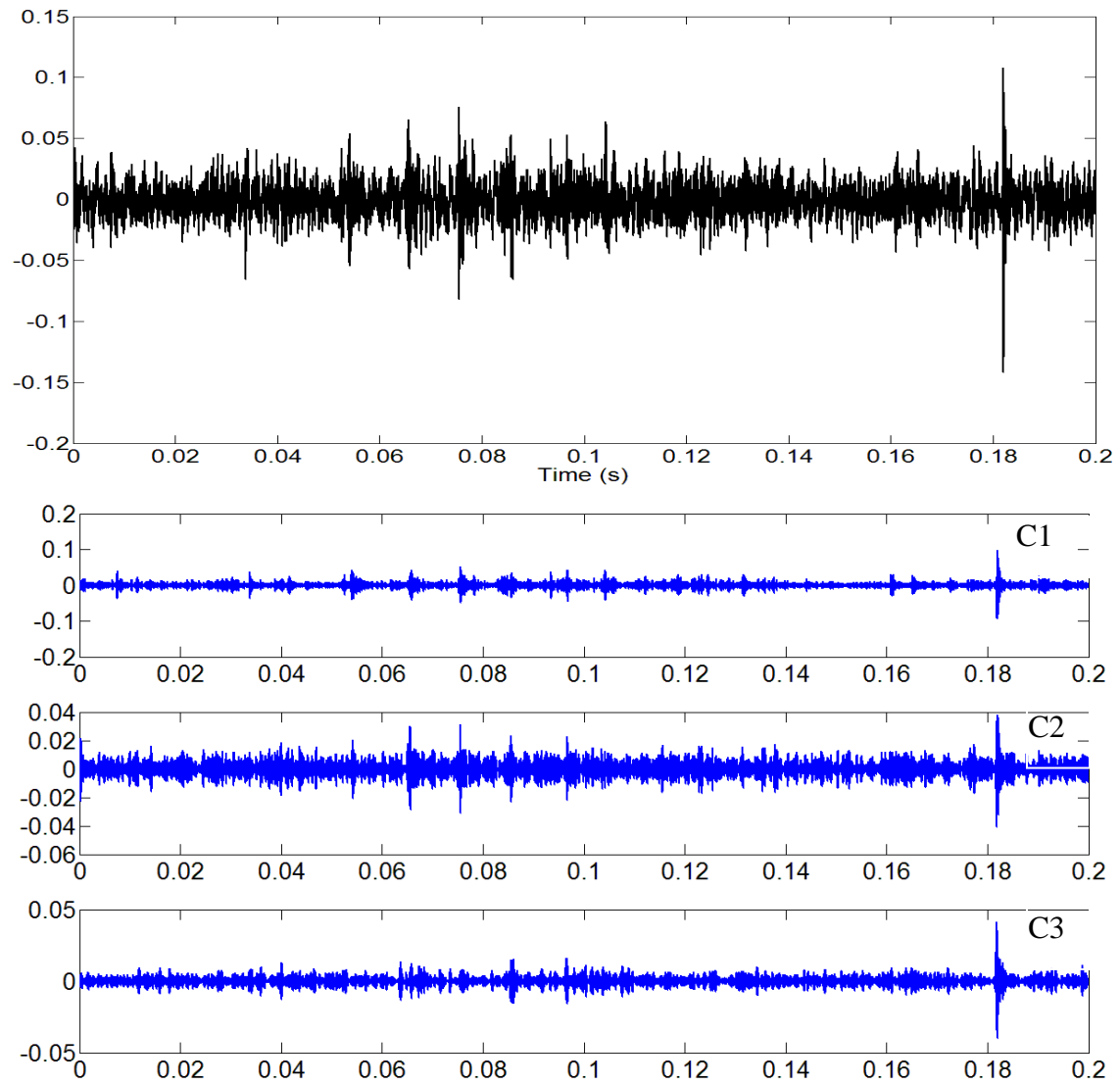


Figure 38. Sample vibration signal of the bearing with cage fault and its first three IMF components

After the IMF components of the vibration signals were obtained by the EMD, the entropy value and the distance value of the energy ratio were calculated as the fault features. The extracted features are shown in Figure 39 and Figure 40.

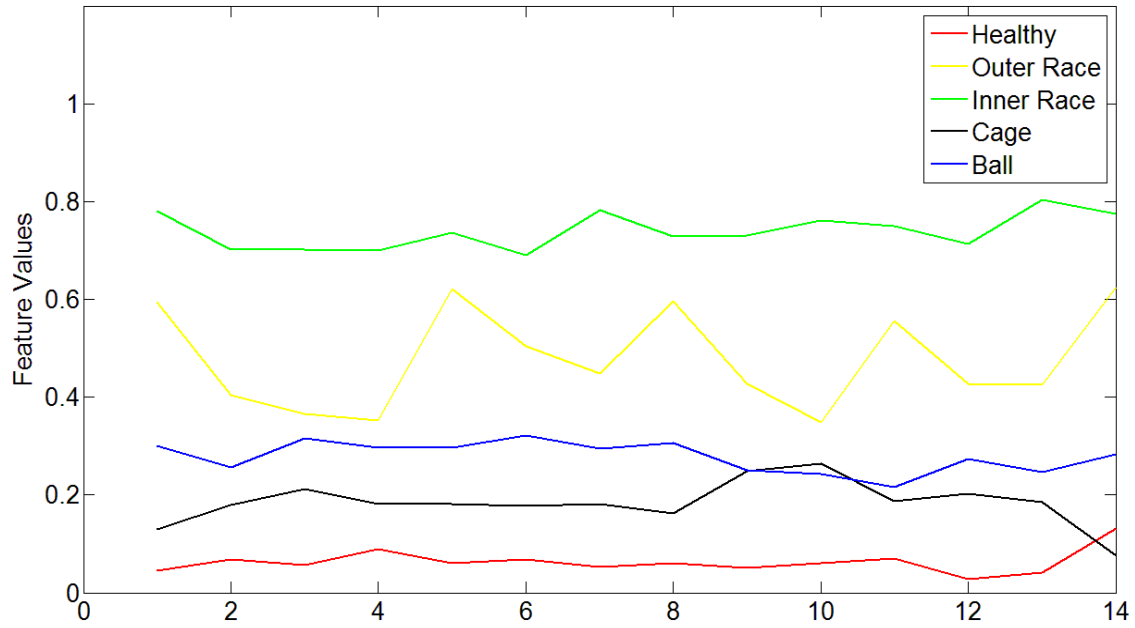


Figure 39. The distance value of the full ceramic bearing with different states

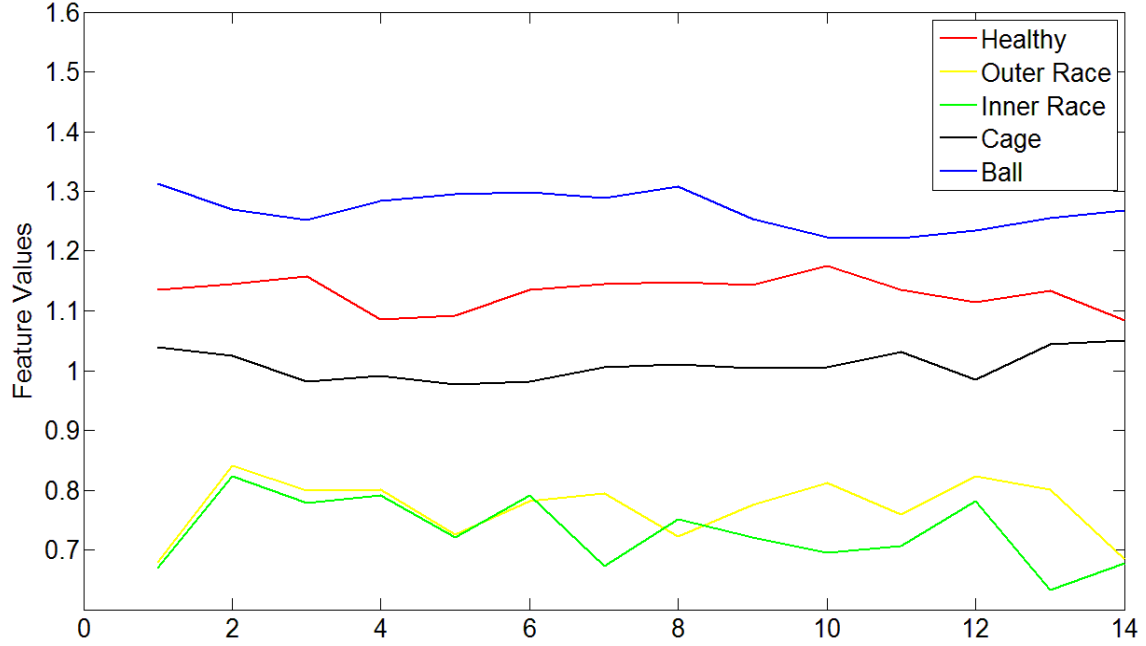


Figure 40. The entropy value of the full ceramic bearing with different states

All the two dimensional vibration CI data generated were split into two groups: 60% of the data were used for training purpose to build the fault classifier and 40% of the data were used for validation to test the performance of the fault classifier. The classification confusion matrix using KNN are provided in Table VIII and the classification results are shown in Table IX. Note that in Table VIII, the values of k are the best k values with the minimum % error determined by the KNN algorithm. The % error is defined as the percentage of data points of a fault type that were misclassified. The % accuracy is defined as the percentage of data points of a fault type that were correctly classified.

Table VIII. The classification confusion matrix using the two dimensional CIs

CIs: <i>distance</i> + <i>entropy</i> ($k = 1$)					
	Predicted Class				
Actual Class	Healthy	Outer race	Inner race	Ball	Cage
Healthy	9	0	0	0	0
Outer race	0	7	0	0	0
Inner race	0	0	8	0	0
Ball	0	0	0	11	0
Cage	0	0	0	0	9

Table IX. The KNN fault diagnosis results using the two dimensional CIs

Fault Type	Error (%)	Accuracy (%)
Healthy	0.00	100.00
Outer race	0.00	100.00
Inner race	0.00	100.00
Ball	0.00	100.00
Cage	0.00	100.00
Overall	0.00	100.00

From the results shown in Table VIII and Table IX, one could see that for full ceramic bearing case study, 100% classification rate was achieved by using the EMD based fault features. From the results shown in Figure 39 one can see that there are overlaps between the value of the distance of bearing with ball fault and bearing with cage fault. And also, in Figure 40, there are overlaps between the value of the entropy of the bearing with inner race fault and bearing with outer race fault. That means, the bearing faults cannot be classified with 100% accuracy using the one dimensional fault feature alone.

4.5 **A Two-Step Vibration Signal Based Plastic Bearing Fault Diagnostics**

In this dissertation, the bearing applications where the inner race of the bearing is mounted on the shaft and rotates with the shaft while the outer race of the bearing is fixed on the bearing house are considered. In the bearing health monitoring of this type of applications, the accelerometers are normally placed on the bearing house. Therefore, the vibration transmission path between the sensors and the bearing outer race is fixed. This type of health monitoring setup makes the vibration of the bearing outer race free of the influence due to the variation of the transmission path and the loading zone. Thus, in comparison with other bearing faults, the outer race fault could be easily detected by the envelope analysis. As mentioned in [142], the most commonly reported results in the literature concerns bearing outer race defects as the outer race defects can be easily seen in the laboratory and often produce the most salient fault features. The basic idea of the two-step approach is that one could use the frequency features obtained by the envelope analysis to separate the outer race fault from other faults and use the time features to separate other faults in the second step.

The process of the two-step approach is shown in Figure 41. As shown in Figure 41, two types of fault features: frequency domain features and time domain features, are extracted as CIs and these CIs are used to train a two-step classification algorithm. After the training, the two-step classification algorithm can be used to classify the bearing fault. The statistical method is first applied to separate the outer race fault from other types of faults based on the fault features extracted by using envelope analysis. After the outer

race fault is separated, the time domain features are used as inputs to a KNN classifier to identify the bearing states. The time domain feature extraction method is described in Section 4.4 of Chapter 4. The frequency domain feature extraction procedure is described in the following section.

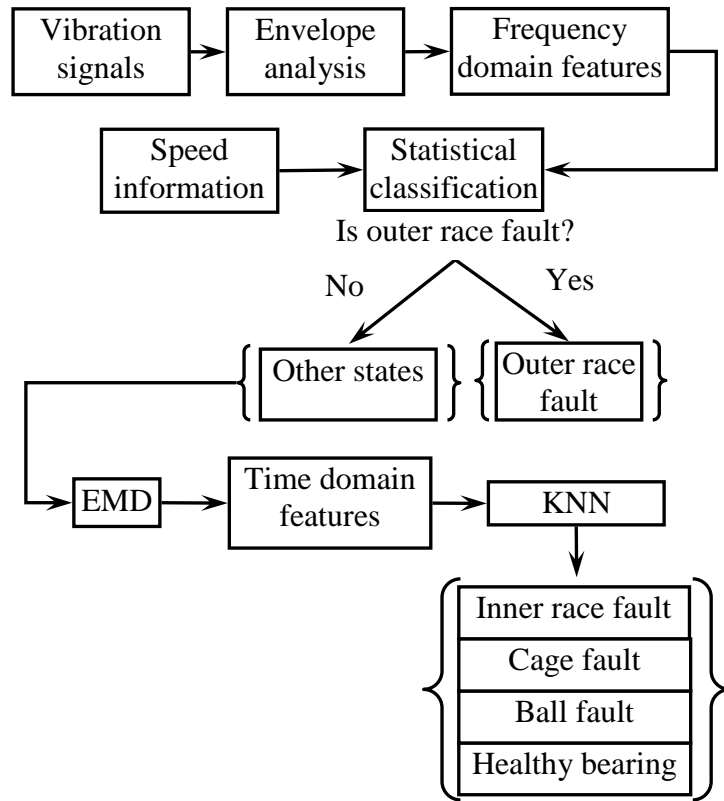


Figure 41. Process of the two-step fault diagnosis approach for plastic bearing

4.5.1 Frequency Features of Plastic Bearings

Theoretically, when a bearing is running at a constant speed, the vibrations are with periodical property. In general, for a ball bearing, there are five fundamental frequencies which can be used to describe the motion of the bearing. These five fundamental frequencies are the shaft rotational frequency F_s , the ball rotational frequency F_b , the ball pass outer race frequency F_{bpo} , the ball pass inner race frequency F_{bpi} , and the cage frequency F_c [52]. The shaft frequency F_s represents the input rotational speed of the shaft and all other fundamental frequencies are related to the value of F_s . According to [52], the ball rotational frequency F_b , the ball pass outer race frequency F_{bpo} , the ball pass inner race frequency F_{bpi} , and the cage frequency F_c , can be expressed as following equations:

$$F_b = \frac{D_c}{2D_b} \left| (F_i - F_o) \left(\frac{D_c^2 - D_b^2 \cos^2 \theta}{D_c^2} \right) \right| \quad (34)$$

$$F_{bpi} = \frac{N_b}{2} \left| (F_i - F_o) \left(\frac{D_c + D_b \cos \theta}{D_c} \right) \right| \quad (35)$$

$$F_{bpo} = \frac{N_b}{2} \left| (F_i - F_o) \left(\frac{D_c - D_b \cos \theta}{D_c} \right) \right| \quad (36)$$

$$F_c = \frac{1}{D_c} \left(F_i \frac{D_c - D_b \cos \theta}{2} + F_o \frac{D_c + D_b \cos \theta}{2} \right) \quad (37)$$

where F_i and F_o are rotational frequency of the inner race and outer race, respectively.

D_b is the diameter of the bearing rolling element, D_c is the mean diameter of the bearing (pitch diameter), and θ is the contact angle of the rolling element.

In this dissertation, the outer race of the plastic bearing is fixed on the bearing house while the inner race of the bearing is attached on the shaft and rotates with the shaft.

Therefore, $F_i = F_s$ and $F_o = 0$. Eq. (34) to Eq. (37) could be recalculated as follows.

$$F_b = \frac{D_c}{2D_b} \left| F_s \left(\frac{D_c^2 - D_b^2 \cos^2 \theta}{D_c^2} \right) \right| \quad (38)$$

$$F_{bpi} = \frac{N_b}{2} \left| F_s \left(\frac{D_c + D_b \cos \theta}{D_c} \right) \right| \quad (39)$$

$$F_{bpo} = \frac{N_b}{2} \left| F_s \left(\frac{D_c - D_b \cos \theta}{D_c} \right) \right| \quad (40)$$

$$F_c = \frac{1}{D_c} \left(F_s \frac{D_c - D_b \cos \theta}{2} \right) \quad (41)$$

If a defect is on bearing inner race and outer race, each time the rolling balls hit the damaged point an impulse signal will be generated. Theoretically, the frequency of the impulse will be the F_{bpo} and F_{bpi} , respectively. If the defect is on the ball of the bearing, then each time the ball hits the outer race or the inner race, an impulse signal will be generated. Theoretically, the frequency of the impulse will be twice the F_b .

Based on the bearing parameters listed in Table V, the theoretical bearing fundamental frequency rate can be calculated and are listed in Table X. When the bearing is running under a constant input rotational speed, a fundamental frequency is the product of the rate multiplied by the rotational speed in Hz.

Table X. Fundamental frequency rate

Fault types	Inner race fault	Outer race fault	Cage fault	Ball Fault
Fundamental frequency rate	5.415	3.585	0.398	4.714

Traditional vibration signal processing techniques such fast FFT is less effective in extracting the bearing fundamental frequencies due to the fact that the wide spectrum of the fault impulse signals is usually buried in the spectrum generated by other rotating components and the mechanical background noises. The fault impulses normally excite a resonance in the mechanical system at higher frequency than the vibration signals of other rotating components and mechanical background noise. As indicated by [143], it is reasonable to consider the resonance as being amplitude modulated at the characteristic defect frequencies. Randall and Antoni [53] provided some examples to explain the ineffectiveness of the traditional vibration signal processing techniques to reveal bearing fault frequencies in comparison with envelope analysis. To separate and demodulate the bearing fault characteristic frequencies, envelope analysis [143] has been used in rolling

element bearing fault detection and diagnosis. Successful applications on bearing fault detection using envelope analysis have been reported in [144-146]. When the envelope technique is used to analyze the bearing vibration signals, the raw vibration signals are first band-pass filtered to reject the low-frequency contents typically associated with shaft imbalance and misalignment and vibration responses of other rotating components in order to increase the fault signal-to-noise ratio. The Hilbert transform is then applied to the band-passed signals to obtain the envelope of the band-passed signals. Finally, frequency spectrum of the envelopes of the band-passed signals is calculated.

Based on the analysis above, frequency domain features from the vibration signals can be extracted by the following steps:

Step 1. Filter the vibration signal with a band-pass filter.

Step 2. Calculate the envelope signal of the band-passed signal.

Step 3. Calculate the Fourier spectrum of the envelope signal.

Step 4. Calculate the summation value $S_{Envelope}$ of the Fourier spectrum around the outer race characteristic frequency.

The $S_{Envelope}$ is then utilized as the input to the statistical classification algorithm. As shown in Figure 41, two types of bearing fault feature, the frequency domain feature and time domain feature are used. The frequency domain feature is utilized to separate the outer race fault of the plastic bearing.

For most vibration based bearing health monitoring applications, since the relative distance between the outer race fault of a bearing and the sensor is fixed, one can simply use traditional frequency domain vibration signal processing methods such as envelope analysis to extract the bearing fundamental frequencies in order to identify the outer race fault. However, the relative distance between the fault on the rotating components of the bearing and the sensor changes as the bearing rotates, thus adding some degree of randomness to the repeatability of the fault impulses. The randomness of the fault impulses will affect the effectiveness of the traditional envelope analysis and frequency domain methodology on bearing fault detection. As shown in Table IV [140, 141], in comparison with steel bearings or ceramic bearings, the plastic bearings are more loosely assembled and easier to be deformed. These inherent properties of plastic bearings add more degrees of randomness into the behavior of the fault impulses and weaken the fault impulse signals. Therefore, using the traditional bearing fundamental frequencies as bearing fault features will not be effective for identifying plastic bearing fault on inner race, balls, and cages. To demonstrate the effects of the randomness of the impulse signals on the traditional envelope analysis, two sets of impulses were generated. The first set of impulses was generated with a fixed time interval between the impulses. The second set of impulses was generated with random time intervals between the impulses. During the simulation, one natural frequency mode was considered. The natural frequency was set to 3 kHz. The occurrence frequency of the simulated impulses was 80 Hz. Figure 42 shows the simulated impulses with a fixed time interval and its envelope frequency spectrum. From Figure 42, one can see clearly the occurrence frequency of 80 Hz.

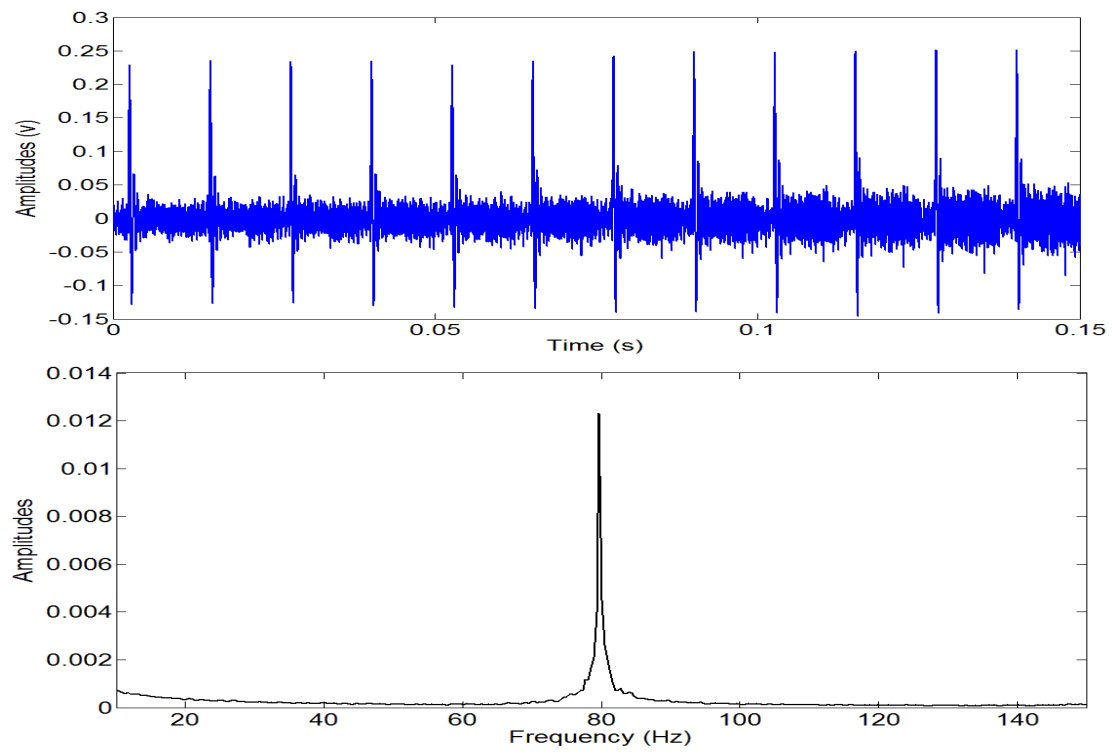


Figure 42. The simulated impulse signal with fixed time intervals and its frequency spectrum

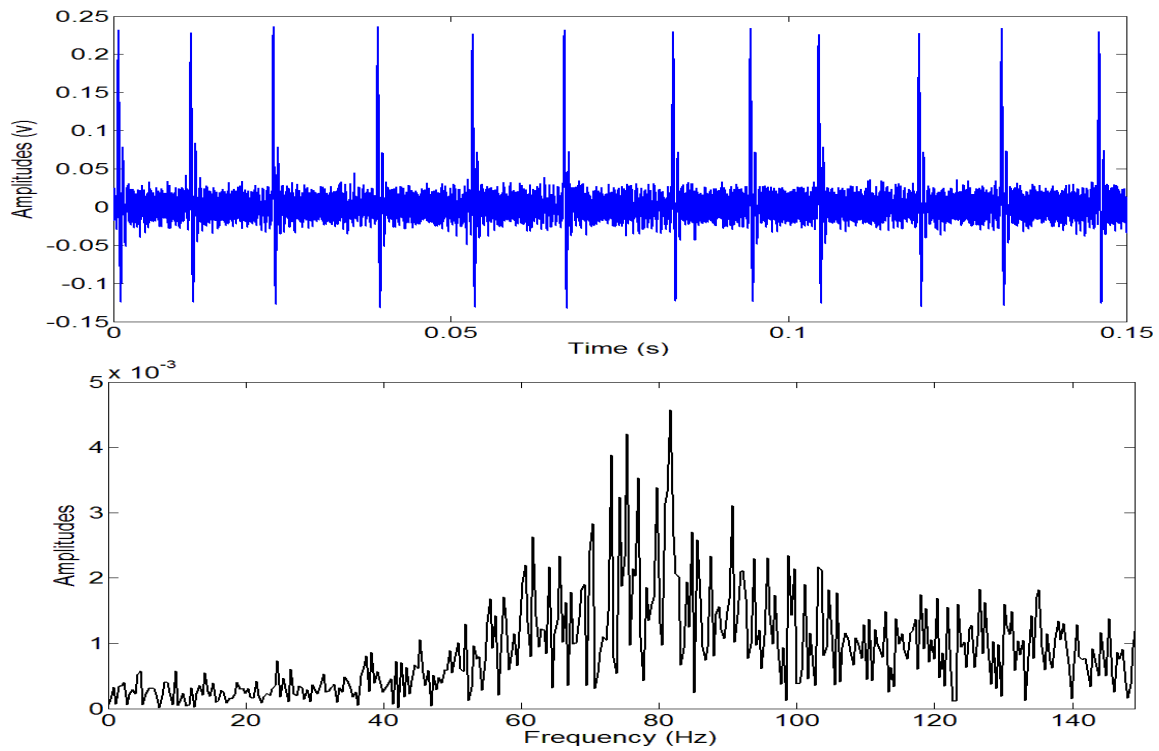


Figure 43. The simulated impulse signal with random time intervals and its frequency spectrum

Figure 43 shows the simulated impulse with random time intervals and its frequency spectrum. From the frequency spectrum shown in Figure 43, one can see that the occurrence frequency of the impulse signals could not be clearly identified due to the randomness introduced into the impulse signals. To enhance the performance of the classification algorithm, time domain features are utilized to separate other bearing states.

4.5.2 Case Study: Plastic Bearing Fault Diagnostics

During the testing, vibration signals were collected with a sampling rate of 102.4 kHz. Totally, four input speeds, 10 Hz, 20 Hz, 40 Hz, and 60 Hz were investigated in this dissertation. Sample vibration signals of healthy bearing and bearings with different types of faults collected with 10 Hz input speed are shown from Figure 44 to Figure 48.

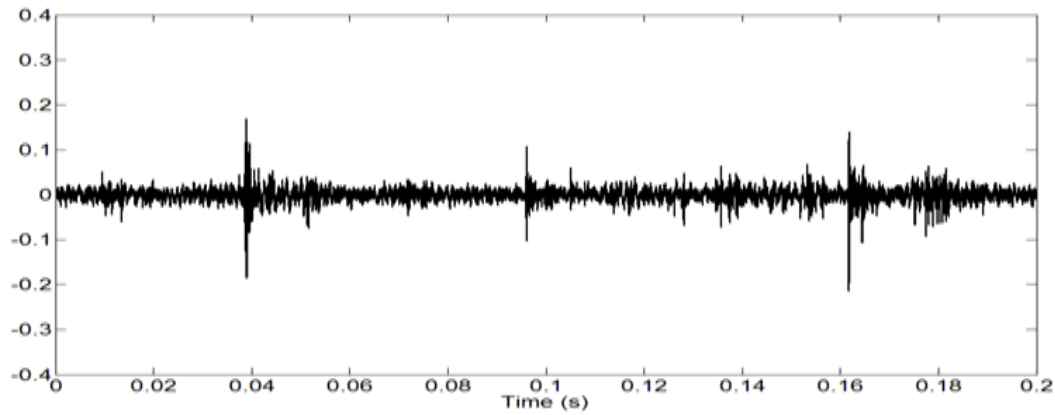


Figure 44. The sample vibration signal of the healthy plastic bearing

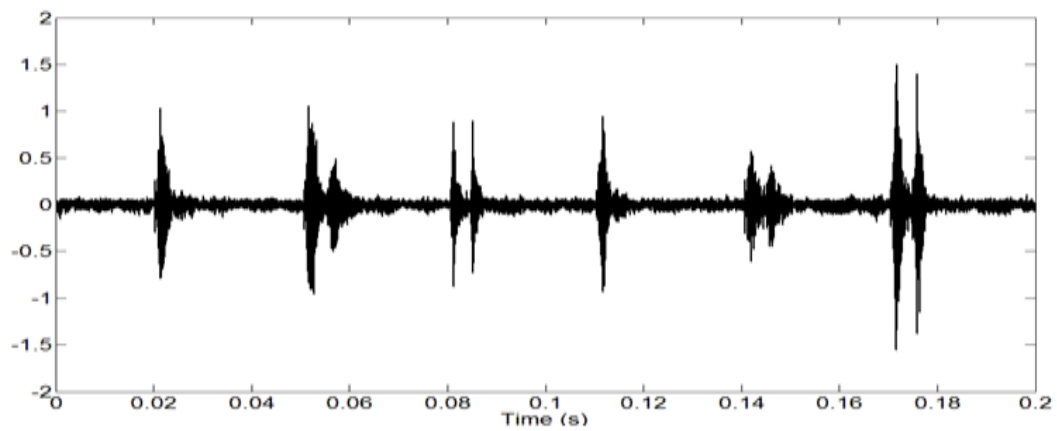


Figure 45. The sample vibration signal of the plastic bearing with outer race fault

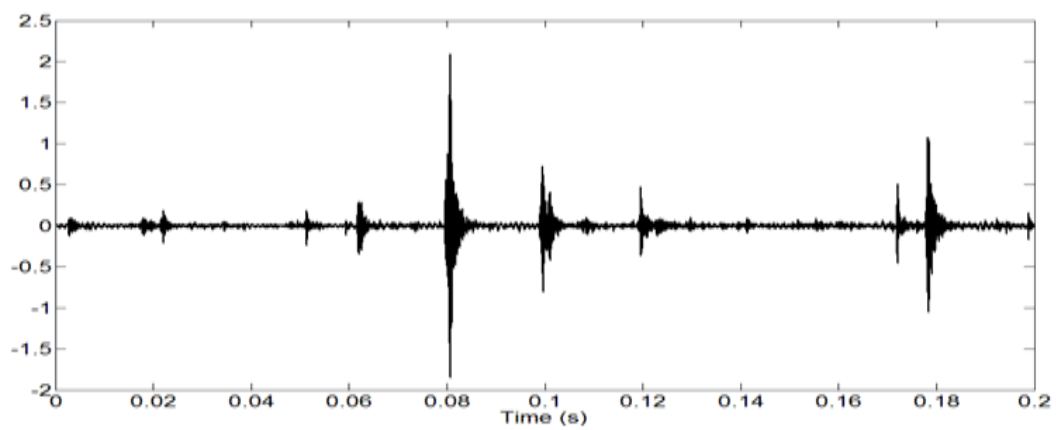


Figure 46. The sample vibration signal of the plastic bearing with inner fault

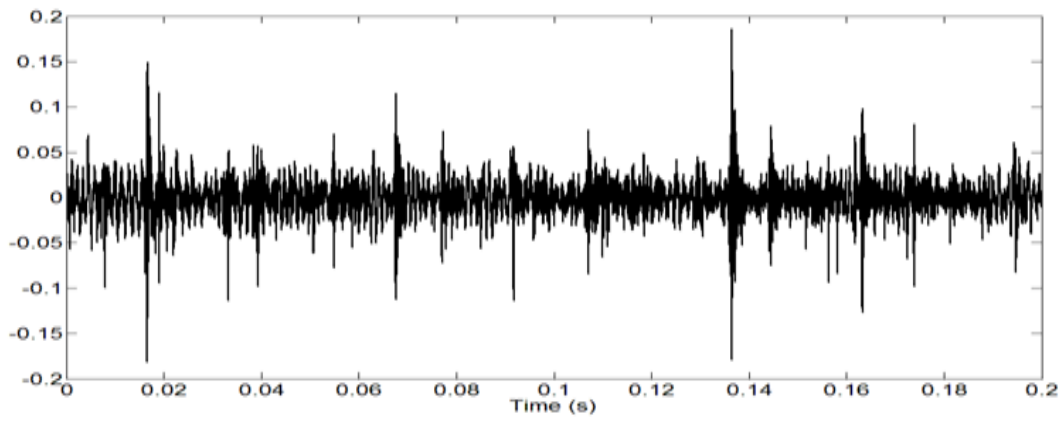


Figure 47. The sample vibration signal of the plastic bearing with ball fault

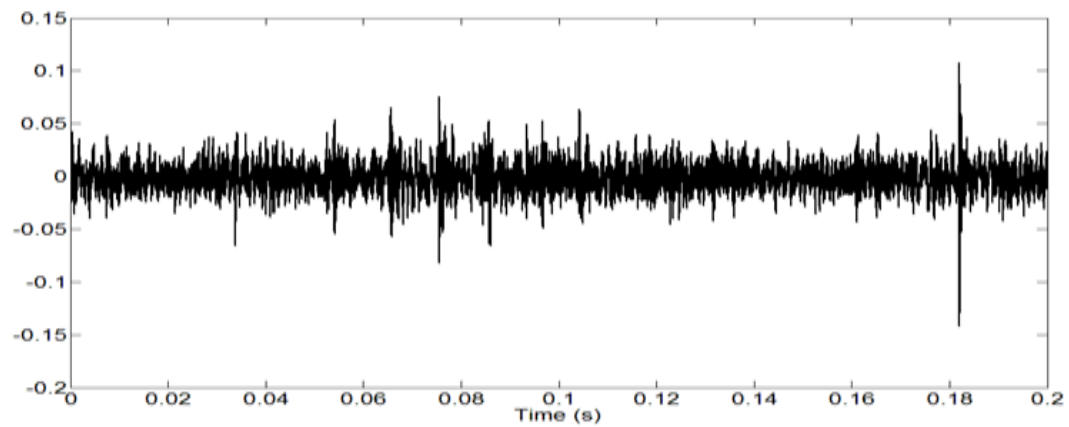


Figure 48. The sample vibration signals of the plastic bearing with cage fault

The vibration signals were processed following the two-step procedure shown in Figure 41. The frequency domain fault features of the healthy bearing, bearing with inner race fault, bearing with ball fault, bearing with cage fault, and the bearing with outer race fault under 10 Hz, 20 Hz, 40 Hz, and 60 Hz input rotating frequency are shown from Figure 49, Figure 50, Figure 51, and Figure 52, respectively. The time domain fault features of the bearings except for the bearing with outer race fault under 10 Hz, 20 Hz, 40 Hz, and 60 Hz input rotating frequency are shown from Figure 53, Figure 54, Figure 55, and Figure 56, respectively.

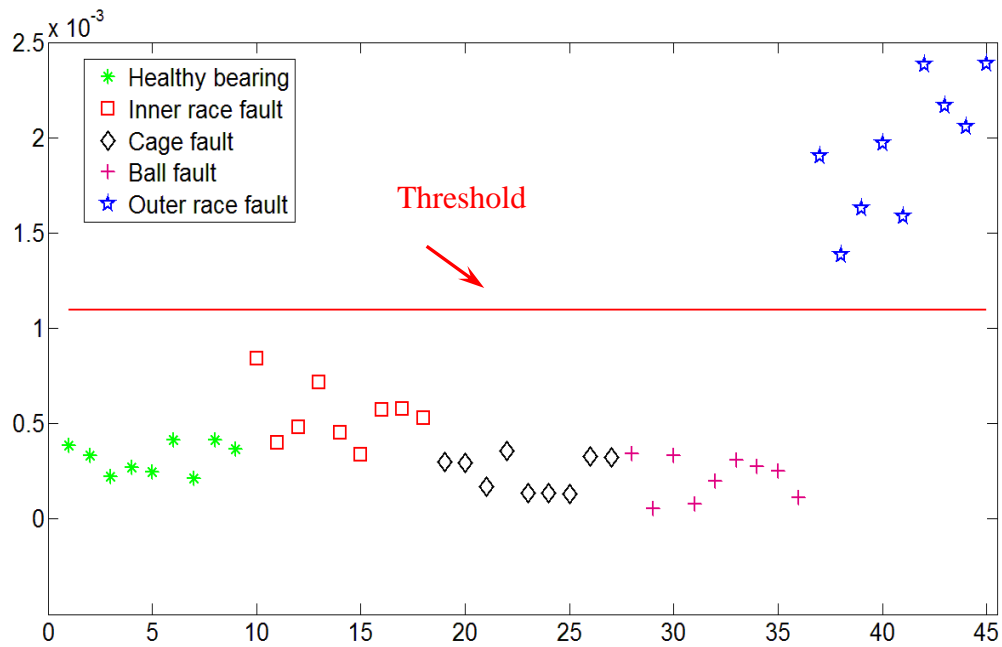


Figure 49. The frequency domain features of the healthy and the bearing with different types of fault with 10 Hz input speed

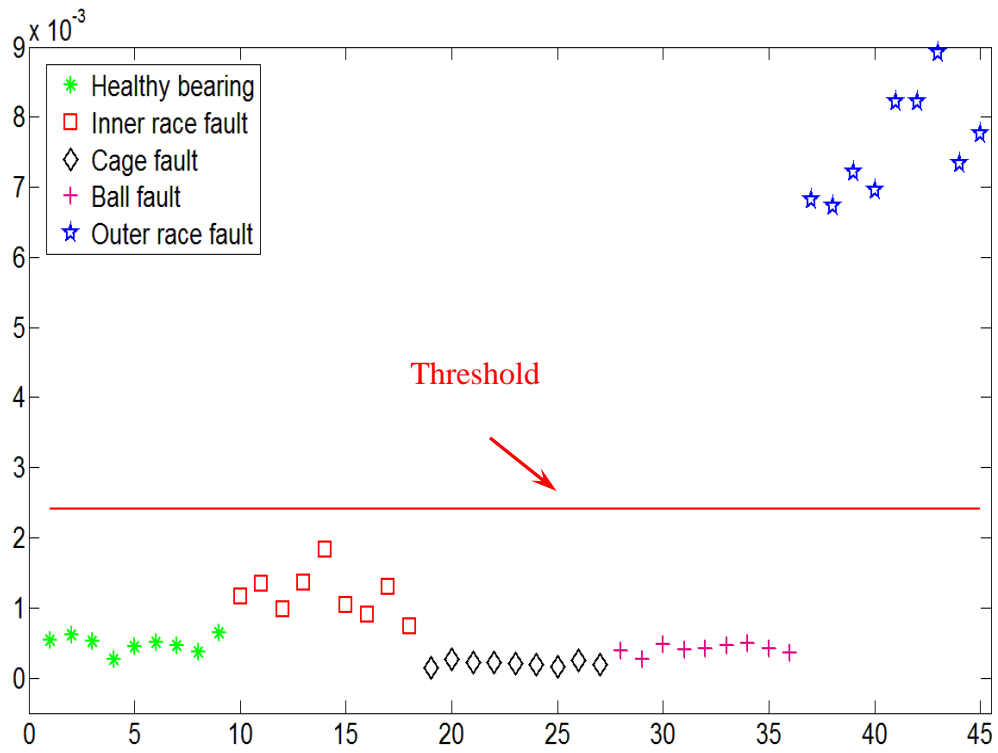


Figure 50. The frequency domain features of the healthy and the bearing with different types of fault with 20 Hz input speed

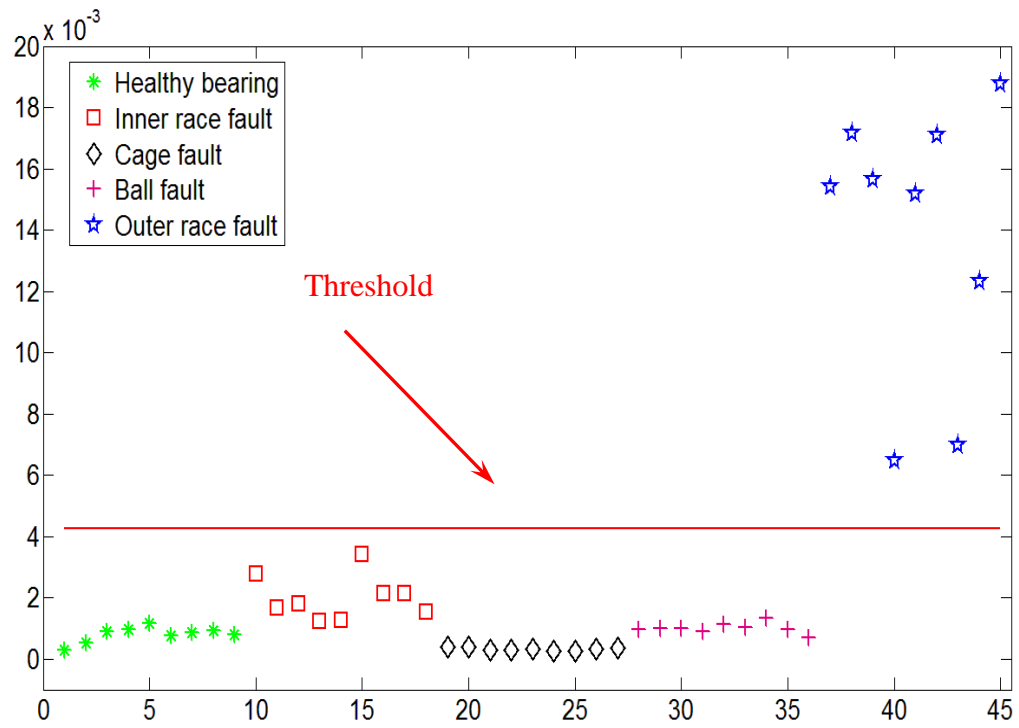


Figure 51. The frequency domain features of the healthy and the bearing with different types of fault with 40 Hz input speed

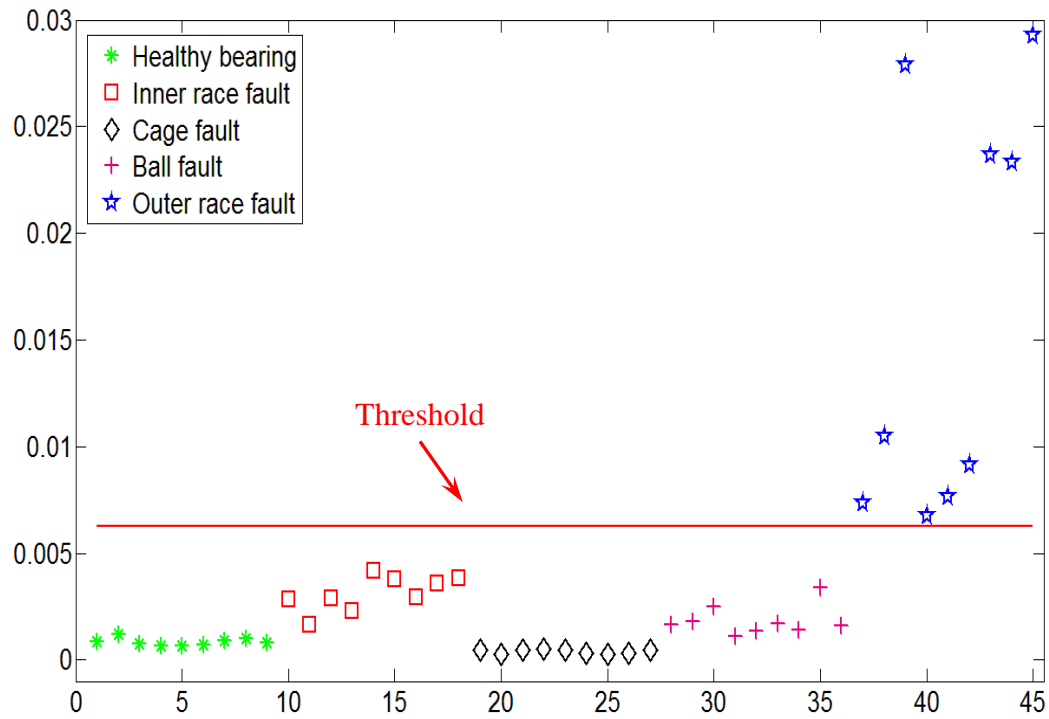


Figure 52. The frequency domain features of the healthy and the bearing with different types of fault with 60 Hz input speed

The red solid lines in the Figures from Figure 49 to Figure 52 represent the threshold value calculated by the frequency domain CIs of the bearing without the outer race fault. As discussed in Section 4.2, the threshold value is calculated by using the Eq. (12). It can be seen from the results shown from the Figures from Figure 49 to Figure 52 that for all the input shaft speeds, the CIs of the bearing with outer race fault and the bearing with other states can be separated by the threshold with 100% accuracy.

For comparison purpose, the KNN algorithm based fault classifier was applied to the same data sets in order to classify bearing faults. The frequency domain CIs were split into two groups: 60% and 40%. The 60% of the CIs were used as the training data to training the KNN algorithm based fault classifier while the other 40% of the CIs were used as validation data to valid the performance of the CIs. The classification results of the KNN algorithm based fault classifier are provided in Table XI. Note that in Table XI, the values of k are the best k values with the minimum % error determined by the KNN algorithm at the validation stage. The % error is defined as the percentage of data points of a fault type that were misclassified.

Table XI. The classification results of the KNN algorithm using frequency domain CIs

Type of Fault	% of Error for Validation			
	10Hz ($k=1$)	20Hz ($k=8$)	40Hz ($k=5$)	60Hz ($k=1$)
Healthy	80.00	80.00	60.00	50.00
Inner race	0.00	0.00	11.11	33.33
Ball	66.67	8.33	16.67	33.33
Cage	62.50	0.00	0.00	0.00
Outer	6.67	0.00	0.00	0.00
Overall	40.74	16.67	16.67	22.22

From Table XI, one can see that if the frequency domain CIs is used to classify the bearing faults, high misclassification rates are obtained. The results in Table XI have

further indicated that using frequency domain CIs alone cannot effectively diagnose other types of plastic bearing faults.

After the outer race fault is separated from other states by using the frequency domain CIs, the time domain CIs are used to diagnose the bearing faults. The time domain CIs are calculated by following the steps described in Section 4.4. The calculated time domain CIs are shown in the Figures from Figure 53 to Figure 56.

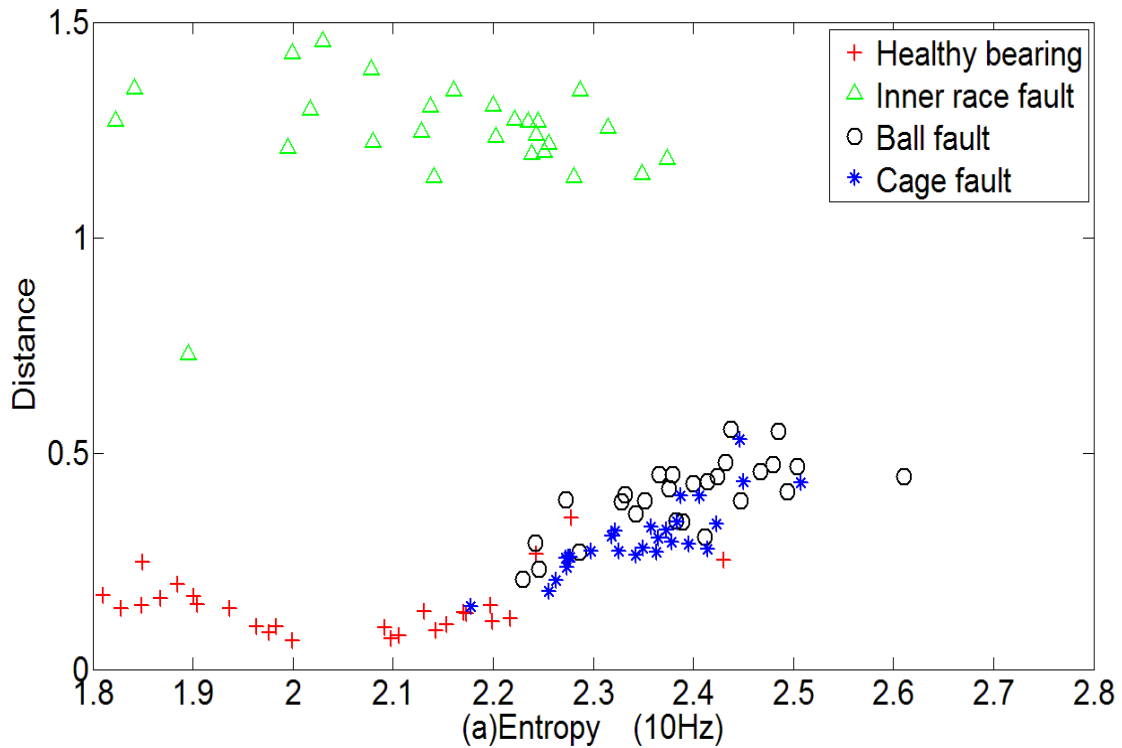


Figure 53. The time domain feature vectors of the plastic bearing running under 10 Hz input frequency

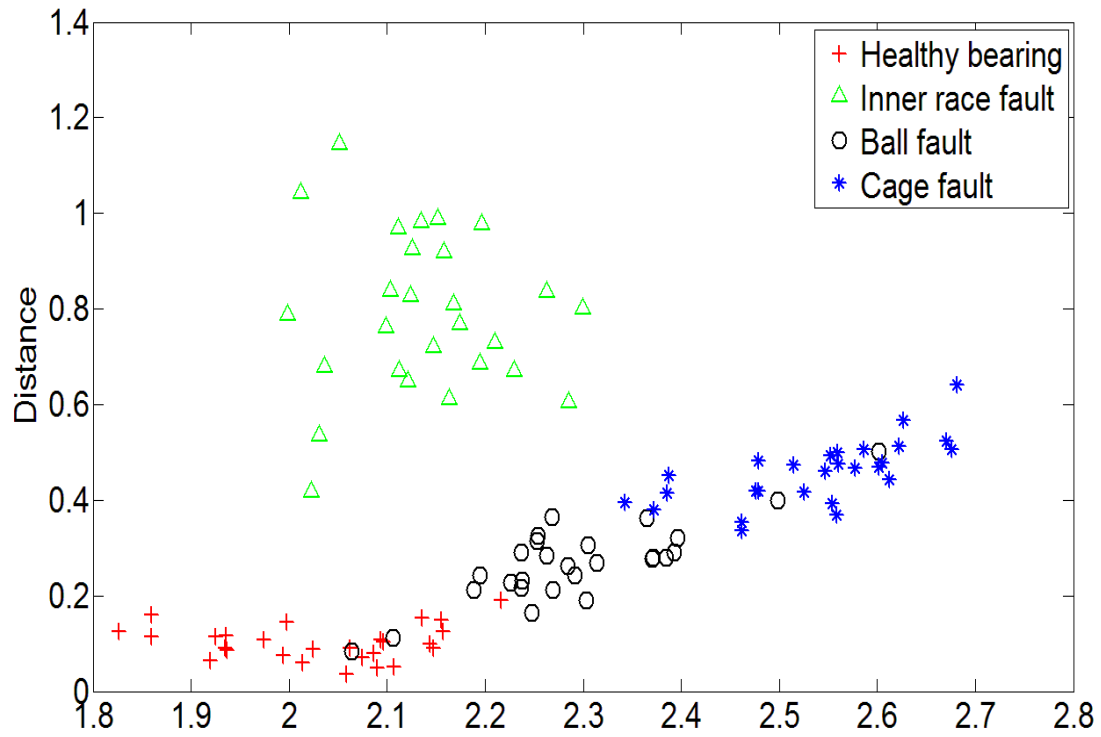


Figure 54. The time domain feature vectors of the plastic bearing running under 20 Hz input frequency

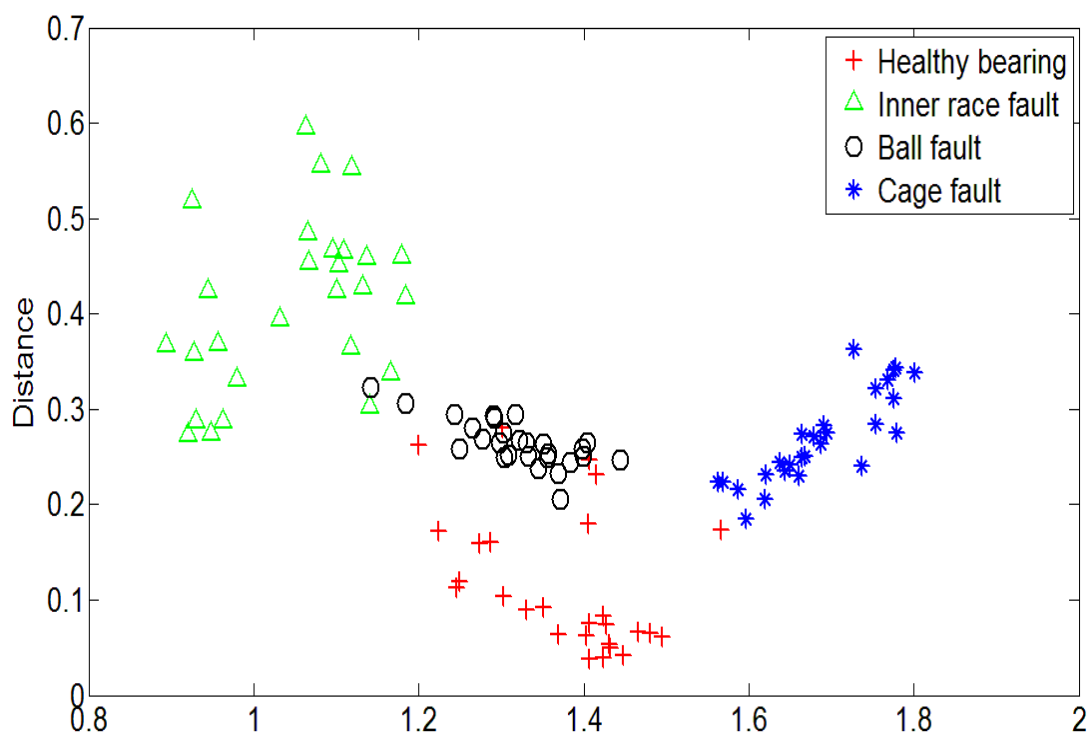


Figure 55. The time domain feature vectors of the plastic bearing running under 40 Hz input frequency

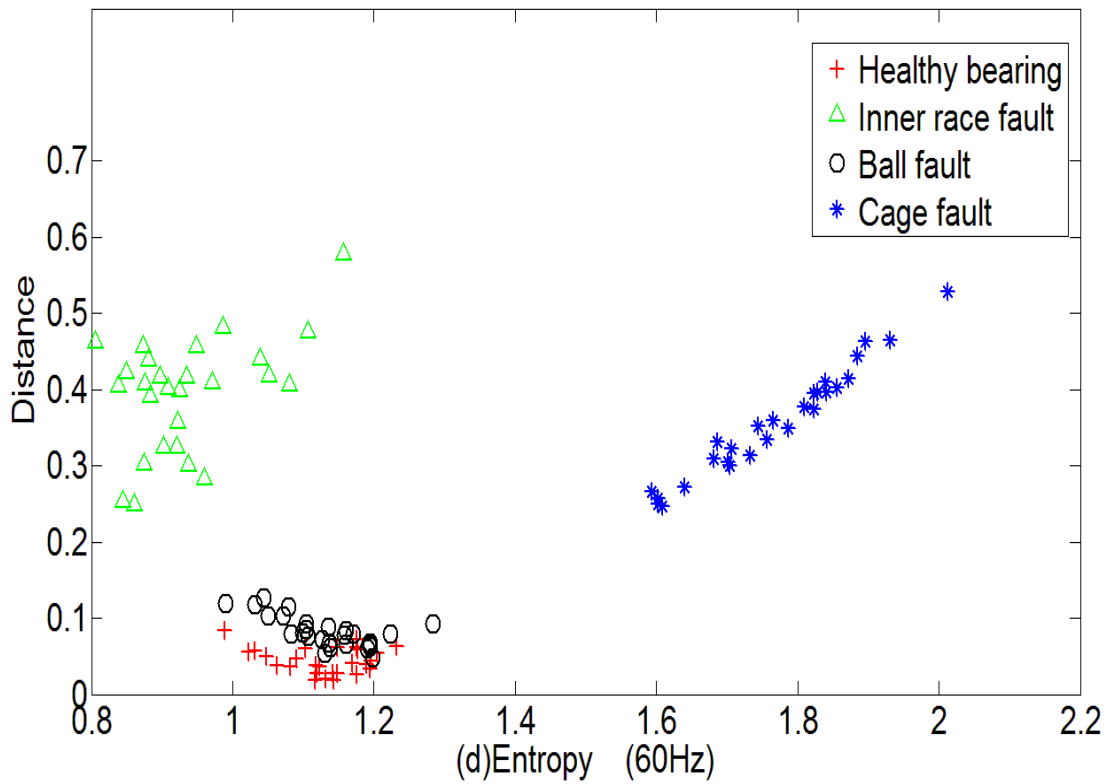


Figure 56. The time domain feature vectors of the plastic bearing running under 60 Hz input frequency

From the results shown in Figures from Figure 53 to Figure 56, one can see a distinct distance between the inner race fault bearings and other bearings and a clear separation of the inner race fault bearings from other bearings. One can also see clear clusters of different bearings although small portions of the clusters are overlapped. It is interesting to see that as the rotational speed decreases, the cluster of the cage fault bearings is getting closer to the cluster of the ball fault bearings. One possible explanation is that the

elastic properties and the stiffness of the plastic bearing discussed in Section 4.5 may weaken the energy of the fault impulse generated by the damaged ball and the cage as rotational speed decreases. Another interesting thing one can observe in the Figures from Figure 53 to Figure 56 is that as the rotational speed increases, the energy level of the ball fault bearings is getting closer to that of the healthy bearings. Again, it could be caused by the increasing deformation of the plastic bearing races as the speed increases.

The time domain CIs, shown in Figures from Figure 53 to Figure 56 were split into two groups: 60% and 40%. The 60% of the CIs were used as the training data to training the KNN algorithm based fault classifier while the other 40% of the CIs were used as validation data to test the performance of the CIs. The classification results of the KNN algorithm based fault classifier are provided in Table XII. Note that in Table XII, the values of k are the best k values with the minimum % error determined by the KNN algorithm at the validation stage. The % error is defined as the percentage of data points of a fault type that were misclassified.

Table XII. The classification results of the KNN algorithm using time domain CIs at the second step of the two-step approach

Type of Fault	% of Error for Validation			
	10Hz ($k=3$)	20Hz ($k=7$)	40Hz ($k=2$)	60Hz ($k=2$)
Healthy	9.09	9.09	36.36	9.09
Inner race	0.00	0.00	16.67	0.00
Ball	33.33	16.67	0.00	8.33
Cage	25.00	0.00	0.00	0.00
Overall	16.28	6.98	13.95	4.65

Let x^1 be the total data points of the faults at the first step and x^2 be the total data points of the faults at the second step. Define x_c^1 and x_c^2 as the number of data points correctly identified at the first and the second step, respectively. Then the fault classification accuracy of the two-step approach can be computed as: $\frac{x_c^1 + x_c^2}{x^1 + x^2} \times 100\%$. For the input speed of 10 Hz, in the first step: $x^1 = 27$, $x_c^1 = 27$; in the second step: $x^2 = 43$, $x_c^2 = 8 + 6 + 10 + 12 = 36$. Therefore, the total fault classification accuracy can be computed as: $\frac{36 + 27}{43 + 27} \times 100\% = 90\%$. In the same fashion, the classification accuracies for other conditions are computed and provided in Table XIII. From Table XIII, one can see that a high classification rate was achieved under different bearing operation conditions.

Table XIII. The Two-Step classification results

Speed	Classification Accuracy
10 Hz	90%
20 Hz	95.7%
40 Hz	91.4%
60 Hz	97.1%

In order to make a comparison with results of the two-step approach shown in Table XIII, a one step approach using time domain CIs and combination of frequency and time domain CIs was used to diagnose all the bearing faults by the KNN based fault classifier. Again, the time domain CIs of all the bearings were split into two groups: 60% and 40%. The 60% of the CIs were used as the training data to training the KNN algorithm based fault classifier while the other 40% of the CIs were used as validation data to test the performance of the CIs. The one step classification results using the time domain CIs are provided in Table XIV.

Table XIV. The one step classification results using only time domain CIs

Type of Fault	% of Error for Validation			
	10Hz ($k=4$)	20Hz ($k=9$)	40Hz ($k=4$)	60Hz ($k=2$)
Healthy	10.00	10.00	30.00	10.00
Inner race	0.00	0.00	11.11	0.00
Ball	33.33	16.67	8.33	8.33
Cage	12.50	0.00	0.00	0.00
Outer race	0.00	0.00	40.00	46.67
Overall	11.11	5.56	20.37	16.67

From Table XIV, one can see that if the time domain CIs are used to classify the bearing faults in one step by the KNN based fault classifier, the overall fault classification accuracy rate are 88.89%, 94.44%, 79.63%, and 83.33% for 10 Hz, 20 Hz, 40 Hz, and 60 Hz speed conditions, respectively. In comparison with the overall classification accuracy rate achieved by using the one step approach, the two-step approach presented in this paper provides a better bearing fault classification performance.

Table XV. The one step classification results using combination of frequency domain and time domain CIs

Type of Fault	% of Error for Validation			
	10Hz ($k=5$)	20Hz ($k=7$)	40Hz ($k=2$)	60Hz ($k=2$)
Healthy	10.00	10.00	30.00	10.00
Inner race	0.00	0.00	11.11	0.00
Ball	25.00	16.67	0.00	0.00
Cage	25.00	0.00	0.00	0.00
Outer race	0.00	0.00	0.00	6.67
Overall	11.11	5.56	7.41	3.70

From Table XV, one can see that if both the frequency and time domain CIs are used to classify the bearing faults in one step by the KNN based fault classifier, the overall fault classification accuracy rate are 88.89%, 94.44%, 92.59%, and 96.30% for 10 Hz, 20 Hz, 40 Hz, and 60 Hz speed conditions, respectively. In comparison with the overall classification accuracy rate achieved by using the one step approach with both the frequency and time domain CIs, the two-step approach presented in this paper provides a better bearing fault classification performance.

4.6 **Interference Cancellation Based Gear Fault Detection**

As described in Section 4.2.3, the vibration signal generated by the fault gear transmission system contains fault impulses, periodic components, and background noise. The periodic components can be treated as the narrowband interference to the fault

impulses while the background noise can be treated as the wideband interference to the fault impulses. To increase the SNR of the gear fault symptom, an interference cancellation based methodology is developed and the process of the methodology is shown in Figure 57. The main idea of the methodology is to remove the periodic signal and background noise from the raw vibration signal and to reveal the gear fault symptoms in a dynamic environment.

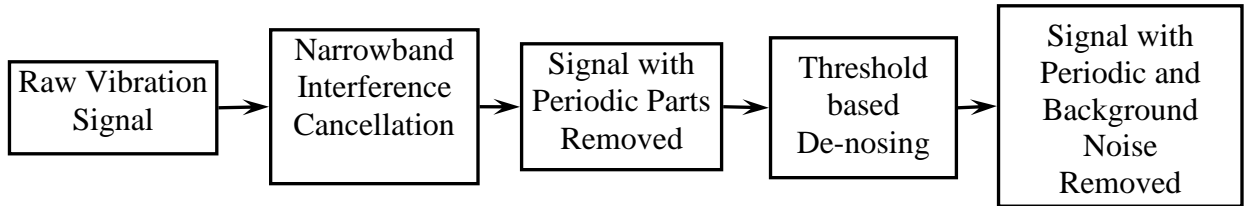


Figure 57. The process of the interference cancellation based gear fault detection methodology

To demonstrate the effectiveness of the developed methodology, a simulation example is shown below. The simulated periodic signal, the impulse signal, the noise signal are shown in Figure 58. The simulated signal changes its frequency at data point 800. For the adaptive algorithm, the μ was set to be 0.98, Δ was set to be 200 and k was set to be 35. The D4 wavelet from the Daubechies family of wavelets was utilized to analyze the

periodic components removed signal. The results obtained by the developed method are shown in Figure 59 and Figure 60.

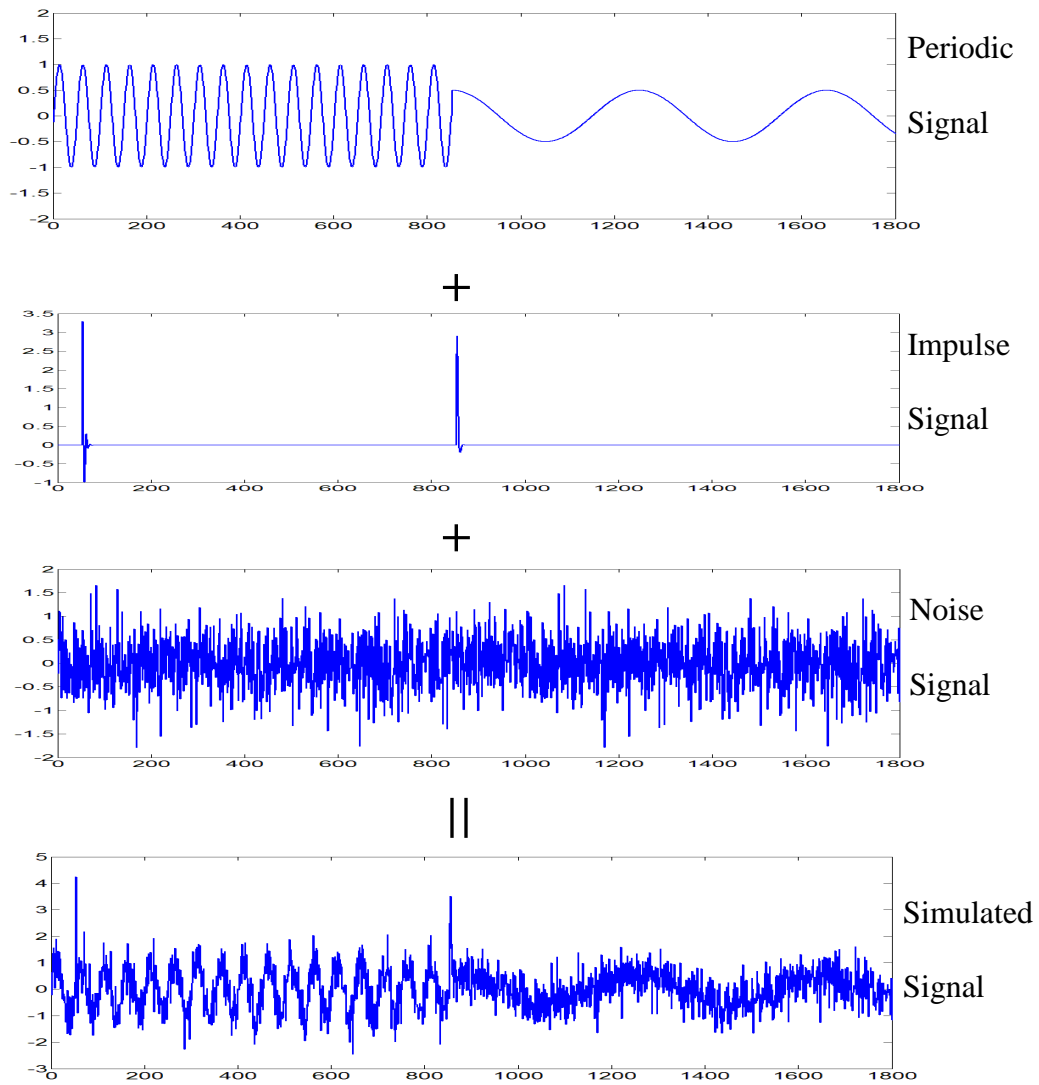


Figure 58. The simulated signal

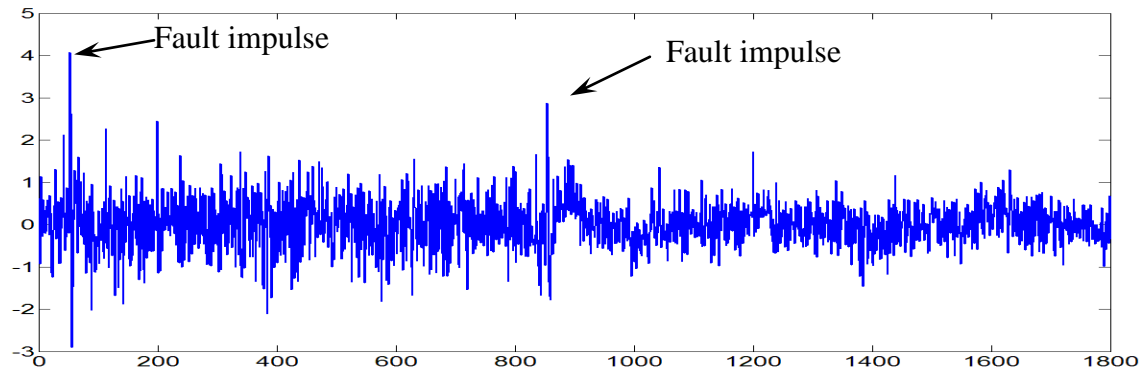


Figure 59. The processed result with the cancellation of the periodic signal

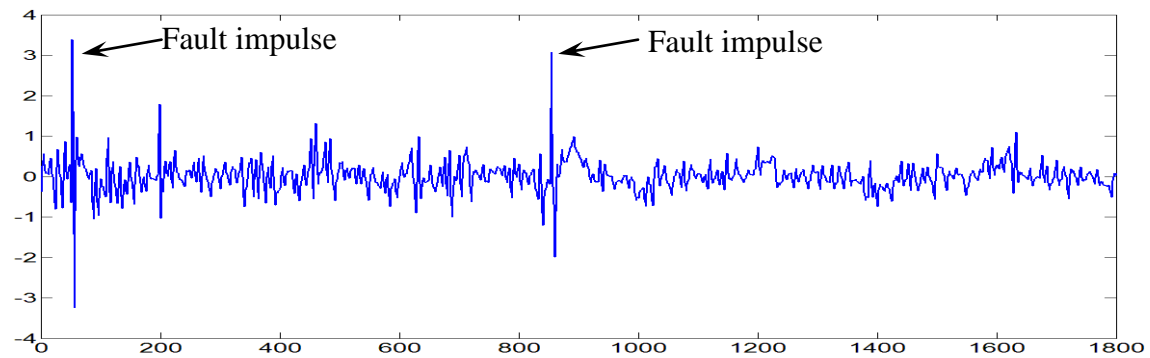


Figure 60. The processed result with the cancellation of both the periodic signal and the background noise

Two accelerometers were mounted vertically and horizontally, respectively on the frame of the gearbox to collect the vibration signals, simultaneously. Both the signals were collected at the sampling rate of 102.4 kHz. The signal collected from the vertically

mounted sensor vertically. One sample vibration signal of the damaged gear is shown in Figure 61 and the frequency spectrum is shown in Figure 62.

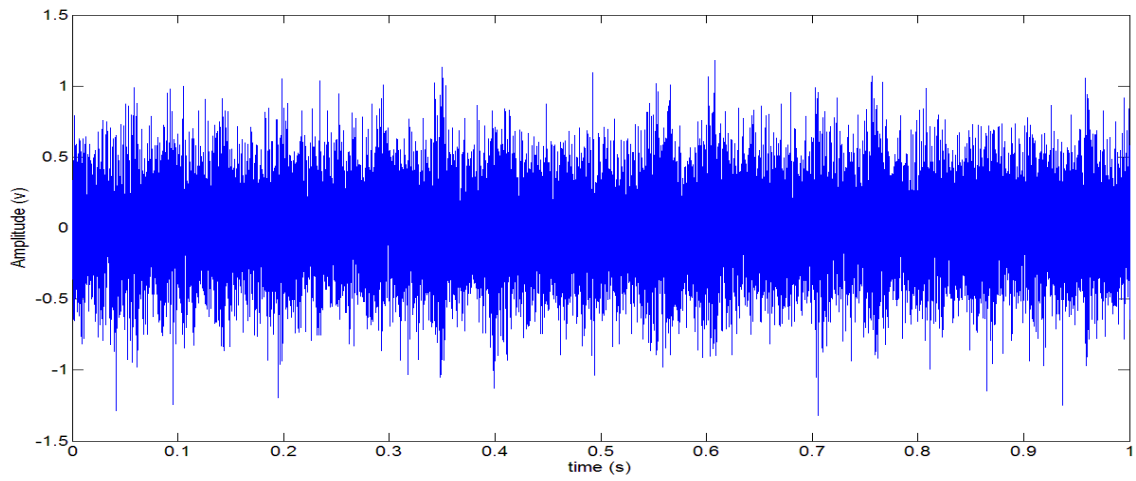


Figure 61. The sample vibration signal of the damaged gearbox

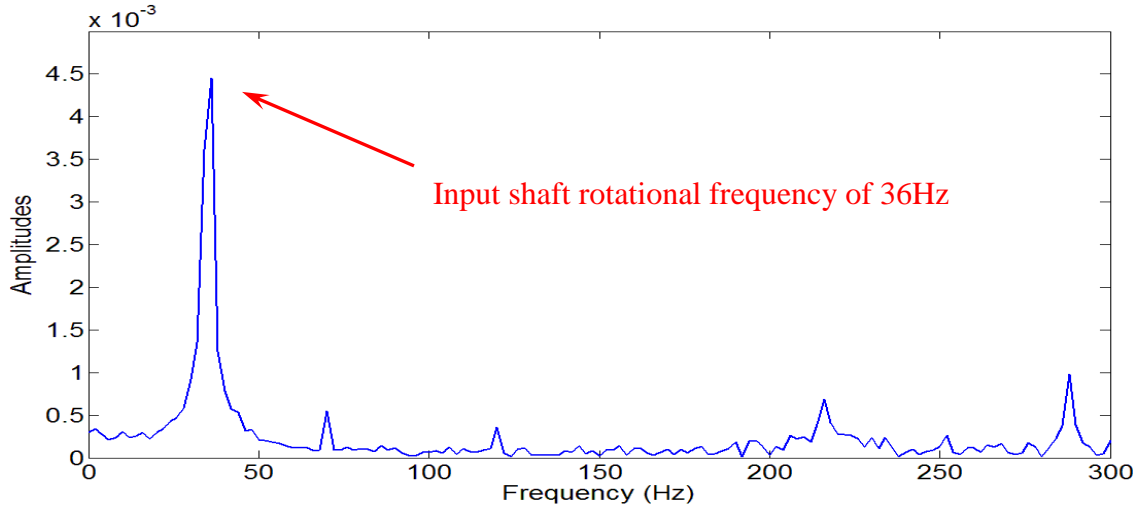


Figure 62. The frequency spectrum of the sample vibration signal of the damaged gearbox

From the raw vibration signal in Figure 61, we can barely see the impulse signal generated by the damaged tooth. The rotational speed for the input shaft was set to be 2160 rpm, corresponding to 36 Hz. According to the structure of the gearbox, under such rotational frequency, the fault characteristic frequency of the gearbox should be 20 Hz. From the frequency spectrum in Figure 62, we see clearly the high peak values at the shaft rotational frequency and its harmonics. However, we could not see any high peak values at the gear fault frequencies. The developed algorithm was applied to process the vibration signal of the damaged gearbox. The parameters of the algorithm was set as follows: the μ was set to be 0.98, Δ was set to be 200, k was set to be 80, and the D4 wavelet from the Daubechies family of wavelets was utilized to in noise removing algorithm. The processed results are shown in Figure 63. From Figure 63, we can see

clearly that the occurring frequency of the impulse signal is 20 Hz, which indicates damage in the gearbox. Also, the frequency spectrum of the processed signal was calculated and shown in Figure 64 and the high peak value at the gear fault frequency is a clear indication of the gear fault.

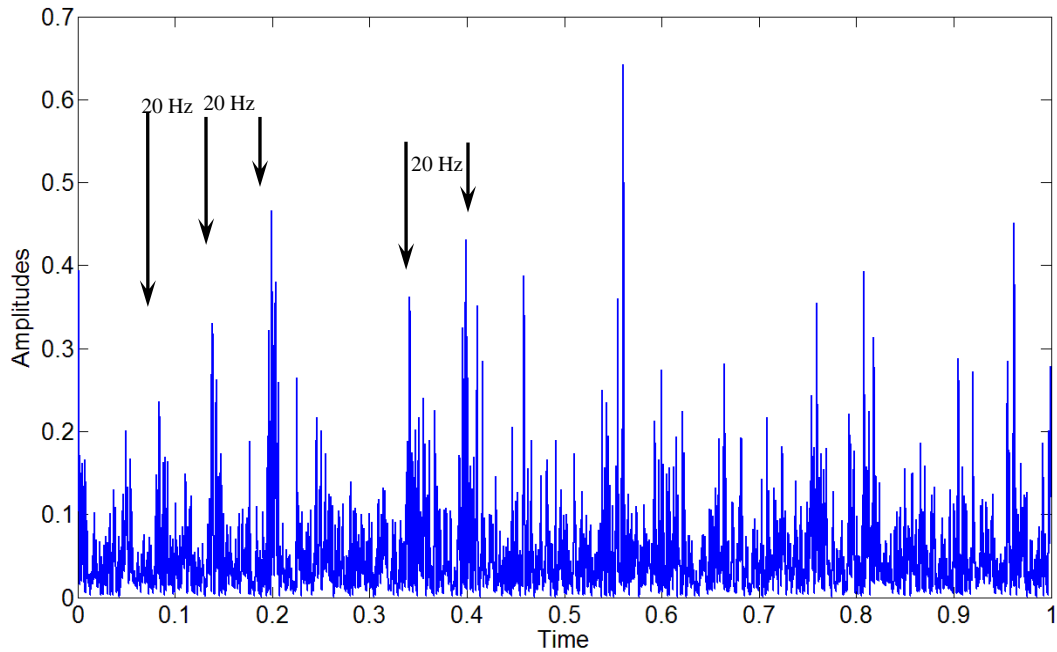


Figure 63. The processed results of the gearbox running under 36 Hz using the interference cancellation algorithm

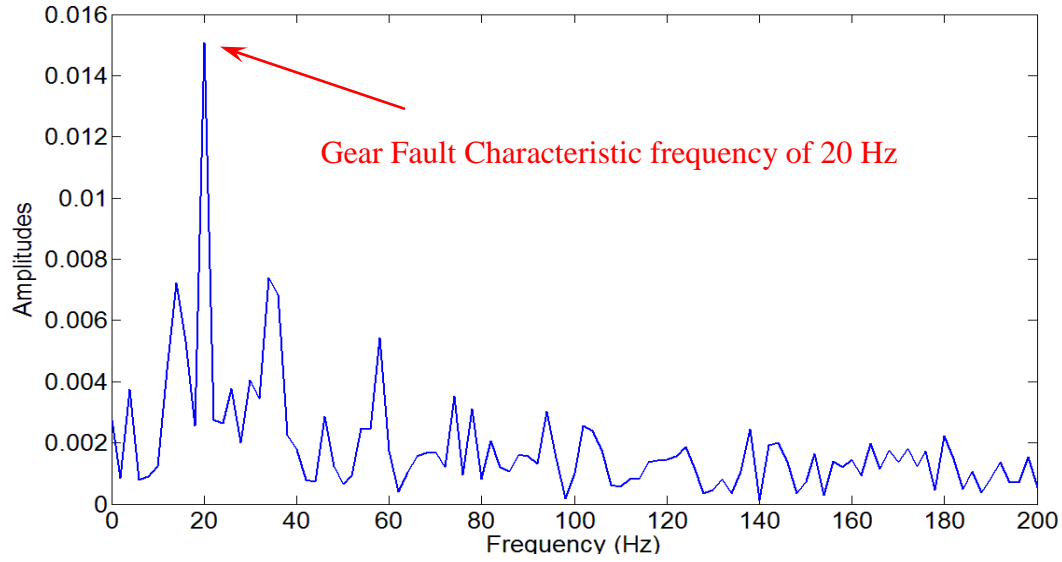


Figure 64. The Fourier spectrum of the processed signal

To show the effectiveness of the presented method under the situation of varying input rotational speed, rotational speed of the input shaft was changed from 36Hz to 24 Hz. An sample vibration signal collected under the 24 Hz operational frequency is shown in Figure 65. The results are shown in Figure 66. From Figure 66, we can see clearly that the occurring frequency of the impulse signal is 13 Hz, which indicates damage in the gearbox.

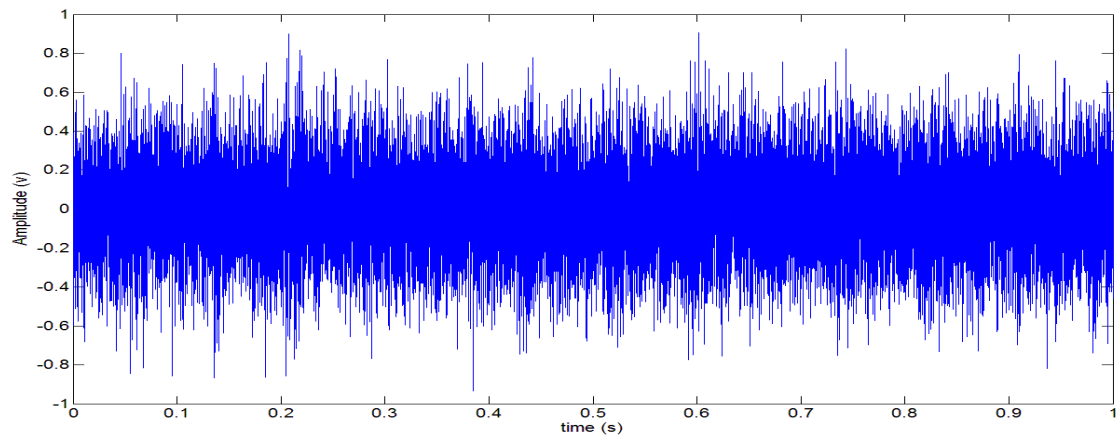


Figure 65. Sample vibration signal collected under input rotational frequency of 24 Hz

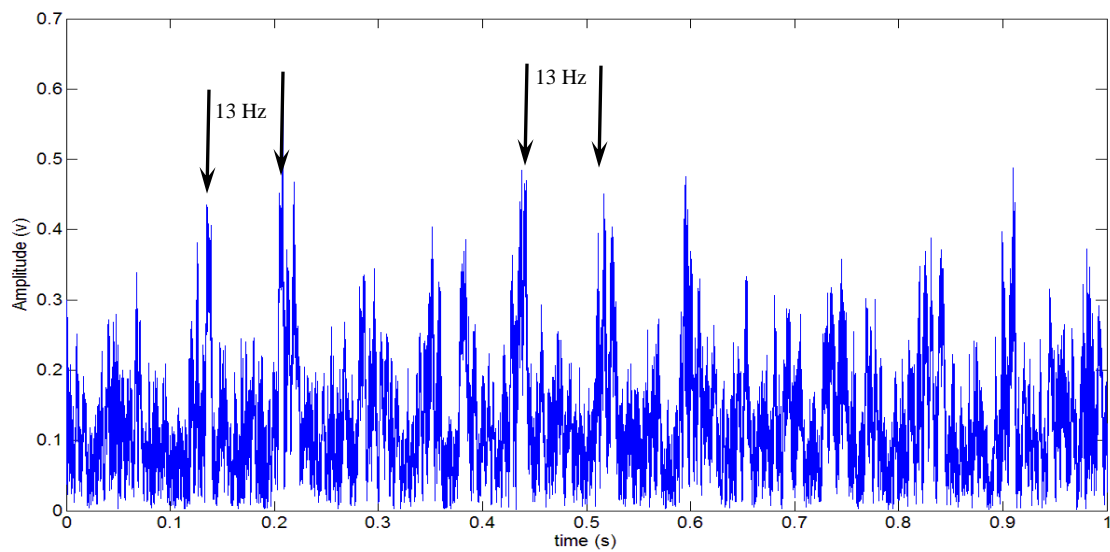


Figure 66. The processed results of the gearbox running under 24 Hz using the interference cancellation algorithm

From the results above, one can see that the developed methodology is effective in detecting gear fault under dynamic operating conditions.

5 AE BASED ROTATING MACHINERY FAULT DETECTION AND DIAGNOSIS

5.1 Introduction

Acoustic emission can be defined as a transient elastic wave generated by the rapid release of energy within a material, for example, the formation of a crack inside the material [147]. AE techniques have been extensively used in the field of NDT for detecting and locating the flaws in structures in many industrial applications, such as pipelines [148], aircraft [149], wind mill [150], and structure health monitoring [151, 152]. Recently, AE based techniques are beginning to attract researchers' attention to machine health monitoring and fault diagnostics [54, 59, 63, 65, 153-157]. As reported in [2], in comparison with the most widely used vibration signals, AE signals have the following advantages:

- (1) Insensitive to structural resonance and unaffected by typical mechanical background noises,
- (2) More sensitive to activities of faults,
- (3) Provide good trending parameters,
- (4) Localization of measurements to the machine being monitored, i.e., AE signals are sensitive to the location of the faults.

These advantages make the AE based techniques potentially more competitive than the vibration based techniques for rotational machinery health monitoring and fault detection. Performance comparison between the AE based technique and the vibration based

methods was conducted by several research papers. Paper [60] presented a comparative study between vibration based bearing defect identification and defect size estimation and acoustic emission based methods. The authors in that paper concluded that AE signals offer earlier fault detection and improved identification capabilities than the vibration signals. In [158], the diagnostic and prognostic capabilities of AE signal, vibration signal and spectrometric oil analysis were conducted for spur gears pitting type fault diagnosis and prognosis. Simple rms value was calculated as both AE and vibration based fault features and Fe concentration was used as the spectrometric oil analysis indicator. The major conclusion of that paper was that AE technique was more sensitive in detecting pitting fault than either the vibration or spectrometric oil analysis techniques and offers good potential for prognostic capabilities. Li *et al.* [159] reported a performance comparison between the vibration and AE based techniques on gear fault detection. In their paper, the traditional AE analysis features such as ring-down count, rise time, rise time slope, and RMS were used as the AE fault features and EMD based technique was used to extract fault features from vibration signals. These features were used as the inputs to a KNN based classification algorithm to identify the damaged gears. They showed that the AE based techniques had higher classification accuracy than the vibration based techniques on gear fault detection.

Unlike the vibration signal based rotating machinery fault detection and diagnosis, until now, only limited research has been conducted on AE based rotating machinery fault diagnosis and prognosis. In [160], the time interval of the acoustic emission signal was measured and related to the bearing fault characteristic frequencies. By obtaining the

time interval information, the fault types of the bearing system were determined. In [161], the effectiveness of the traditional AE parameters, amplitude, RMS, energy and AE counts were investigated on the bearing fault detection with different operating conditions. The results in the two paper show that the RMS and AE counts are effective in detecting different types of bearing faults with varying operating conditions. In [162], three traditional AE parameters, event duration, peak amplitude and energy were used to form a three dimensional fault feature vectors and the feature vectors were used as the input to a classifier based on fuzzy c-mean technique for bearing fault diagnosis. Tandon and Nakra [163] used AE counts and peak amplitudes of continuous AE signals as the fault features on bearing outer race fault diagnostics. In [164], the duration of the AE bursts were used to estimate the defect size of the roller bearing outer race. In [165], the transmission path effects were investigated and then the growing cracks on gear tooth were monitored successfully by using the AE signals. The authors in [166] investigated the capability of AE signal based techniques in detecting gear tooth pitting fault with deferent defect sizes. The ring-down counts, peak amplitude, energy, and the distribution of the events of the AE signals were calculated as fault features for gear pitting fault. Successful detection was reported. In [167], the authors place the AE sensors on the bearing house and the crack in gear tooth was detected by using AE signal based techniques. The results shown in [167] have demonstrated the capabilities of AE for detecting fatigue cracks in gear teeth. One critical issue in applying AE signal based techniques for rotating machinery health monitoring, fault detection, diagnosis, and prognosis is how to quantify the AE signal. Several difficulties in quantifying AE signals for rotating machinery health monitoring, fault detection, diagnostics include [2]:

- (1) AE signals generated on the rotating machines are normally characterized with certain non-stationary behavior.
- (2) The attenuation of the AE signals.
- (3) Higher sampling frequency is needed to collect AE signals.

To analyze signals with non-stationary properties, traditional frequency analysis techniques such as Fourier analysis is ineffective. Time-frequency methods, such as wavelet analysis, HHT, and so on, are proven to be an most effective methods[104]. Li *et al.* [168] conducted research on gear fault location detection using AE signals and presented a wavelet analysis based AE feature quantification methodology. The effectiveness of their methodology was validated using real gear seeded fault test data. One challenge in using wavelet analysis based methodology for AE feature quantification is that the basic wavelet function (mother wavelet) needs to be determined before the transformation can be performed. The choice of wavelet function will directly affect the effectiveness of identifying the fault features hidden within the dynamic signals [118]. Unfortunately, until now, there is no systemic way on choosing the mother wavelet in rotational machinery vibration signal analysis. Recently, a newly developed adaptive signal processing method called HHT is developed by Huang et al. [112] are proven to be effective in analyzing signal with non-stationary property [118]. EMD is not constrained by the difficulties in function and parameter selection since EMD itself is an adaptive signal processing method. Up to today, very limited research has been reported in the literature on an EMD based AE feature extraction for mechanical fault diagnosis. In both [169, 170], the continuous AE signals were processed with EMD to obtain the AE

features defined as energy ratios for fault diagnosis. However, two different fault diagnostic approaches were used in these papers. In [169], the energy ratios were used as inputs to a neural network based fault diagnostic method. In [170], the energy ratio of the intrinsic mode function (IMF) components was treated as the input vectors to the support vector machine (SVM) to identify the tool wear. In both papers, no de-noising was applied to the IMF components and features extracted from the AE signals contain both the fault contents and noises. Both the SVM and neural network techniques used for fault detection in these two papers are supervised learning based approaches. A limitation of supervised learning based approaches in fault detection is that they require known fault data for training purpose. In real application, these fault data are rarely available. According to [171], one difficulty in applying AE based technique for rotational machinery health monitoring and diagnostics is the attenuation of the AE signals. In the experimental setup described in [157, 172], the AE sensors were attached directly onto the surface of the spur gears. In fact, in most rotational machinery health monitoring applications, placing sensors in such a close distance to the rotational components is impractical. Usually, the sensors will be attached or mounted on the outer surface of the machines rather than directly be on the surface of the rotational parts. In such case, there will be a significant attenuation before the AE signals are picked up by the AE sensors. As a result, the signal-to-noise ratios of the collected AE signals are usually lower than those generated at the source. To extract the features from the AE signals for fault detection, noises should be removed to increase the signal-to-noise ratio of the AE signals.

In this Chapter, the effectiveness of the traditional AE features is investigated. Then two quantification methodologies, Laplace wavelet based methodology and EMD based methodology on AE burst type signal for gear fault detection and prognostics are presented. The effectiveness of the proposed methodologies is demonstrated by using the real gear seeded fault data collected on the STG notional gearbox test rig.

The remainder of the chapter is organized as follows. Section 5.2 provides the theoretical basis. Section 5.3 presents the experimental setup and data collection. The effectiveness of the traditional AE features in gear fault detection is shown in Section 5.4. Laplace wavelet based AE quantification methodology and experimental analysis results are shown in Section 5.5. Section 5.6 presents EMD based AE quantification technique and its experimental evaluation. A data mining based bearing fault diagnosis system by using AE signal and a full ceramic bearing case study are presented in Section 5.7.

5.2 **Theoretical Basis**

5.2.1 **Laplace Wavelet**

The Laplace wavelet[173] is defined by

$$\psi(\omega, \xi, \tau, t) = \psi_{\gamma}(t) = \begin{cases} Ae^{-\frac{2\pi f(t-\tau)\xi}{\sqrt{1-\xi^2}}} e^{-j2\pi f(t-\tau)}, & t \in [\tau, \tau + W_s] \\ 0, & else \end{cases} \quad (42)$$

where $j = \sqrt{-1}$, the parameters vector $\gamma = \{f, \xi, \tau\}$ determines the wavelet properties.

These parameters (f, ξ, τ) are denoted frequency $f \in R^+$, viscous damping

ratio $\xi \in [0,1] \in R^+$, and time index $\tau \in R$. The coefficient A is an arbitrary scaling factor, used to scale each wavelet to unity norm. The range Ws ensures the wavelet is completely supported and has nonzero finite length but the parameter Ws is generally not explicitly expressed.

An inner product operation measures the correlation between signals. Correlation of the signal with a Laplace wavelet measures similarity between frequency and damping properties of the wavelet, $\psi_\gamma(t)$, and the system which generated the signal $x(t)$. A correlation coefficient $\kappa_\gamma(\tau) \in R$ is defined to quantify the correlation degree between a Laplace wavelet $\psi_\gamma(t)$ and a time signal $x(t)$

$$\kappa_\gamma(\tau) = \sqrt{2} \frac{|\langle \psi_\gamma(t), x(t) \rangle|}{\|\psi_\gamma(t)\|_2 \|x(t)\|_2} \quad (43)$$

$\kappa_\gamma(\tau)$ is a multivariate function of the variables $\gamma = \{f, \xi, \tau\}$. This correlation coefficient considers the angle between the vectors with the maximum correlation occurring for vectors whose angle is 0.

A useful correlation coefficient $\nu(\tau)$ is defined for modal analysis to correlate frequency and damping at each time value. Peaks of $\nu(\tau)$ for a given τ relate to the wavelets with the strongest correlation to the signal. Define $\nu(\tau)$ as the peak value of $\kappa_\gamma(\tau)$ at each τ and define \bar{f} and $\bar{\xi}$ as the parameters of the Laplace wavelet associated with the peak correlation. Therefore, $\nu(\tau)$ can be defined as, $\nu(\tau) = \max_{f \in F, \xi \in Z} \kappa_{\{f, \xi, \tau\}} = \kappa_{\{\bar{f}, \bar{\xi}, \tau\}}$.

The Eq. above searches for a maximum value across f and ς . This search can use subsets of F and Z to find local maximum and compute a $\nu(\tau)$ vector at each time index.

A test signal with known properties is used to demonstrate this method. Consider a test signal $f(t)$.

$$f(t) = e^{-\frac{\xi_0}{\sqrt{1-\xi_0^2}} \omega_0 (t-t_0)} \sin(\omega_0 (t-t_0)) \quad (44)$$

In Eq. (44), the $\xi_0 = 0.04, \omega_0 = 20\pi$, and $t_0 = 0$. The sampling rate is set to be 200 Hz.

One of the Laplace wavelet is plotted in Figure 67.

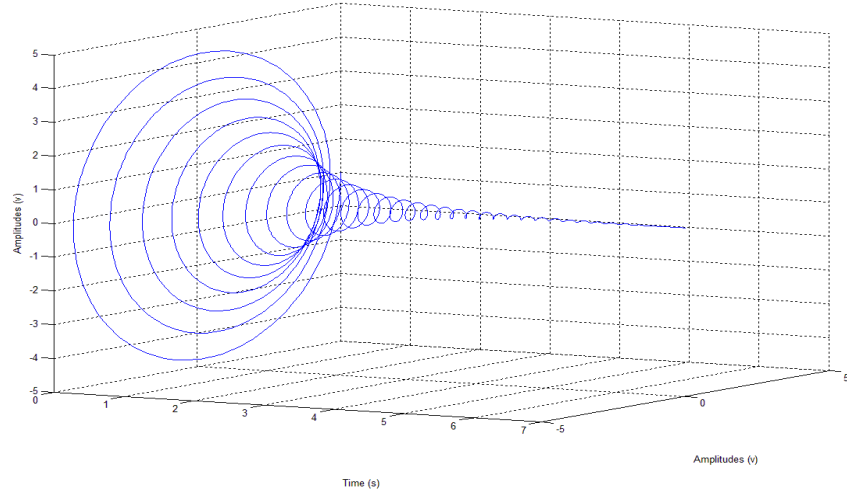


Figure 67. Laplace wavelet

A correlation coefficient $\kappa_\gamma(\tau) \in R$ is defined to quantify the correlation degree between a Laplace wavelet $\psi_\gamma(t)$ and a time signal $x(t)$

$$\kappa_\gamma(t) = \sqrt{2} \frac{\left| \langle \psi_\gamma(t), x(t) \rangle \right|}{\left\| \psi_\gamma(t) \right\|_2 \left\| x(t) \right\|_2} \quad (45)$$

$\kappa_\gamma(t)$ is a multivariate function of the variables $\gamma = \{f, \xi, \tau\}$.

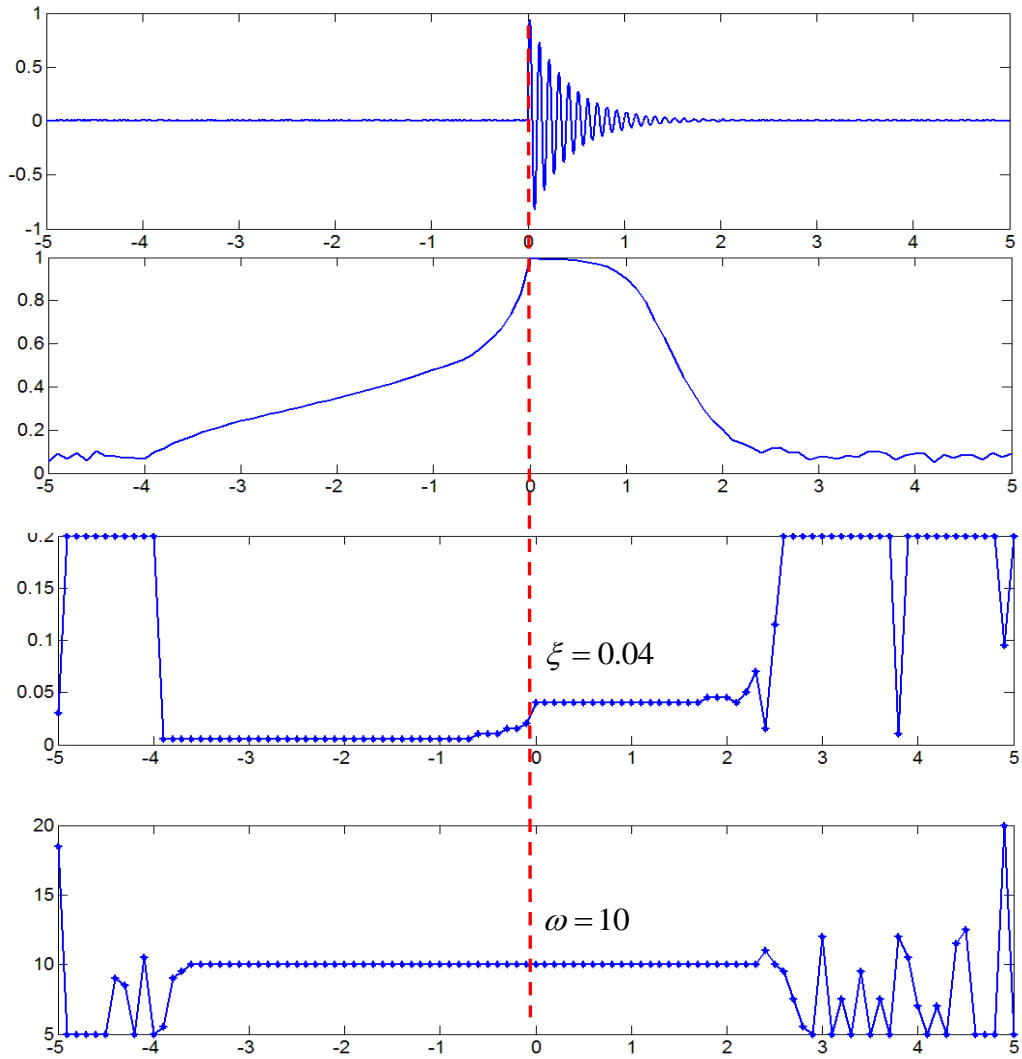


Figure 68. The simulated results

From the results in Figure 68, we can see the effective of the Laplace wavelet in identifying the damping ratio and the frequency for the simulated signal.

5.3 Experiment Setup and Data Acquisition

As mentioned by Everson and Cheraghi [174], the AE signals could be separated into two different types: burst type and continuous type. Burst type signals contain pulses over a period of time above background signals and can be separated with limited overlap. Continuous type signals do not have any significant resolutions between individual pulses. The AE signals generated by a rotational machine with localized faults such as cracks belong to the burst type signals [175]. One major advantage of using burst type AE signals for fault detection is that shorter sampling period will be needed. Therefore fewer storage spaces and less computational burden will be added to the real monitoring systems. As the developed methodologies and tools in this research are used for rotating machine localized fault detection and diagnostics, the burst type AE signals are collected and used in the dissertation.

AE signals collected from both the notional STG gearbox test rig and a bearing test rig were used in this chapter.

5.3.1 Pencil Break Test for Sampling Rate Selection

Since a too high sampling rate may create a huge burden to both the data acquisition system and signal processing system, choosing a suitable sampling rate is very important. Although the frequency range of the AE source in a rotational machine is typically between 100 kHz and 1 MHz [64], the mechanical transmission path between the AE

sources and the location of the AE sensors acts as a low pass filter. Because of the effect of this low pass filter, it is necessary to conduct an experiment to determine the frequency contents of the signal picked by the AE sensors in order to choose the right sampling rate. In the experiments, a pencil lead break test was utilized to determine the sampling rate. Pencil break tests are widely used in the area of NDT and a pencil lead break test is a simple test that can generate a broadband AE signals.

The pencil lead break test was conducted on the surface connected the damaged output driving gear and the output driven gear. The sampling frequency was first chosen to be 2 MHz. The collected signal and its Fourier spectrum are shown in Figure 69.

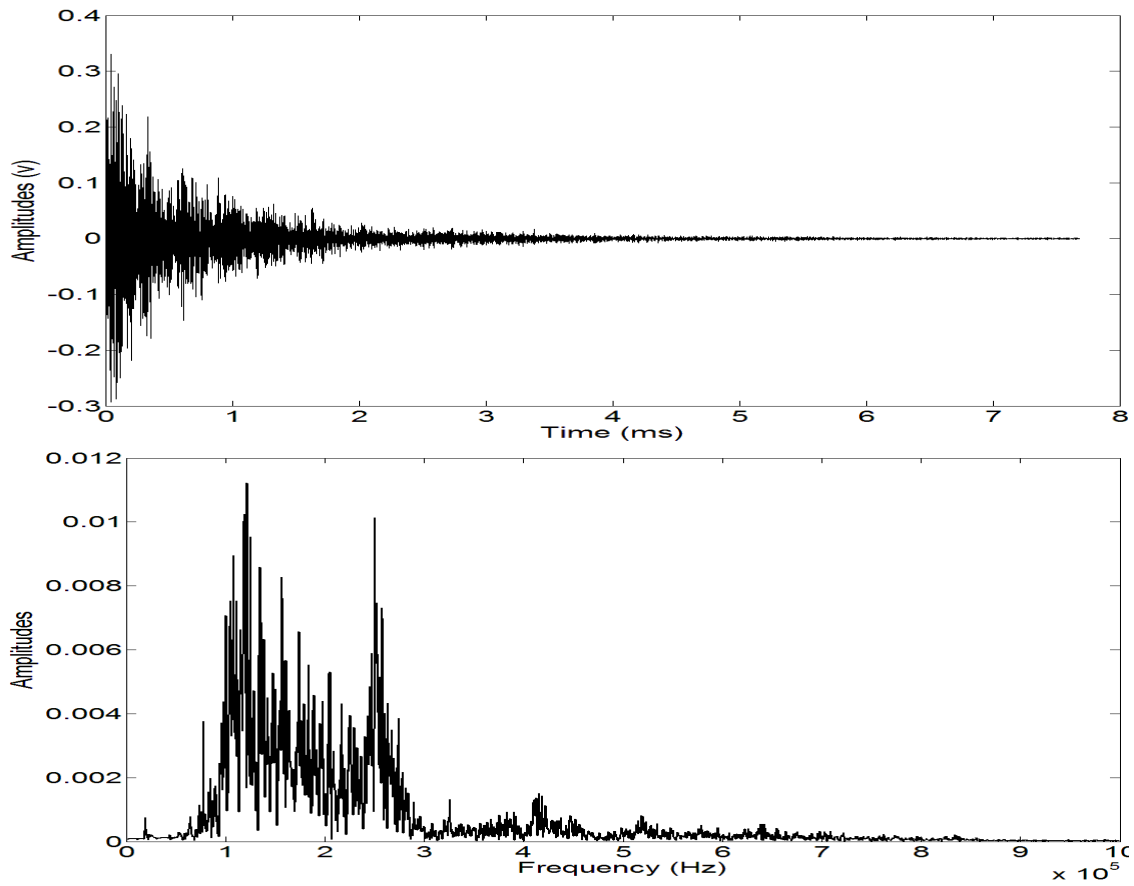


Figure 69. The pencil lead break test and its Fourier spectrum

From the results above, we can see that the frequency range of the AE burst is between 100 kHz to 250 kHz. A number of experiments were conducted using different sampling rates. Five different sampling rates were used: 50 kHz, 200 kHz, 500 kHz, 1 MHz and 2 MHz. The RMS value and the peak signal-to-noise ratio of the AE bursts under these sampling rates are provided in Table XVI.

Table XVI. The RMS and SNR of the AE bursts under different sampling rates

Sampling Rate	2 MHz	1 MHz	500 kHz	200 kHz	50 kHz
RMS	0.0398	0.0363	0.0318	0.0075	0.0052
Peak SNR	12.58	19.21	22.46	—	—

From Table XVI, we can see that when the sampling rate is below 500 kHz, the energy level of the AE burst measured by RMS is reduced by one order. Therefore, it is not meaningful to compute the SNR when the sampling rate is less than 500 kHz. This result indicates that some contents in the AE bursts were lost when the sampling rate was set too low. However, as the sampling rate increased, more noisy contents were sampled and the SNR decreased as a result. Based on the result in Table XVI, a sampling rate of 500 kHz was selected. Throughout investigation, the AE signals were collected under a sampling rate of 500 kHz.

5.3.2 Gear Seeded Fault Test

To simulate gear faults developed on the gear tooth, two types of seeded gear fault were created on the output side driving gear of the notional STG gearbox test rig. One was gear with tooth loss; the other was gear with root tooth crack. For the gear with tooth loss fault, three different damage levels were investigated. They are 20% of one gear

tooth loss, 50% of one gear tooth loss and 100% of one gear tooth loss on the output side driving gear was chipped. The healthy driving gear on the output side is shown in Figure 21 in the Chapter 4.

The damaged gear with 20% tooth loss, 50% tooth loss, and 100% tooth loss are shown in Figure 70, Figure 71, and Figure 72, respectively.

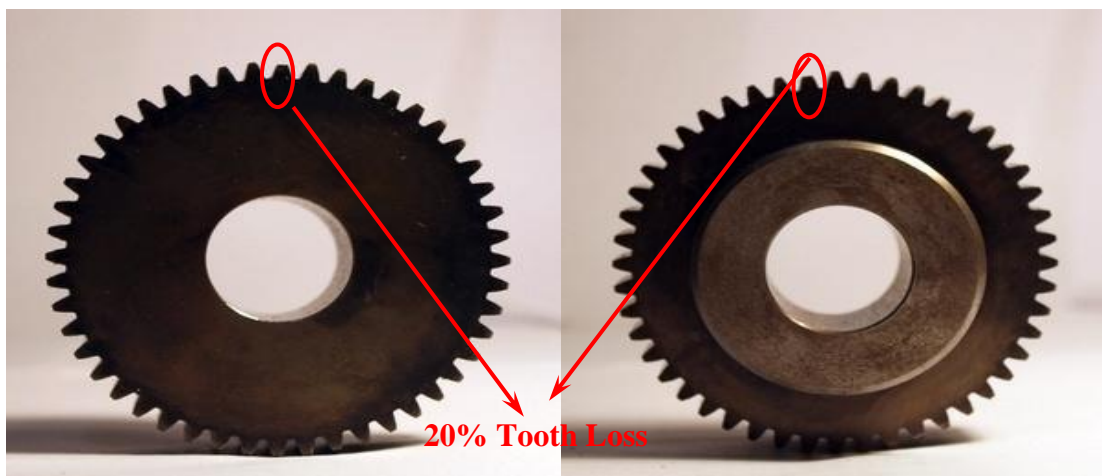


Figure 70. The damaged gear with 20% tooth loss

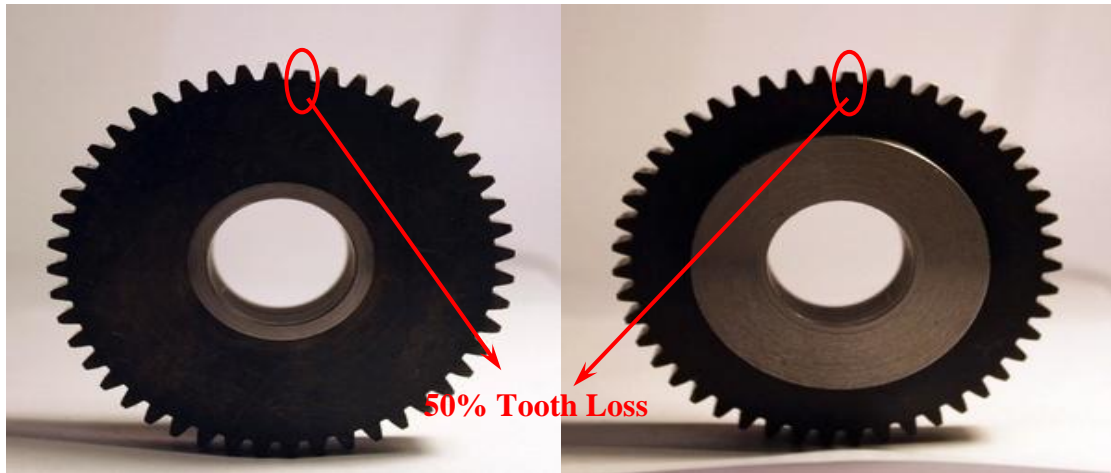


Figure 71. The damaged gear with 50% tooth loss

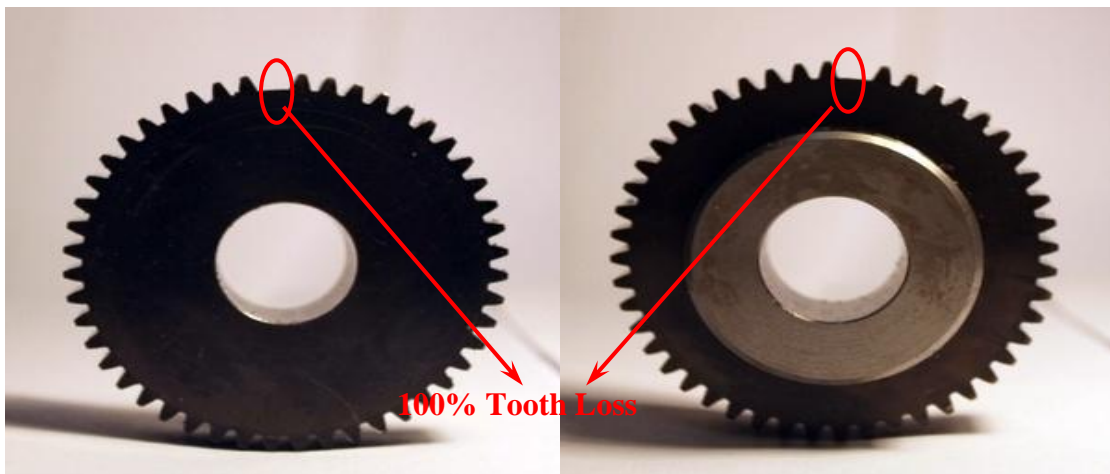


Figure 72. The damaged gear with 100% tooth loss

The damaged gear with 50% root tooth crack is shown in Figure 22 in Chapter 4. The gear was damaged by cutting the root of a gear tooth with a depth equal to half width of the gear tooth by EDM with a wire of 0.5 mm diameter to simulate the root crack damage in real applications.

5.3.3 Full Ceramic Bearing Fault Test

For the bearing experiments, the bearing test rig shown in Figure 24 in Chapter 4 is used. Four types of bearing seeded faults, bearing outer race fault, bearing inner race fault, rolling element fault and bearing cage fault, were investigated in this dissertation. The different types of faulty bearings are shown in Figure 25 in Chapter 4. The location of the sensor is shown in Figure 73.

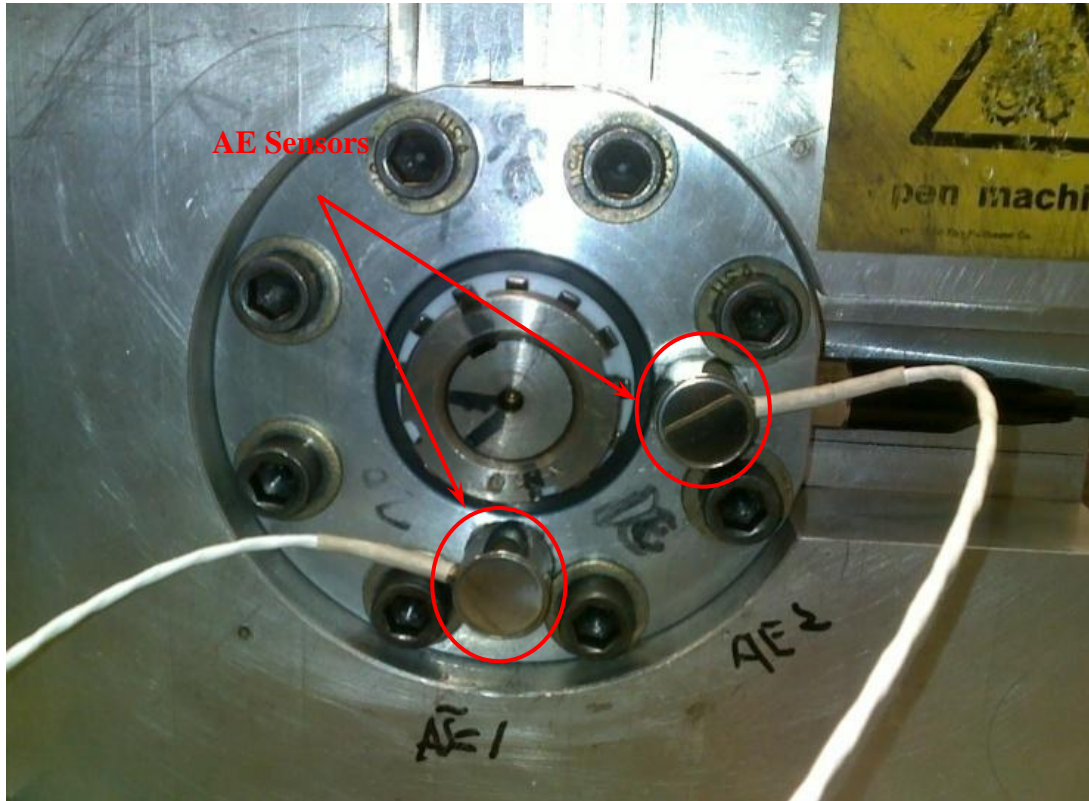


Figure 73. The location of the AE sensors

5.4 Traditional AE Feature Based Gear Fault Detection

The effectiveness of the traditional AE features in gear fault detection is investigated. The performance of the AE based technique is compared with that of the vibration analysis. The process for the fault detection on STG based on both vibration signal and AE signal is shown in Figure 74.

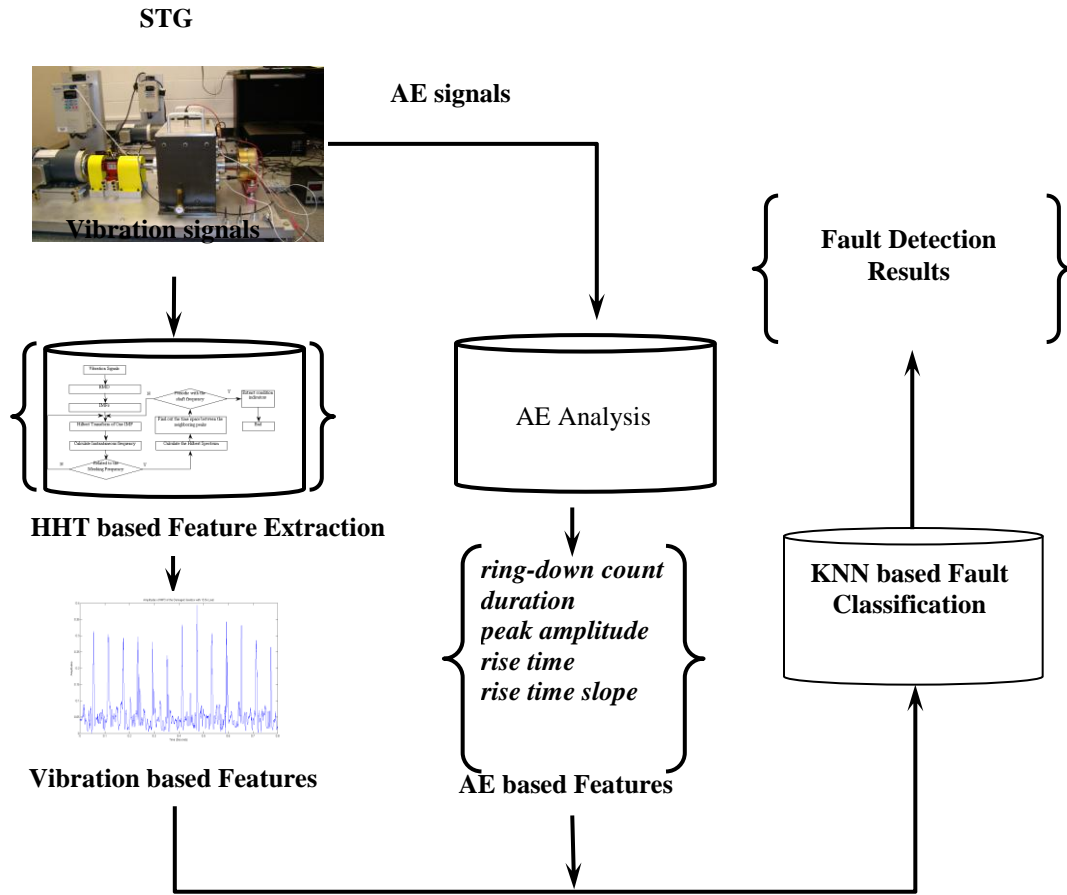


Figure 74. The process for fault diagnostics on STG

As shown in Figure 74, AE signals and vibration signals are pre-processed to obtain the fault feature vectors and these feature vectors are used as the input to a KNN based fault classifier. The accuracy rate of the KNN classifier is used to evaluate the performance of the two techniques. The higher the accuracy rate, the better the technique is.

For calculating AE based fault feature vector, the traditional AE parameters are utilized. In NDT area, seven AE features are used. The seven AE features include: (1) ring-down count, (2) duration, (3) peak amplitude, (4) rise time, (5) rise time slope, (6) RMS, (7) Kurtosis. The ring-down count is defined as the number of threshold crossing made by an acoustic emission event. The duration is defined as the time between the initial rise of acoustic emission energy above the threshold and the time at which the acoustic emission energy decays below the threshold. The peak value is the absolute value of the highest voltage attained by a single acoustic emission event. The rise time is defined as the time between the initial crossing of the threshold and the time at which the peak amplitude occurs. The rise time slope is defined as the peak amplitude minus the threshold voltage divided by the rise time. RMS is defined by equation (46) and Kurtosis is defined by equation (47) as follows:

$$RMS = \sqrt{\frac{1}{n} \sum_{i=1}^n x_i^2} \quad (46)$$

where x_i is the signal.

$$Kurtosis = \frac{\frac{1}{n} \sum_{i=1}^n (x_i - \bar{x})^4}{\left(\frac{1}{n} \sum_{i=1}^n (x_i - \bar{x})^2\right)^2} \quad (47)$$

where x_i is the signal and \bar{x} is the mean value of the signal.

For calculating vibration based fault feature vectors, the EMD was applied to the vibration signals and the IMF components which contain the gear mesh frequency components are selected. The RMS, peak value, kurtosis, and the amplitude of the shaft frequency of the damaged gear in the Fourier spectrum of the selected IMF components were calculated as the features.

Sample AE waveform of both the healthy gearbox and the damaged gearbox are shown in Figure 75 and Figure 76, respectively.

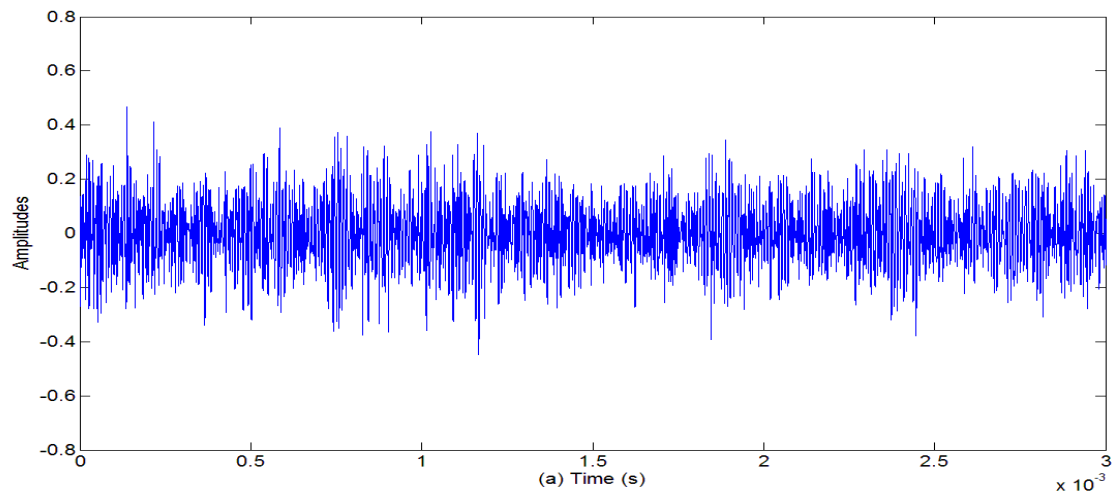


Figure 75. The sample acoustic emission signals of the healthy gearbox

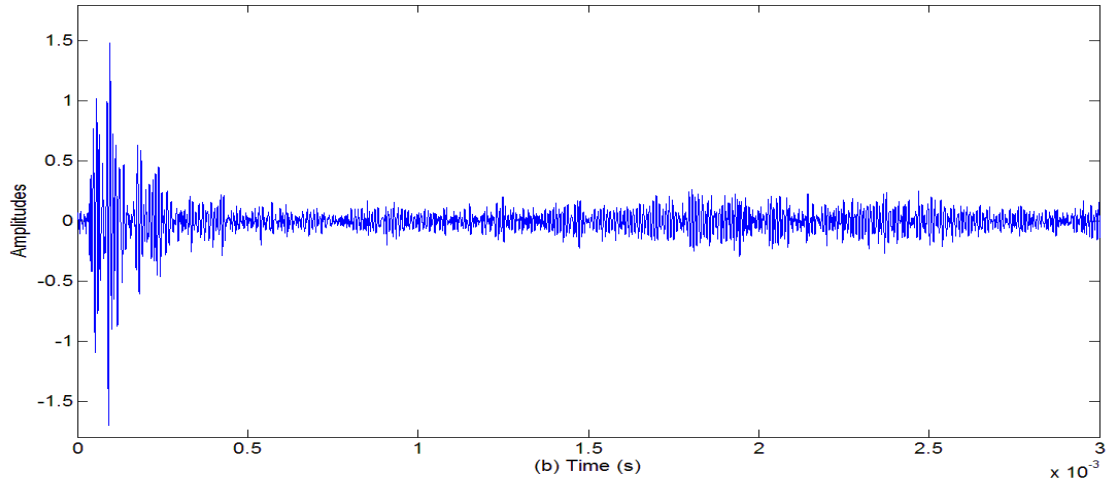


Figure 76. The sample acoustic emission signals of the damaged gearbox

The features were extracted for every dataset for both the healthy gearbox and the damaged gearbox to generate 300 feature vectors. From the generated feature vectors, 150 of the healthy gearbox and 150 of the damaged gearbox were used as the training features to train the KNN classifier. Then the rest of the feature vectors were used for classification. The classification results are shown in Table XVII.

Table XVII. The confusion matrix for fault detection using AE signals

	Predicted Classes	
Actual Classes	Healthy Gearbox	Damaged Gearbox
Healthy Gearbox	50	0
Damaged Gearbox	0	50

From Table XVII, we can see that an accuracy of 100% to classify healthy or damaged state of the gearbox using AE signals was achieved.

Sample vibration signal of the healthy gearbox data is shown in Figure 77 and that of the damaged gearbox is shown in Figure 78.

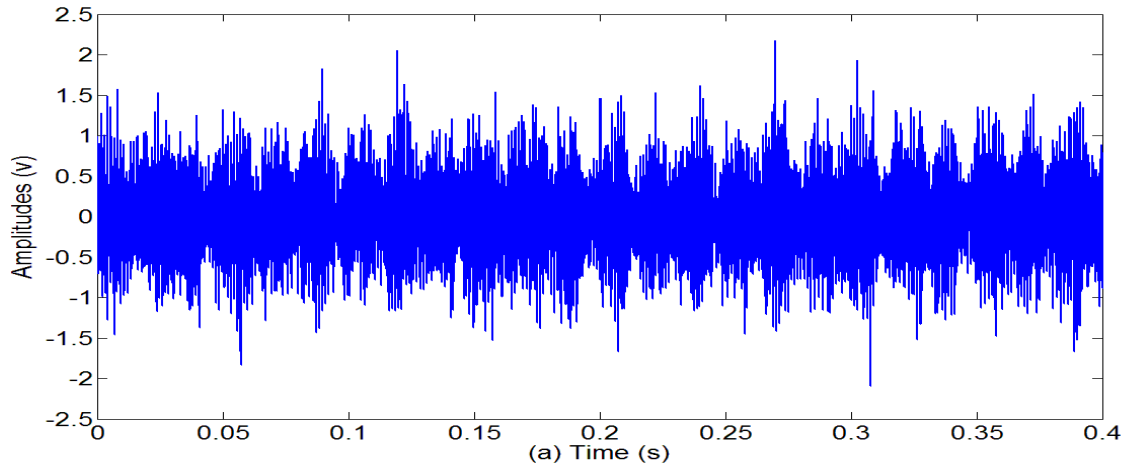


Figure 77. The vibration signal of the healthy gearbox

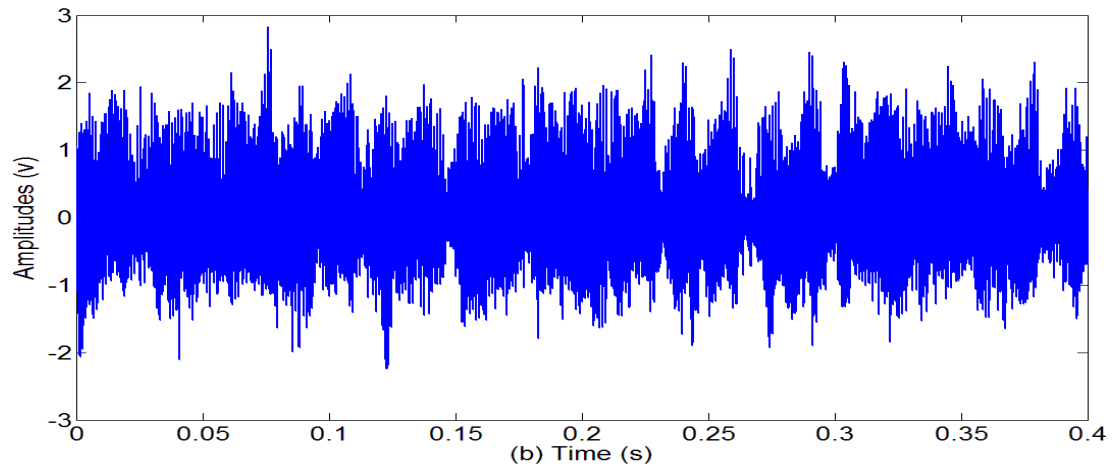


Figure 78. The vibration signal of the damaged gearbox

The EMD was applied to the vibration signals. For this case, the 3rd IMF component was chosen because of this IMF component was associated with the gear meshing

frequency of 1600 Hz. The RMS, peak value, kurtosis, and the amplitude of the shaft frequency of the damaged gear in the Fourier spectrum of the 3rd IMF component were calculated as the features.

The features were extracted for every dataset for both the healthy gearbox and the damaged gearbox to generate 300 feature vectors. From the generated feature vectors, 150 of the healthy gearbox and 150 of the damaged gearbox were used as the training features to train the KNN classifier. Then the rest of the feature vectors were used for classification. The classification results are shown in Table XVIII. From Table XVIII, we can see that the classification accuracy is 95%.

Table XVIII. The confusion matrix for fault detection using vibration

Actual Classes	Predicted Classes	
	Healthy Gearbox	Damaged Gearbox
Healthy Gearbox	45	5
Damaged Gearbox	0	50

By comparing the results of AE and vibration, we can see that AE signals are sensitive to the gear fault in the split torque gearbox test rig case study.

5.5 **Laplace Wavelet Based AE Signal Quantification Methodology**

Develop an effective quantification methodology is critical important in applying AE signal based techniques for rotating machinery health monitoring, fault detection, diagnosis, and prognosis. In this research, a Laplace wavelet based AE signal quantification methodology has been developed. The coefficients of the Laplace wavelet are optimized by using the exhausted search technique. The maximum of the kurtosis value of the wavelet coefficient is used as the objective function for the optimization problem. The Process of the Laplace wavelet based AE signal quantification methodology is shown in Figure 79.

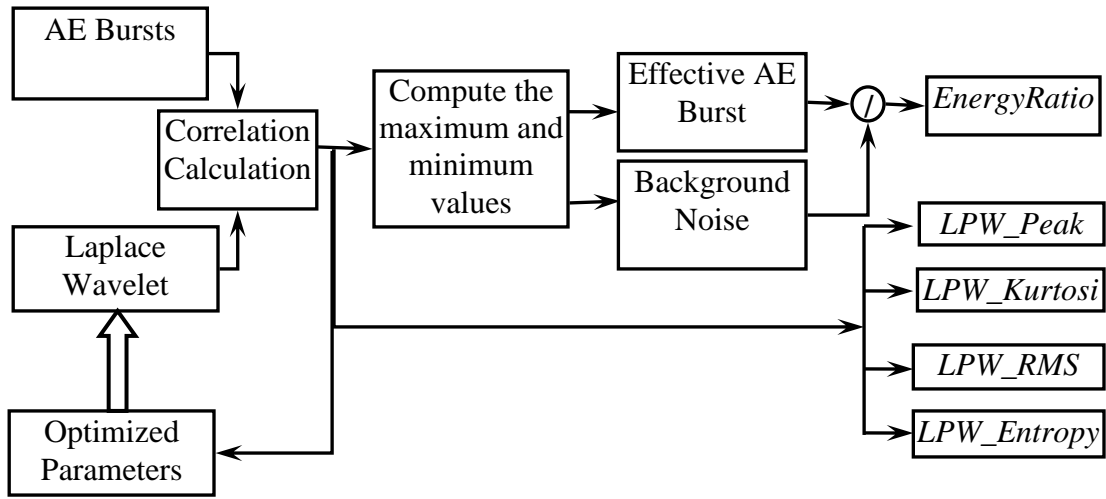


Figure 79. The process of Laplace wavelet based AE signal quantification methodology

As shown in Figure 79, the AE features are calculated by using Laplace wavelet processed AE bursts. The parameters of the Laplace wavelet are optimized by maximizing the kurtosis value of the wavelet coefficient. The AE features include features extracted from Laplace wavelet processed AE bursts: the *Energy Ratio*, the peak value (*LPW_Peak*), the kurtosis value (*LPW_Kurtosis*), the *rms* value (*LPW_RMS*), and entropy value (*LPW_Entropy*). Here, the Laplace wavelet is used as a correlation filter to process the AE bursts.

The *Energy Ratio* is defined as,

$$Energy\ Ratio = \frac{E_Background}{E_AEburst} = \frac{\int_{t=0}^T AE_Background^2(t)dt}{\int_{t=0}^T AE_Signal^2(t)dt} \quad (48)$$

For a discrete signal, Eq.(49) is used:

$$Energy\ Ratio = \frac{E_Background}{E_AEburst} = \frac{\sum_{t=1}^N AE_Background^2(t)}{\sum_{t=1}^N AE_Signal^2(t)} \quad (49)$$

If we can represent a discrete AE burst by $x = [x_1, x_2, \dots, x_i, \dots, x_n]$, then the *rms* value and the kurtosis value can be calculated by the following equations:

$$RMS = \sqrt{\frac{1}{n} \sum_{i=1}^n x_i^2} \quad (50)$$

$$Kurtosis = \frac{\frac{1}{n} \sum_{i=1}^n (x_i - \bar{x})^4}{(\frac{1}{n} \sum_{i=1}^n (x_i - \bar{x})^2)^2} \quad (51)$$

The entropy of signal x is defined by the following equation:

$$Entropy = -\sum_{i=1}^n x_i \log x_i \quad (52)$$

The Laplace wavelet coefficient may be calculated as a fault features. As known to the research community, the shape of the mother wavelets is important in wavelet decomposition. For Laplace wavelet, the shape parameters include, damping ratio ξ which controls the decay rate of the exponential envelope in the time domain and in the

frequency domain it regulates the resolution of the wavelet and damping frequency ω which controls the number of significant oscillations of the wavelet in the time domain and determine the center frequency in the frequency domain. In order to optimize the wavelet shape parameters, we need to develop a suitable objective function. For our case, the AE bursts generated by the damaged gears are impulse like signals and the kurtosis value is an indicator that reflects the peak of a signal. A higher kurtosis value indicates high-impulsive content of the signal. Therefore, the kurtosis of a wavelet transform output may be treated as the objective function in finding the optimal value of ξ and ω .

$$\phi(\xi, \omega) = \frac{\sum_{n=1}^N |WT(s(t), \psi_{\xi, \omega}(t))|^4}{\left[\sum_{n=1}^N |WT(s(t), \psi_{\xi, \omega}(t))|^2 \right]^2} \quad (53)$$

where, $s(t)$ is a signal, WT is the inner product of $s(t)$ with the mother wavelet $\psi_{\xi, \omega}(t)$.

By maximizing $\phi(\xi, \omega)$, we can get the optimal ξ and ω .

In practice, the Laplace wavelet shape coefficients f, ξ are first identified by using a typical known AE bursts, generated by the damaged gearbox. In this dissertation, the f, ξ are identified by using an exhausted search to find the maximum value of the correlation coefficients between the AE bursts and the Laplace wavelet. For demonstration purpose, a typical sample AE burst is used to demonstrate the process. The sample AE burst is shown in Figure 80. The signal was processed using the Laplace wavelet and the Laplace wavelet coefficients with different wavelet parameters are

shown in Figure 81. By searching the space shown in Figure 81, we could find that at the maximum correlation coefficient, $f=105000$, and $\xi=0.08$. In Eq. (7), τ is the time step parameter used in computing the wavelet coefficients and it determines the time resolution of the Laplace wavelet coefficients in our research, the value of τ was computed approximately as $1/f$ to be 0.00001 s.

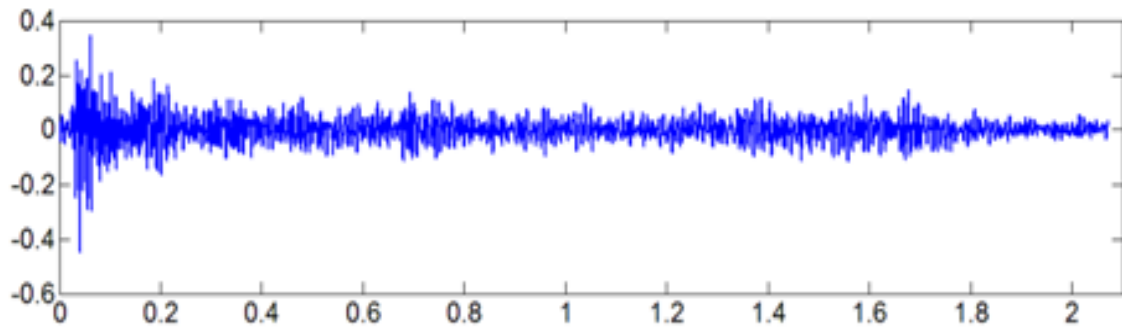


Figure 80. A sample AE burst generated by the damaged gearbox

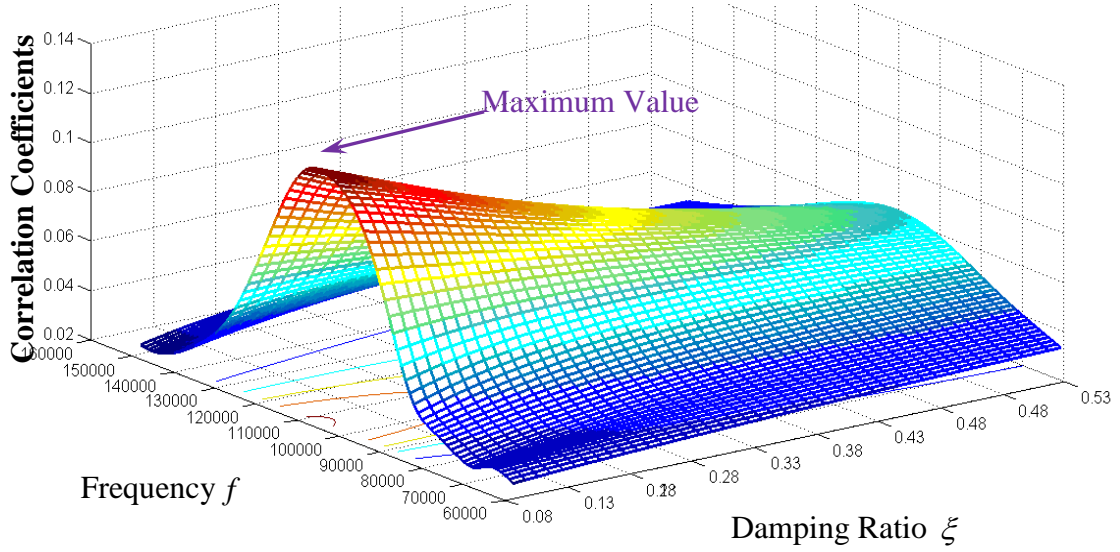


Figure 81. The correlation coefficient between the AE burst and the Laplace wavelet

After f and ξ are determined, the correlation coefficients between the AE burst and the Laplace wavelet for the rest of the AE bursts could be calculated. The effective AE burst ($E_AEBurst$) in Eq. (49) is defined as the signal between the time when the first maximum correlation coefficient occurs plus and minus τ and the time when the second maximum correlation coefficient occurs plus and minus τ . And the background noise in Eq. (49) is defined as, the signal between the time when the first minimum correlation coefficient occurs plus and minus τ and the time when the second minimum correlation coefficient occurs plus and minus τ .

After the location of the AE burst signal and the background signal are located, the time window length needed to be determined. Too small window length cannot capture the whole characteristics of the AE burst waveform and makes the extracted fault features easier to be contaminated by the noise. While too large window length makes the signal contains more uncorrelated signals and thus makes the extracted fault features less sensitive to the fault.

Laplace wavelet coefficients represent a possible way to determine the window length of the AE burst since the AE burst signal provides a larger correlation coefficient with the Laplace wavelet. The window length can be determined by using the following equation.

$$Threshold \leq \kappa_{\gamma}(\tau) = \sqrt{2} \frac{|\langle \psi_{\gamma}(t), x(t) \rangle|}{\|\psi_{\gamma}(t)\|_2 \|x(t)\|_2} \quad (54)$$

The flowchart of finding the window length is shown in Figure 82.

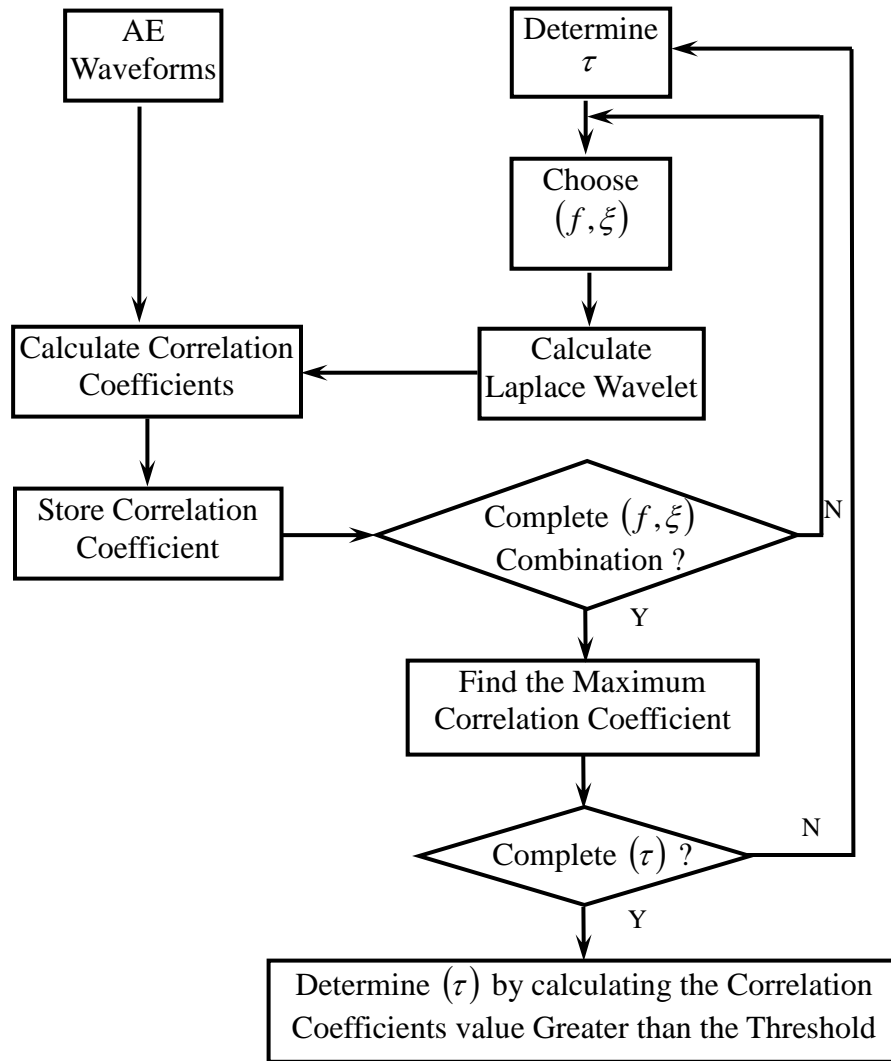


Figure 82. The flowchart of finding window length

The simulated signal in Eq. (20) is re-used here to demonstrate the concept. The Laplace wavelet is applied to the simulated signal and the results are shown in Figure 83. In this simulated example, when threshold value is set as 0.95, the burst signal window length

for the simulated signal is 0.98 seconds. The noise window length is the same as the burst window length and it is 0.98 seconds.

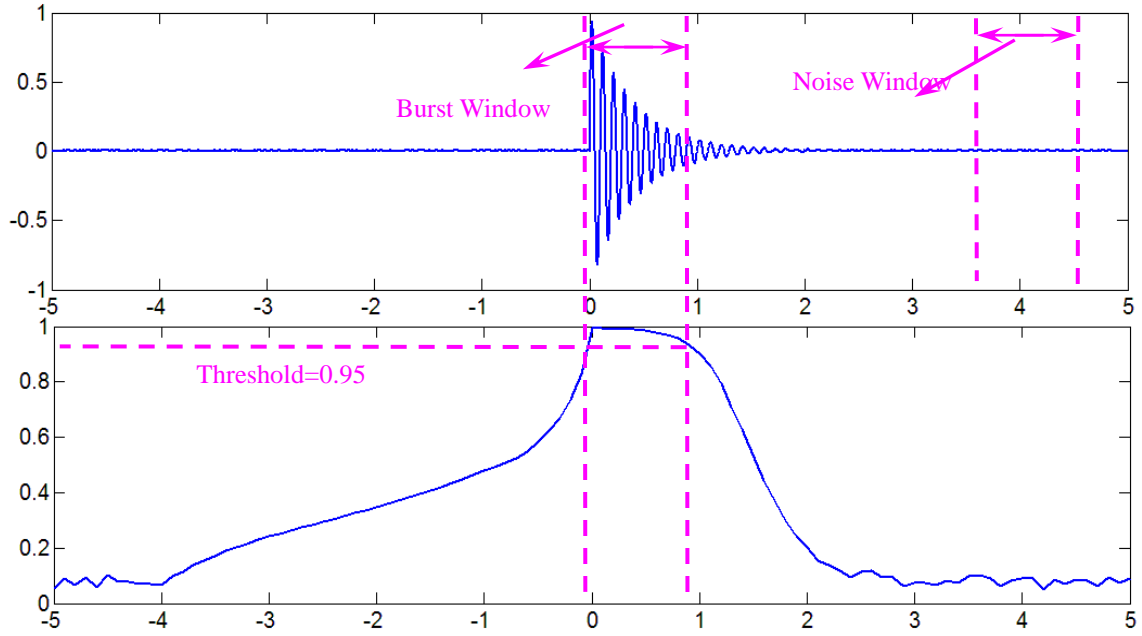


Figure 83. The simulated results

A real AE waveform from the damaged gearbox is used here to illustrate the effectiveness of the proposed method. The AE waveform and the correlation coefficients are shown in Figure 84.

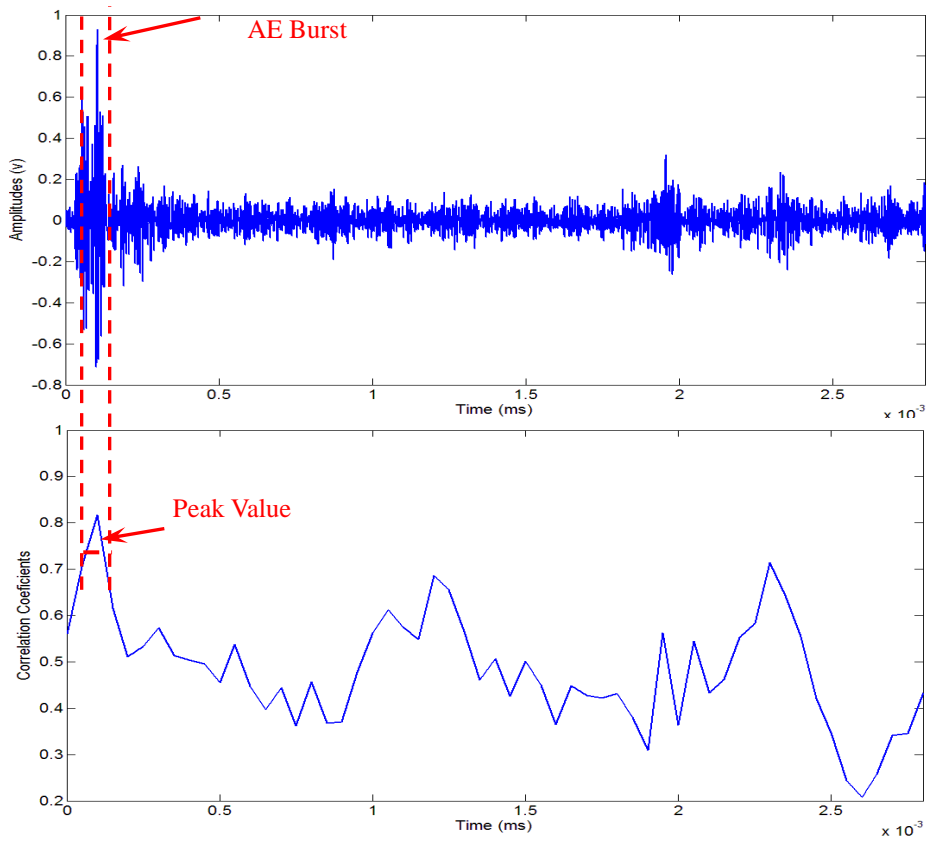


Figure 84. The real AE waveform generated by the damaged gearbox and its correlation coefficients

From the results for both the simulated signal and the real AE waveform, we can see that the threshold based method is capable of determining the window length for detecting the AE burst.

5.5.1 Case Study: STG Gear Test Rig Experiment

To quantify the correlation between the AE based condition indicators and the gear damage levels, three gear damage levels were investigated in this research: 0% tooth loss (healthy gear), 20% tooth loss, and 100% tooth loss. For each damage level, three different loadings were applied: 0% loading, 50% loading, and 100% loading. The AE sampling rate was set at 500 kHz and 500 AE bursts were collected for each damage level and loading condition. The processed results are shown in the following tables.

Table XIX. The AE features of the gearbox with 0% damage level

AE Features	Loading		
	0%	50%	100%
<i>Kurtosis</i>	6.210	3.675	3.440
<i>RMS</i>	0.090	0.135	0.129
<i>Peak</i>	0.541	0.616	0.543
<i>Energy Ratio</i>	37.248	17.017	15.36
<i>LPW_kurtosis</i>	12.076	7.665	6.950
<i>LPW_peak</i>	0.300	0.318	0.288
<i>LPW_Entropy</i>	46.076	61.446	59.874
<i>LPW_RMS</i>	0.060	0.079	0.075

Table XX. The feature of the gearbox with 20% damage

AE Features	Loading		
	0%	50%	100%
<i>Kurtosis</i>	11.832	10.158	8.851
<i>RMS</i>	0.051	0.047	0.047
<i>Peak</i>	0.459	0.410	0.384
<i>Energy Ratio</i>	39.791	27.891	25.084
<i>LPW_kurtosis</i>	18.255	16.530	16.514
<i>LPW_peak</i>	0.165	0.137	0.134
<i>LPW_Entropy</i>	28.769	26.965	26.847
<i>LPW_RMS</i>	0.029	0.025	0.025

Table XXI. The features of the gearbox with 50% damage

AE Features	Loading		
	0%	50%	100%
<i>Kurtosis</i>	12.699	14.495	12.651
<i>RMS</i>	0.037	0.035	0.035
<i>Peak</i>	0.314	0.321	0.312
<i>Energy Ratio</i>	42.431	39.664	31.142
<i>LPW_kurtosis</i>	11.331	12.055	10.739
<i>LPW_peak</i>	0.093	0.088	0.081
<i>LPW_Entropy</i>	22.843	21.475	21.486
<i>LPW_RMS</i>	0.020	0.018	0.018

Table XXII. The features of the gearbox with 100% damage

AE Features	Loading		
	0%	50%	100%
<i>Kurtosis</i>	15.111	12.423	13.368
<i>RMS</i>	0.048	0.047	0.043
<i>Peak</i>	0.455	0.406	0.386
<i>Energy Ratio</i>	56.099	41.924	44.220
<i>LPW_kurtosis</i>	15.474	13.274	13.335
<i>LPW_peak</i>	0.150	0.137	0.124
<i>LPW_Entropy</i>	27.958	27.737	25.885
<i>LPW_RMS</i>	0.028	0.027	0.025

The correlation between the AE features and the damage levels under three different loading conditions are shown in Figure from Figure 85 to Figure 90. In these Figures, the maximum value of each feature is normalized to be 1. For the 0% loading condition, the correlation between the raw AE features and the damage levels is shown in Figure 85 and the correlation between Laplace wavelet processed AE features and the damage levels in Figure 86.

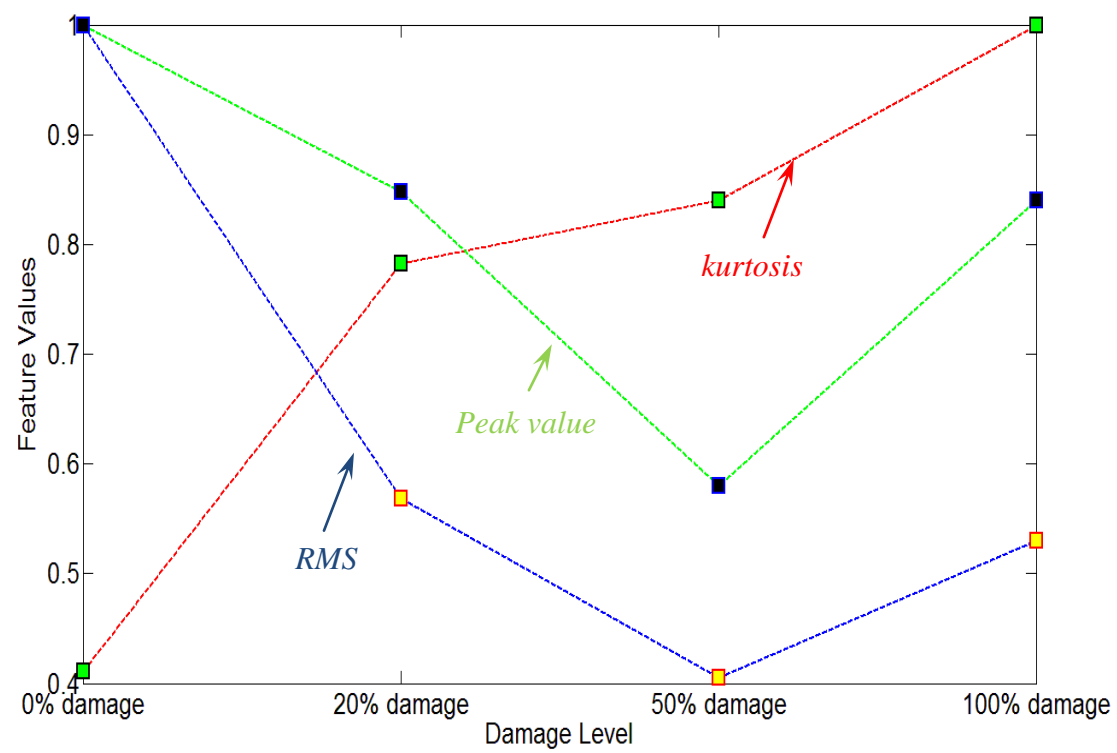


Figure 85. The features extracted from the raw AE bursts of the gearbox with 0% loadings

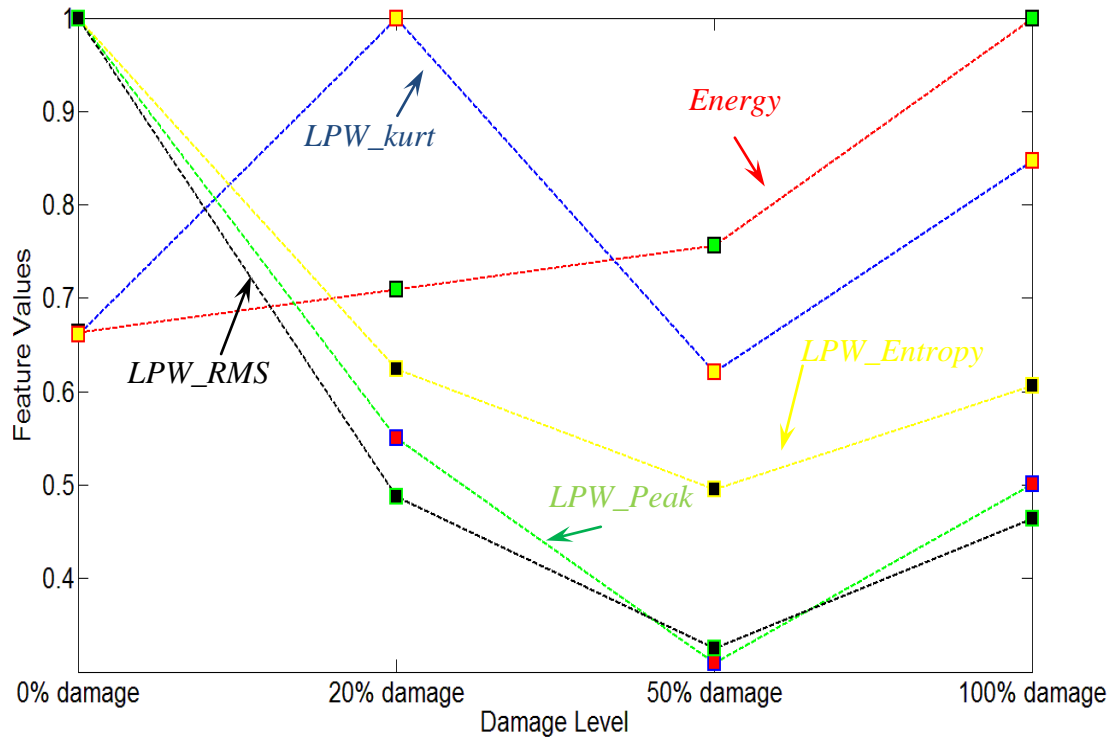


Figure 86. The features extracted from the processed AE signals of the gearbox with 0% loadings

From Figure 85 and Figure 86, we can see that the kurtosis value of the raw AE bursts and the energy ratio value of the Laplace wavelet processed signal show a consistent correlation between the AE feature values and damage levels, i.e., the AE feature values increase as the damage level increases.

For the 50% loading condition, the correlation between the raw AE features and the damage levels is shown in Figure 87 and the correlation between Laplace wavelet processed AE features and the damage levels in Figure 88.

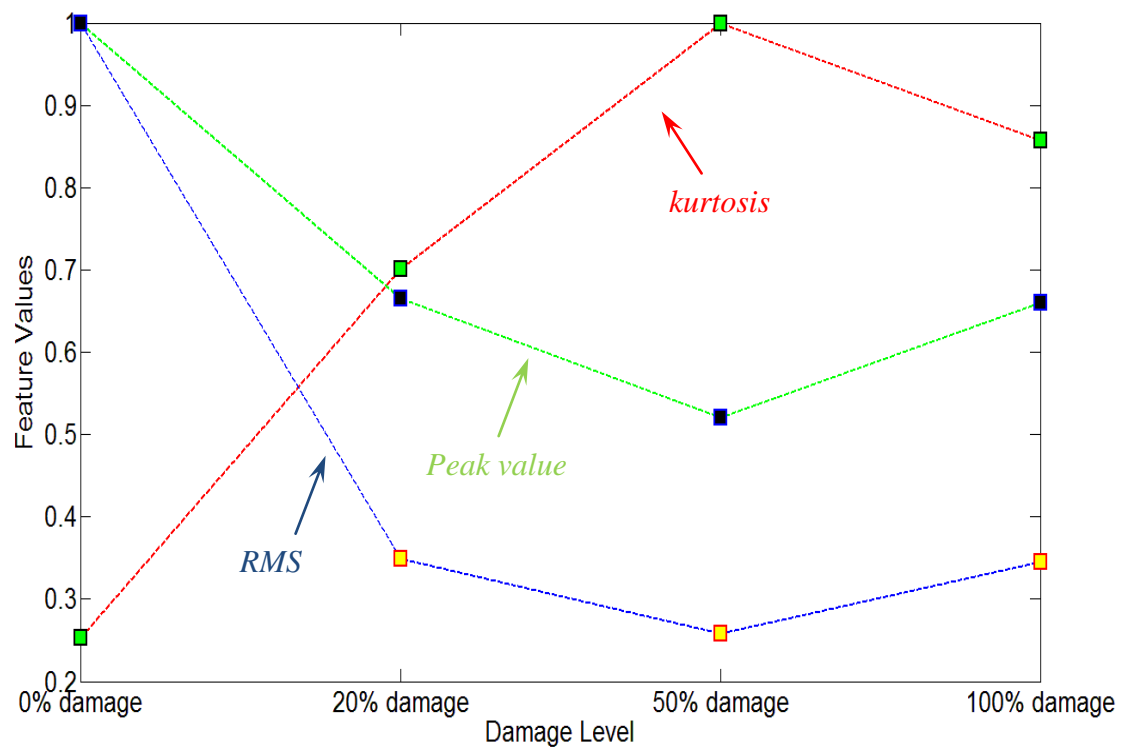


Figure 87. The features extracted from the raw AE signals of the gearbox with 50% loadings

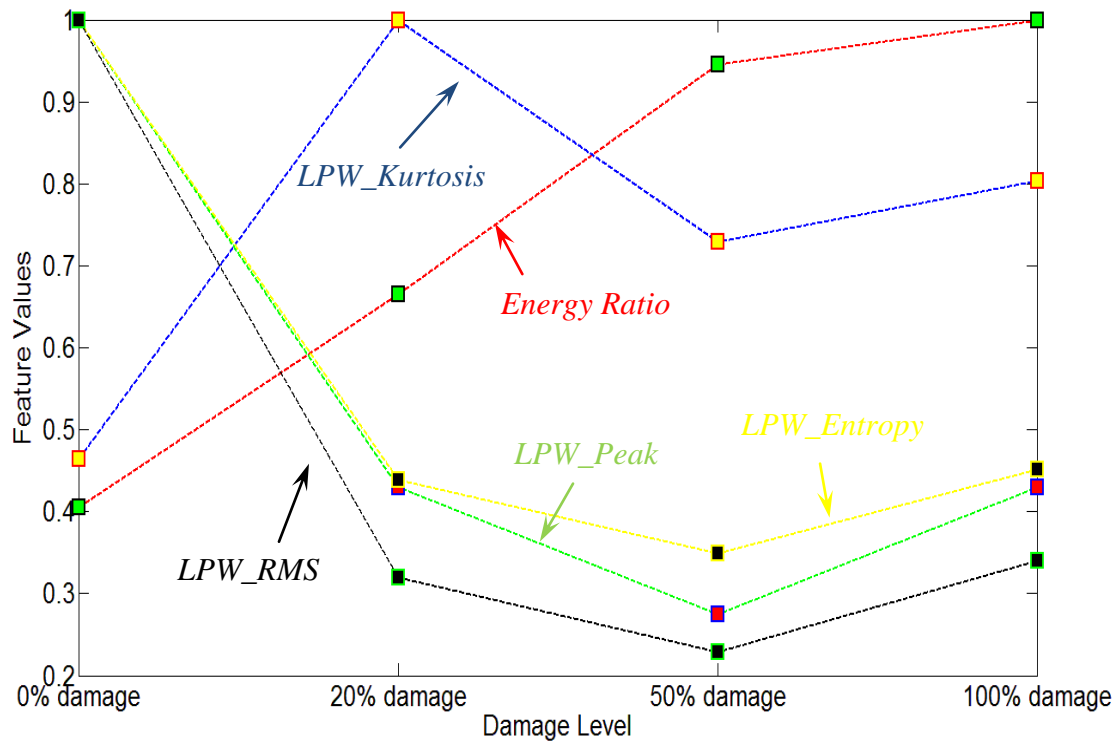


Figure 88. The features extracted from the processed AE signals of the gearbox with 50% loadings

From Figure 87 and Figure 88, we can see we can see that only the energy ratio value of the Laplace wavelet processed signal show a consistent correlation between the AE feature values and damage levels, i.e., the AE feature values increase as the damage level increases.

For the 100% loading conditions, the correlation between the raw AE features and the damage levels is shown in Figure 89 and the correlation between Laplace wavelet processed AE features and the damage levels in Figure 90.

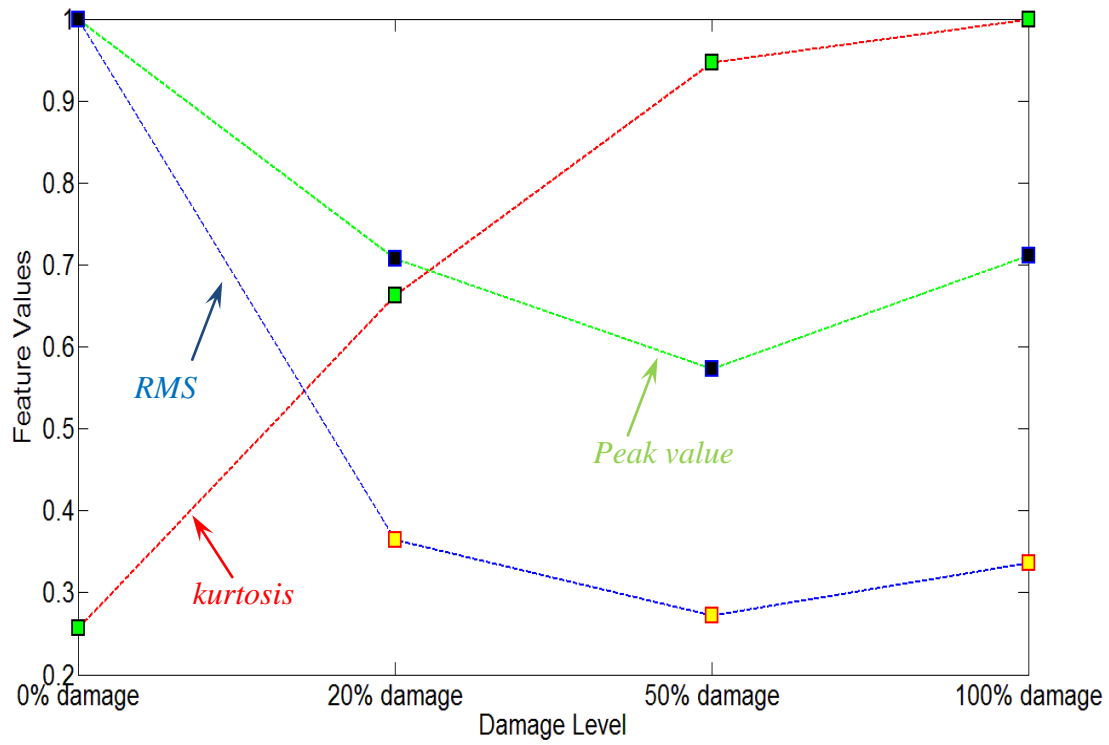


Figure 89. The features extracted from the raw AE signals of the gearbox with 100% loadings

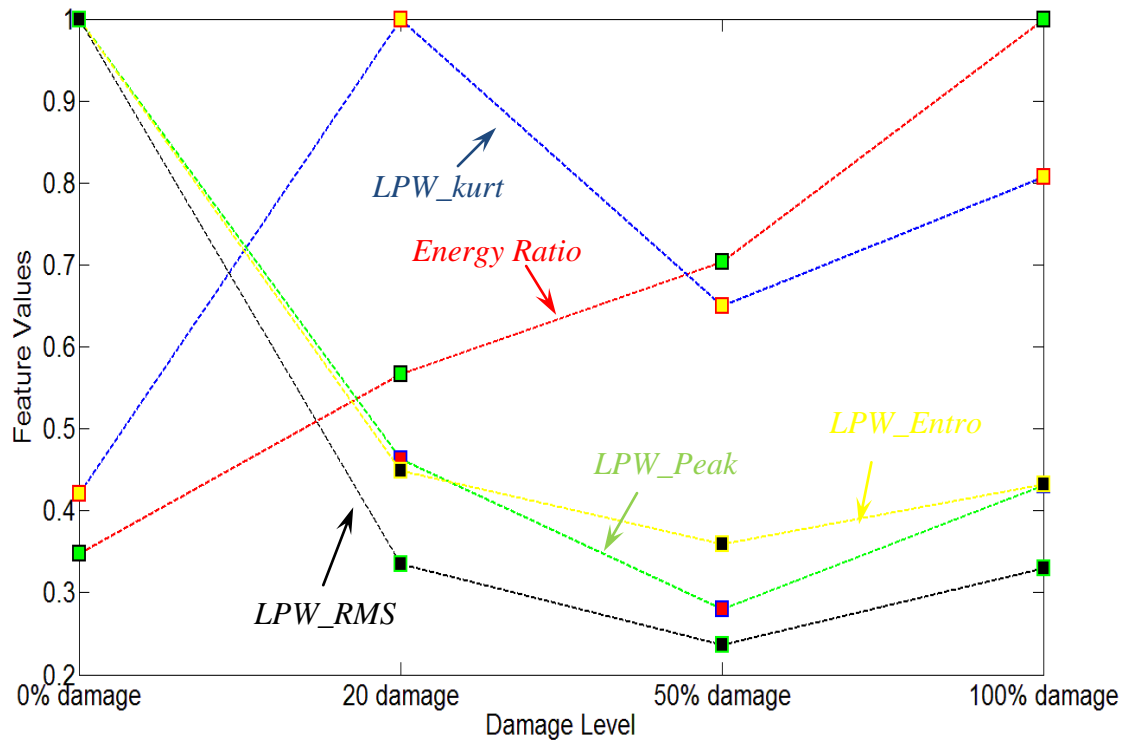


Figure 90. The features extracted from the processed AE signals of the gearbox with 100% loadings

From Figure 89 and Figure 90, we could see we can see that the kurtosis value of the raw AE bursts and the energy ratio value of the Laplace wavelet processed signal show a consistent correlation between the AE feature values and damage levels, i.e., the AE feature values increase as the damage level increases.

From the results shown above, one can see that only energy ratio value of the Laplace wavelet processed signal shows a consistent correlation between the AE feature values and damage levels under different loading conditions.

5.6 **EMD Based AE Quantification Methodology**

The framework of the methodology for rotating machinery health monitoring and fault detection using EMD based AE feature quantification is provided in Figure 91. The developed EMD based AE quantification methodology incorporates a threshold based de-noising technique into EMD to increase the signal-to-noise ratio. A single compressed AE feature is calculated by fusing the features extracted from the de-noised signals. The compressed AE features are then used for fault detection based on a statistical method.

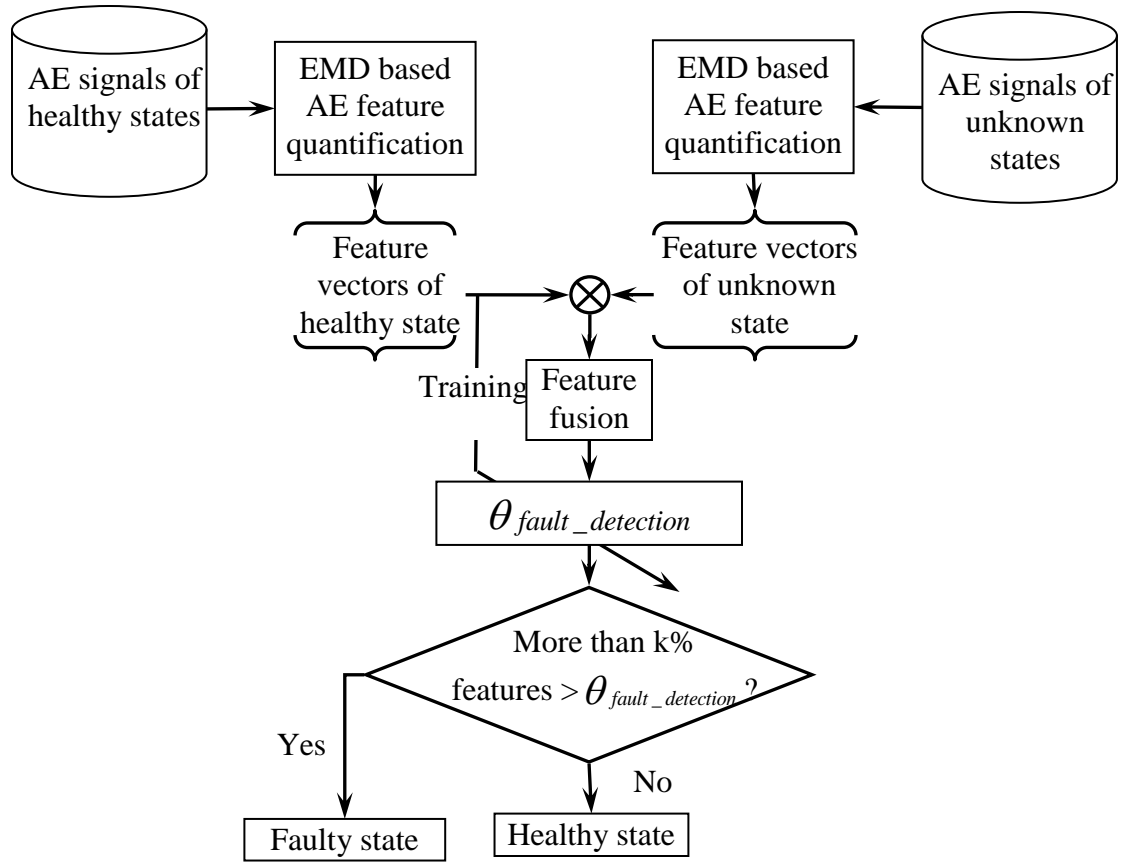


Figure 91. The framework of the EMD based AE quantification methodology for rotating machine fault detection methodology

As shown in Figure 91, the AE based fault detection methodology consists of two major parts: EMD based AE feature quantification and statistical analysis based fault detection. These two major components of the methodology are explained in the next sections.

5.6.1 The EMD Based AE Feature Quantification

As shown in Figure 91, AE bursts from both healthy and faulty systems are collected and then decomposed into the IMF components by the EMD method. A threshold based technique similar to wavelet de-noising method reported in [131] is applied to every IMF components. In general, a de-nosing threshold can be setup using four methods:

- (1) the universal threshold,
- (2) adaptive threshold selection based on principle of Stein's unbiased risk estimate,
- (3) heuristic threshold selection,
- (4) mini maxi threshold.

According to [131], universal threshold can achieve a noise-free reconstruction. In real time applications, one more advantage of using the universal threshold is that the threshold only needs to be calculated once for each AE signal. For computing the threshold of a group of AE burst type signals, using a universal threshold can save a huge amount of time and is more efficient in real time applications. Therefore a universal threshold is applied in this dissertation. The universal threshold is computed by using the first IMF component, which is the finest component among all the IMF components. The soft-thresholding based de-noising rule as described in [131] is used in the developed methodology as Eq. (55):

$$y_s = \begin{cases} y - t, & y > t \\ 0 & |y| < t \\ y + t, & y < -t \end{cases} \quad (55)$$

where: y_s represents a de-noised IMF component, y the IMF component before de-noising, $t = \hat{\sigma}\sqrt{2\log N}$ the de-noising threshold, $\hat{\sigma}$ the estimation of the standard deviation (STD) of the noise, N the length of y . In this research, the de-nosing threshold t in Eq. (55) is computed using the first IMF component.

According to [176], the standard deviation of the noise can be estimated by using the robust median estimator. In analyzing the burst type AE signals, one can observe that the AE bursts are symmetric around 0 and there are no extreme values. In this case, the mean value will be close to the median value. In practical applications, the calculation of mean is easier than that of median, since the calculation of median involves additional sorting. To reduce the computational complexity, one can use mean deviation instead of median absolute deviation to estimate the standard deviation of the noise. The standard deviation of the noise can be expressed as Eq. (56):

$$\hat{\sigma} = \frac{1}{0.6745 \times N} \sum_{n=0}^N |y_1(n) - \bar{y}_1| \quad (56)$$

where: y_1 is the first IMF component with N sampling points and \bar{y}_1 is the mean of y_1 .

Since for burst type AE signals, the mean of the sampled signals is very close to 0, Eq. (56) can be expressed as Eq. (57):

$$\hat{\sigma} = \frac{1}{0.6745 \times N} \sum_{n=0}^N |y_1(n)| \quad (57)$$

After the threshold-based de-noising, the de-noised IMF components are reconstructed to form a new signal by simply adding these de-noised IMF components together. Six AE parameters are extracted from the reconstructed signals as the fault features: (1) *ring-down count* (2) *duration* (3) *peak amplitude* (4) *rise time* (5) *RMS* (6) *crestfactor*. The definition of these features can be found in section 5.4 of Chapter 5.

After the 6 features are extracted, they are compressed into a single feature by calculating the Mahalanobis distance between the calculated AE features and the AE features of the healthy state. The compressed AE feature CF is defined as:

$$CF = \sqrt{(x - \mu)^T S^{-1} (x - \mu)} \quad (58)$$

where, x is a multivariate vector $x = (x_1, x_2, x_3, \dots, x_N)^T$ from a group of values with mean $\mu = (\mu_1, \mu_2, \mu_3, \dots, \mu_N)^T$ and S is the covariance matrix. The compressed feature could be used for fault detection.

5.6.2 The Statistical Analysis Based Fault Detection

To detect the fault, detection criteria should be developed based on the compressed feature. As the compressed feature measures the Mahalanobis distance from AE features of the healthy state, a damaged state will have a larger compressed feature value than that of the healthy state. Therefore, we can choose a detection criterion such that if a certain percentage of the data whose compressed features are greater than a fault detection

threshold then we can say there is a fault. In fact, this detection criterion can be established based on statistical analysis as following.

Since the distribution of the compressed feature cannot guarantee to be a normal distribution, Chebyshev's inequality can be used for any unknown distribution. Theoretical parts on how to use the Chebyshev's inequality to establish a fault detection threshold value is discussed in the Chapter 4 and will not discuss in this section again. Here the desired false alarm rate is set as 0.05, then the fault detection threshold can be computed as:

$$\theta_{fault_detection} = \frac{1}{N} \sum_{i=1}^N CF(i) + 4.4721 \sqrt{\frac{1}{N-1} \left[\sum_{i=1}^N \left(CF(i) - \frac{1}{N} \sum_{i=1}^N CF(i) \right)^2 \right]} \quad (59)$$

5.6.3 Gear Seeded Fault Case Study Results

AE burst type signals were collected from both the healthy gearbox and damaged gearbox under 3 different loading conditions: 0% loading, 50% loading and 100% loading, and were processed by using EMD. Even though the AE signals were collected from two AE sensors during the tests, only the AE signals from the nearest AE sensor to the faulty gear were used for analysis purpose. For demonstration, the first four IMF components of the decomposition of the healthy gearbox and the damaged gearbox under 0% loading condition are shown in Figure 92 and Figure 93, respectively.

Note that in both Figure 92 and Figure 93, the red lines are the universal de-nosing threshold computed based on the first IMF component.

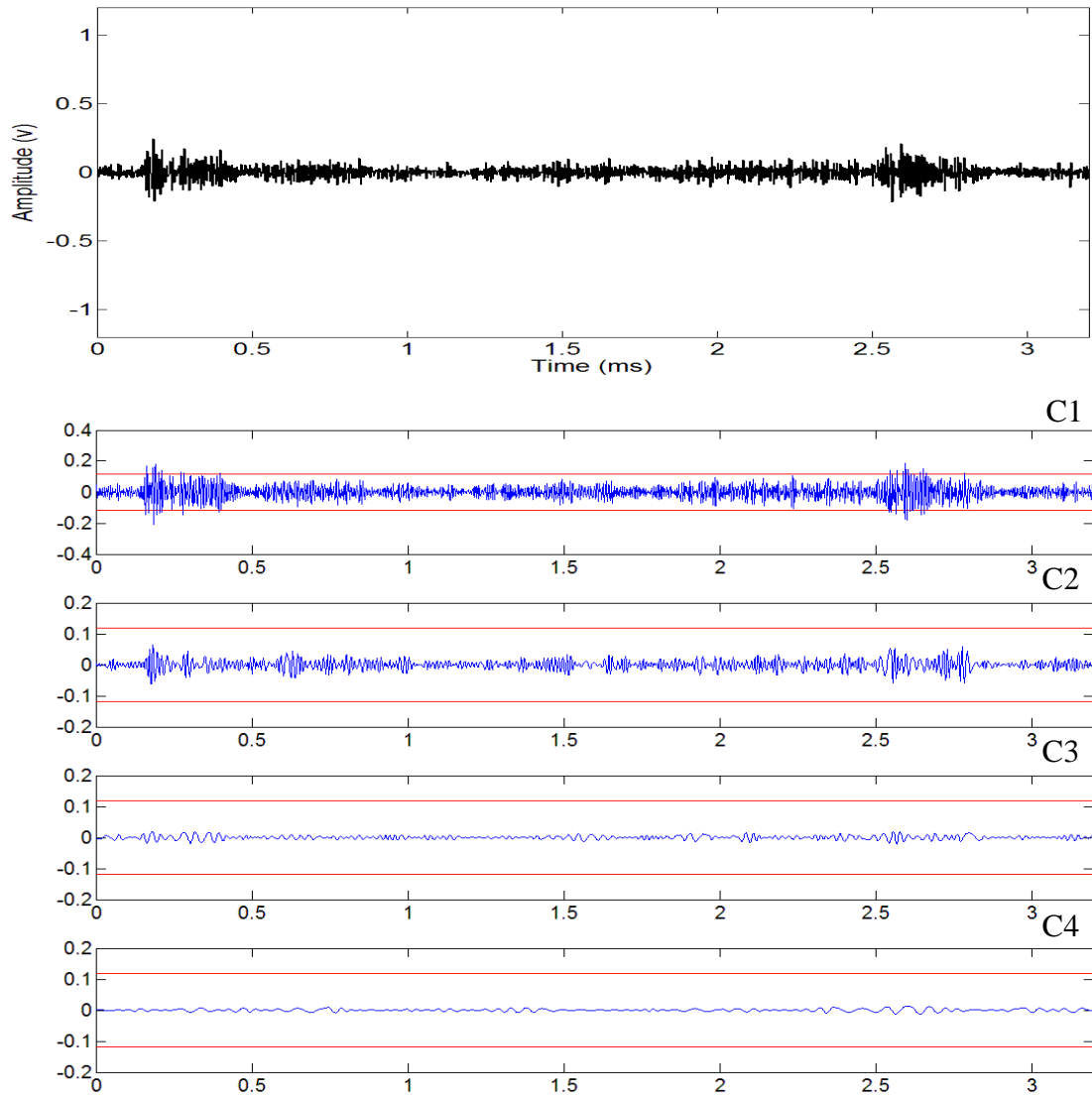


Figure 92. The first four IMF components of the healthy gearbox under 0% loading condition

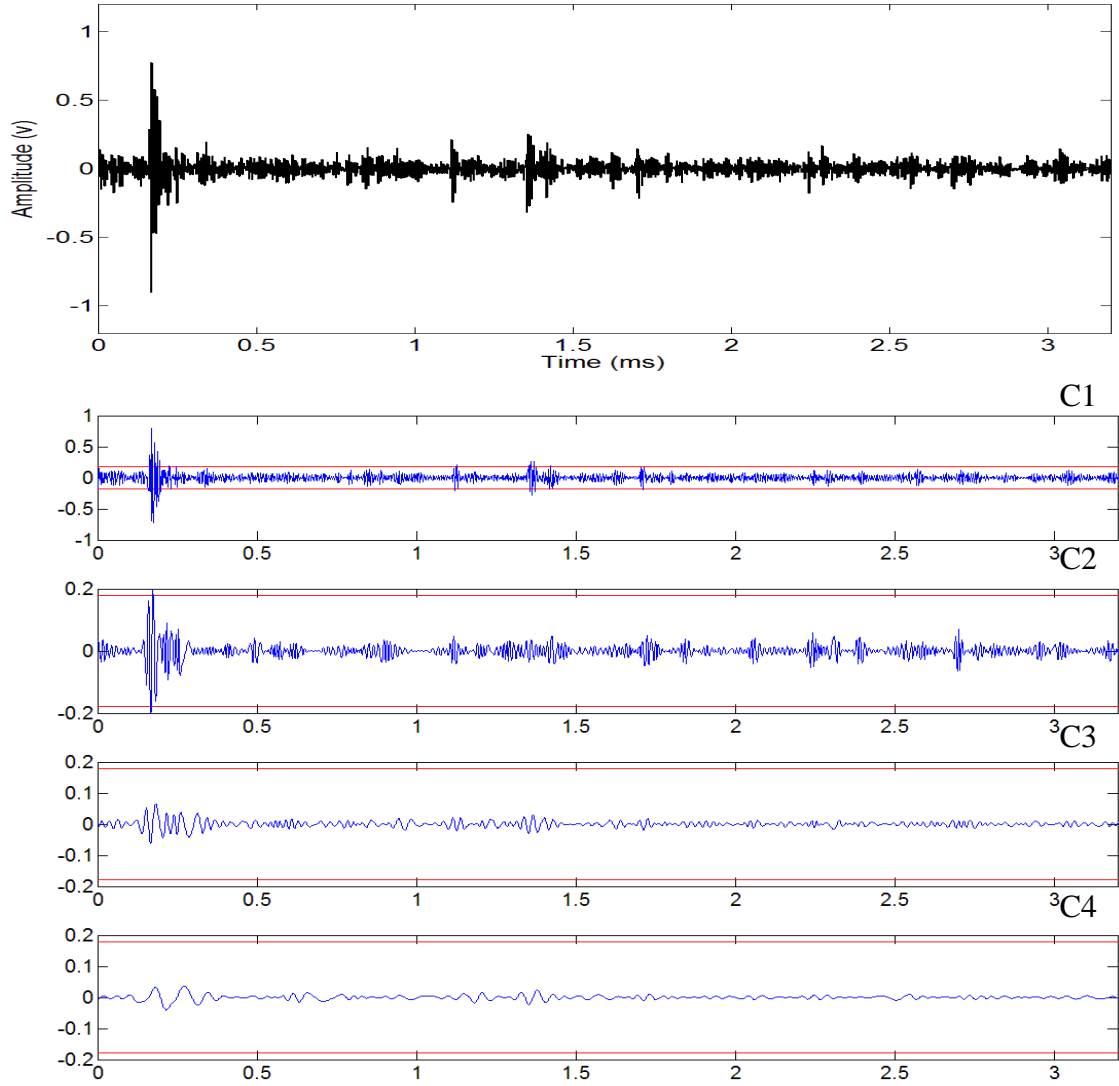


Figure 93. The first four IMF components of the damaged gearbox under 0% loading condition

After the decomposition, the soft-threshold based de-noising technique was applied and the de-noised signal was obtained as shown in Figure 94 and Figure 95, respectively.

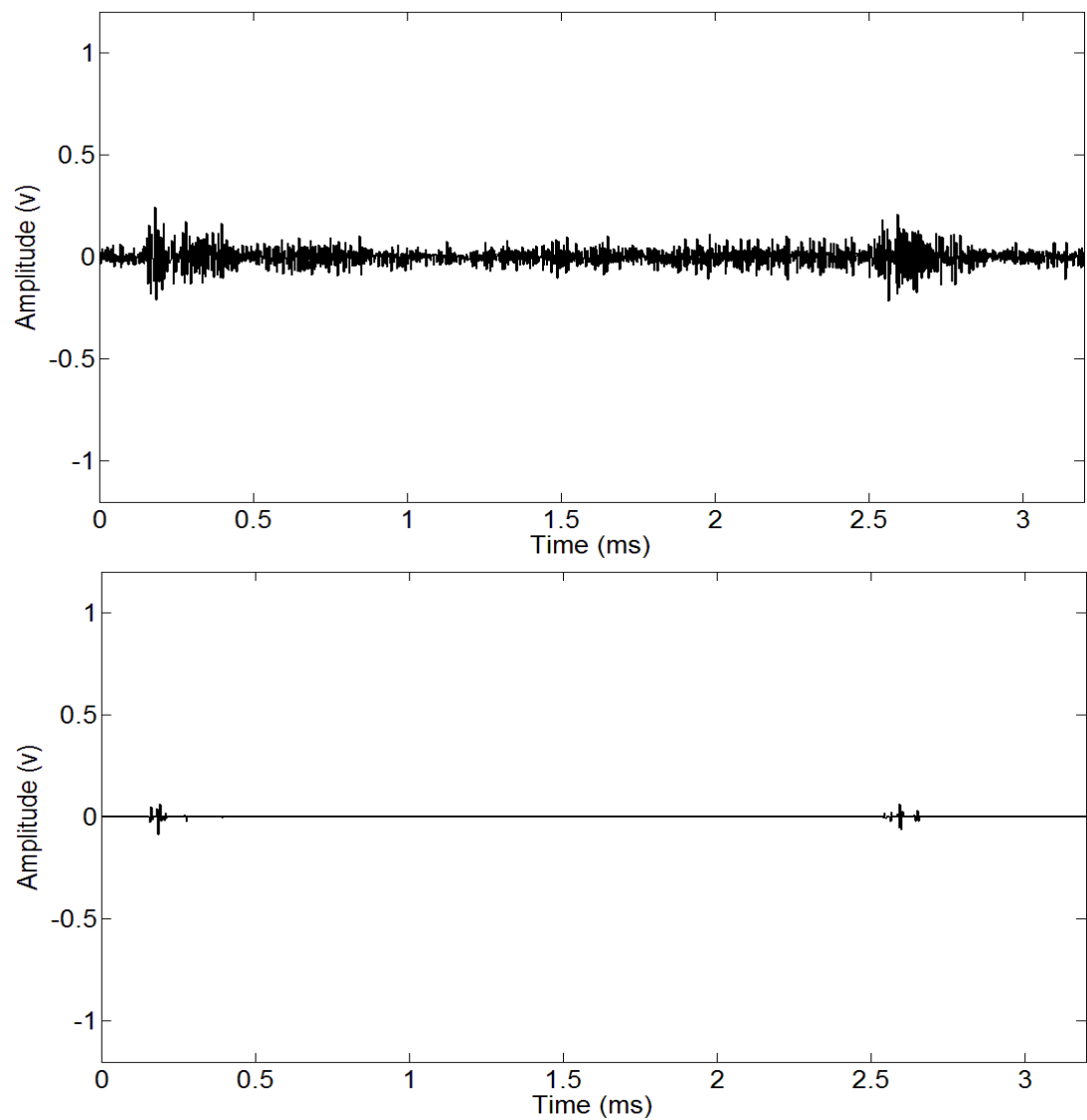


Figure 94. The de-noised signal of the healthy gearbox by using Hilbert-Huang transform under 0% loading condition

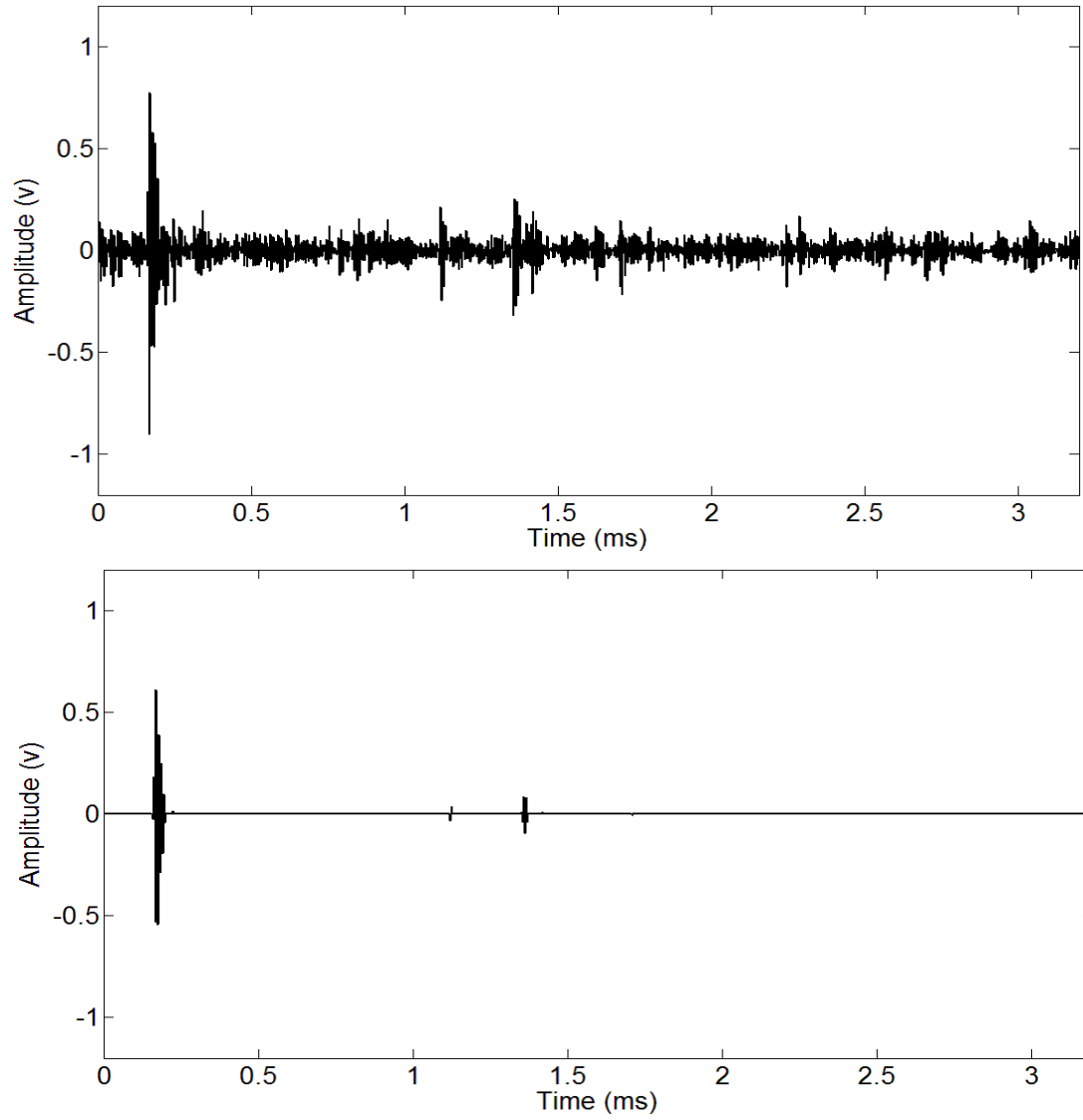


Figure 95. The de-noised signal of the damaged gearbox by using Hilbert-Huang transform under 0% loading condition

During the experiments, the rotational speed of the input shaft was controlled to be constant at 60Hz. Totally, one thousand AE signals collected from the healthy gearbox

and damaged gearbox under three different loading conditions were processed and after the reconstruction, six AE traditional features were calculated as shown in Table XXIII.

Table XXIII. The AE features of both healthy gearbox and damaged gearbox

Loading Condition	Gearbox State		RMS	Crest Factor	Peak Value	Count	Duration	Rise Time
0% Loading Condition	Healthy	Mean	0.0028	37.82	0.19	0.19	0.0000003	0.001
		Std	0.0022	6.92	0.08	0.55	0.000002	0.012
	Damaged	Mean	0.019	37.42	0.68	3.44	0.0007	0.31
		Std	0.015	6.18	0.57	2.87	0.0009	0.68
50% Loading Condition	Healthy	Mean	0.0053	35.36	0.18	0.81	0.00002	0.004
		Std	0.004	6.34	0.14	1.46	0.00001	0.014
	Damaged	Mean	0.027	33.10	0.90	6.10	0.012	0.36
		Std	0.014	4.99	0.49	3.02	0.001	0.73
100% Loading Condition	Healthy	Mean	0.004	35.34	0.14	0.38	0.00002	0.0024
		Std	0.0031	6.54	0.10	0.85	0.0002	0.014
	Damaged	Mean	0.04	28.55	1.05	12.36	0.0002	0.025
		Std	0.023	4.69	0.78	6.95	0.0002	0.039

The compressed features of both healthy and damaged gearboxes under 0% loading, 50% loading, and 100% loading are shown in Figure 96, Figure 97, and Figure 98, respectively. The thresholds for gear fault detection under 0% loading condition, 50% loading condition and 100% loading condition were calculated as: 17.92, 23.70, and 27.01, respectively. We can see that for 0% loading condition, only 0.3% of the feature points of the healthy gearbox are greater than the threshold, while 87.64% of the feature points of the damaged gearbox are greater than the threshold. For 50% loading condition, only 0.6% of the feature points of the healthy gearbox are greater than the threshold, while 92.48% of the feature points of the damaged gearbox are greater than the threshold. For 100% loading condition, only 0.3% of the feature points of the healthy gearbox are greater than the threshold, while 94.36% of the feature points of the damaged gearbox are greater than the threshold. These results clearly indicate that the developed methodology is effective in detecting the gear fault.

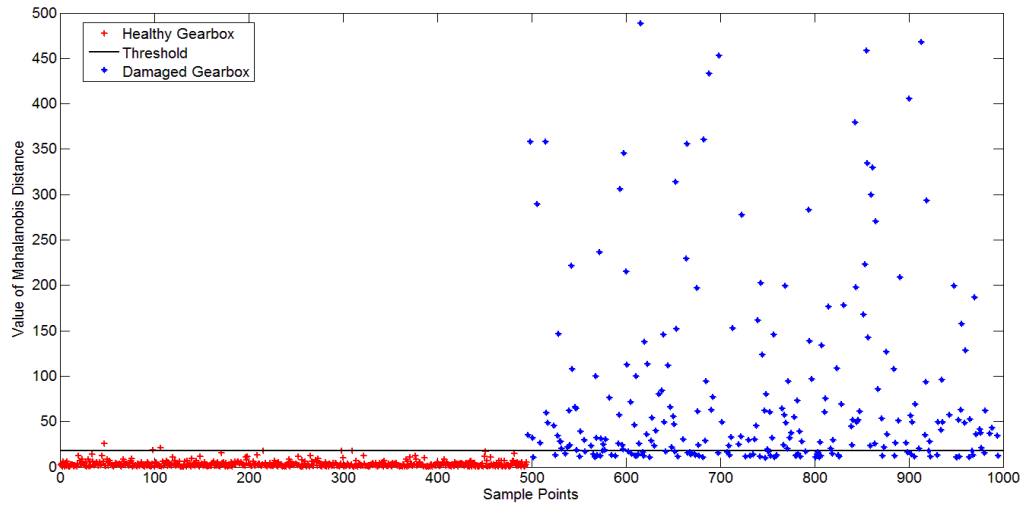


Figure 96. The compressed AE features for healthy and damaged gearbox under 0% loading condition

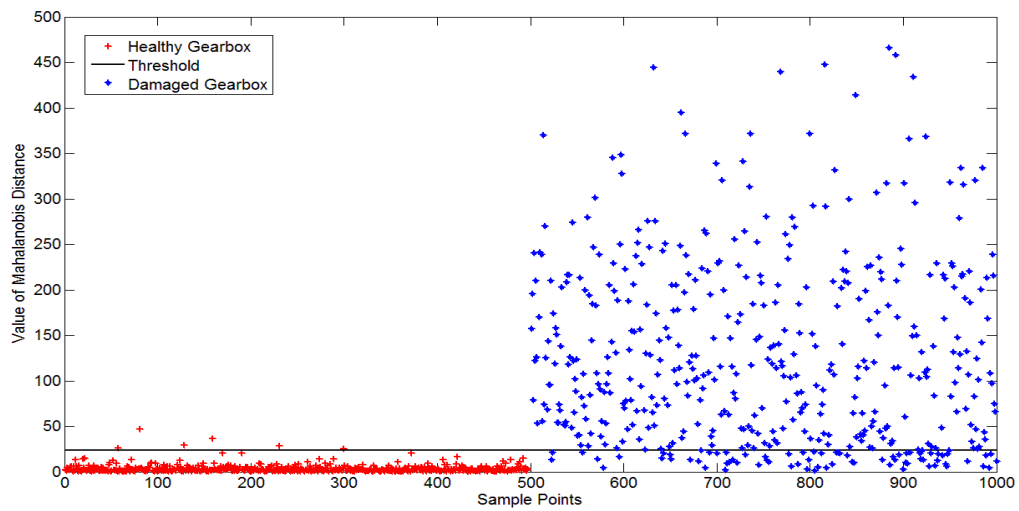


Figure 97. The compressed AE features for healthy and damaged gearbox under 50% loading condition

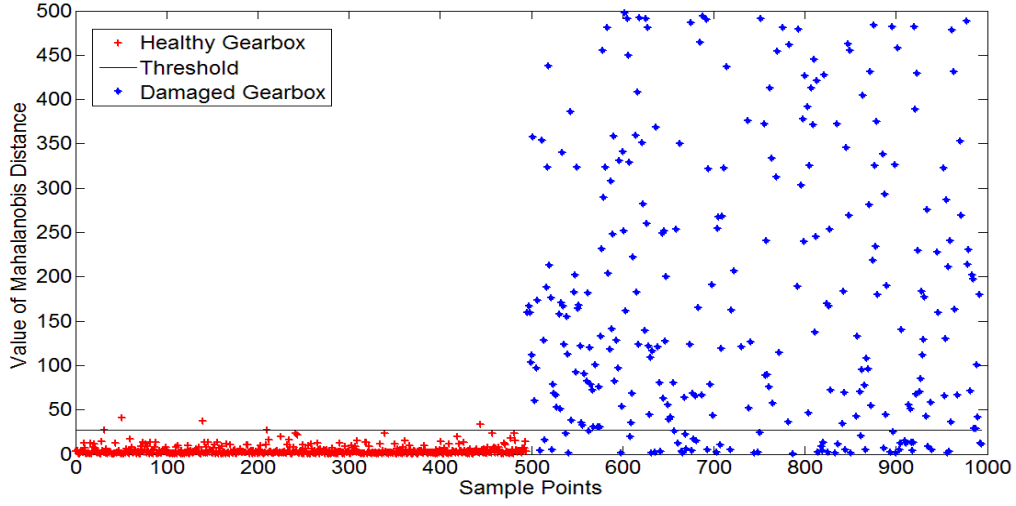


Figure 98. The compressed AE features for healthy and damaged gearbox under 100% loading condition

In order to compare the gear fault detection performance comparison of the compressed AE features with the existing EMD based AE features reported in the literature, the energy ratios of the IMF components as computed in [169, 170], were extracted. According to [169, 170], the energy of a signal $s(t)$ of size L is defined as:

$$Energy = \sum_{t=1}^L s(t)^2 \quad (60)$$

And the energy ratio for i^{th} IMF component y_i of signal $s(t)$ is calculated as:

$$Energy\ ratio(i) = \frac{\sum_{i=1}^L y_i^2}{Energy} \quad (61)$$

The AE bursts were first processed to obtain the IMF components and the energy ratios were computed using the first four IMF components for further calculation. The energy ratios for other IMF components were not calculated because the signals were too weak. Totally, 1000 AE bursts collected from both the healthy gearbox and the damaged gearbox under 3 different loading conditions were processed and the energy ratio means and the standard deviations of the first four IMF components are shown in Table XXIV.

Table XXIV. The energy ratio means and the standard deviations of the first four IMF components of both healthy gearbox and damaged gearbox

Loading Condition	Gearbox State		IMF1	IMF2	IMF3	IMF4
0% Loading Condition	Healthy	Mean	0.95	0.01	0.017	0.009
		Std	0.024	0.016	0.003	0.0025
	Damaged	Mean	0.99	0.12	0.02	0.01
		Std	0.04	0.04	0.009	0.006
50% Loading Condition	Healthy	Mean	0.95	0.097	0.02	0.008
		Std	0.025	0.017	0.003	0.002
	Damaged	Mean	0.94	0.14	0.02	0.001
		Std	0.03	0.02	0.005	0.003
100% Loading Condition	Healthy	Mean	0.94	0.10	0.017	0.0085
		Std	0.024	0.017	0.0031	0.002
	Damaged	Mean	0.95	0.12	0.02	0.009
		Std	0.04	0.03	0.0055	0.008

The energy ratios of the IMF components of gearbox running under 0% loading, 50% loading, and 100% loading were used as the feature vectors to compute the compressed feature as shown in Figure 99, Figure 100, and Figure 101. We can see that for 0% loading condition, only 0.5% of the feature points of the healthy gearbox are greater than

the threshold, while 62.67% of the feature points of the damaged gearbox are greater than the threshold. For 50% loading condition, only 0.2% of the feature points of the healthy gearbox are greater than the threshold, while 69.82% of the feature points of the damaged gearbox are greater than the threshold. For 100% loading condition, only 0.4% of the feature points of the healthy gearbox are greater than the threshold, while 66.83% of the feature points of the damaged gearbox are greater than the threshold. These results indicate that the compressed features computed using existing EMD based approaches are effective in detecting the gear fault. However, by examining the percentage of the compressed features of the damaged gearbox that were greater than the threshold as shown in Table XXV , we can see that the AE features extracted using the method presented in this paper gave more weights towards making the correct fault detection decision than the feature vectors extracted using the methods presented in [169, 170]. The results show that the AE features extracted using the proposed method are more sensitive to the gear fault than those by the existing EMD based AE feature extraction methods.

Table XXV. Comparison of % compressed fault features that are greater than the fault detection threshold

Loading Condition		0%	50%	100%
% Compressed fault features that are greater than the fault detection threshold	Compressed AE features in this paper	87.34	91.88	94.06
	Compressed AE features presented in [169, 170]	62.16	69.62	66.43

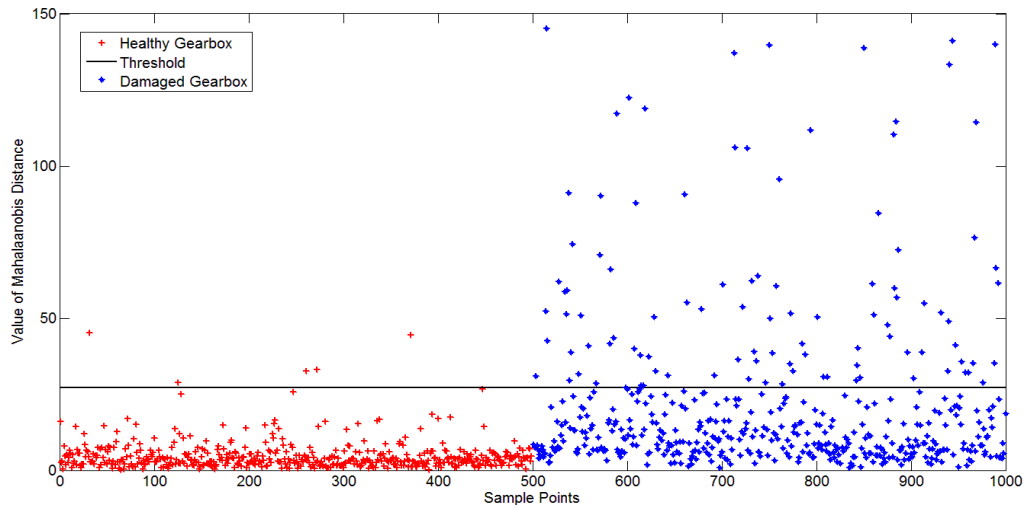


Figure 99. The compressed AE features calculated by using the energy ratio of the IMF components for healthy and damaged gearbox under 0% loading condition

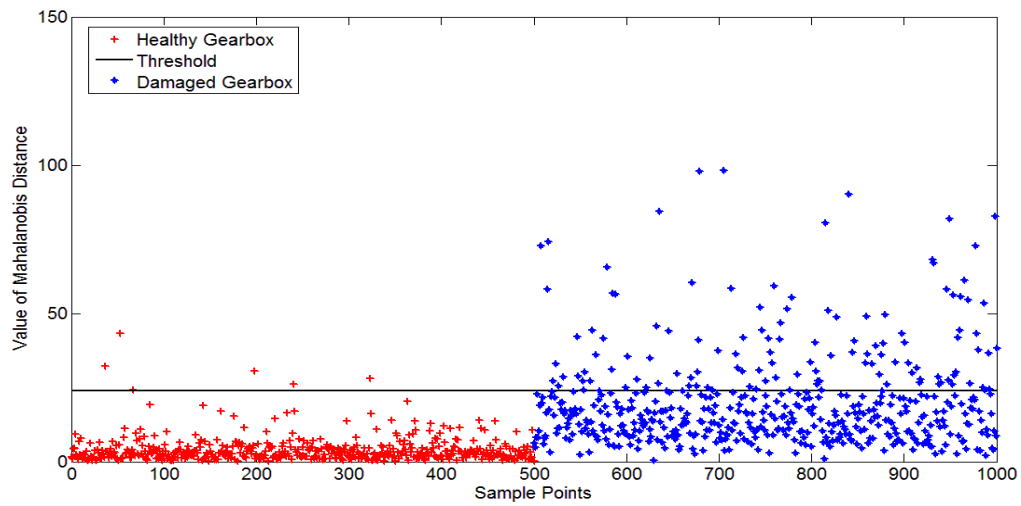


Figure 100. The compressed AE features calculated by using the energy ratio of the IMF components for healthy and damaged gearbox under 50% loading condition

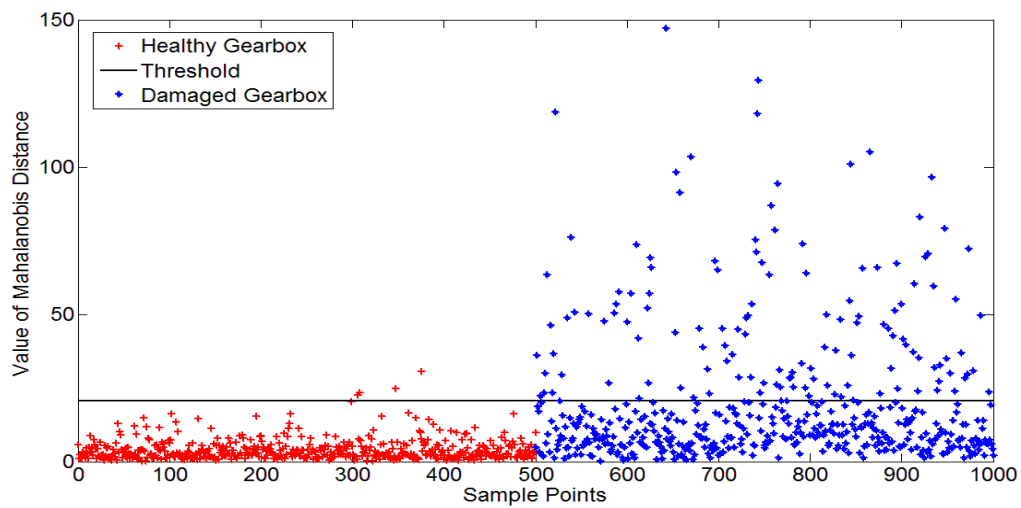


Figure 101. The compressed AE features calculated by using the energy ratio of the IMF components for healthy and damaged gearbox under 100% loading condition

6 CONCLUSIONS

This dissertation has provided a literature review on rotating machinery fault detection and diagnostics. The design and development of a notional split torque gearbox type gearbox test rig was presented. The theoretic basis and the development of both vibration signal and acoustic emission signal based methodologies for rotating machinery fault detection and diagnostics have been presented. The effectiveness of the developed methodologies was validated by using the gear seeded faults on the developed STG type gearbox test rig and the real bearing seeded faults on a bearing run-to-failure test rig.

The contributions of this research are summarized as follows:

- (1) An EMD based vibration feature and condition indicator extraction methodology for rotating machinery fault detection and diagnosis has been developed.
- (2) A two-step vibration signal based bearing fault diagnostics methodology for plastic bearings has been developed.
- (3) A vibration signal based gear fault detection system based on interference cancellation has been proposed.
- (4) A Laplace wavelet based acoustic emission signal quantification methodology for rotating machinery fault detection and diagnostics has been developed.
- (5) An EMD based acoustic emission quantification methodology has been developed.
- (6) A notional split-torque gearbox test rig has been designed and developed.

- (7) Experiments have been designed and implemented on the custom designed notional STG test rig and bearing run-to-failure test rig. Both vibration and acoustic emission signals have been collected during the experiments. The effectiveness of the developed methodologies has been validated by the bearing and gear seeded fault test data.

Future research includes:

- (1) Further work should be conducted on investigation of the effectiveness of the developed methodologies by using the real data from the real life applications.
- (2) In this research, only constant operation condition was applied. In real applications the operation conditions, such as, speeds, loading, and so on, are fluctuating. Therefore, further research should be conducted on the developed methodology under dynamic operation conditions.

CITED LITERATURE

- [1] Jardine, A. K. S., Lin, D., and Banjevic, D.: A review on machinery diagnostics and prognostics implementing condition-based maintenance, *Mechanical Systems and Signal Processing*, vol. 20, pp. 1483-1510, 2006.
- [2] Holroyd, T.: *Acoustic emission & ultrasonics monitoring handbook*. Oxford, UK: Coxmoor Publishing Company, 2000.
- [3] CoorsTek, I. *Plastic bearings & bushings*. Available: http://www.coorstek.com/products/plastic_bearings.asp, 2011.
- [4] KMS Bearings, I. *Applications for plastic ball bearings*. Available: http://www.kmsbearings.com/pbb_appl.htm, 2011.
- [5] Cox, H. *Plastic and Food Safe Bearings*. Available: <http://ezinearticles.com/?Plastic-and-Food-Safe-Bearings&id=2084640>, 2011.
- [6] Jalan, A. K. and Mohanty, A.: Model based fault diagnosis of a rotor-bearing system for misalignment and unbalance under steady-state condition, *Journal of Sound and Vibration*, vol. 327, pp. 604-622, 2009.
- [7] Loparo, K. A., Adams, M., Lin, W., Abdel-Magied, M. F., and Afshari, N.: Fault detection and diagnosis of rotating machinery, *IEEE Transactions on Industrial Electronics*, vol. 47, pp. 1005-1014, 2002.
- [8] Bangura, J. and Demerdash, N.: Diagnosis and characterization of effects of broken bars and connectors in squirrel-cage induction motors by a time-stepping coupled finite element-state space modeling approach, *IEEE Transactions on Energy Conversion*, vol. 14, pp. 1167-1176, 1999.
- [9] Isermann, R. and Balle, P.: Trends in the application of model-based fault detection and diagnosis of technical processes, *Control Engineering Practice*, vol. 5, pp. 709-719, 1997.

- [10] Isermann, R.: Model-based fault-detection and diagnosis-status and applications, *Annual Reviews in control*, vol. 29, pp. 71-85, 2005.
- [11] Kim, C. E., Jung, Y. B., Yoon, S. B., and Im, D. H.: The fault diagnosis of rotor bars in squirrel cage induction motors by time-stepping finite element method, *IEEE Transactions on Magnetics*, vol. 33, pp. 2131-2134, 1997.
- [12] Fiser, R. and Ferkolj, S.: Application of a finite element method to predict damaged induction motor performance, *IEEE Transactions on Magnetics*, vol. 37, pp. 3635-3639, 2001.
- [13] Howard, I., Jia, S., and Wang, J.: The dynamic modelling of a spur gear in mesh including friction and a crack, *Mechanical Systems and Signal Processing*, vol. 15, pp. 831-853, 2001.
- [14] Dong, H., Chen, X., Li, B., Qi, K., and He, Z.: Rotor crack detection based on high-precision modal parameter identification method and wavelet finite element model, *Mechanical Systems and Signal Processing*, vol. 23, pp. 869-883, 2009.
- [15] Sekhar, A.: Model-based identification of two cracks in a rotor system, *Mechanical Systems and Signal Processing*, vol. 18, pp. 977-983, 2004.
- [16] Paya, B., Esat, I., and Badi, M.: Artificial neural network based fault diagnostics of rotating machinery using wavelet transforms as a preprocessor, *Mechanical Systems and Signal Processing*, vol. 11, pp. 751-765, 1997.
- [17] Tse, P. and Atherton, D.: Prediction of machine deterioration using vibration based fault trends and recurrent neural networks, *Journal of vibration and Acoustics*, vol. 121, p. 355, 1999.
- [18] Sanz, J., Perera, R., and Huerta, C.: Fault diagnosis of rotating machinery based on auto-associative neural networks and wavelet transforms, *Journal of Sound and Vibration*, vol. 302, pp. 981-999, 2007.

- [19] Huang, R., Xi, L., Li, X., Richard Liu, C., Qiu, H., and Lee, J.: Residual life predictions for ball bearings based on self-organizing map and back propagation neural network methods, *Mechanical Systems and Signal Processing*, vol. 21, pp. 193-207, 2007.
- [20] Wu, S. and Chow, T. W. S.: Induction machine fault detection using SOM-based RBF neural networks, *Industrial Electronics, IEEE Transactions on*, vol. 51, pp. 183-194, 2004.
- [21] Yang, D. M., Stronach, A., MacConnell, P., and Penman, J.: Third-order spectral techniques for the diagnosis of motor bearing condition using artificial neural networks, *Mechanical Systems and Signal Processing*, vol. 16, pp. 391-411, 2002.
- [22] Li, B., Chow, M. Y., Tipsuwan, Y., and Hung, J. C.: Neural-network-based motor rolling bearing fault diagnosis, *IEEE Transactions on Industrial Electronics*, vol. 47, pp. 1060-1069, 2000.
- [23] Vyas, N. S. and Satishkumar, D.: Artificial neural network design for fault identification in a rotor-bearing system, *Mechanism and machine theory*, vol. 36, pp. 157-175, 2001.
- [24] Jack, L. and Nandi, A.: Fault detection using support vector machines and artificial neural networks, augmented by genetic algorithms, *Mechanical Systems and Signal Processing*, vol. 16, pp. 373-390, 2002.
- [25] Li, R. and He, D.: Rotational Machine Health Monitoring and Fault Detection Using EMD Based Acoustic Emission Feature Quantification, *IEEE Transactions on Instrumentation and Measurement*, (Accepted), 2011.
- [26] David, H., Ruoyu, L., Zade, M., and Junda, Z.: A data mining based full ceramic bearing fault diagnostic system using AE sensors, *IEEE Transactions on Neural Networks*, (Accepted), 2011.
- [27] Lou, X. and Loparo, K. A.: Bearing fault diagnosis based on wavelet transform and fuzzy inference, *Mechanical Systems and Signal Processing*, vol. 18, pp. 1077-1095, 2004.

- [28] Sugumaran, V., Muralidharan, V., and Ramachandran, K.: Feature selection using decision tree and classification through proximal support vector machine for fault diagnostics of roller bearing, *Mechanical Systems and Signal Processing*, vol. 21, pp. 930-942, 2007.
- [29] Ballal, M. S., Khan, Z. J., Suryawanshi, H. M., and Sonolikar, R. L.: Adaptive neural fuzzy inference system for the detection of inter-turn insulation and bearing wear faults in induction motor, *IEEE Transactions on Industrial Electronics*, vol. 54, pp. 250-258, 2007.
- [30] Dempsey, P.: Gear damage detection using oil debris analysis, *NASA Technical Memorandum 210936*, pp. 1-15, 2001.
- [31] Peng, Z., Kessissoglou, N., and Cox, M.: A study of the effect of contaminant particles in lubricants using wear debris and vibration condition monitoring techniques, *Wear*, vol. 258, pp. 1651-1662, 2005.
- [32] Dempsey, P.: Gear damage detection using oil debris analysis, *Gear Technology*, vol. 20, pp. 12-17, 2003.
- [33] Yan, X., Zhao, C., Lu, Z., Zhou, X., and Xiao, H.: A study of information technology used in oil monitoring, *Tribology International*, vol. 38, pp. 879-886, 2005.
- [34] Dempsey, P. J., Kreider, G., and Fichter, T.: Investigation of tapered roller bearing damage detection using oil debris analysis, in *IEEE Aerospace Conference*, Big Sky, Montana, March 4 - 11, 2006
- [35] Dempsey, P. and Afjeh, A.: Integrating oil debris and vibration gear damage detection technologies using fuzzy logic, *Journal of the American Helicopter Society*, vol. 49, pp. 109-116, 2004.
- [36] Toliyat, H. A. and Lipo, T. A.: Transient analysis of cage induction machines under stator, rotor bar and end ring faults, *IEEE Transactions on Energy Conversion*, vol. 10, pp. 241-247, 1995.

- [37] Schoen, R. R., Lin, B. K., Habetler, T. G., Schlag, J. H., and Farag, S.: An unsupervised, on-line system for induction motor fault detection using stator current monitoring, *Industry Applications, IEEE Transactions on*, vol. 31, pp. 1280-1286, 1995.
- [38] Douglas, H., Pillay, P., and Ziarani, A. K.: A new algorithm for transient motor current signature analysis using wavelets, *IEEE Transactions on Industry Applications*, vol. 40, pp. 1361-1368, 2004.
- [39] Ye, Z., Wu, B., and Sadeghian, A.: Current signature analysis of induction motor mechanical faults by wavelet packet decomposition, *IEEE Transactions on Industrial Electronics*, vol. 50, pp. 1217-1228, 2003.
- [40] Bellini, A., Filippetti, F., Franceschini, G., Tassoni, C., and Kliman, G. B.: Quantitative evaluation of induction motor broken bars by means of electrical signature analysis, *IEEE Transactions on Industry Applications*, vol. 37, pp. 1248-1255, 2001.
- [41] Blodt, M., Granjon, P., Raison, B., and Rostaing, G.: Models for bearing damage detection in induction motors using stator current monitoring, *IEEE Transactions on Industrial Electronics*, vol. 55, pp. 1813-1822, 2008.
- [42] Zhou, W., Habetler, T. G., and Harley, R. G.: Bearing fault detection via stator current noise cancellation and statistical control, *IEEE Transactions on Industrial Electronics*, vol. 55, pp. 4260-4269, 2008.
- [43] Ibrahim, A., El Badaoui, M., Guillet, F., and Bonnardot, F.: A new bearing fault detection method in induction machines based on instantaneous power factor, *IEEE Transactions on Industrial Electronics*, vol. 55, pp. 4252-4259, 2008.
- [44] Immovilli, F., Cocconcelli, M., Bellini, A., and Rubini, R.: Detection of generalized-roughness bearing fault by spectral-kurtosis energy of vibration or current signals, *IEEE Transactions on Industrial Electronics*, vol. 56, pp. 4710-4717, 2009.

- [45] Trajin, B., Regnier, J., and Faucher, J.: Comparison between stator current and estimated mechanical speed for the detection of bearing wear in asynchronous drives, *IEEE Transactions on Industrial Electronics*, vol. 56, pp. 4700-4709, 2009.
- [46] Akin, B., Orguner, U., Choi, S., and Toliyat, A.: A simple real-time fault signature monitoring tool for motor drive embedded fault diagnosis systems, *IEEE Transactions on Industrial Electronics*, vol. 58, pp. 1-1, 2011.
- [47] Akin, B., Orguner, U., Toliyat, H. A., and Rayner, M.: Phase-sensitive detection of motor fault signatures in the presence of noise, *IEEE Transactions on Industrial Electronics*, vol. 55, pp. 2539-2550, 2008.
- [48] Frosini, L. and Bassi, E.: Stator current and motor efficiency as indicators for different types of bearing faults in induction motors, *IEEE Transactions on Industrial Electronics*, vol. 57, pp. 244-251, 2010.
- [49] Kar, C. and Mohanty, A.: Monitoring gear vibrations through motor current signature analysis and wavelet transform, *Mechanical Systems and Signal Processing*, vol. 20, pp. 158-187, 2006.
- [50] Bellini, A., Filippetti, F., Tassoni, C., and Capolino, G.: Advances in diagnostic techniques for induction machines, *IEEE Transactions on Industrial Electronics*, vol. 55, pp. 4109-4126, 2008.
- [51] El Hachemi Benbouzid, M.: A review of induction motors signature analysis as a medium for faults detection, *IEEE Transactions on Industrial Electronics*, vol. 47, pp. 984-993, 2000.
- [52] Braun, S. and Braun, S. G.: *Mechanical signature analysis: theory and applications*. Burlington, Massachusetts, USA: Academic Press, 1986.
- [53] Randall, R. B. and Antoni, J.: Rolling element bearing diagnostics--A tutorial, *Mechanical Systems and Signal Processing*, vol. 25, pp. 485-520, 2011.

- [54] Samuel, P. and Pines, D.: A review of vibration-based techniques for helicopter transmission diagnostics, *Journal of Sound and Vibration*, vol. 282, pp. 475-508, 2005.
- [55] Al-Dossary, S., Hamzah, R., and Mba, D.: Observations of changes in acoustic emission waveform for varying seeded defect sizes in a rolling element bearing, *Applied Acoustics*, vol. 70, pp. 58-81, 2009.
- [56] Nivesrangsarn, P., Steel, J., and Reuben, R.: AE mapping of engines for spatially located time series, *Mechanical Systems and Signal Processing*, vol. 19, pp. 1034-1054, 2005.
- [57] Lee, D., Hwang, I., Valente, C., Oliveira, J., and Dornfeld, D.: Precision manufacturing process monitoring with acoustic emission, *International Journal of Machine Tools and Manufacture*, vol. 46, pp. 176-188, 2006.
- [58] Hanchi, J. and Klamecki, B.: Acoustic emission monitoring of the wear process, *Wear*, vol. 145, pp. 1-27, 1991.
- [59] Toutountzakis, T., Tan, C., and Mba, D.: Application of acoustic emission to seeded gear fault detection, *NDT & E International*, vol. 38, pp. 27-36, 2005.
- [60] Al-Ghamd, A. and Mba, D.: A comparative experimental study on the use of acoustic emission and vibration analysis for bearing defect identification and estimation of defect size, *Mechanical Systems and Signal Processing*, vol. 20, pp. 1537-1571, 2006.
- [61] Couturier, J. and Mba, D.: Operational bearing parameters and acoustic emission generation, *Journal of Vibration and Acoustics*, vol. 130, pp. 024502.1-024502.5, 2008.
- [62] He, Y., Yin, X., and Chu, F.: Modal analysis of rubbing acoustic emission for rotor-bearing system based on reassigned wavelet scalogram, *Journal of Vibration and Acoustics*, vol. 130, p. 061009, 2008.

- [63] Eftekharnjad, B. and Mba, D.: Seeded fault detection on helical gears with acoustic emission, *Applied Acoustics*, vol. 70, pp. 547-555, 2009.
- [64] Elforjani, M. and Mba, D.: Detecting natural crack initiation and growth in slow speed shafts with the acoustic emission technology, *Engineering Failure Analysis*, vol. 16, pp. 2121-2129, 2009.
- [65] Raja Hamzah, R. and Mba, D.: The influence of operating condition on acoustic emission (AE) generation during meshing of helical and spur gear, *Tribology International*, vol. 42, pp. 3-14, 2009.
- [66] Li, X.: A brief review: acoustic emission method for tool wear monitoring during turning, *International Journal of Machine Tools and Manufacture*, vol. 42, pp. 157-165, 2002.
- [67] Rashidi, M. and Krantz, T.: Dynamics of a split torque helicopter transmission, *NASA Technical Memorandum 105681*, pp. 1-14, 1992.
- [68] White, G.: Split torque transmission, US Patent, 1984.
- [69] Gmirya, Y.: Split torque gearbox for rotary wing aircraft with translational thrust system, *US Patents*, 6270038, 2005.
- [70] Bechhoefer, E., Li, R., and He, D.: Quantification of condition indicator performance on a split torque gearbox, *Journal of Intelligent Manufacturing (to appear)* <http://www.springerlink.com/content/p177840x16g1l412/> (on-line version), 2011.
- [71] White, G.: Design study of a split-torque helicopter transmission, *Proceedings of the Institution of Mechanical Engineers, Part G: Journal of Aerospace Engineering*, vol. 212, pp. 117-123, 1998.
- [72] Reeves, C. W.: *Machine & Systems Condition Monitoring Series: Vibration Monitoring Handbook*. Oxford UK, : Coxmoor Publishing Company, 1998.

- [73] PCB: Model 603C01 user Manual, 2002.
Available:
http://www.pcb.com/spec_sheet.asp?model=603C01&item_id=9275
- [74] Corp., P. A.: *Wideband Sensors*, 2011.
Available:
<http://www.pacndt.com/index.aspx?go=products&focus=/sensors/wideband.htm>.
- [75] Cooley, J. and Tukey, J.: An algorithm for the machine calculation of complex Fourier series, *Mathematics of computation*, vol. 19, pp. 297-301, 1965.
- [76] Braun, S. and Braun, S.: *Mechanical signature analysis: theory and applications*. London: Academic Press, 1986.
- [77] Swansson, N., Howard, I., and Forrester, B.: Fault detection and location in helicopter transmissions: trends in health and usage monitoring, in *Australian Aeronautical Conference*, Melbourne, Australia, 1989, p. 288.
- [78] Forrester, B., Use of the Wigner–Ville distribution in helicopter transmission fault detection, in *Proceedings of Australian Symposium on Signal Processing and Applications*, Adelaide, Australia, 1989, pp. 17–19.
- [79] Stewart, R.: Some useful data analysis techniques for gearbox diagnostics, *University of Southampton, Southampton, England*, 1977.
- [80] McFadden, P.: Examination of a technique for the early detection of failure in gears by signal processing of the time domain average of the meshing vibration, *Mechanical Systems and Signal Processing*, vol. 1, pp. 173-183, 1987.
- [81] McFadden, P.: A revised model for the extraction of periodic waveforms by time domain averaging, *Mechanical Systems and Signal Processing*, vol. 1, pp. 83-95, 1987.

- [82] McFadden, P.: Determining the location of a fatigue crack in a gear from the phase of the change in the meshing vibration, *Mechanical Systems and Signal Processing*, vol. 2, pp. 403-409, 1988.
- [83] Wang, W. and McFadden, P.: Decomposition of gear motion signals and its application to gearbox diagnostics, *Journal of vibration and Acoustics*, vol. 117, p. 363, 1995.
- [84] Houjoh, H., Ratanasumawong, C., and Matsumura, S.: Utilization of synchronous averaging for inspection of tooth surface undulations on gears, *Journal of Applied Mechanics*, vol. 74, pp. 269-273, 2007.
- [85] Stander, C., Heyns, P., and Schoombie, W.: Using vibration monitoring for local fault detection on gears operating under fluctuating load conditions, *Mechanical Systems and Signal Processing*, vol. 16, pp. 1005-1024, 2002.
- [86] McFadden, P.: Interpolation techniques for time domain averaging of gear vibration, *Mechanical Systems and Signal Processing*, vol. 3, pp. 87-97, 1989.
- [87] Wang, W. and Wong, A.: Autoregressive model-based gear fault diagnosis, *Journal of vibration and Acoustics*, vol. 124, pp. 172-179, 2002.
- [88] Kim, J., Udpa, L., and Udpa, S.: Multi-stage adaptive noise cancellation for ultrasonic NDE, *NDT & E International*, vol. 34, pp. 319-328, 2001.
- [89] Baydar, N. and Ball, A.: A comparative study of acoustic and vibration signals in detection of gear failures using Wigner-Ville distribution, *Mechanical Systems and Signal Processing*, vol. 15, pp. 1091-1107, 2001.
- [90] Kaewkongka, T., Joe, Y., Rakowski, R., and Jones, B.: A comparative study of short time Fourier transform and continuous wavelet transform for bearing condition monitoring, *International Journal of COMADEM*, vol. 6, pp. 41-48, 2003.
- [91] Griffin, D. and Lim, J.: Signal estimation from modified short-time Fourier transform, *IEEE Transactions on Acoustics, Speech and Signal Processing*, vol. 32, pp. 236-243, 1984.

- [92] Portnoff, M.: Time-frequency representation of digital signals and systems based on short-time Fourier analysis, *IEEE Transactions on Acoustics, Speech and Signal Processing*, vol. 28, pp. 55-69, 1980.
- [93] Kim, B., Lee, S., Lee, M., Ni, J., Song, J., and Lee, C.: A comparative study on damage detection in speed-up and coast-down process of grinding spindle-typed rotor-bearing system, *Journal of Materials Processing Technology*, vol. 187, pp. 30-36, 2007.
- [94] Staszewski, W., Worden, K., and Tomlinson, G.: Time-frequency analysis in gearbox fault detection using the Wigner-Ville distribution and pattern recognition, *Mechanical Systems and Signal Processing*, vol. 11, pp. 673-692, 1997.
- [95] Qian, S. and Chen, D.: Decomposition of the Wigner-Ville distribution and time-frequency distribution series, *IEEE Transactions on Signal Processing*, vol. 42, pp. 2836-2842, 1994.
- [96] Li, H., Zheng, H., and Tang, L.: Wigner-Ville distribution based on EMD for faults diagnosis of bearing, *Fuzzy Systems and Knowledge Discovery*, pp. 803-812, 2006.
- [97] Staszewski, W. and Tomlinson, G.: Application of the wavelet transform to fault detection in a spur gear, *Mechanical Systems and Signal Processing*, vol. 8, pp. 289-307, 1994.
- [98] Zheng, H., Li, Z., and Chen, X.: Gear fault diagnosis based on continuous wavelet transform, *Mechanical Systems and Signal Processing*, vol. 16, pp. 447-457, 2002.
- [99] Lin, J. and Qu, L.: Feature extraction based on Morlet wavelet and its application for mechanical fault diagnosis, *Journal of Sound and Vibration*, vol. 234, pp. 135-148, 2000.
- [100] Chow, T. and Hai, S.: Induction machine fault diagnostic analysis with wavelet technique, *IEEE Transactions on Industrial Electronics*, vol. 51, pp. 558-565, 2004.

- [101] Nikolaou, N. and Antoniadis, I.: Rolling element bearing fault diagnosis using wavelet packets, *NDT & E International*, vol. 35, pp. 197-205, 2002.
- [102] Sun, Q. and Tang, Y.: Singularity analysis using continuous wavelet transform for bearing fault diagnosis, *Mechanical Systems and Signal Processing*, vol. 16, pp. 1025-1041, 2002.
- [103] Baydar, N. and Ball, A.: Detection of gear failures via vibration and acoustic signals using wavelet transform, *Mechanical Systems and Signal Processing*, vol. 17, pp. 787-804, 2003.
- [104] Liu, B., Riemenschneider, S., and Xu, Y.: Gearbox fault diagnosis using empirical mode decomposition and Hilbert spectrum, *Mechanical Systems and Signal Processing*, vol. 20, pp. 718-734, 2006.
- [105] Yu, Y.: A roller bearing fault diagnosis method based on EMD energy entropy and ANN, *Journal of Sound and Vibration*, vol. 294, pp. 269-277, 2006.
- [106] Loutridis, S.: Damage detection in gear systems using empirical mode decomposition, *Engineering Structures*, vol. 26, pp. 1833-1841, 2004.
- [107] Cheng, J., Yu, D., Tang, J., and Yang, Y.: Application of frequency family separation method based upon EMD and local Hilbert energy spectrum method to gear fault diagnosis, *Mechanism and machine theory*, vol. 43, pp. 712-723, 2008.
- [108] Gao, Q., Duan, C., Fan, H., and Meng, Q.: Rotating machine fault diagnosis using empirical mode decomposition, *Mechanical Systems and Signal Processing*, vol. 22, pp. 1072-1081, 2008.
- [109] Wu, F. and Qu, L.: Diagnosis of subharmonic faults of large rotating machinery based on EMD, *Mechanical Systems and Signal Processing*, vol. 23, pp. 467-475, 2009.

- [110] Durak, L. and Arikan, O.: Short-time Fourier transform: two fundamental properties and an optimal implementation, *IEEE Transactions on Signal Processing*, vol. 51, pp. 1231-1242, 2003.
- [111] Wang, W. Q., Ismail, F., and Farid Golnaraghi, M.: Assessment of gear damage monitoring techniques using vibration measurements, *Mechanical Systems and Signal Processing*, vol. 15, pp. 905-922, 2001.
- [112] Huang, N., Shen, Z., Long, S., Wu, M., Shih, H., Zheng, Q., Yen, N., Tung, C., and Liu, H.: The empirical mode decomposition and the Hilbert spectrum for nonlinear and non-stationary time series analysis, *Proceedings of the Royal Society of London A*, vol. 454, pp. 903-995, 1998.
- [113] Huang, N., Wu, M., Long, S., Shen, S., Qu, W., Gloersen, P., and Fan, K.: A confidence limit for the empirical mode decomposition and Hilbert spectral analysis, *Proceedings of the Royal Society of London. Series A: Mathematical, Physical and Engineering Sciences*, vol. 459, p. 2317, 2003.
- [114] Gaberson, H. A.: The use of wavelets for analyzing transient machinery vibration, *Sound and Vibration*, vol. 36, pp. 12-17, 2002.
- [115] Sheen, Y. T. and Hung, C. K.: Constructing a wavelet-based envelope function for vibration signal analysis, *Mechanical Systems and Signal Processing*, vol. 18, pp. 119-126, 2004.
- [116] Yoshida, A., Ohue, Y., and Ishikawa, H.: Diagnosis of tooth surface failure by wavelet transform of dynamic characteristics, *Tribology International*, vol. 33, pp. 273-279, 2000.
- [117] Wang, W. and McFadden, P.: Application of wavelets to gearbox vibration signals for fault detection, *Journal of Sound and Vibration*, vol. 192, pp. 927-939, 1996.
- [118] Yan, R. and Gao, R.: Hilbert–Huang transform-based vibration signal analysis for machine health monitoring, *IEEE Transactions on Instrumentation and Measurement*, vol. 55, pp. 2320-2329, 2006.

- [119] Rai, V. and Mohanty, A.: Bearing fault diagnosis using FFT of intrinsic mode functions in Hilbert-Huang transform, *Mechanical Systems and Signal Processing*, vol. 21, pp. 2607-2615, 2007.
- [120] Li, R. and He, D.: Hilbert transform based gearbox fault diagnosis, in *62nd Meeting of the Society for Machinery Failure Prevention Technology*, Virginia Beach, VA, 2008.
- [121] Yu, D., Cheng, J., and Yang, Y.: Application of EMD method and Hilbert spectrum to the fault diagnosis of roller bearings, *Mechanical Systems and Signal Processing*, vol. 19, pp. 259-270, 2005.
- [122] Yang, J., Lei, Y., Lin, S., and Huang, N.: Hilbert-Huang based approach for structural damage detection, *Journal of engineering mechanics*, vol. 130, p. 85, 2004.
- [123] Yang, Z., Yang, L., and Qi, D.: Detection of spindles in sleep EEGs using a novel algorithm based on the Hilbert-Huang transform, *Wavelet Analysis and Applications*, pp. 543-559, 2007.
- [124] Huang, H. and Pan, J.: Speech pitch determination based on Hilbert-Huang transform, *Signal Processing*, vol. 86, pp. 792-803, 2006.
- [125] Wu, Z. and Huang, N. E.: A study of the characteristics of white noise using the empirical mode decomposition method, *Proceedings of the Royal Society of London. Series A: Mathematical, Physical and Engineering Sciences*, vol. 460, p. 1597, 2004.
- [126] Randall, R.: A new method of modeling gear faults, *Journal of Mechanical Design*, vol. 104, pp. 259-267, 1982.
- [127] Endo, H. and Randall, R.: Enhancement of autoregressive model based gear tooth fault detection technique by the use of minimum entropy deconvolution filter, *Mechanical Systems and Signal Processing*, vol. 21, pp. 906-919, 2007.
- [128] Ljung, L.: *System Identification: Theory for the User*. New Jersey, USA: Prentice Hall, 1999.

- [129] Benesty, J. and Huang, Y.: *Adaptive signal processing: applications to real-world problems*: Springer, 2003.
- [130] Ljung, L. and Gunnarsson, S.: Adaptation and tracking in system identification--a survey, *Automatica*, vol. 26, pp. 7-21, 1990.
- [131] Donoho, D.: De-noising by soft-thresholding, *IEEE Transactions on Information Theory*, vol. 41, pp. 613-627, 1995.
- [132] Ching, P., So, H., and Wu, S.: On wavelet denoising and its applications to time delay estimation, *IEEE Transactions on Signal Processing*, vol. 47, pp. 2879-2882, 2002.
- [133] Mallat, S.: A theory for multiresolution signal decomposition: The wavelet representation, *IEEE transactions on pattern analysis and machine intelligence*, vol. 11, pp. 674-693, 1989.
- [134] He, D. and Bechhoefer, E.: Development and validation of bearing diagnostic and prognostic tools using HUMS condition indicators, in *2008 IEEE Aerospace Conference, AC, March 1, 2008 - March 8, 2008*, Big Sky, MT, United states, 2008.
- [135] Richard O. Duda, Peter E. Hart, and Stork, D. G.: *Pattern Classification (2nd Edition)*: A Wiley-Interscience Publication, 2001.
- [136] Cover, T. and Hart, P.: Nearest neighbor pattern classification, *Information Theory, IEEE Transactions on*, vol. 13, pp. 21-27, 1967.
- [137] Niizeki, S.: Ceramic bearings for special environments, *Development of NSK Extra-Capacity Sealed-Clean TM Roll Neck Bearings*, vol. 64, p. 17, 2000.
- [138] Pujari, V. and Collins, W.: All ceramic bearing, Google Patents, 2000.
- [139] Dempsey, P., Certo, J., and Morales, W.: Current status of hybrid bearing damage detection, *Tribology Transactions*, vol. 48, pp. 370-376, 2005.

- [140] BearingWorks.Inc.: *Ring and Ball Materials*, 2011. Available: http://www.bearingworks.com/technical_data/ring_and_ball_materials.php.
- [141] WS.Hampshire.Inc.: *Plastic material properties*, 2011. Available: <http://www.wshampshire.com/plastic-properties.html>.
- [142] Stack, J. R., Harley, R. G., and Habetler, T. G.: An amplitude modulation detector for fault diagnosis in rolling element bearings, *IEEE Transactions on Industrial Electronics*, vol. 51, pp. 1097-1102, 2004.
- [143] McFadden, P. and Smith, J.: Vibration monitoring of rolling element bearings by the high-frequency resonance technique--a review, *Tribology International*, vol. 17, pp. 3-10, 1984.
- [144] Tandon, N. and Choudhury, A.: A review of vibration and acoustic measurement methods for the detection of defects in rolling element bearings, *Tribology International*, vol. 32, pp. 469-480, 1999.
- [145] McNerny, S. and Dai, Y.: Basic vibration signal processing for bearing fault detection, *IEEE Transactions on Education*, vol. 46, pp. 149-156, 2003.
- [146] Patil, M., Mathew, J., and RajendraKumar, P.: Bearing signature analysis as a medium for fault detection: A review, *Journal of Tribology*, vol. 130, pp. 014001-014007, 2008.
- [147] Pao, Y., Gajewski, R., and Ceranoglu, A.: Acoustic emission and transient waves in an elastic plate, *The Journal of the Acoustical Society of America*, vol. 65, pp. 96-105, 1979.
- [148] Miller, R., A. Pollock, D. Watts, J. Carlyle, A. Tafuri, and Yezzi, J.: A reference standard for the development of acoustic emission pipeline leak detection techniques, *NDT & E International*, vol. 32, pp. 1-8, 1999.
- [149] Bailey, C.: Acoustic emission for in-flight monitoring on aircraft structures, *Materials Evaluation*, vol. 34, pp. 165-171, 1976.

- [150] Frankenstein, B., Hentschel, B., Schubert, F., and Schubert, L.: Condition monitoring of windmill rotor blades, in *Proceedings of the Fourth European Workshop on Structural Health Monitoring*, Cracow, Poland, 2008.
- [151] Gong, Z., Nyborg, E., and Oommen, G.: Acoustic emission monitoring of steel railroad bridges, *Materials Evaluation*, vol. 50, pp. 883-887, 1992.
- [152] Ohtsu, M., Shigeishi, M., Iwase, H., and Koyanagit, W.: Determination of crack location, type and orientation in concrete structures by acoustic emission, *Magazine of Concrete Research*, vol. 43, pp. 127-134, 1991.
- [153] Choudhury, A. and Tandon, N.: Application of acoustic emission technique for the detection of defects in rolling element bearings, *Tribology International*, vol. 33, pp. 39-45, 2000.
- [154] Mba, D. and Rao, R.: Development of acoustic emission technology for condition monitoring and diagnosis of rotating machines; bearings, pumps, gearboxes, engines and rotating structures, *The Shock and Vibration Digest*, vol. 38, 2006.
- [155] Li, R. and He, D.: Hilbert-Huang transform based acoustic emission signal quantification for rotational machine health monitoring and diagnostics in *MFPT: The Applied Systems Health Management Conference 2011*, Virginia Beach, VA, May 10-12, 2011.
- [156] James Li, C. and Li, S.: Acoustic emission analysis for bearing condition monitoring, *Wear*, vol. 185, pp. 67-74, 1995.
- [157] Tan, C. and Mba, D.: Identification of the acoustic emission source during a comparative study on diagnosis of a spur gearbox, *Tribology International*, vol. 38, pp. 469-480, 2005.
- [158] Tan, C., Irving, P., and Mba, D.: A comparative experimental study on the diagnostic and prognostic capabilities of acoustics emission, vibration and spectrometric oil analysis for spur gears, *Mechanical Systems and Signal Processing*, vol. 21, pp. 208-233, 2007.

- [159] Li, R., He, D., and Bechhoefer, E.: Gear fault detection for the split torque transmission system using acoustic emission and vibration signals, in *Annual Conference of the Prognostics and Health Management Society* San Diego, CA, 2009.
- [160] Yoshioka, T., Korenaga, A., Mano, H., and Yamamoto, T.: Diagnosis of rolling bearing by measuring time interval of AE generation, *Journal of Tribology*, vol. 121, p. 468, 1999.
- [161] Morhain, A. and Mba, D.: Bearing defect diagnosis and acoustic emission, *Proceedings of the Institution of Mechanical Engineers, Part J: Journal of Engineering Tribology*, vol. 217, pp. 257-272, 2003.
- [162] Kaewkongka, T. and Au, Y.: Application of acoustic emission to condition monitoring of rolling element bearings, *Measurement & Control*, vol. 34, pp. 245-7, 2001.
- [163] Tandon, N. and Nakra, B.: Defect detection in rolling element bearings by acoustic emission method, *Journal of acoustic emission*, vol. 9, pp. 25-28, 1990.
- [164] Mba, D.: The use of acoustic emission for estimation of bearing defect size, *Journal of Failure Analysis and Prevention*, vol. 8, pp. 188-192, 2008.
- [165] Singh, A., Houser, D., and Vijayakar, S.: Detecting gear tooth breakage using acoustic emission: a feasibility and sensor placement study, *Journal of Mechanical Design*, vol. 121, pp. 587-593, 1999.
- [166] Tandon, N. and Mata, S.: Detection of defects in gears by acoustic emission measurements, *Journal of acoustic emission*, vol. 17, pp. 23-27, 1999.
- [167] Pullin, R., Clarke, A., Eaton, M., Holford, K. M., Evans, S., and McCorry, J.: Detection of cracking in gear teeth using acoustic emission, *Applied Mechanics and Materials*, vol. 24, pp. 45-50, 2010.

- [168] Li, R., He, D., and Bechhoefer, E.: Gear fault location detection for split torque gearbox using AE sensors, in *the 2010 American Helicopter Society 66th Annual Forum*, Phoenix, AZ, 2010.
- [169] Cui, J., Zheng, X., Li, M., Li, Z., and Liu, D.: Health diagnosis for aircraft based on EMD and neural network, in *2009 International Conference on Measuring Technology and Mechatronics Automation*, Zhangjiajie, Hunan, China, April, 2009.
- [170] Xu, T. and Feng, Z.: Tool wear identifying based on EMD and SVM with AE sensor, in *The Ninth International Conference on Electronic Measurement and Instruments*, Beijing, China, August, 16-18, 2009.
- [171] Tan, C. and Mba, D.: Limitation of acoustic emission for identifying seeded defects in gearboxes, *Journal of Nondestructive Evaluation*, vol. 24, pp. 11-28, 2005.
- [172] Toutountzakis, T. and Mba, D.: Observations of acoustic emission activity during gear defect diagnosis, *NDT & E International*, vol. 36, pp. 471-477, 2003.
- [173] Freudinger, L. C., Lind, R., and Brenner, M. J.: Correlation filtering of modal dynamics using the Laplace wavelet, in *16th international modal analysis conference*, Santa Barbara, CA, February 2-5, 1998.
- [174] Everson, C. and Hoessein Cheraghi, S.: The application of acoustic emission for precision drilling process monitoring, *International Journal of Machine Tools and Manufacture*, vol. 39, pp. 371-387, 1999.
- [175] Dolinek, S. and Kopa, J.: Acoustic emission signals for tool wear identification, *Wear*, vol. 225, pp. 295-303, 1999.
- [176] Donoho, D. and Johnstone, J.: Ideal spatial adaptation by wavelet shrinkage, *Biometrika*, vol. 81, p. 425, 1994.

VITA

NAME: Ruoyu Li

EDUCATION: B.S., Automatic Control, Guilin Institute of Electronic Technology, Guilin, China, 2002

M.S., Control Theory and Control Engineering, Guilin Institute of Electronic Technology, Guilin, China, 2005

ACADEMIC EXPERIENCE: Research Assistant, Department of Mechanical and Industrial Engineering, University of Illinois at Chicago, Chicago, Illinois, 2008 – 2011

TEACHING EXPERIENCE: Lecturer, College of Computer and Control Engineering, Guilin University of Electronic Technology, Guilin, China, 2005 – 2007

Teaching Assistant, Department of Mechanical and Industrial Engineering, University of Illinois at Chicago, Illinois, 2010

PUBLICATIONS: He, D., Li, R., Zhu, J., and Zade, M.: A data mining based full ceramic bearing fault diagnostic system using AE sensors, *IEEE Transactions on Neural Networks* (accepted), 2011.

Li, R. and He, D.: Rotational machine health monitoring and fault detection using EMD based acoustic emission feature quantification, *IEEE Transactions on Instrumentation and Measurement* (accepted), 2011.

Li, R., Sopon, P., and He, D.: Fault features extraction for bearing prognostics, *Special Issue on Condition-based Maintenance: Theory and Applications, Journal of Intelligent Manufacturing* (to appear), 2011. Available: <http://www.springerlink.com/content/y0837q18265w0855/>

He, D., Li, R., and Bechhofer, E.: Stochastic modeling of damage physics for mechanical component prognostics using condition indicators, *Special Issue on Machinery Health Monitoring, Diagnosis and Prognosis, Journal of Intelligent Manufacturing* (to appear), 2011. Available: <http://www.springerlink.com/content/h8p424h76364p842/>

Bechhofer, E., Li, R., and He, D.: Quantification of condition indicator performance on a split torque gearbox, *Special Issue on Machinery Health Monitoring, Diagnosis and Prognosis, Journal of Intelligent Manufacturing* (to appear), 2011.

Available:

<http://www.springerlink.com/content/p177840x16g1l412/>

Li, R. and He, D.: Mechanical transmission system multiple faults diagnosis using Hilbert-Huang transform, *International Journal for Manufacturing Science & Technology*, vol. 11, No. 2, pp. 33 – 42, 2010.

He, D., Bechhoefer, E., Ma, J., Li, R., and Dempsey, P.: A particle filtering based approach for gear prognostics in *Diagnostics and Prognostics of Engineering Systems: Methods and Techniques*, Edited by S. Kadry, IGI Global, New York, NY, 2012.

He, D., Li, R., Zade, M., Zhu, J.: Development and evaluation of AE based condition indicators for full ceramic bearing fault diagnosis, *Proceedings of the 2011 IEEE PHM Conference*, Denver, CO, June 21 – 23, 2011.

He, D. and Li, R.: A new vibration signal processing method for gearbox fault detection, *Proceedings of the 2011 IEEE PHM Conference*, Denver, CO, June 21 – 23, 2011.

He, D., Li, R., Zade, M., and Zhu, J.: An investigation on full ceramic bearing fault diagnosis using AE sensors, *Proceedings of the 24th International Congress on Condition Monitoring and Diagnostics Engineering Management (COMADEM2011)*, Stavanger, Norway, May 30 - June 1, 2011.

Li, R. and He, D.: Hilbert-Huang transform based acoustic emission signal quantification for rotational machine health monitoring and diagnostics, *Proceedings of The 2011 Conference of the Society for Machinery Failure Prevention Technology*, Virginia Beach, VA, May 10 – 13, 2011.

He, D. and Li, R.: Using HHT based acoustic emission feature quantification for rotating machine fault detection, *Proceedings of the 2011 American Helicopter Society (AHS) International Forum*, Virginia Beach, VA, May 2 – 5, 2011.

Li, R. and He, D.: Development of an advanced narrow-band interference cancellation method for gearbox fault detection, *Proceedings of the 2011 American Helicopter Society (AHS) International Forum*, Virginia Beach, VA, May 2 – 5, 2011.

He, D., Menon, P., Li, R., Seckiner, S., and Bechhoefer, E.: Gear fault location detection for split torque gearbox using AE sensors, *Proceedings of the 2010 Annual Conference of the Prognostics and Health Management Society*, Portland, OR, October 10 – 16, 2010.

He, D., Li, R., and Bechhofer, E.: Split torque gearbox fault diagnosis using AE sensors, *Proceedings of the 2010 Industrial Engineering Research Conference*, Cancun, Mexico June 5 – 9, 2010.

He, D., Panyala, A., Li, R., and Ma, J.: The use of vibration signals for ceramic bearing prognostics, *Proceedings of the 2010 Industrial Engineering Research Conference*, Cancun, Mexico June 5 – 9, 2010.

He, D., Li, R., and Bechhofer, E.: Split torque type gearbox fault detection using acoustic emission and vibration sensors, *Proceedings of the 2010 IEEE International Conference on Networking, Sensing and Control*, Chicago, IL, April 10 – 12, 2010.

Li, R., Ma, J., Panyala, A., and He, D.: Hybrid ceramic bearing prognostics using particle filtering, *Proceedings of The 2010 Conference of the Society for Machinery Failure Prevention Technology*, Huntsville, AL, April 13 – 15, 2010.

Li, R., He, D., and Bechhoefer, E.: Gear fault location detection for split torque gearbox using AE sensors, *Proceedings of the 2010 American Helicopter Society (AHS) International Forum*, Phoenix, AZ, May 10 – 13, 2010.

Li, R., He, D., and Bechhoefer, E.: Investigation on fault detection for split torque gearbox using acoustic emission and vibration signals, *Proceedings of 2009 Annual Conference of the Prognostics and Health Management Society*, San Diego, CA, September 27 – October 1, 2009.

He, D., Li, R., and Bechhoefer, E.: Stochastic modeling of damage physics for mechanical component prognostics using condition indicators, *Proceedings of ASME IDETC/CIE*, San Diego, CA, August 30 – September 2, 2009.

Li, R. and He, D.: Using Hilbert-Huang transform for gearbox fault diagnosis under light loading conditions, *Proceedings of 2009 MFPT Conference*, Dayton, OH, April 28 – 30, 2009.

Li, R., Sopon, P., and He, D.: Fault features extraction for bearing prognostics, *Proceedings of International Conference on Industrial Engineering and Systems Management*, Montreal, Canada, May 13 – 15, 2009.

Bechhoefer, E., Li, R., and He, D.: Quantification of condition indicator performance on a split torque gearbox, *Proceedings of the 2009 AHS Forum*, Grapevine, TX, May 27 – 29, 2009.

Li, R., He, D., and Bechhoefer, E.: On quantification of bearing damage for lifecycle prognostics, *Proceedings of the 2009 AHS Forum*, Grapevine, TX, May 27 – 29, 2009.

Li, R. and He, D.: Hilbert-Huang transform based gearbox fault diagnosis, *Proceedings of the 2008 MFPT Conference*, Virginia Beach, VA, May 6 – 8, 2008.